Development of novel polymeric and composite Nano-Structured Micro-Porous Materials for impact resistance applications

Pier Paolo Greco

School of Chemical Engineering and Advanced Materials

Newcastle University, United Kingdom

A Thesis Submitted to Newcastle University for the Degree of Doctor of Philosophy in Chemical Engineering

Newcastle Upon Tyne, 2014

Disclaimer

This thesis is submitted in fulfilment of the requirements for the degree of Doctor of Philosophy at Newcastle University, Newcastle upon Tyne, United Kingdom. All the studies described within are solely my work otherwise expressly stated, and were undertaken at the School of Chemical Engineering and Advanced Materials under the guidance and supervision of Professor Galip Akay and Professor Stephen Bull between March 2010 and August 2013.

I certify that none of the material offered in this thesis has been previously submitted for a degree or any other qualification at the above or any other university or institute.

Neither the author nor the Newcastle University at Newcastle upon Tyne accepts any liability for the contents of this document.

Abstract

Impact resistant materials (IRMs) are widely used in the automotive and packaging industry. Their main purpose is the protection of the transported occupants or goods. Cellular materials as well as structures combine lightness with large deformation under load. The energy absorption mechanism is provided by limiting the peak load and ensuring the elastic deformation of the IRMs. Polymeric foams are largely used as IRMs due to their cellular structure. Prediction of the foam properties in terms of Young's Modulus (Elastic Modulus) and the onset of Plateau Region can be related to the foam density and the mechanical properties of the bulk material (Gibson and Ashby model). The structure of the foam is only partly accounted for in the Gibson and Ashby model in terms of material density.

However, it is possible to produce cellular materials with the same density but very different internal architectures. This cannot easily be exploited in conventional polymer foams but the processing of High Internal Phase Emulsion (PolyHIPE) and its polymerisation route to produce PolyHIPE Polymers (PHPs) can produce materials with very different structures. Experiments have revealed that the PHPs properties are dictated by their detailed structure. Elastic PHPs with: 1) varying ratio of polymerizable oil phase with respect to aqueous phase and 2) varying mixing time/energy input were produced and tested by mechanical compression at different temperatures and strain rates. The elastic modulus increases with a quadratic law as a function of the polymerizable oil phase content of the HIPE when the mixing time is the same, as predicted by the model. The Specific Absorption Energy (SAE), represented by the area under the stress-strain curve, increases in a similar way.

Increasing mixing time on HIPE has the effect of modifying the cellular structure. Smaller pores and narrower distribution of pores are observed. Such features are consistent for any set of PHPs densities and represent a design tool when some specific mechanical characteristics are prescribed.

The assessment of process-structure-properties relationships was performed by combining the mechanical response of the various PHPs with the imaging of their structure by Scanning Electron Microscopy. The properties of PHPs were benchmarked with reference to two commercially available products. One material is characterised by a porous structure with a relatively high Young's Modulus, while the other by a non-porous and composite-like solid structure with lower elastic modulus. The properties of the PHPs can be engineered to shift from a foam-like material to a composite-like through the processing parameters which in turn

modify the material porous structure. The temperature has very limited effect on the PHPs material unlike for the reference commercial materials.

The enhancement of properties (increasing Elastic Modulus and SAE) induced by changing the processing route are remarkable for such a class of porous materials. When plotted on a Modulus-Density chart, the PHPs fill an existing material-chart gap, representing a new class of materials and opening new possibilities as IRMs.

Presentations and publications

1. Akay, G., P.P. Greco, H. Hasan and D. Thumbarathy (2013), *Preparation of Catalytic Hyper-cross-linked PolyHIPE Polymers*. EPF 2013 European Polymer Congress, 16-21 June 2013, Pisa, Italy.
2. Greco, P. P., S. J. Bull and G. Akay (2012). *Improved Mechanical behaviour of Hierarchical Porous foams by Nature Inspired PolyHIPE Processing*. Cellular Materials - CELLMAT 2012, 7-9 November 2012. Dresden, Germany
3. Paper to be Submitted: Greco, P. P., S. J. Bull and G. Akay (2013). "*Effects of processing on structure and properties of PolyHIPE polymers*". Polymer Engineering & Science.

Dedication

I dedicate this work to Veronica and our Families, Regina, Giampaolo, Enzo, Carla, Giuseppe and Giacomo for their continuous support and never-ending patience. To Chloe, for bringing so much happiness.

Acknowledgement

This greatly challenging experience would not have been possible without the contribution of my supervisors, Professor Akay and Professor Bull to whom I express my deepest gratitude.

My special thanks go to my Sponsoring Company Try & Lilly Ltd, in the persons of Tony Jennions and Margaret Doak, for allowing me to contribute to the project.

As this journey began, I was happily introduced into the Process Intensification and Miniaturisation (PIM) Group at the School of Chemical Engineering and Advanced Materials (CEAM) at Newcastle University and in particular, my sincere thanks go to Dr Teresa Ndlovu, Dr Kui Zhang and Dr Bandara Dissanayake for being supportive, inspirational and, above all, close friends.

Many thanks to the "Workshop and Millennium Lab guys" for their unlimited patience, readiness and for always surprising me with their outcomes, Neville Dickman for his efforts with the mechanical test frames and Pauline Carrick of Advanced Chemical and Material Analysis (ACMA) for the microscopy sessions and finally to the staff people of CEAM I have been dealing with.

A very special thanks go to Luca Biselli, a precious friend and a talented architect.

Table of Contents

List of Figures

List of Tables

Abbreviations and Nomenclature

Chapter 1 – Introduction

"Although human subtlety makes a variety of inventions [...], it will never devise an invention more beautiful, more simple, or more direct than does nature, because in her inventions nothing is lacking, and nothing is superfluous".

- Leonardo da Vinci

Impact resistant materials (IRMs) are nowadays gaining increasing attention for multiple reasons; among the first and most influential, the protection of military personnel by means of body armours and helmets against projectiles and high velocity low-mass objects (Erwin, 2009). More common protective devices such as helmets for cyclists are available for a larger audience. Safety helmets used for protection by operators in various industrial activities also represent a wide category. Although the velocities that these devices are designed to work at are far lower than the ballistic velocity (< 1000 m/s), they are also subject to higher and higher quality and performance standards.

Many materials already perform as *Impact Resistant Materials* (IRMs); among these, a particularly suitable class of materials is represented by *Foams* (Gibson and Ashby, 1997; Lu and Yu, 2003). Although a wide variety of synthetic foams can be produced to satisfy diversified requirements, addressing multiple criteria such as light-weight, strength and comfort is still an open challenge (Ashby, 2011).

It should be pointed out that the performance of any material is dictated by multiple factors that are very often in contradiction. Factors like cost, availability, and process feasibility may be addressed by an adequate level of preliminary investigations but, an understanding of the impact of processing on the properties of a material may not be fully understood without considering the effects on its structure. Therefore, any final usage of a material is likely to represent the best possible compromise among a series of criteria.

For these reasons, many research drivers aim at maximising the material performance by relating it to material structure. Thus, the development of a novel class of materials that is designed with a newer approach and whose structure and properties can be related to their processing is highly desirable.

This research study has been inspired by analysing the behaviour of some naturally occurring materials as IRMs. The design by nature (also known as bio-mimicry) of the orange fruit skin has been investigated and it has been recognised that its remarkable performance as an IRM is provided by an ordered (hierarchical) structural arrangement of the fruit inner porous skin. Such a structural

arrangement exploits the variation of the skin pore diameter towards the inner part of the fruit. This hierarchical layout results in an outstanding impact absorption capacity.

While foams can be produced from almost any class of materials, the hierarchy of the porous structure cannot be controlled at any satisfactory level despite some newer kind of synthetic foams that incorporate other compounds to create foams-within-foams. Thus, the processing of foams with a hierarchical porous structure cannot yet be controlled to achieve desired properties or structures (Klempner *et al.*, 2004).

A novel class of hierarchically porous materials has been produced by polymerising *High Internal Phase Emulsions* (PolyHIPEs). This class of materials is characterised by an intrinsic hierarchy among the pores whose diameter can be as little as few microns, unlike conventional foams whose pores can be as large as several millimetres. Another unique characteristic of PolyHIPEs is the presence of interconnecting pores whose size can be in the range of hundreds of nanometres. For these dimensional characteristics, PolyHIPEs are known as Nano-Structured Micro-Porous Materials (NSMPMs). Moreover, the presence of these interconnecting pores has been successfully exploited in fundamental research fields such as in chemical catalysis, membrane design, tissue engineering to name just a few.

The tailorability of the PolyHIPEs structure has been investigated in the light of the bio-mimicking of the orange fruit skin. A relevant degree of control on the pore size and distribution of PolyHIPEs formulated with an elastomer to produce *Elastic PolyHIPEs* (EPHPs) has been achieved by adopting two design strategies.

An increase in the polymerizable (solid) phase of the EPHPs has resulted in the enhancement of the elastic modulus and energy absorption properties, mainly due to an increase of the thickness of the cellular structure.

The other strategy instead has focussed on the processing of the HIPEs. Longer *homogenisation time* (the additional time the emulsion is stirred after the addition of the water phase has been completed) resulted in a remarkable modification of the structure. Smaller pore diameter and narrower distribution have been obtained and, consequently, dramatic changes in the mechanical performance have been observed.

The relationship between the Process-Structure-Properties of the EPHPs has thus been studied and established. The mechanical performance in terms of energy

absorption has increased when both solid content and homogenisation time increased with the latter being more effective in modifying the hierarchical porous structure.

Furthermore, HIPE processing (increased homogenisation time) has revealed that the structure of the resulting EPHPs can be modified to such an extent that EPHPs may behave either as foams or as composites (spring-like behaviour) and that EPHPs hierarchical structure can be tailored to meet and exceed a required level of energy absorption as provided by two commercially available IRMs.

In summary, PolyHIPEs are polymeric porous materials characterised by a hierarchical pore structure layout which can be tailored at processing levels unlike conventional foams. PolyHIPEs mechanical behaviour is remarkably different from that of foams thanks to its hierarchical pores variable size and distribution. This layout has intrinsic advantages and can be modified and controlled by process variables of PolyHIPEs manufacturing to create lighter, more robust and more effective IRM compared to conventional foams.

1.1. Aims and objectives

This project aims at demonstrating that the ability to modify the structure of elastic-PolyHIPEs (EPHPs) materials is of fundamental importance, particularly when the materials are characterised by a unique (hierarchical) structural layout. The ability to modify the structure in a controlled and predictable way enables the design of a material, or class of materials, that behaves in a very specific manner.

In this study, the process-structure-properties relationship for the development of EPHPs as impact resistant materials (IRMs) has been established.

As the structure of EPHPs dominates their performances, this aim has been further accomplished by comparing the EPHPs performances with those of two commercially available IRMs.

Such commercially available materials, known as *GPhlex* and *D3O* have been selected due to their distinct characteristics. Although their structural details are provided in the dedicated sections, it is worth anticipating that GPhlex is a porous vinyl-nitrile based foam material, while D3O is a non-porous composite material made of a less stiff elastic matrix which incorporates dense-solid spherical particles.

While both materials provide distinct mechanical properties as reflected by the stress vs. strain curves, the influence of their structure is limited. The stiffness depends mainly on the materials they are made from and the overall mechanical

behaviour is affected more by such materials than their structure. The importance of the benchmarking materials performance as IRMs and its comparison with that of the EPHPs becomes particularly evident when the compression test loading conditions and the temperature are varied. It can be anticipated that the performance of the reference materials resulted to be affected by the testing conditions (loading rate and temperature). As a consequence, the need for studying and developing EPHPs that would perform satisfactorily under different conditions emerged and constantly guided the study.

The objectives set in order to accomplish the aim of this study are:

i. Exploiting the existence of structural similarities (hierarchical structure) between nature design protective shell of the orange fruits and PolyHIPEs

ii. Modifying the amount of polymerizable phase (solid content) and measuring its impact towards the required performance as an IRM as set by two commercially available materials

iii. Determination of EPHPs stiffness and energy absorption characteristics such as Young's modulus and specific absorbed energy from stress vs. strain curves of EPHPs produced with different solid content and homogenisation time

iv. Identification and quantification of structural modifications of EPHPs by means of scanning electron microscopy

v. Evaluation of mechanical energy input due to mixing time and its effect on structural changes

vi. Evaluation of the effects of temperature variations on the EPHPs (and benchmarking commercially available materials) mechanical performance by compression testing at low, room and high temperature

vii. Evaluation of the effects of variable compression strain rate and comparison with effect of temperature to assess the time-temperature superposition principle

viii. Determination of the stability transfer time for HIPEs in order to identify optimal emulsion stability window and maximum emulsion transfer/pumping time

ix. Implementation of the Gibson and Ashby model for the prediction of EPHPs Young's modulus

x. Plot a property chart that qualitatively shows the range of properties EPHPs and the two benchmark materials features (Stiffness and Structure Filling)

xi. Identification of a gap in the material selection charts (Ashby Charts) and filling of such a gap with EPHPs

All the objectives have been met by means of rigorous testing and statistical analysis (where applicable) as described in the methodology chapter.

1.2. Project's background

This section provides the background of the project and the approach that was adopted to fulfil the aims. IRMs with lighter weight, more effective impact energy absorbance and more comfortable to wear were, in fact, the ultimate objective of the study, for which the concept of bio-mimicry, also known as the "Design from Nature", was applied at an early stage.

Along with the bio-mimicry concept, constant material properties/structure inputs were provided by the benchmark materials. These reference materials not only provided the operating scenario but also the project driving factor. It is in fact determined through this study that benchmark materials performances were used to produce EPHPs with different solid content and porous structure.

An ideal project map, called structure-property plan is shown in Fig. 1-1. The plan shows the two benchmark materials (GPhlex and D3O) main mechanical and structural characteristics: stiffness and porosity. In addition, the map shows where a low density ethylene vinyl acetate copolymer (EVA foam) would be. While GPhlex is a porous material and has a higher elastic modulus (i.e. stiffness), D3O is a less stiff composite material. The EVA foam is a much more compliant material due to its typical low density. It is worth noting that the three materials are located in different positions of the map.

Qualitatively, GPhlex is close to the maximum stiffness and at an intermediate porosity while D3O is a non-porous but less stiff material. Moreover, with reference to low density/highly porous EVA foams, they are compliant therefore are located on left hand side of the plan. When comparing all the materials it can be seen that porous materials can be stiffer than composites.

Such differences highlight that a gap between the two benchmark materials exists and it offers the opportunity to design materials that can offer improved properties. Desired properties such as light-weight and high stiffness therefore require the development of a novel class of materials, located on the right hand side of the plan as shown by the dashed area.

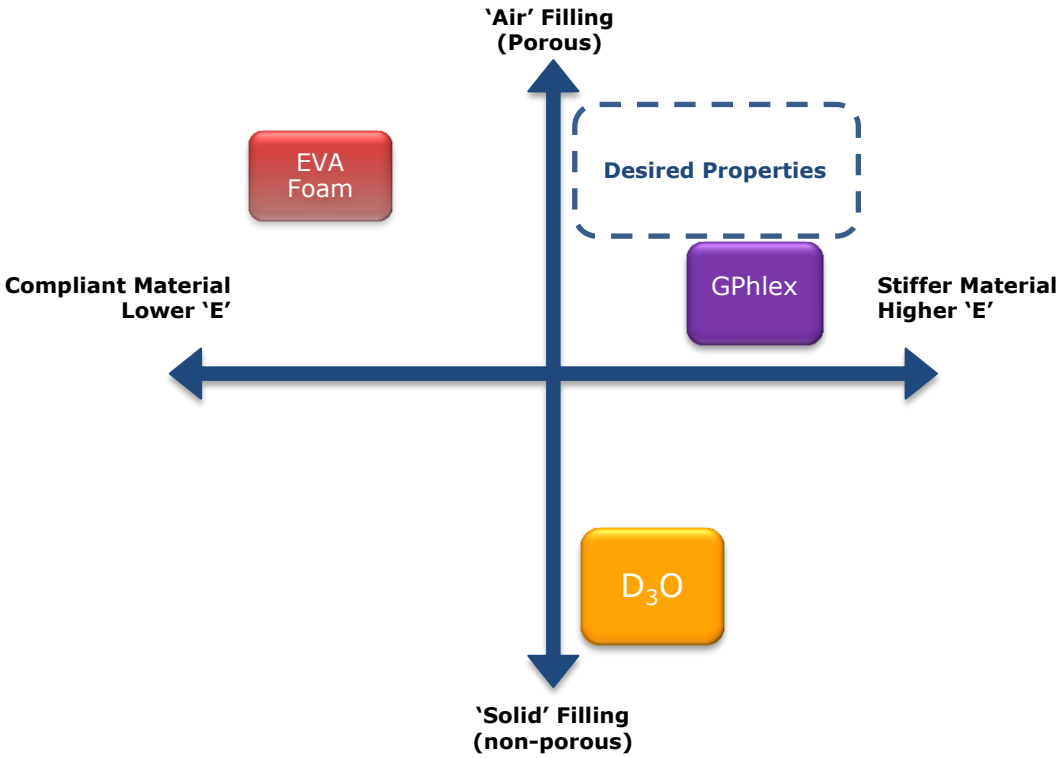

Fig. 1-1: Structure-Properties Plan. The materials are located according to their filling component, either solid or air (vertical axis) and stiffness (Young's modulus) on the horizontal axis. Dashed area represents the desired properties a novel material should possess (high porosity/stiffness).

Inspiration from nature-designed protective shells for fruits like oranges, nutshells and coconuts provided the understanding of the way that natural materials structure is adapted to improve performances, while its comparison with PolyHIPEs highlighted their structural hierarchy similarities. A particularly effective comparison was that between Elastic PolyHIPEs (EPHPs) and orange skin in terms of elastic, porous structures with varying diameter, a layout that has enabled Nature to effectively protect the fruit from a free fall of up to 5 metres from tall orange trees.

Varying pore diameter layouts of elastic protective layers designed by nature were studied, and the mimicking of such effective hierarchical structures was done by manipulating two factors that affect the EPHPs outcome: 1) solid content (or oil phase content) and 2) the homogenisation time (t_H) that is the time of stirring that follows the formation of the High Internal Phase Emulsion (HIPE).

A schematic project and process development flow diagram illustrated in Fig. 1-2. The nature design served as an inspiring model in which the hierarchical layout was determined to be the distinctive sign for the specific function of impact energy absorption and the EPHPs were used as mimicking synthetic materials. Their tailorability in terms of porosity, average pore size diameter and distribution, as

well as pores' wall thickness by means of process parameters modification was the primary objective of this study.

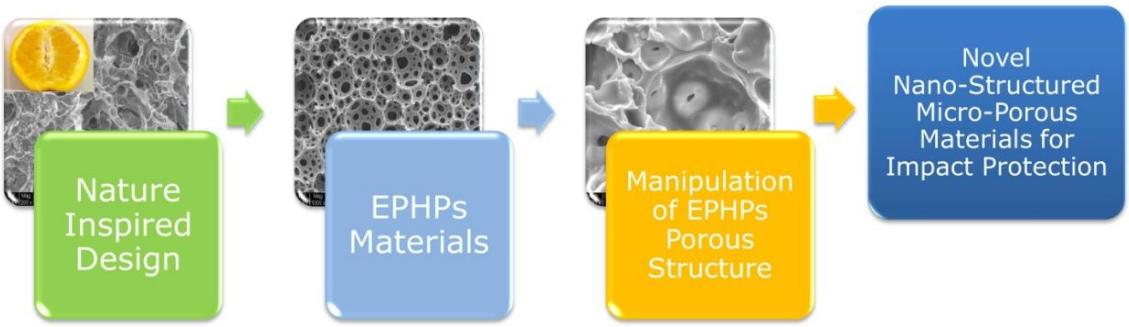

Fig. 1-2: schematic project development flow diagram. Design and nature (biomimetics) as inspiring concepts were applied to exploit PolyHIPEs hierarchical structure similarities with those of natural materials and later modified to produce novel impact protection materials. The background pictures are actual Scanning Electron Microscopy images of produced EPHPs samples.

The steps that constituted the Project Development are detailed in the next sections and chapters. Each of them provides an in-depth approach to the cause-effect relationships between the EPHPs structure and its mechanical properties, as well as how the processing parameters affect and control the structure. Fig. 1-3 shows the typical two approaches that can be used to enhance the mechanical properties of a material: 1) the direct changes in the manufacturing (i.e. processing conditions, materials used, etc.) or 2) processing the material to modify its hierarchical porous structure to seek adequate mechanical properties.

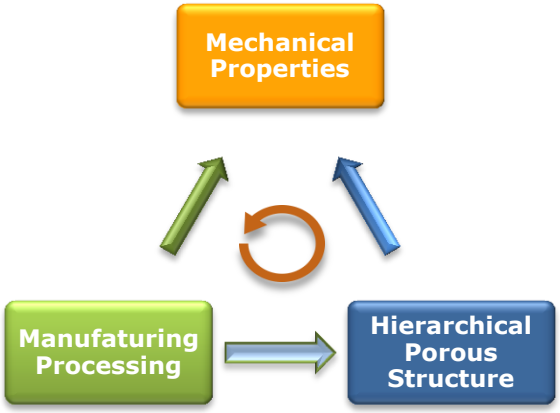

Fig. 1-3: EPHPs Processing-Structure-Properties relationship cycle represents an effective way to gather the effects that manufacturing process has on EPHPs Structure and how the changes in the structure are reflected by the Mechanical Properties.

The manufacturing process of materials changes to obtain a set of desired mechanical properties can generally be termed as a "*trial and error*" scheme, while that of including the step of modifying also the structure, which in this case is the hierarchical porous structure to provide the distinctive feature of the PHPs, is termed "*Knowledge Based*" approach.

Throughout the next chapters, this approach will become evident as it was understood that the manipulation of the structure produced more remarkable results than the manufacturing of different PHPs using a single process alone.

The cyclic symbol in the centre of Fig. 1-3 means that the approach of Process-Structure-Property assessment needed to be constantly used as an EPHP design guideline. Modifications of the manufacturing process were the result of the identification of the EPHPs Structure, assessed by means of Scanning Electron Microscopy (SEM), which was in turn reflected into a set of satisfactory mechanical properties.

1.3. Achievements

A new class of IRMs inspired by the biomimetics principles applied to the PHPs material has been created in this project. In the widely used Ashby Material Selection Chart(s) relating the stiffness (by Young's Modulus) with the material density the gap existing between foams and elastomers was filled in by the EPHPs, offering the material scientist and engineers a new class of lightweight materials with adequate stiffness to look at and to further exploit.

The series of EPHPs that successfully met and exceeded the benchmark performance of commercially available IRMs properties were several: those with solid content higher than 35% and homogenisation time of 15 minutes, as well as those with 20% solid content and homogenisation time of 20 or 25 minutes. These two parameters, overall, needed to combine so that the multiple goals such as, stiffness, energy absorption, and ease of handling could be achieved.

Most notably the sample named S30-20, was 1) lighter ($\rho_{S30\text{-}20}$ = 250 kg/m^3) than the lightest of the two reference materials GPhlex and D3O (260 kg/m^3 and 590 kg/m^3 respectively), 2) stiffer ($E_{S30\text{-}20}$ = 2100 kPa), 3) with an energy absorption of 230 mJ/mL at room temperature (compared to GPhlex 78.5 mJ/mL and D3O with 136 mJ/mL at room temperature) and 4) with adequate handling properties.

1.4. Thesis outline

The development of an innovative class of IRMs inspired by the biomimetics principles applied to the EPHPs materials, is presented in detail in this study according to the following main chapters:

Chapter 1 – Introduction: this chapter provided the preliminary driving factors for the research project and the basic information on the inspirational principles that were applied as well as the aims and objectives of the study. The project outline

provided a conceptual map for the development of bio-mimicking innovative IRMs with diversified process, structure and property relationships.

Chapter 2 – Literature Review: in this chapter the most relevant literature with reference to the significance of IRMs and their nature design solutions are reviewed. Extensive details on the deformation mechanics of foams (as in the Gibson and Ashby model) are also provided in order to develop an understanding of the behaviour of porous materials. Structural features such as the pore size and distribution are considered. Areas where refinement of the porous structure by means of more advanced modelling techniques is required are also presented. The formation of high internal phase emulsions (HIPEs), their stabilisation factors and polymerisation route to originate elastic PolyHIPEs (EPHPs) is presented. The mechanical behaviour of PolyHIPEs is reviewed.

Chapter 3 – Methodology: this chapter aims at reporting how the Aims and Objectives were implemented by following a dedicated methodology. The details of the experimental setup and the process variables that were used to produce the various classes of EPHPs are provided, from a) the preparation of the emulsion, and b) the moulding of the emulsion to c) the curing (polymerisation) process outcome. Different classes of EPHPs with higher solid content and different processing times were prepared and tested to meet the performances of two reference materials set as benchmark. At an early stage, very light-weight EPHPs with 10% polymeric solid content were first produced and compared with orange skin for bio-mimicry assessment via Scanning Electron Microscopy (SEM). Mechanical Compression Testing was used to determine their mechanical properties such as Stiffness - given by the Young Modulus (E) and the Specific Absorbed Energy (SAE), the amount of energy the EPHPs would absorb elastically. Both parameters were assessed at three different temperatures (room, low (4-6°C) and high (45-55°C)) to identify the sensitivity (viscoelastic behaviour) of each EPHP as an increase of temperature softens the polymers while a decrease strengthen them.

Chapter 4 - Results and discussion: this chapter presents, analyses and discusses the effects on the EPHPs material properties and performances due to the modifications of a) emulsion solid content and b) the emulsion homogenisation time. These parameters demonstrated to have profound effects onto the microstructure of the porous polymers, namely on 1) the pores' diameter (the average value and its distribution) and 2) the pores' walls' thickness. The modifications that were brought into the structure enabled the identification of key structural changes and, consequently, required mechanical performances could be related to them. Compression testing at low strain rates (1 mm/min) was

performed at room, low and high temperature to assess the influence of the temperature and relate it to the structure of each EPHP class. Compression tests at increasing rates (up to 50 mm/min) were performed to qualitatively identify the Time and Temperature Superposition Principle (TTSP). Furthermore, the moulding process is analysed in details and it was possible to identify each EPHP class' dependency to the moulding conditions to obtain samples' geometrical stability and homogeneity.

Chapter 5 – Conclusions and future work: this chapter analyses the results in the light of the overall target of developing novel, bio-mimicry IRMs at laboratory scale. The influence of the solid content and the processing time are emphasised in terms of advantages and limitations they pose to the targets. Conclusions are drawn in terms of 1) the successful production of EPHPs capable of delivering the required energy absorption capabilities, particularly at high temperature where the reference material GPhlex energy absorption is reduced to a half with respect to room temperature, by means of a material which is 2) lighter that the reference ones and that 3) behaves like a highly porous air-solid composite. The improvements of process control are believed to be a priority for future work. As the materials' properties are structure controlled, a small scale up of the manufacturing process with higher degree of control is likely to enhance their structure-properties relationship.

Chapter 2 – Literature Review

"It is no good to try to stop knowledge from going forward;
ignorance is never better than knowledge".
- Enrico Fermi

This chapter reviews the most relevant literature that has formed the background of this work. Diversified sources including journal articles, conferences proceedings, patents and books were used. The literature review aims at offering the foundations of the energy absorption capabilities of materials prior to analyse the most up to date existing knowledge, gaps and trends that justified the need for this work and its novelty. The review then aims at supporting the findings that were explored experimentally in this work by investigating similar areas of research.

By ideally starting with the definition and the importance of the concept of impact absorption, then "what" and "why" some materials (and structures) act as impact resistant materials is explained. Materials' characteristics and behaviour that are distinctively important are introduced and discussed. A particularly effective reference source comes from the investigation of Nature Design. In fact, a particular structure and assembly that serves for a specific purpose, optimised along thousands of years is identified, analysed and later mimicked.

Material properties and structural differences existing between nature and man-made design are identified and discussed. Hierarchical design of the natural IRMs is highlighted and its importance is examined for various cases. Synthetic foams can be considered to be the most suitable material to absorb (impact) energy and their typical mechanical behaviour is presented, analysed and an analytical model fully discussed, together with its limitations.

A novel class of synthetic materials originated by polymerising High Internal Phase Emulsion polymers (PolyHIPEs), is introduced, investigated and exploited as IRMs. PolyHIPEs have been studied for more than 30 years but, their wide range of applications has mainly been focusing on their morphology (structure), with very limited research attention to their mechanical properties. PolyHIPEs have an intrinsic hierarchical pore structure that can be tailored. Such feature and the possibilities of modifying the PolyHIPEs structure, is assessed by applying changes to the PolyHIPEs processing route.

The effects of processing route on material structure and properties are assessed and discussed.

2.1. Impact resistant materials

IRMs are widely present in every day moments. For example, comfortable and prolonged walking is ensured by the right materials in the shoe-sole. Every step taken corresponds to a localised, repeated impact that the material is designed to withstand without breaking. Car seating also is a very common experience. The differences in seating between a city and a sport car can be recalled easily. Rather compliant materials are preferred for seating in the city car to offer high level of comfort, compared to a sensation of a much stiffer material for a sports car instead. The sensations can be translated into measurable properties such as the displacement of the bottom cushion when sitting.

Cars have become increasingly more comfortable and safer for the occupants and this is in part due to the continuous research of better IRMs that started receiving attention in the late 1970s from the automotive and military sectors (Johnson and Reid, 1977). The outer shell (body) of a mass production car is made of steel, which is capable of bearing the loads of the whole remaining parts of the car and of course the dynamic loads during motion. More expensive cars also use aluminium in the body and in the engine to lighten the weight while increasing the strength-to-weight ratio. Neither steel nor aluminium as such can be considered IRMs; car frames' parts can be given a predefined layout and shape that would deform progressively upon impact, thus absorbing a relevant amount of energy due to a large change in shape. The goal is to preserve the structural integrity of the car's passenger compartment (Lu and Yu, 2003).

In order to highlight the importance of the passenger safety in the automotive industry, the United Nations (UN) organisation launched in 2011 a 10 years "Action for road safety" programme, aiming at improving the global road safety (UN, 2010). The UN programme is implemented by the Organisation of Economic Co-operation and Development (OECD) for European and Western Countries (IRTAD, 2013). Road traffic casualties in western countries have a massive impact on the health and economic sectors. In 2010 1.3 million people were killed in road accidents, while 50 million were injured worldwide.

Road accidents mainly involve people in their working age and the overall health, social, economic and development costs associated can be as large as 3% of a national Gross Domestic Product (GDP). For the United Kingdom (UK), the road safety trends are quite satisfactory, with a 47.1% reduction of fatalities in the 2001-2010 decade and 18.5% decrease for the latest 2009-2010 data. A

comparison of the short-term trends in road fatalities between the UK and many other countries is shown in Fig. 2-1.

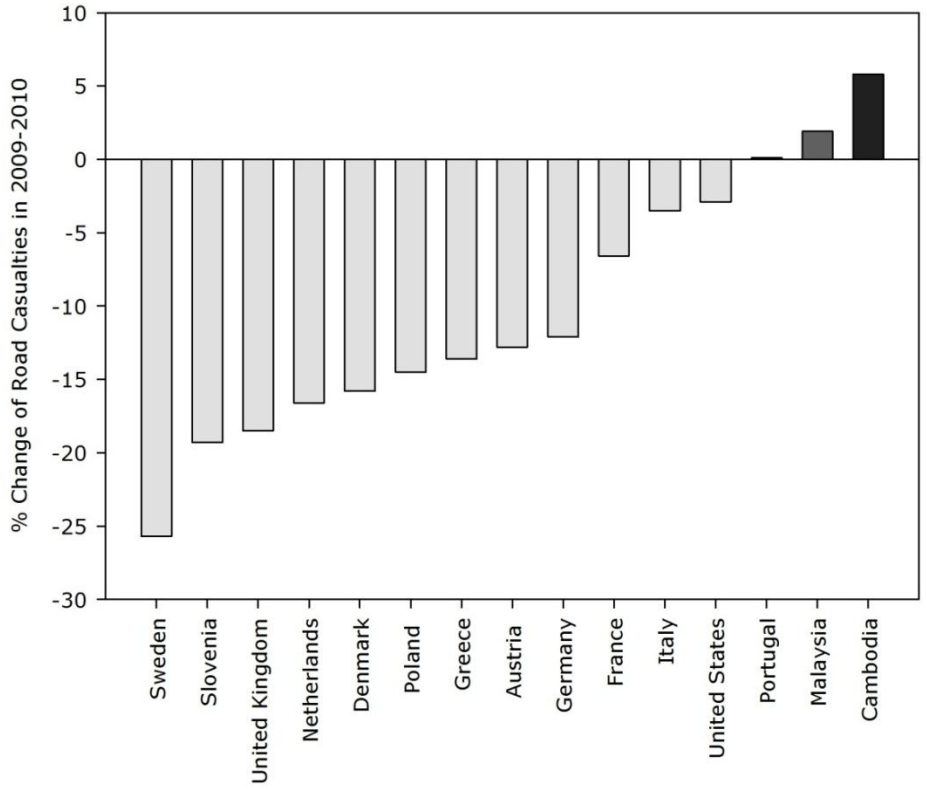

Fig. 2-1: short term (2009-2010) % change of road casualties for some Western and Eastern Countries, adapted from (IRTAD, 2013).

These positive results are obtained by a combination of safer cars being built and the engineering of safer roads. An opposite trend is observed for rapidly developing countries (right end of Fig. 2-1), where an easier access for the population to rather old motorised vehicles and a premature road network result in an increase of fatalities. Fatalities rate and risks are measured mainly in 3 ways: 1) Fatalities per 100,000 population, 2) per billion vehicle-kilometres and 3) per 10,000 registered vehicles.

Although a combination of all the 3 ways would produce a more detailed scenario, each indicator has relative advantaged to the others. As an example, the last indicator would be considered a weak one in developing countries where de-registration and removal from circulation of scrapped vehicles was not carefully monitored. In such a case, the population indicator would be more appropriate if also combined with the average mileage record.

In the UK as a result of increased cars' safety and road design engineering, the proposal to increase the speed limit in the motorways, from the current 70 miles per hour (mph) to 80 mph is under consideration. The UK Department for Transport

(DfT) monitoring and implementing activities provide supporting evidence of greatly reduced mortality rates in recent years for speed limits that were set in 1965 (DfT, 2012), a time when both cars and road safety were far from todays' technological and materials advances.

A particular category of road users, the cyclists, has however registered the lowest decrease in fatalities rate (-7%) in 2009-2010 compared to an average reduction of 15% for the other users. With 1.6% decrease of overall road traffic due to economy slowdown and rather cold winters, the pedal cyclist users increased by 1%. Such a moderate increase would not justify the limited reduction in fatalities. A possible cause may reside in the fact that in 2013, the wearing of a safety helmet is yet not compulsory in the UK (IRTAD, 2013).

The importance of adequate protection in the event of an impact is then manifested. A safety helmet that is usually worn in construction sites (safety hat) is designed to absorb the energy of a falling body. The kinetic energy of such an object should not exceed 50 J (i.e., an object of 5 kg dropped from the height of one meter). Bicycle helmets are instead designed to withstand an amount of energy twice as much as that of the safety hats (Lu and Yu, 2003).

In the event of an impact, the resulting maximum acceleration that the protected head experiences should not exceed 300 g (with g=9.81 m/s^2 as the acceleration due to gravity). Such a large number may be of little significance if not related to the likelihood of suffering a deadly damage to the skull and brain. The design of these two safety helmets may be evident. The hat has a rigid outer shell with a wearing and head-shell connection system that enables the load to be spread over a larger area. This layout minimises the acceleration peaks. The bicycle helmet follows a similar concept but the insertion of a material between the head and the outer shell plays a fundamental role. The absorption of a much higher energy is obtained by deformation and/or controlled collapse of this material.

In order to assess the head's tolerance to impacts, the car industry has been relying on two indexes: 1) the *Gadd Severity Index* (GSI), (Gadd, 1962) based on a modification of the earlier work by Lissner and co-workers where the effects of impacts on cadavers heads were first assessed (Lissner *et al.*, 1960) and 2) the *Head Injury Criterion* (HIC) (Versace, 1970) which aims at identifying the most damaging part of the acceleration pulse during the impact (King and Viano, 2000).

The numerical value of both indexes coincides and must be lower than 1000. The mathematical formulae for the GSI and HIC are reported in Table 2-1.

Table 2-1: Gadd Severity Index (GSI) and Head Injury Criterion (HIC) formulae, adapted from (Lu and Yu, 2003).

Index	Formula	Safe Limit Value	Notes
GSI	$\int_0^T a^{2.5}dt$	< 1000	t, time in μs T, total pulse duration in ms with 0.25<T<50 ms a, acceleration in m/s^2
HIC	$\max(t_2-t_1)[\frac{1}{t_2-t_1}\int_{t_1}^{t_2} a(t)dt]^{2.5}$	< 1000	t_1 and t_2 in ms, initial and final time of the pulse for which HIC reaches a maximum value

A practical result of the two indexes is that of providing a numerical value that accounts for a head deceleration which is likely to be survival (safe limits of GSI and HIC <1000).

Limitations to the validity of the indexes have been recognised, in particular their inability to taking into consideration angular acceleration (King and Viano, 2000; Lu and Yu, 2003; Marjoux *et al.*, 2008) but they have since their introduction become part of the car safety standard and no other indexes are yet so widely accepted.

The differences in the impact absorption structures and materials used for the vehicle body and the passenger compartment may appear relatively large but similarities are evident. Steel and aluminium may be considered as IRMs from a structural perspective then designing the body structure so that a frontal impact deforms it into a predictable way, is the conventional approach. Low carbon steel is used as it is more ductile, than structural steel and so is aluminium. The associated large deformations provide the required energy absorption capability (Zhou, 2001; Lu and Yu, 2003).

A vehicle body frame of a modern car is shown in Fig. 2-2. The structural details and the variety of materials used are visible.

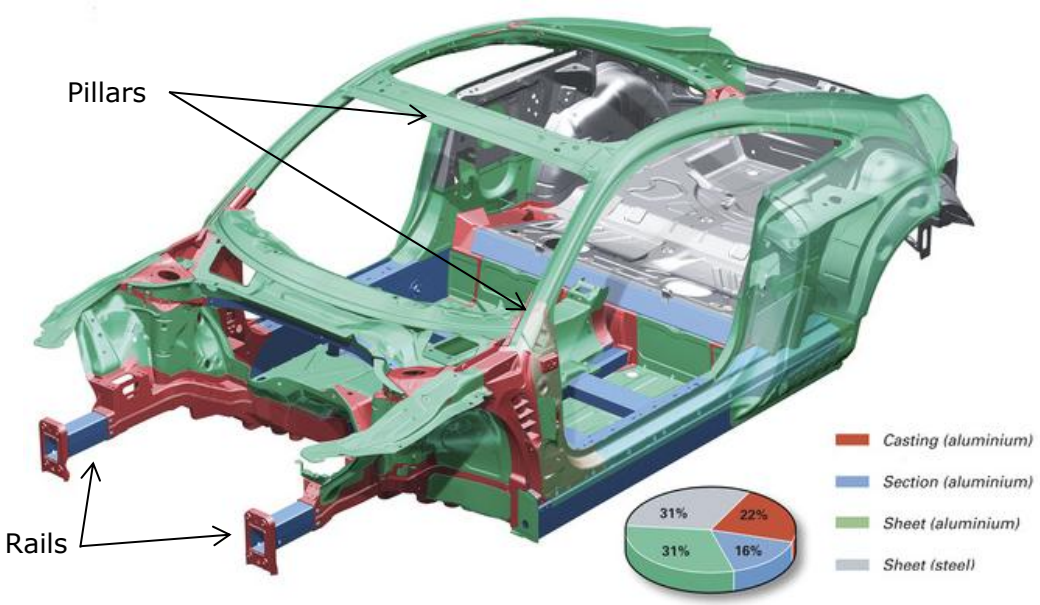

Fig. 2-2: body structure and materials used for AUDI TT. The arrows show the pillars and rails that provide impact/energy absorption, adapted from (Audiusa.com, 2013).

Many parts of a vehicle body are recognisable as thin-walled columns (called pillars) that provide structural integrity to the passengers' compartment and rails that act as the main collapsible energy absorbers. The variety of materials used, ensures lightweight and structural strength.

The shape of the pillars is typically a thin-walled geometry. Not only does this enable weight reduction, but a much higher specific stiffness compared to the fully filled geometry is provided. By selecting the right ratio between the thickness and the width (shape factor), a thin-walled tube (or beam) can be even more 50 times stiffer than a solid geometry (Ashby, 2010).

This particular geometrical factor introduces some key elements that an energy absorbing material should come with. The thin walled geometry immediately resembles a cellular structure, particularly if a typical array of thin-walled tubes is chosen (Fig. 2-3).

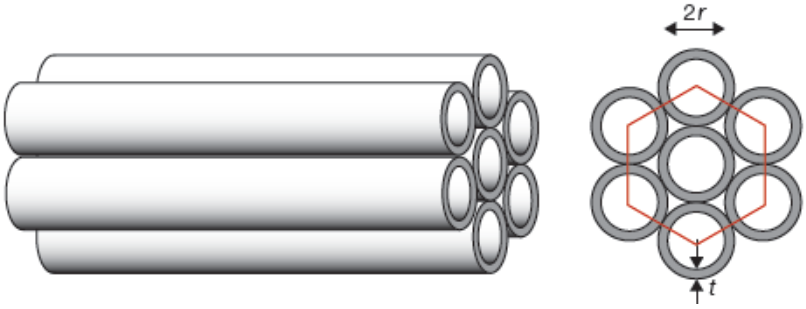

Fig. 2-3: thin-walled tubes arranged around a single, central tube. The layout is that of a honeycomb (hexagonal section), from (Ashby, 2010).

The hexagonal layout, a landmark of bee honeycombs is recognisable. When comparing solid materials and structures with thin-walled ones, the amount of solid that has been removed leaves room for a structural empty space. Shaping a material into a proper structure is then a key factor in pursuing efficiency (Ashby and Cebon, 1993; Ashby, 2010). With efficiency, the use of the lowest amount of material for given loading conditions and purposes is sought after.

Material structures and relatively simple shape factors are related to each other and simple mathematical expressions are available. An ideal logical relationships' scheme among materials, function and shape is shown in Fig. 2-4.

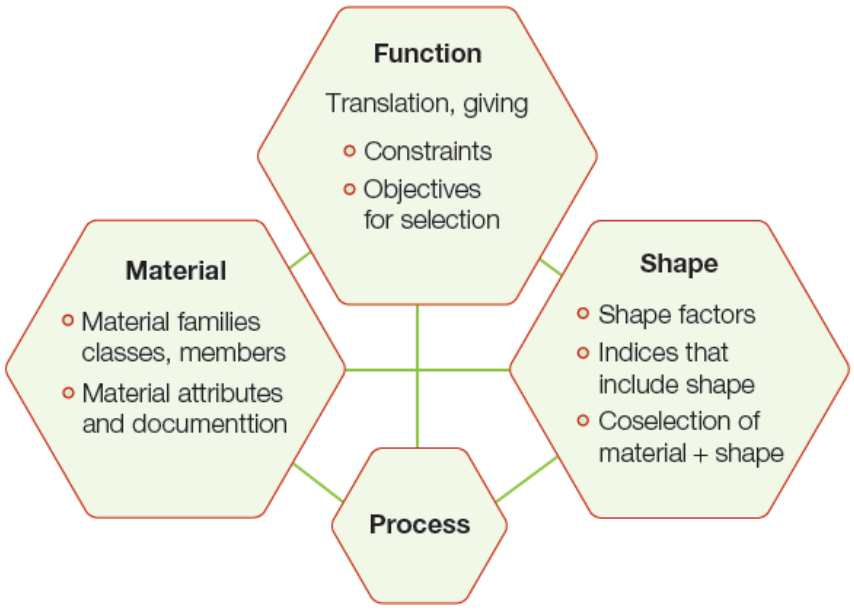

Fig. 2-4: relationships among material, function, shape and processing routes, (Ashby, 2010).

The material function is set at the design stage and the right material, as well as its shape play a fundamental role. Furthermore reliable processing route to shape the selected material must be available. Depending on the application, economical factors may become stringent and the whole selection process may need to be adjusted to meet not just mechanical criteria, but also economical and more sustainable ones.

The structural arrangement of the thin-walled tubes resembling a honeycomb is also a distinct mark of highly regular synthetic porous material (known in the engineering and material science fields as honeycombs). It is for such reason that this class of materials is largely employed for energy absorption upon impact or when a large deformation is useful upon loading and weight savings are highly sought after.

The energy absorption is the result of both the material deformation and the mode of the deformation. Energy can be equivalently related to the product of force and displacement. A large change in the material displacement (or volume, when the force acts on a surface and becomes a pressure load) can be one way for pursuing the kinetic energy absorption required.

The typical behaviour of porous (cellular) materials is described in details in a dedicated section later; at this introductory stage, it will suffice to consider that the ideal materials is one which combines the ability of deforming itself upon impact and not transferring the load towards other parts of the system. An example of large deformation properties is experienced when elastomers are considered. Elastomers are effectively used in sealing. Rubbery materials (both synthetic and natural) are inserted between two different pieces/devices and their large deformation provides the required contact and sealing effect. Elastomers are capable of getting stretched (or compressed) to a large extent thanks to the ability of their building molecules to easily slide past each other. The meaning of the word elastomer itself contains the concept of elasticity.

Such materials behaviour is can be seen as that of a spring. The impact energy is converted into elastic energy by the spring and it will be later/immediately given back. In the case of a car impact, the effect on the occupants would be even more deleterious as the change in the momentum would be higher and so would the deceleration (likelihood of exceeding the value of 1000 for GSI and HIC). A plastic deformation instead would dissipate the energy at the expenses of the material, not of the occupants. A fracturing of the IRM would imply that the material absorbs energy by fracturing, possibly in a pre-determined way. The net result especially in the latter case is that the material would not be reusable and a second impact event would find the system unprotected.

It is then of particular importance to be able to tailor the material properties and its structure so that a particular set of objectives (or constraints) is met.

This section provided a brief introduction on the importance of providing adequate impact protection and it also introduced the basic requirements that a material should have to act as an IRM. The structure and mechanical behaviour of a particular Natural layout arrangement is presented in the next sections. Such structure is compared with a class of synthetic materials whose structure can be modified in order to mimic the design of Nature.

2.2. Biomimetics, definition and origins

Biomimetics, also known as biomimicry (and formerly as bionics), is defined as the science of constructing artificial systems that have some of the characteristics of living systems (Schmitt, 1969). Biomimetics is not a specialized science but an inter-science discipline; it finds new ideas for useful artificial machines and systems. Biomimetics also describes an "Inspired by Nature" approach to develop an in-depth understanding on mechanics, kinetics as well as material properties of living systems.

Many authors have studied the structure and the hierarchical assembly of nature design and highlighted the main differences with man-made design. Among the most evident, engineering design seeks the maximum benefit from a given material while Nature seeks it from structural shapes made of different materials. With such assembly, the structure is capable of responding to multiple and likely to evolve conditions (Jeronimidis and Atkins, 1995). The integration of use and function further evidenced by many researchers (Bar-Cohen, 2005; Naik and Stone, 2005; Bar-Cohen, 2006; Vincent *et al.*, 2006; Vincent, 2009) as the objective for a more complete mimicking of Nature design. A shift in the Engineering Paradigm (EP) has been proposed by Roeder (2010). The Modified Material Science and Engineering Paradigm (MMSEP) extend the engineering paradigm commonly adopted by technologists and engineers. As the EP is focused mainly on three factors: 1) Processing, 2) Structure and 3) Properties, the integration of biology into the EP results in a fourth factor to be considered: Performance. Processing, Structure and Properties along with Performance have been traditionally related each other in the EP as represented in Fig. 2-5. However, this paradigm does not account for hierarchy and adaptability, two distinctive characteristics of Nature design (Roeder, 2010).

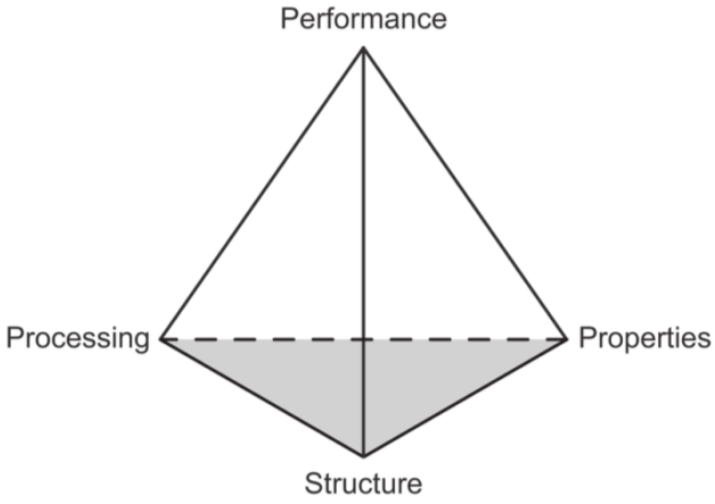

Fig. 2-5: Principles of the Engineering and Materials Paradigm, indicated by the figure's vertexes, (Roeder, 2010).

In the common EP, the performance factor stays on top of the other factors. In Nature design instead, the hierarchical structure is at the heart of the design, as it needs to adapt to the required performance. The development, anatomy and the adaptation to stimulus of biological systems are aimed to be accounted for in the MMESP as schematically shown in Fig. 2-6:

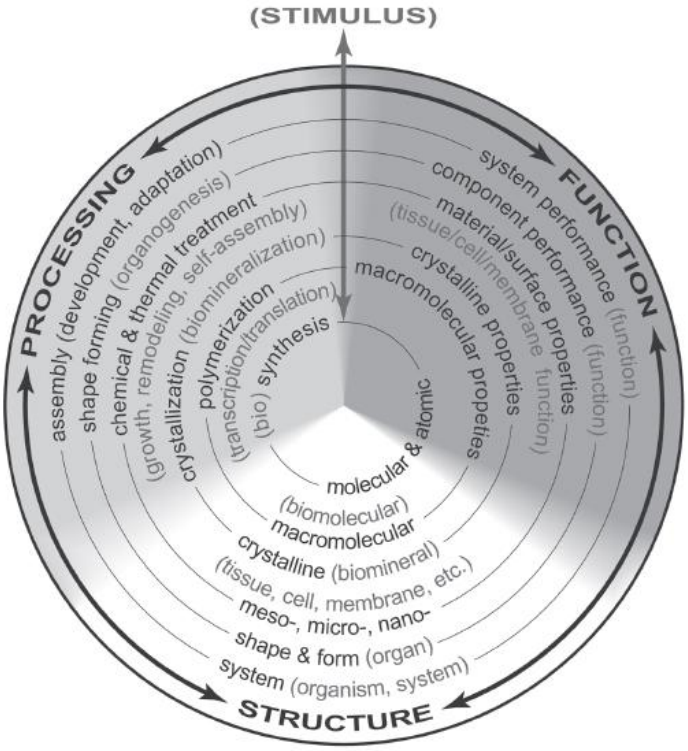

Fig. 2-6: parallels between the EP and the MMESP. Characteristics of the biological world (in parenthesis) are paired with those of the conventional approach: material processing, structure and function, each enclosed in the three sectors of the cone, (Roeder, 2010).

The pairing of biological systems characteristics is made with processing (development), structure (anatomy or form) and properties respectively. The MMESP cone-shaped scheme is also able to represent the length scale of a system, thus the hierarchy at each step. Atomic and molecular assembly is located at the centre as the origin point. As the system grows in hierarchy and complexity (towards the edges), each of the three sectors is aimed at growing simultaneously, rather than sequentially as proposed by Roeder (2010).

The outer stimuli by which a biological system is required to adapt and perform can be paired, for example, with varying mechanical loads, electric fields, chemical concentration gradient, when engineering and materials systems are considered.

2.3. Natural materials and impact protection

Several natural material have been used for centuries to provide multiple functions before modern materials became available and could replace or enhance some of the natural materials properties. Availability of natural materials has been a key for economical usage and among the most used natural materials, wood, cork and balsa still occupy a large production and consumption volume as they represent a class of materials used for structural and many other applications (Gibson and Ashby, 1997). The general characteristics of such natural materials are highlighted in the next sections.

2.3.1. Wood

Wood is still the material with the highest rate of yearly production and overcomes the production of steel more than two times (Bowyer *et al.*, 2007; Ajani, 2011). Wood has been used for structural (building) applications and has been known for its remarkable mechanical performances when a weight savings are the primary objectives. A particular case is that of the Mosquito airplane; it was the first WWII bomber that implemented structural sandwiches made of plywood skins that were bonded with balsa cores (Hoff, 1951). This case highlighted the desirable characteristics of a natural material that is stiff and light at the same time.

However the mechanical characteristics of wood depend on the direction the load is applied. Materials whose mechanical behaviour is independent of the load direction are called isotropic; those with dependence on direction are called anisotropic. Wood exhibits properties that vary on the three mutually perpendicular axes and for this reason is termed orthotropic (Gibson and Ashby, 1997). However, the difference in properties for the tangential and radial direction is moderate and wood can be considered anisotropic (Bowyer *et al.*, 2007). The wood layout varies according to the direction and typical arrangements include aligned, elongated pores in the tree rise direction (called also fibres), radial channels called rays, and larger sap channels along the tangential direction (Lakes, 1993).

The schematic structure of wood is depicted in Fig. 2-7A where in the radial direction, the alternate presence of elongated cellulose fibrils, hemicellulose as a binder and a lignin matrix form the radial layout of the wood. Fig. 2-7B shows a scanning electron micrograph highlighting the structural differences in the axial (vertical) and tangential direction.

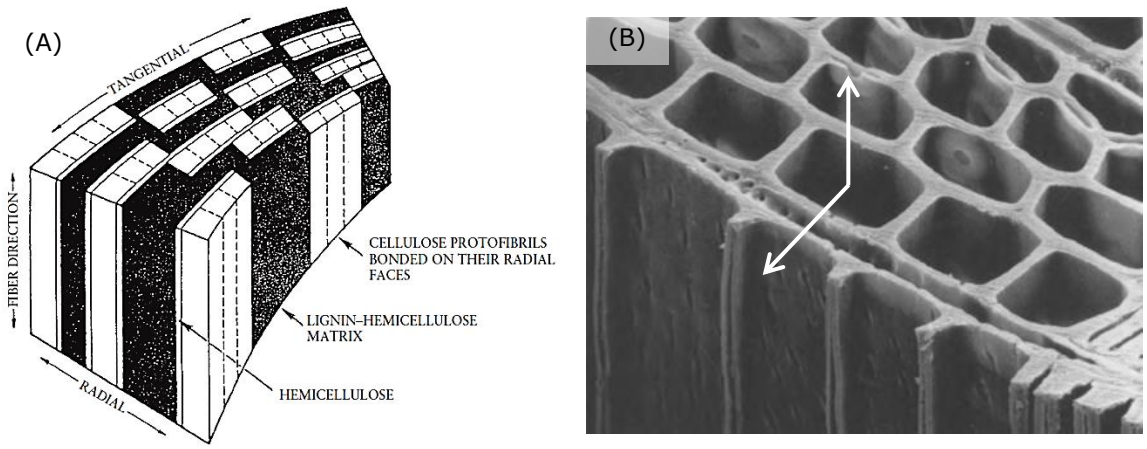

Fig. 2-7: A) structure of wood in the radial, tangential and axial direction and B) scanning electron micrograph of axial and tangential view (indicated by the arrows) of Sitka spruce (*Picea sitchensis*), adapted from (Bowyer *et al.*, 2007).

The structural shape of each configurations serves a particular function; more specifically the hollow prismatic cell with varying wall thickness adequately support the loading stresses of the tree (Lakes, 1993; Wegst and Ashby, 2004). Several types of wood are used according to their specific characteristics. Few examples of the variety of properties are given by Gibson and Ashby (1997). Ash is used to produce baseball bats and frames for cars and trucks due to its high shock resistance, bamboo for building purposes as it is flexible and strong.

2.3.2. Balsa

Balsa has an even wider range of applications: 1) structural in rafts and floats, 2) thermal insulation due to its very low thermal conductivity, 3) cushioning and 4) cores for sandwich panels (Easterling *et al.*, 1982; Ashby *et al.*, 1995; Gibson and Ashby, 1997). Such variety of applications and uses are also possible because of remarkably low density of balsa, which spans from 40 to 320 kg/m^3, and its strength (Easterling *et al.*, 1982). Similarly to other type of wood, the mechanical properties are anisotropic, with the highest stiffness measured when load is applied axially. Radial and tangential moduli are similar and both one order of magnitude smaller than the axial modulus (Easterling *et al.*, 1982).

2.3.3. Cork

Cork is a small tree whose main commercially relevant product is the thick layer of its bark that grows again when removed. Cork is almost impermeable to any fluid and it functions as a thermal insulator. Heat and moisture losses are then prevented (Gibson and Ashby, 1997). This particular feature is still exploited industrially as cork is largely used in refrigerators as well as in rocket boosters. Its acoustic insulation properties make cork a perfectly suitable material when noise reduction or abatement is required (i.e. in submarines and recording studios).

Furthermore, not only is cork capable offering high level of thermal and acoustic insulation, it has remarkably high energy absorption properties (Gibson and Ashby, 1997). All these features have a common ground and are then related to corks' structural arrangement. As shown earlier for wood, the cork structure varies in the three mutual perpendicular directions (Fig. 2-8) and SEM images reveal the difference cells layouts.

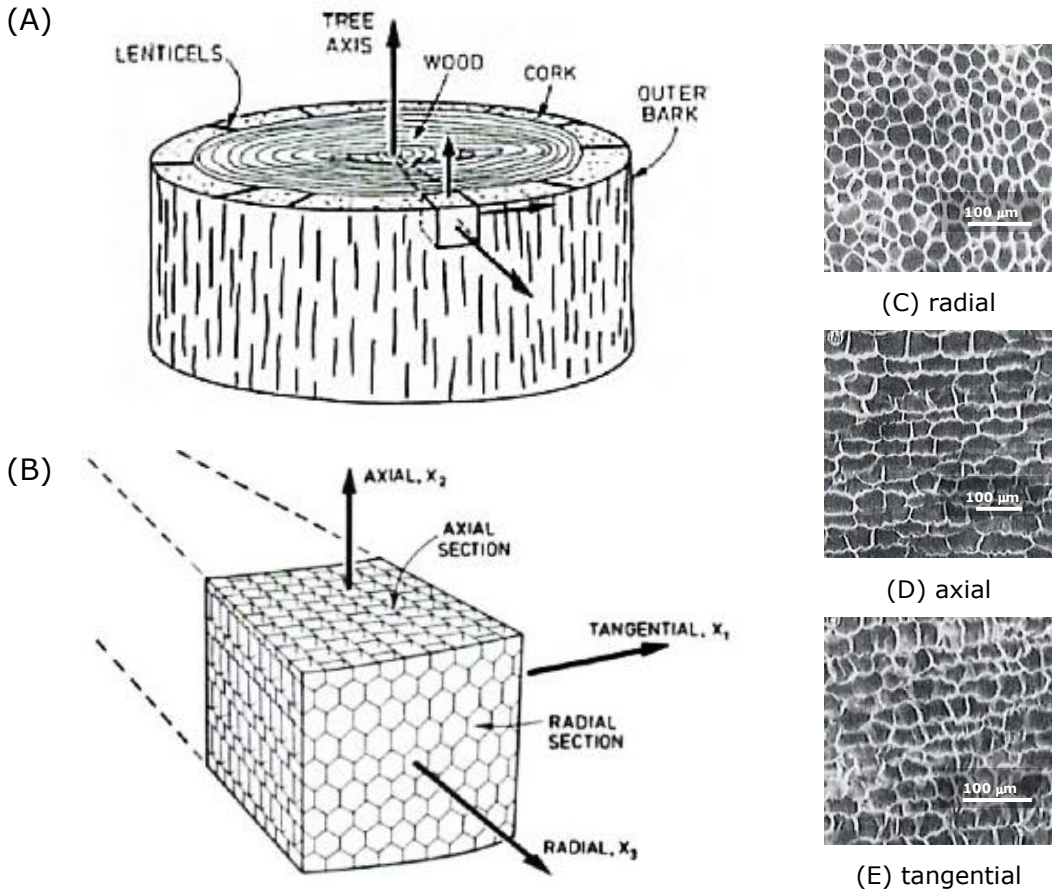

Fig. 2-8: schematic drawing of cork tree (A) and outer cork layer (B). (C), (D) and (E) scanning electron micrograph of the three indicated mutual directions cells layout, adapted from Gibson and Ashby (1997).

In the radial direction, the cells arrangement does not resemble regular hexagons as in honeycombs or in wood; a combination of six, five, seven and eight sided geometries are present but the average number of cells is six (Gibson and Ashby, 1997). A particular feature of cork axial cells is that they are stacked like a wall but they also show that their walls are corrugated. Such corrugations introduce a predefined deformation method that Gibson and Ashby (1997) called concertina or bellows.

The cells dimensions vary and for cork, such variation spans from 20 μm for the hexagon side and 1 μm for the hexagon wall in the radial direction, to 40 μm of the cell in the axial direction and 15 μm in the radial direction. These dimensions are

remarkably smaller than other type of woods and as reported by Gibson and Ashby (1997) cork cells sizes are closer to those of microporous foams than conventional polymeric foams. For the latter type of foams, cells size ranges from a fraction of millimetres to several millimetres.

Cork is widely used in energy absorption and packaging applications. Its cellular architecture is responsible for large deformation at relatively low load values. The cell walls start to collapse at low stress levels and progressively deform, thus preventing high stresses to be transferred to the protected/transported good (Gibson and Ashby, 1997).

The use of cork as widely available energy absorption materials has been influenced by the introduction of polystyrene foam. Polystyrene foam has practically replaced cork in common packaging needs due to its low price and availability worldwide.

2.3.4. Hierarchical structure layout

An important contribution to the bio-mimicking of hierarchy, structure and function for Nature design inspired IRM has been made recently by Fischer *et al.* (2010) and Seidel *et al.* (2010). In their articles on nature inspired concept generators, the excellent damping characteristics of the pummel (*Citrus Maxima*) and its capability of not showing skin damages upon free falling from up to 10 m were attributed to the hierarchy of the pores that form the inner skin of the fruit.

A series of repeated free falling tests with fruits weighing ~1 kg was performed and it was determined that 90% of the impact energy was dissipated without damage to the fruit (Seidel *et al.*, 2010).

The authors also investigated this remarkable resistance from a functional point of view; if fruits split upon impact, they would not survive so adequate protection needed to be provided. The inner and outer skin of the pummel were further analysed. It was found that the outer skin arrangement is composed of densely packed cells (epidermis) while the white, spongy mesocarp is characterised by a layer with varying pore diameter (Fig. 2-9).

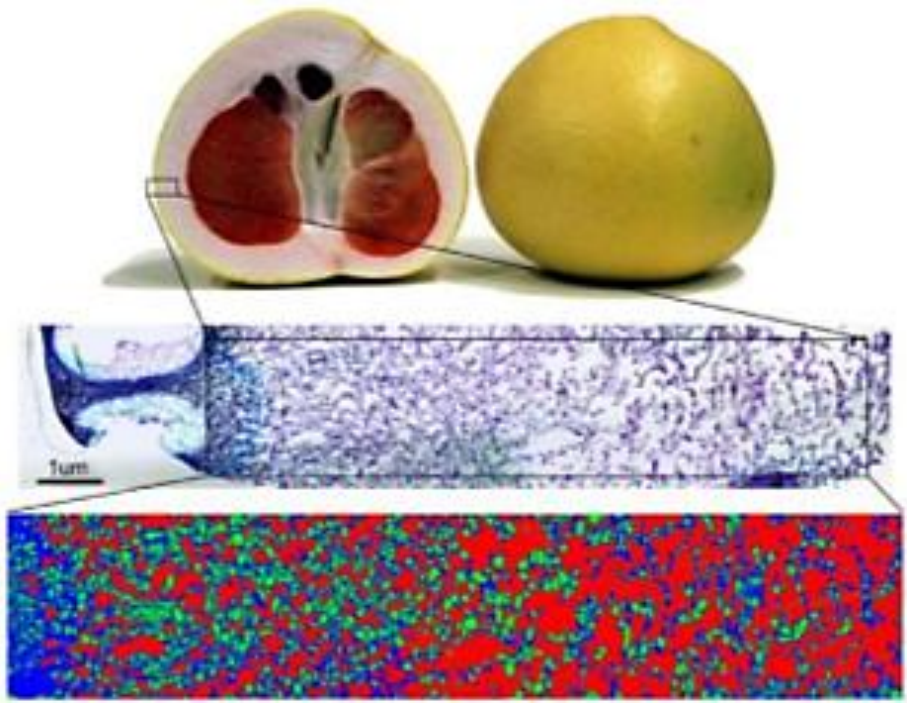

Fig. 2-9: change in citrus maxima's pore size from exocarp (external layer) towards mesocarp (internal layer). Bottom part of the picture shows a Light Microscopy image of Toluidine Blued stained sample of 10 μm thickness. Colour coding: Blue for cell wall, Green for cell lumen and Red for intercellular space, adapted from (Seidel *et al.*, 2010).

The diameter of this cellular layout increases towards the inner fruit. The impact absorption capabilities of the fruit were then attributed to the hierarchy of the fruit skin as a whole.

A relatively compact outer skin is able to transfer the load to an inner hierarchically organised cellular structure. The latter is organised so that the cell pore diameter increases towards the fruit in a continuous way so that the load is transferred to larger cells (Fischer *et al.*, 2010). Following the hierarchical investigation of the pummel, the authors produced a series of metallic foams based on bismuth and tin ($Bi_{75}Sn_{43}$) that showed a mechanical behaviour similar to that of the fruit. However, the need of using several layers of different foams for an optimal result was acknowledged.

Hierarchical structure layout does not belong only to the outer skin of fruits as discussed earlier. It was acknowledged already that the Nature Design is driven by the simultaneous growth of the material(s) and the whole organism using the principles of biologically controlled self-assembly (Fratzl, 2007). Such approach can be termed as *bottom-up*, a process in which the materials and structure develop towards a function, opposite to the common engineering approach of *top-down*, where the function dictates the choice of the material(s) and the assembly.

According to Fratzl (2007) and many other authors (Mattheck and Burkhardt, 1990; Lakes, 1993; Vincent *et al.*, 2006; Chen *et al.*, 2008; Speck and Speck, 2008; Vincent, 2009) the fundamental difference between man-made and Nature Design can be found at the length scale level.

Natural materials start assembling at molecular level (i.e. building blocks) and progressively grow in size with a dynamic optimisation process (Jeronimidis and Atkins, 1995).

2.3.5. Fruit skin as an impact resistant material

In the previous section, it was shown that efficient protection of the fruit depends on the structure of the fruit skin. The function that a hierarchical structure is requested to perform varies, and so does the structure in order to adapt to the external variations.

Seidel *et al.* (2010) investigated the skin structure of coconut (Cocos Nucifera) and Macadamia and compared it with that of the pummel. By relating the environments in which these fruits grow, they accounted for several differences in the fruit protection design. For the coconut, a combination of fibrous outer skin aiming at providing a damping effect (coconut trees can be as high as 25 m) and an inner, tough structure that proved to be highly effective in preventing salty water to penetrate it, thus preserving the fruit content. The macadamia fruit instead has a single layered tough outer shell. The aim of such layout is that of offering the highest resistance to puncturing.

A comparison of the three skin protection systems developed by Nature is shown in Fig. 2-1.

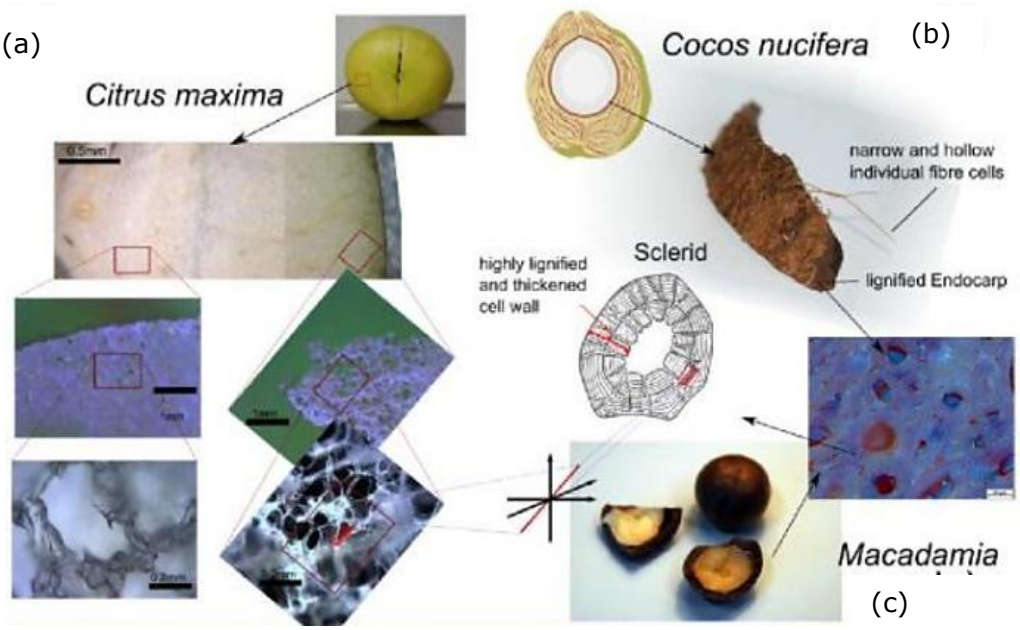

Fig. 2-10: citrus maxima micro photographs showing the appearance of the mesocarp towards the endocarp (a) compared with Coconut "*Cocos nucifera*" (b), and Nutshell "*Macadamia*" (*c*). The *citrus maxima* shows a *spongy* mesocarp, the coconut has a combination of fibrous mesocarp and tough endocarp, while the nutshell has an entirely tough shell, adapted from (Seidel *et al.*, 2010).

The outer skins of three fruits and their remarkably different structure were found to be consistent with the function(s) and the external environment stimuli they were required to cope with. Further details on the importance of Nature hierarchical design are given in the next section.

2.4. Structure and mechanical behaviour of honeycombs and foams

While describing the importance of the material, shape and structural factors, a few examples of Nature Design were given in the previous section. Honeycombs are still today, one of the most studied examples of nature-engineered structures. Eminent scientists in the past were captivated by the beauty and almost perfect regularity of natural porous materials. Among them Hooke analysed the structure of cork (which highly resembles that of a bee honeycomb) with his own improved microscope in the 17th century. Darwin stated that the honeycomb was a masterpiece of engineering assembly and that its shape was perfect in economising labour and wax.

The maximum packing for both bi-dimensional and 3D cases had been an open question for many centuries. When Lord Kelvin determined the shape of (regular) objects with highest packing configuration and minimum surface area in three dimensions (3D) in the late 19th century, it was believed that the most effective geometry had been found. The geometry of such a solid called tetrakaidecahedron

is shown in Fig. 2-11 and consists of a polyhedron with 14 faces (6 quadrilateral and 8 hexagonal).

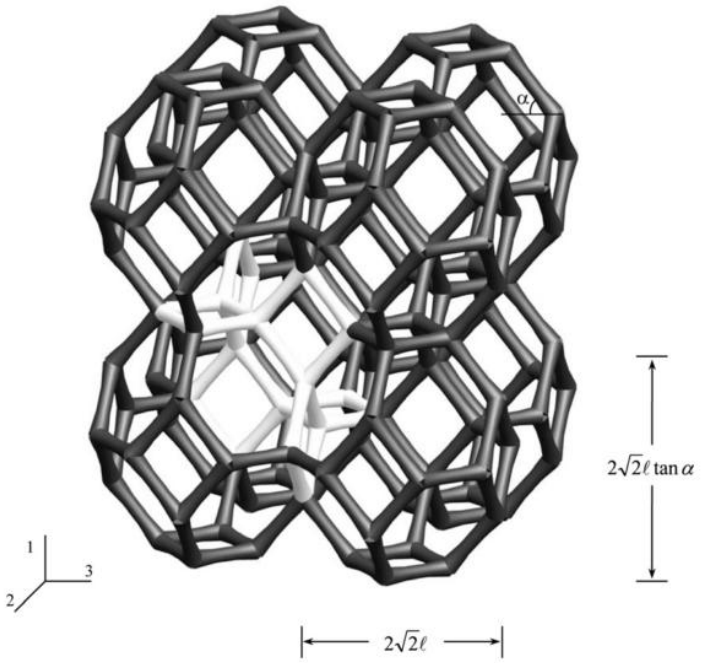

Fig. 2-11: a cluster of Kelvin cells (tetrakaidecahedron) with typical l-parameterised dimensions. The ratio between vertical and horizontal length (> 1) indicates anisotropy (Jang *et al.*, 2010).

The maximum packing, thus the lowest surface area per unit volume would be obtained by a tetrakaidecahedron with slightly curved faces.

Recently, Weaire and Phelan (1994) demonstrated that this was not the case. Another polyhedral with an even lower surface area per unit volume (about 0.3% lower than that dictated by Kelvin) has been found. The authors used a software called Surface Evolver.

The structure shown in Fig. 2-12 was reported to be analogous to that of β-tungsten, some clathrate compounds (Weaire and Phelan, 1994) and chromium-silicon alloys (Kusner and Sullivan, 1996).

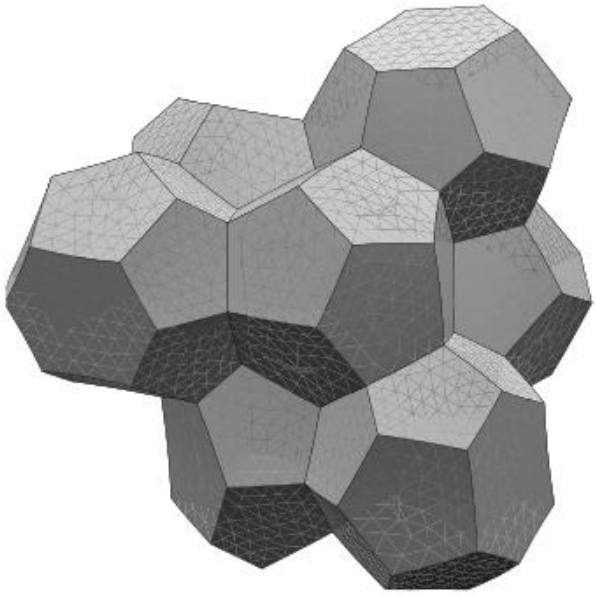

Fig. 2-12: Weaire-Phelan unit foam is comprised of eight cells stacked in columns in three mutually perpendicular directions. A dodecahedron is visible in the front, surrounded by 7 tetrakaidecahedrons with parallel hexagonal faces, adapted from (Kusner and Sullivan, 1996).

The geometrical layout of 2D and 3D arrays has a distinctive effect on how such assemblies behave when subjected to loads. In particular, the focus is given towards compression loadings in the in-plane directions.

The next section introduces the key features of the two different geometries (honeycombs as 2D and foams as 3D arrays) and an analytical model to study the mechanical behaviour of honeycombs (2D) is presented. Such a model, which has been extensively subjected to refining revisions, not only represents the most suitable way for the understanding of mechanical response of honeycombs, but it also provides the foundations for the study of mechanical behaviour of foams.

2.4.1. Microstructure of honeycombs

In two dimensions, it is known that the hexagon is the space-filling plane figure whose perimeter encloses the highest area, and a useful representation of such property can be seen in Fig. 2-13.

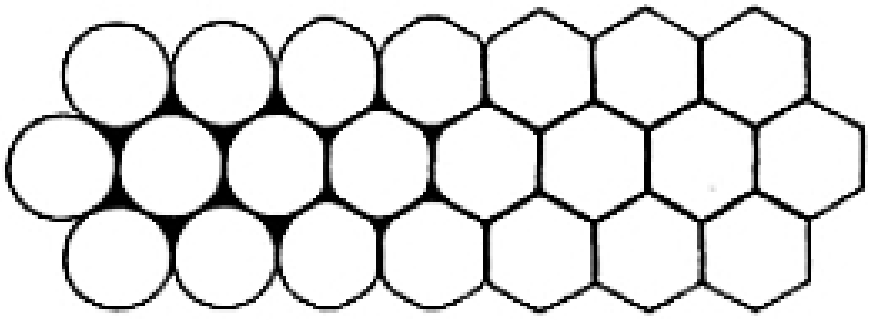

Fig. 2-13: minimisation of voids existing in packing of circles when shifting towards regular hexagons (left to right), a recurring geometry in Honeycombs, (Pearce, 1990).

On the left side, several circles are shown packing together and the voids present among the contacting circles do represent an unfilled surface. It can be efficiently filled if the circles turn into hexagons. Such efficient 2D packing is proven and it is a recurring design adopted by Nature.

Gibson *et al.* (1982) defined honeycombs as two-dimensional array of prismatic cells or, more briefly, as 2D cellular materials. The extension of such definition to three dimensions defines foams as three-dimensional arrays of polyhedral cells, or 3D cellular materials (Gibson and Ashby, 1982). As mentioned earlier, the energy absorption characteristics of materials largely rely on their structure. The need for an understanding of how honeycombs respond (deform) to loading stresses in different directions was firstly partially satisfied by Abd El-Sayed *et al.* (1979). They developed a simple analytical model which related the elastic response of a honeycomb in both in-plane and out-of-plane conditions. The analytical findings were supported by experimental results and the authors concluded that beyond elastic deformation, largely due to a wall-bending mechanism, the hexagonal cells develop plastic hinges at the ends of the wall members and behave as an elasto-plastic mechanism.

According to Gibson *et al.* (1982), the need to extend the work performed by Abd El-Sayed, Jones et al., was based upon the fact that the in-plane elastic and shear collapse had not been analysed. On these grounds, a complete analytical study, extensively supported by experimental tests made by the authors and many others using different materials honeycombs was presented.

The work produced by Gibson and Ashby and other co-workers (Easterling *et al.*, 1982; Gibson and Ashby, 1982; Gibson *et al.*, 1982; Gibson, 1989; Ashby *et al.*, 1995) and that culminated with the well-known book titled *Cellular Solids* (Gibson and Ashby, 1997) has been widely accepted as a practical standard way to study the mechanical behaviour of honeycombs and foams. They related some of the fundamental properties of cellular materials (both in 2D or 3D) to the density of the cellular material being tested or examined.

This sort of description (in particular for honeycombs) is on one hand rather satisfactory at the engineering level, and relies on properties that can be easily measured (i.e. the density of the cellular material and that of the material the honeycomb/foam is made from), on the other hand has been subjected to further refinement for foam modelling. In particular, investigation has been active on identifying the best descriptive model to be used for foams, in contrast to the simple cubical array studied by Gibson and Ashby.

Particular interest in developing a realistic, representative model of foams has been expressed by other researchers belonging to other disciplines, not necessarily engineering. A more detailed review of such studies and their findings is presented in the microstructure of foams section.

2.4.2. Mechanics of honeycombs

The need to understand and predict how a honeycomb reacts when subjected to loads has been the driving factor for developing a series of theoretical approaches that would be representative of experimental results. The most successful model has been proposed by Gibson *et al.* (1982) and highlights the different deformation mechanisms that take place when a honeycomb is compressed.

A useful representation is that of a honeycomb made up of regular hexagons. The in-plane deformation can take place in two mutually perpendicular directions and the starting point adopted in the model was that of characterising a single cell with typical dimensional parameters, as shown in Fig. 2-14.

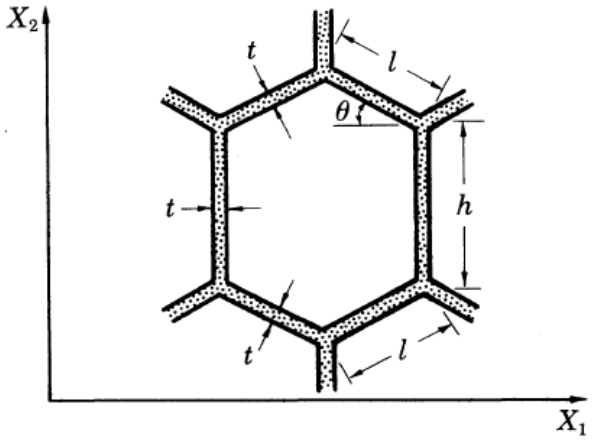

Fig. 2-14: a single hexagonal cel and its geometrical parameter. The two axes represent the in-plane loading directions, from (Gibson *et al.*, 1982).

In order to assess the validity of their findings, the authors produced a series of samples for which the ratio of t/l, h/l and θ were varied.

When a hexagonal cell is loaded (stress) in the X_1 or X_2 direction it undergoes a deformation (strain). A set of stress-strain curves for elastic, plastic and brittle materials is shown in Fig. 2-15.

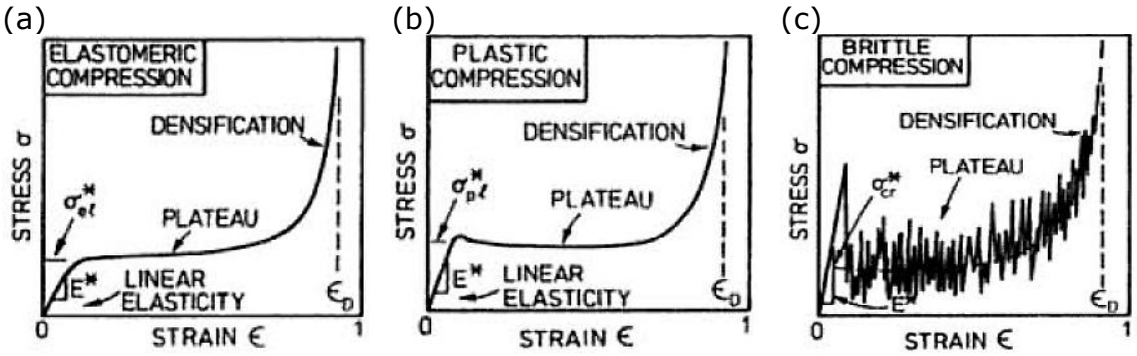

Fig. 2-15: honeycombs stress-strain compression curves for (a) elastomers, (b) plastic and (c) brittle materials, adapted from (Gibson and Ashby, 1997).

Depending on the stress, initially a proportional strain is observed. This behaviour is referred to as the linear elastic behaviour and is described by the *Young's Modulus* (*E*). E is the slope of the initial, linear part shown in the stress-strain curve.

Upon increasing the stress, the linear elastic behaviour is followed by an almost horizontal curve (called *Plateau region*) which is a distinctive feature of energy absorbing materials as mentioned in the previous sections. The stress at which the shift from elastic to Plateau region is observed is termed σ_e, σ_p and σ_c according to the nature of the material (elastic, plastic or brittle).

The area below the stress-strain curve is the energy per unit volume and is the exploited characteristic for energy absorbing materials. Further application of stress beyond the Plateau causes the cell walls to contact one another. This condition is called *densification* and it is identified by a sharp increase of stress in the plot. Such a condition should be avoided in energy absorbing materials. The high stress would be also experienced by the protected item and the honeycomb would then completely collapse. The almost vertical slope of the curve at full densification is identified by the densification strain ε_D.

The mechanisms that dictate the conditions of the Plateau region were provided by Gibson *et al.* (1982) and depend on the nature of the material the honeycomb is made of:

- Elastic bending of the cell walls if the material is elastic
- Plastic yielding of the cell walls if the material is plastic (or elasto-plastic)
- Creep as a result of time-dependent visco-elastic behaviour
- Brittle fracture of the whole structure if the material is brittle

The three distinctive regions can be studied by using the hexagonal cell and applying the equilibrium principles of statics (i.e. forces, moments, displacements). It can be anticipated that the regular hexagon introduces a series of analytical simplifications that contribute to the elegance of the equations. It was anticipated

that the basic honeycomb mechanical properties could be obtained by measuring the density ρ of the honeycomb and relating it to that of the solid material it is originated from ρ_s.

The cell shown in Fig. 2-14 has a density given by:

$$\frac{\rho}{\rho_S} = \frac{(2+h/l)t/l}{2cos\theta(h/l+sin\,\theta)} \qquad \textbf{Eqn. 2-1}$$

which for regular hexagon (Θ=30°) and (h=l) becomes:

$$\frac{\rho}{\rho_S} = \frac{2}{\sqrt{3}}\,\frac{t}{l} \qquad \textbf{Eqn. 2-2}$$

The regular hexagon cell density can then be determined by referring to its geometry. When the cell is compressed in X_1 or X_2 directions, the deformation in the elastic region is firstly schematised as shown in Fig. 2-16 and the two Young's Moduli E_1 and E_2 can be determined.

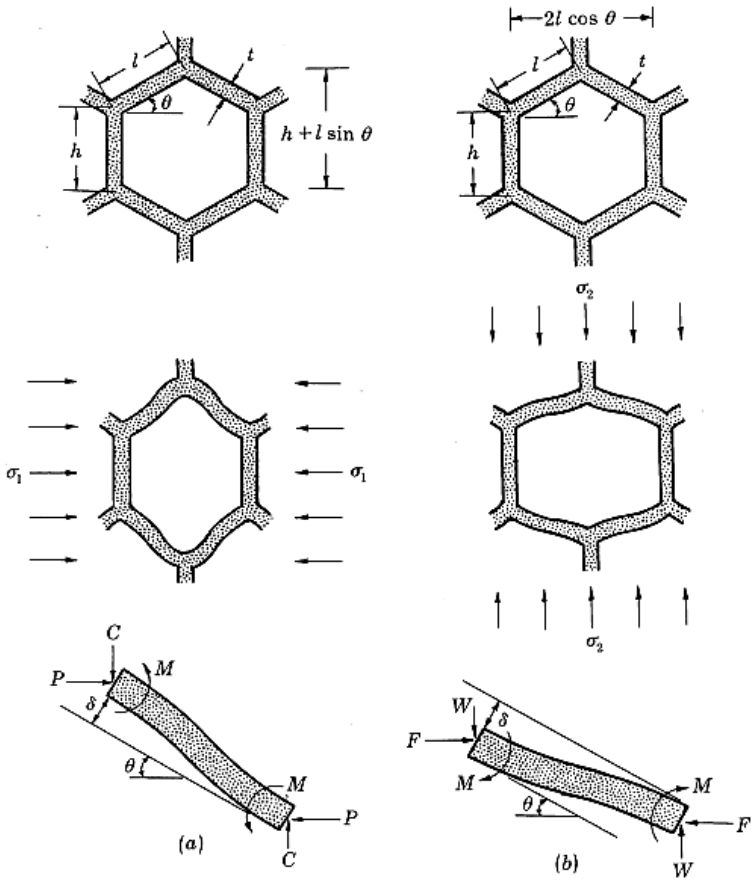

Fig. 2-16: deformation of a hexagonal cell in the X_1 (left) and X_2 (right) mutually perpendicular directions. (a) and (b), forces' moments balance in X_1 and X_2 direction for the cell upper right strut respectively, from (Gibson *et al.*, 1982).

Gibson *et al.* (1982) assumed that the strain experienced by the cell was small and that the struts could be modelled as beams constrained at both ends (Timoshenko, 1955). Further simplifications were included such as the absence of shear deformation and compression of the beam.

The beams are characterised by thickness t and depth b and elastic modulus as E_S. Such simplifying assumptions were proven to be acceptable as the additional conditions would be overcome by the experimental error. For high density honeycombs (i.e. t/l=1/4) however, the complete analysis cannot be avoided.

The equilibrium of moments and forces applied to the beam at the bottom of Fig. 2-16 can be written as:

$$M=\frac{1}{2}\ P\,l\sin\theta \qquad \textbf{Eqn. 2-3}$$

$$P=\sigma_1(h+l\sin\theta)b \qquad \textbf{Eqn. 2-4}$$

and, from standard beam theory, they obtained the deflection of the wall δ:

$$\delta=\frac{P\,l^3\sin\theta}{12E_SI} \qquad \textbf{Eqn. 2-5}$$

with I as the second moment of inertia for a wall of uniform thickness.
The corresponding strain is:

$$\varepsilon_1=\frac{\delta\sin\theta}{l\cos\theta}=\frac{\sigma_1(h+l\sin\theta)\,b\,t^2\sin^2\theta}{12E_S\,I\cos\theta} \qquad \textbf{Eqn. 2-6}$$

Then, the *Young's Modulus* in the X_1 direction is simply σ_1/ε_1, thus:

$$\frac{E_1}{E_S}=\left(\frac{t}{l}\right)^3\frac{\cos\theta}{(h/l+\sin\theta)\sin^2\theta} \qquad \textbf{Eqn. 2-7}$$

The loading in the X_2 direction is analysed similarly and the deformation of the cell is shown by the beam at the bottom of Fig. 2-16. Equilibrium conditions applied on the beam of length l and depth b result in $F=0$ and $W=\sigma_2 lb\cos\theta$.
The momentum M is then:

$$M=\frac{W\,l\cos\theta}{2} \qquad \textbf{Eqn. 2-8}$$

and the corresponding wall deflection is:

$$\varepsilon=\frac{Wl^3\cos\theta}{12E_SI} \qquad \textbf{Eqn. 2-9}$$

The component $\delta\cos\theta$ which is parallel to X_2 gives a strain:

$$\epsilon_2=\frac{\delta\cos\theta}{h+l\sin\theta}=\frac{\sigma_2 bl^4\cos^3\theta}{12E_sI(h+l\sin\theta)} \qquad \textbf{Eqn. 2-10}$$

and the Young's Modulus in the X_2 direction is given by σ_2/ε_2, thus:

$$\frac{E_2}{E_S}=\left(\frac{t}{l}\right)^3\frac{(h/l+\sin\theta)}{\cos^3\theta} \qquad \textbf{Eqn. 2-11}$$

By equating the relationships of the Young's Moduli in both directions, $E_1/E_S=E_2/E_S$ as the modulus of the solids is the same, one obtains:

$$\frac{E_1}{E_S}=\frac{E_2}{E_S}=2.3\left(\frac{t}{l}\right)^3 \qquad \textbf{Eqn. 2-12}$$

The *Young's Modulus* of regular hexagons, with walls of uniform thickness is, for both directions, the same, proving that such array is isotropic (Gibson *et al.*, 1982; Warren and Kraynik, 1987; Gibson and Ashby, 1997).

A further confirmation of the isotropic properties of the regular honeycomb has been provided by Warren and Kraynik (1987) who calculated the four independent in-plane elastic moduli by including the effects of cell wall axial and bending stiffness. One of these moduli has been already introduced as the Young's Modulus, also called the elastic modulus *E*. The other three are 1) the S*hear modulus G*, 2) the *Bulk modulus K* and 3) the *Poisson Ratio* ν.

For isotropic materials, two independent moduli can be used to determine a third one. The relationships are shown in Table 2-2. Anisotropic materials have remarkably different moduli according to the directions of the load. Wood and balsa, as described earlier, are representative of this class of materials. Moduli for anisotropic materials need to be measured in the loading directions as mutual relationships do not apply as in the case of isotropic materials.

2.4.2.1 Shear Stress and Shear Modulus

While the Young's Modulus *E* describes the response of a material upon compression or tensile loading thus the linear part of the stress-strain curve, the Shear Modulus *G* describes to what extent a material deforms when a shear load is applied. The Bulk modulus *K* refers to how a material responds to the hydrostatic pressure. The Poisson Ratio v is defined as the ratio (with a negative sign) between the lateral to the axial strain when loaded in the axial direction (these definitions can be found in material science and engineering well known textbook such as Callister (2000) or Ashby (2011).

Table 2-2: mutual relationship among mechanical properties moduli for an isotropic material. Young's, Shear, Bulk moduli and Poisson ratio.

Young's Modulus	Shear Modulus	Bulk Modulus	Poisson Ratio
$E=\frac{3G}{1+G/3K}$	$G=\frac{E}{2(1+\nu)}$	$K=\frac{E}{3(1-2\nu)}$	$\nu=-\frac{\epsilon_2}{\epsilon_1}$

The effect of shearing load on honeycombs with uniform and non-uniform thickness wall was studied by Warren and Kraynik (1987). The shear stress and its effects on a honeycomb cell are shown in Fig. 2-17.

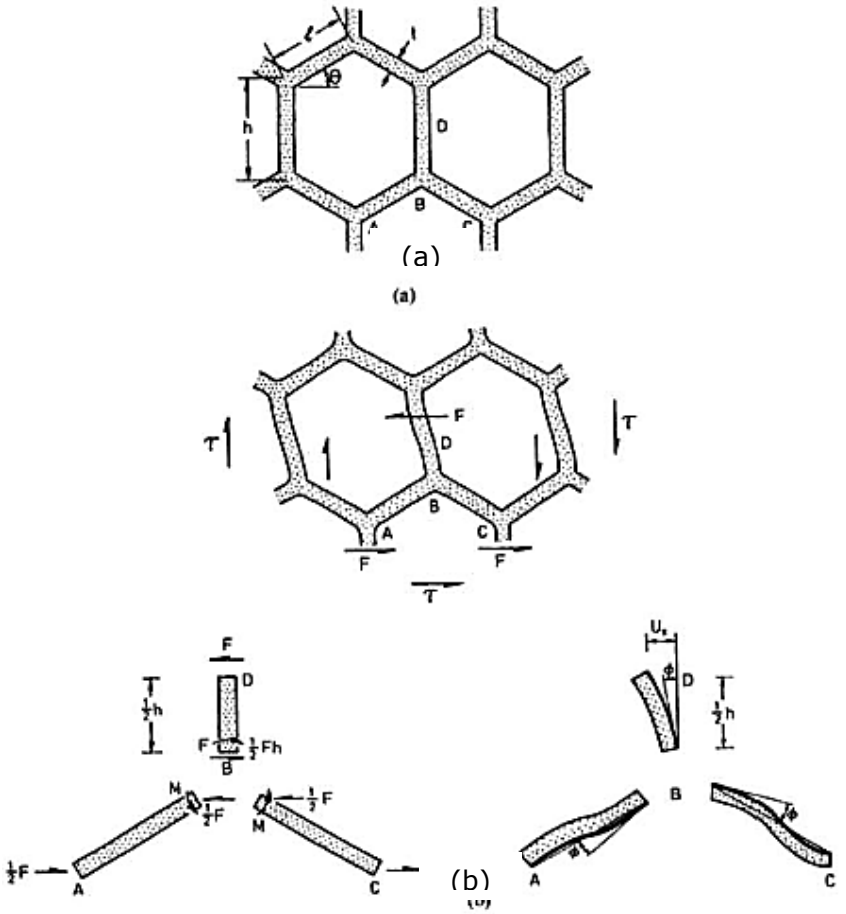

Fig. 2-17: shear stress deformation of a honeycomb. (a) undeformed, (b) deformed cells and details of the stresses acting on the beams causing rotation and displacement of the cell elements, from (Gibson and Ashby, 1997).

The shear deflection u_S is caused only by the bending of the beam BD and its consequent rotation on B (measured by the angle ϕ). By summing all the force moments in B, the moments applied to the member AB and BC can be found $M=F\,h/4$ and by using the previous result for the beam displacement $\delta=Ml^2/(6E_SI)$, the angle of rotation ϕ is derived by:

$$\phi=\frac{Fhl}{24E_SI} \qquad \textbf{Eqn. 2-13}$$

The deflection due to shear of D with respect to B is given by:

$$u_S=\frac{1}{2}\phi\, h+\frac{F}{3E_SI}\left(\frac{h}{2}\right)^3=\frac{Fh^2}{48E_SI}(l+2h) \qquad \textbf{Eqn. 2-14}$$

It is now possible to calculate the shear strain γ:

$$\gamma = \frac{2U_S}{(h + l \sin\theta)} = \frac{Fh^2}{24E_S I} \frac{(l+2h)}{(h+l\sin\theta)} \qquad \textbf{Eqn. 2-15}$$

The shear stress $\tau = F/(2lbcos\theta)$ determines the shear modulus:

$$G_{12}^* = \frac{\tau}{\gamma} \qquad \textbf{Eqn. 2-16}$$

or, by taking into account the expression for E_S, it becomes:

$$\frac{G_{12}^*}{E_S} = \left(\frac{t}{l}\right)^3 \frac{(h/l + \sin\theta)}{(h/l)^2(1+2h/l)\cos\theta} \qquad \textbf{Eqn. 2-17}$$

which for uniform, regular hexagons reduces to:

$$\frac{G_{12}^*}{E_S} = 0.57\left(\frac{t}{l}\right)^3 \qquad \textbf{Eqn. 2-18}$$

and by considering that the Poisson Ratio (as the negative ratio of the two perpendicular strains) in both directions:

$$\nu_{12}^* = -\frac{\varepsilon_2}{\varepsilon_1}$$

and

$$\nu_{21}^* = -\frac{\varepsilon_1}{\varepsilon_2} \qquad \textbf{Eqn. 2-19}$$

is equal to 1 for regular hexagons, the Shear Modulus becomes:

$$\frac{G_{12}^*}{E_S} = \frac{1}{4}\frac{E}{E_S}$$

or

$$G_{12}^* = \frac{1}{4}E \qquad \textbf{Eqn. 2-20}$$

which again confirms the isotropic nature of the honeycomb. As $G^*_{12}=E/[2(1+\nu)]$, by substituting $\nu=1$ the Shear Moduli can be expressed as a function of two other parameters (moduli).

2.4.2.2 Non-elastic behaviour

The analysis presented above investigated the linear-elastic behaviour. Non-linear elastic behaviour is however of even more relevant importance as honeycombs exploit energy absorption by undergoing large deformation at relatively constant stress. Many authors investigated the mechanisms that dictate the non-elastic behaviour (Gibson *et al.*, 1982; Maiti *et al.*, 1984; Gibson, 1989; Papka and Kyriakides, 1994; Silva *et al.*, 1995; Gibson and Ashby, 1997; Simone and Gibson, 1998).

In particular, Papka and Kyriakides (1994) identified the effect of geometry and material irregularities that originated load instability and shear deformation of the hexagonal array. Such corrective effects were acknowledged to be smaller than the experimental error in the model presented by Gibson and Ashby (1997).

There is a widely accepted evidence that overall a series of deformation mechanisms exist for a honeycomb subjected to compressive load. Such deformation mechanism series can be reported as, according to Gibson and Ashby (1997):

a) *Linear-elastic deformation* - dominated by the cell wall bending. The cellular nature of the honeycomb reflects and exploits this behaviour.
b) *Elastic Buckling* – the cell walls are considered as beams of constant section loaded at both ends and they buckle when the *Euler buckling load* is exceeded. The critical load for buckling to occur is (Timoshenko and Gere, 1961):

$$P_{crit} = \frac{n^2 \pi^2 E_S I}{h^2} \qquad \textbf{Eqn. 2-21}$$

The factor *n* refers to the *rotational stiffness* of the point (node) where the tree cell walls meet. Basically, due to geometric and loading conditions, free or no rotation is allowed. These two conditions are expressed by two different values of *n*.

The conditions that determine the value of *n* were identified and reported by Gibson and Ashby (1997). The deformation of a regular hexagonal array is shown in Fig. 2-18 where the rotational stiffness n is determined at the node B, where three beams (AB, BC and EB) intersect. The load that acts on column EB, the one that has buckled is $P=2\sigma_2 lbcos\theta$ and the elastic collapse which occurs when $P = P_{crit}$ is given by:

$$\frac{(\sigma^*_{el})_2}{E_S} = \frac{n^2 \pi^2}{24} \frac{t^3}{l\, h^2} \frac{1}{cos\theta} \qquad \textbf{Eqn. 2-22}$$

The value of n, which also is dependent on the *h/l* ratio, was derived to be laying between the no-rotation and free rotation, and for regular hexagons, n=0.69 (Gibson and Ashby, 1997).

The simple beam theory, valid for $t/l < 1/4$ enables to determine the stress at which a regular hexagons collapse:

$$\frac{(\sigma^*_{el})_2}{E_S} = 0.22 \left(\frac{t}{l}\right)^3 \qquad \textbf{Eqn. 2-23}$$

The strain at which the stress causes collapse is found by substituting the elastic modulus $E/E_S = 2.3(t/l)^3$ in Eqn. 2-23:

$$(\varepsilon^*_{el})_2 = \frac{(\varepsilon^*_{el})_2}{E} = \frac{1}{10} \qquad \textbf{Eqn. 2-24}$$

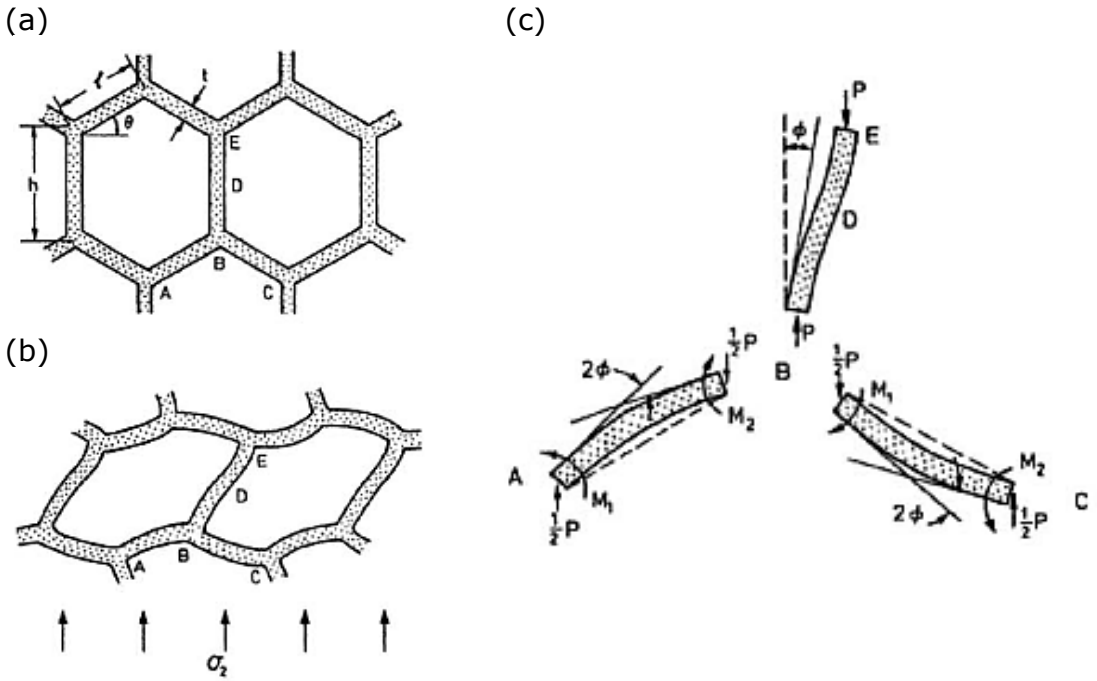

Fig. 2-18: deformation of a honeycomb due to elastic buckling when compressed in X_2 direction (a) undeformed, (b) deformed cells and (c) details of the stresses acting on the beams AB, BC and EB causing rotation and displacement of the cell elements, from (Gibson and Ashby, 1997).

The equations above then enable the prediction of the limit of elastic bending. They can be used to predict the stress and the strain at which buckling is theoretically expected to occur. In designing an energy adsorbing material whose desired collapse mechanism is linear elastic, followed by elastic buckling, such two design equations may suffice.

Furthermore the model, developed for regular hexagons, has shown that there is no dependence on the honeycomb density. The most important condition to be satisfied (which is almost always satisfied in practical design) is t/l < 1/4. The validity of the model was verified experimentally by testing many different materials with varying hexagon geometric parameters. A comparison between the model and the experiments is shown in Fig. 2-19. The theoretical and experimental results adherence was remarkably good (Gibson *et al.*, 1982; Gibson, 1989; Gibson and Ashby, 1997; Silva and Gibson, 1997; Simone and Gibson, 1998).

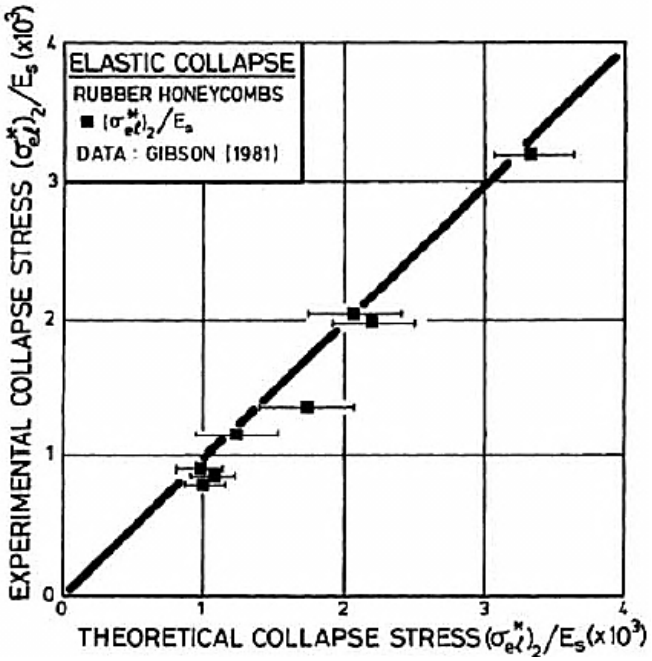

Fig. 2-19: comparison between theoretical (solid line, Eqn. 2-22) and experimental elastic collapse stress of elastomeric honeycombs made of hexagons with varying values of *h/l, h* and *θ*, (Gibson and Ashby, 1997).

Further deformation mechanisms described by Gibson *et al.* (1982) are:

c) *Plastic collapse* – occurs in elastic-plastic materials (as many polymers), when the (elastic) bending moment of the cell reaches the fully plastic moment. Such deformation is irreversible and originates the plateau region in the stress-strain curve. The mechanism is associated with the development of plastic hinges on the cells (Fig. 2-20).

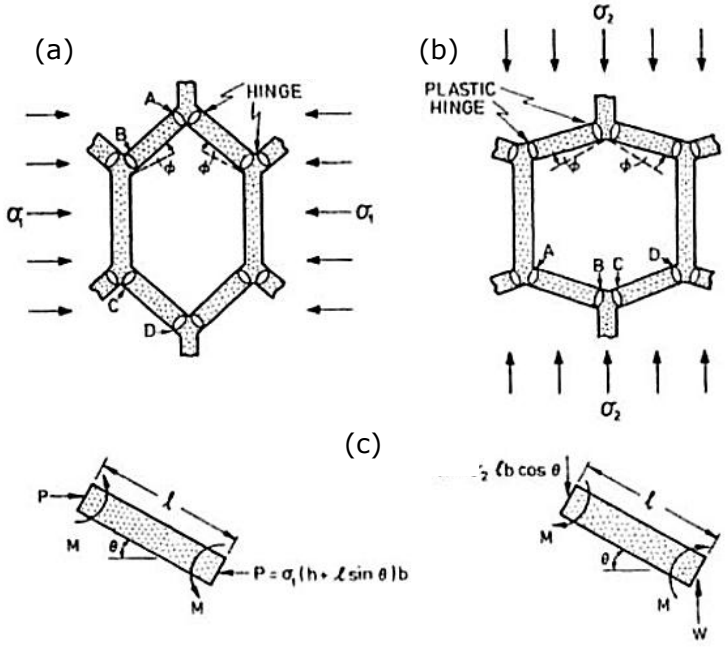

Fig. 2-20: plastic deformation processes in X_1 (a) and X_2 (b) directions with plastic hinges formation. (c) forces and stresses acting on the representative cell elements, adapted from (Gibson and Ashby, 1997).

The analysis of the stresses and moments on the hinged beams leads to the determination of both axial and shear stresses.

The axial σ_{pl} and shear stress τ_{pl} at which plastic collapse occurs for regular hexagons are given by:

$$\frac{\sigma^*_{pl}}{\sigma_{ys}} = \frac{2}{3}\left(\frac{t}{l}\right)^2 \qquad \textbf{Eqn. 2-25}$$

and

$$\frac{(\tau^*_{pl})_{12}}{\sigma_{ys}} = \frac{1}{2\sqrt{3}}\left(\frac{t}{l}\right)^2 \qquad \textbf{Eqn. 2-26}$$

Experimental results by Gibson *et al.* (1982); Gibson and Ashby (1997); Onck *et al.* (2001) demonstrated that the theoretical values were consistently higher. They associated the lower values from the experiments due to imperfections in the tested samples such as a) the presence of defects, b) non-constant ratios and c) the distribution of solid at the edges of the beams. Papka and Kyriakides (1994) analysed the plastic collapse of an aluminium honeycomb and identified the collapse mechanism pathway. The elastic deformation of the specimen was uniform while the plastic collapse was localised. The collapse of a row of cells continues until densification before being transmitted to adjacent rows. The process is repeated upon further stress before the whole specimen reaches densification. A Finite Element Method (FEM) model (Fig. 2-22) was produces by the same authors and it showed to reproduce the behaviour well and the dependence of σ_{pl} on the squared of relative density (Eqn. 2-25) was confirmed (Gibson and Ashby, 1997).

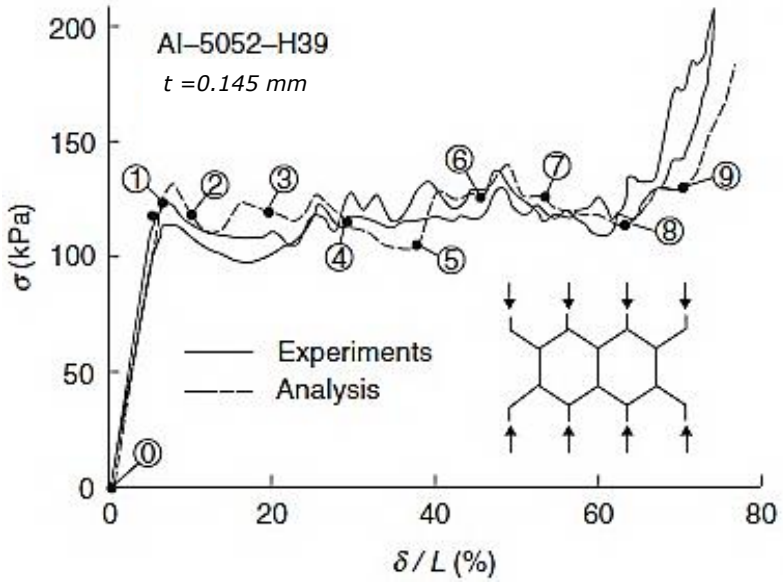

Fig. 2-21: measured and FEM modelled stress-strain curve of an aluminium honeycomb, (Papka and Kyriakides, 1994).

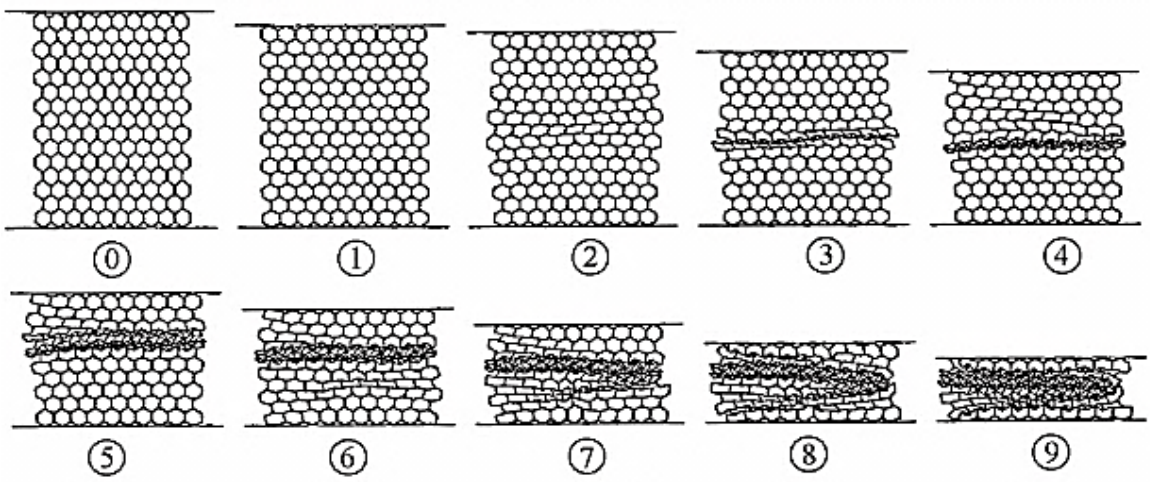

Fig. 2-22: FEM modelled compression sequence (1-9) of aluminium honeycomb compression. Numbering corresponds to points as indicated on stress-strain curve of Fig. 2-21, (Papka and Kyriakides, 1994).

For brittle materials it was anticipated that the collapse mechanism would be that of brittle failure.

d) *Brittle Failure* – occurs as progressive crushing in compression (while in tension the fracture is fast). The initial mechanism is again initiated by bending of the cell walls and when the collapse load in exceeded, progressive fracture occurs. The schematic representation of brittle failure is shown in Fig. 2-23.

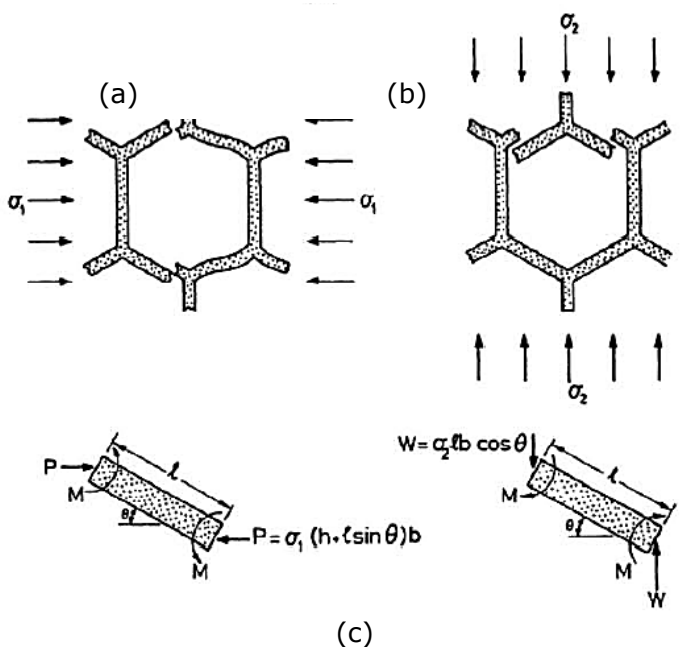

Fig. 2-23: brittle fracture process in X_1 (a) and X_2 (b) directions. (c) forces and stresses acting on the representative cell elements, adapted from (Gibson and Ashby, 1997).

The crushing strength in the two directions is calculated by:

$$\frac{(\sigma^*_{cr})_1}{\sigma_{fs}} = \frac{1}{3(h/l + \sin\theta)\sin\theta}\left(\frac{t}{l}\right)^2 \qquad \textbf{Eqn. 2-27}$$

and

$$\frac{(\sigma_{cr}^{*})_2}{\sigma_{fs}} = \frac{1}{3\cos^3\theta}\left(\frac{t}{l}\right)^2 \qquad \textbf{Eqn. 2-28}$$

that, for regular hexagons, reduces to

$$\frac{\sigma_{cr}^{*}}{\sigma_{fs}} = \frac{4}{9}\left(\frac{t}{l}\right)^2 \qquad \textbf{Eqn. 2-29}$$

and the isotropic nature of the regular hexagon is proved also in the crushing mode.

2.4.2.3 Viscoelastic behaviour

Gibson and Ashby (1997) investigated the deformation of honeycombs made of visco-elastic materials. *Visco-elastic deformation* occurs *in polymeric materials that operate at* temperatures near or above the *Glass Transition Temperature* (*Tg*).

Tg is defined as the threshold temperature below which the polymer is hard and glassy and above which the polymer is rubbery (ASM-International, 2003). The *Tg* reflects the onset of the movements of the molecules in the polymer due to temperature and is itself an indicator of visco-elasticity. For such reasons not only *Tg* is a function of the conditions of the applied temperature-change range, but also on loading testing conditions at which it was determined.

An immediate consequence of the effects of temperature on a *thermoplasti*c and *thermoset* polymeric material is the lowering of the Elastic modulus (Fig. 2-24).

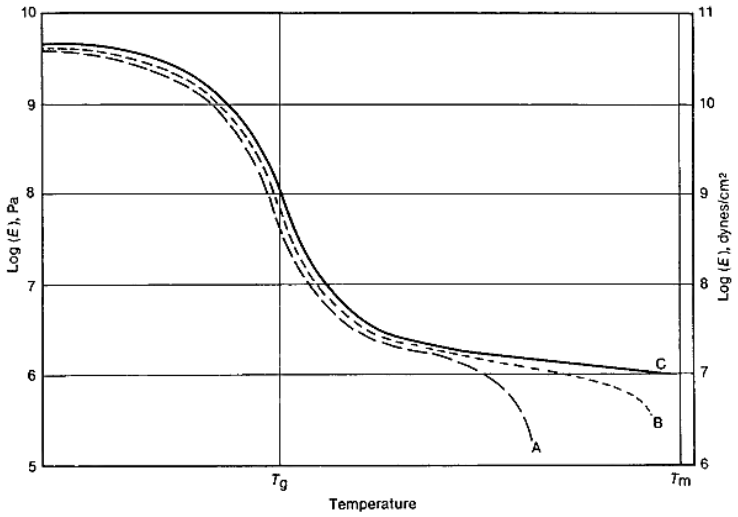

Fig. 2-24: effect of temperature on Elastic modulus of idealised Polymers. (A) amorphous thermoplastic, (B) semicrystalline thermoplastic and (c) thermoset polymer.

The main difference between thermoplastic and thermoset materials is that thermoplastic materials melt and become liquid above the melting temperature,

while thermoset do not melt. The latter condition is due to the presence of crosslinks among the polymer chains.

A further evidence of the mutual effects of temperature and loading conditions is shown in Fig. 2-25.

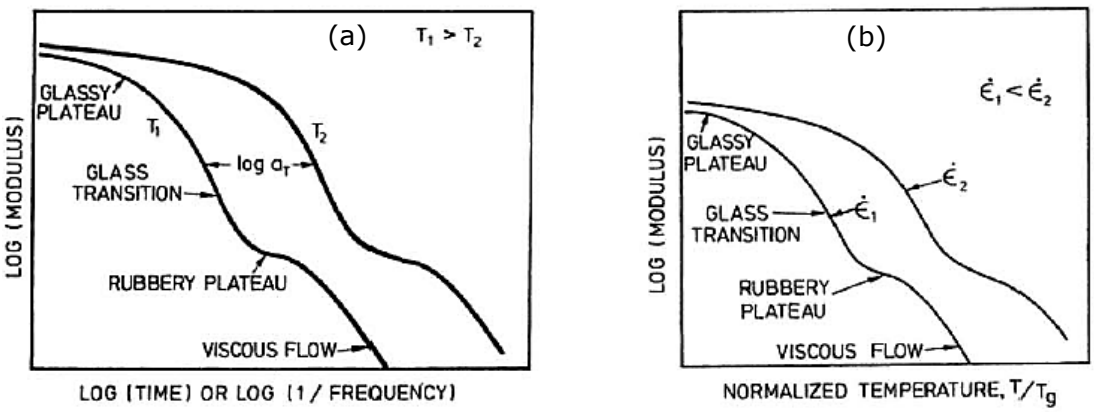

Fig. 2-25: variation of elastic modulus of a polymer with (a) temperature and (b) with loading time. at indicates the shift factor. Adapted from (Gibson and Ashby, 1997).

The *time-temperature correspondence* was identified by Williams *et al.* (1955) and it enables the elastic modulus to be calculated at a different temperature if the modulus is known for one. The scaling law on the horizontal axis can be expressed as:

$$E_s(t, T_0) = E_S\left(\frac{t}{a_t}, T_1\right) \qquad \textbf{Eqn. 2-30}$$

where t and T_0 are the initial (known) loading time and temperature, T_1 as the calculated temperature and at the shift factor to account for the equivalent loading time at T_1. The value of a_t when $T_0 = Tg$ was obtained by Williams *et al.* (1955) and it enabled to develop a relationship between Tg and any other temperature above it, provided that $T1 < (Tg + 100)$ °C :

$$log\ a_t = \frac{-C_1(T_1 - T_g)}{C_2 + T_1 - T_g} \qquad \textbf{Eqn. 2-31}$$

The two constants are valid for a wide range of materials but better estimation can be obtained by testing the material of interest (Mark, 2007).

The visco-elastic behaviour is originated by the solid material and it is kept by the cellular solid. It is then of particular interest to assess the changes in the material properties due either to temperature or loading rate, as the two conditions are likely to occur during the operating life of the IRM.

The analysis of visco-elastic honeycombs was presented by (Gibson and Ashby, 1997). They modelled the cell by a modified *Voigt* element, comprised of two parts: 1) a spring of stiffness E_{S2} in parallel with a Dashpot (which models the viscous behaviour) and 2) another spring of stiffness E_{S1} in series with the first element. They presented the equation describing the visco-elastic behaviour for a regular hexagon:

$$\dot{\varepsilon}_1 + \frac{E_{S2}}{\eta_s}\epsilon = \frac{\sqrt{3}l^3}{4t^3}\left\{\frac{\dot{\sigma}}{E_{S1}} + \frac{\sigma}{\eta_S}\left(\frac{E_{S1} + E_{S2}}{E_{S1}}\right)\right\} \qquad \textbf{Eqn. 2-32}$$

and analysed two cases: 1) slow and 2) rapid loading time.
When loading is applied slowly, the first terms on both sides of the equation become negligible and the strain ε is:

$$\varepsilon = \frac{\sqrt{3}l^3}{4t^3}\left\{\left(\frac{E_{S1} + E_{S2}}{E_{S1}}\right)\right\} \qquad \textbf{Eqn. 2-33}$$

When the load is applied rapidly instead:

$$\varepsilon = \frac{\sqrt{3}l^3}{4t^3}\frac{\sigma}{E_{S1}} \qquad \textbf{Eqn. 2-34}$$

In order to complete the investigation on visco-elastic materials, the case of constant stress ($\dot{\sigma}=0$) applied to the honeycomb was considered and the time-dependent strain is:

$$\epsilon = \frac{\sqrt{3}l^3}{4t^3}\sigma\left(\frac{E_{S1} + E_{S2}}{E_{S1}E_{S2}}\right)\left(1 - e^{-\frac{E_{S2}}{\eta_S}\tau}\right) \qquad \textbf{Eqn. 2-35}$$

where τ is the time. The time constant for such relaxation conditions is represented by η_2/E_{S2} and it depends only on the material of the wall, regardless of the honeycomb density, while the magnitude of the effects depend on the honeycomb characteristics (Gibson and Ashby, 1997).

2.4.2.4 Densification

The last regime to be analysed upon compression is *Densification*. It occurs at large strains and it is an indication that the struts are contacting each other. Whether the cells have collapsed by elastic buckling, plastic hinges or fracture, the analysis can be made on the basis of geometrical terms. In the case of regular hexagons, the theoretical strain at which densification starts would correspond to the cellular material porosity $\theta=1-(2\sqrt{3})(t/l)$ (Gibson and Ashby, 1997). However, this theoretical value (~0.7 for $t/l=1/4$) is higher than that found in experiments on foams, where densification starts at ($\theta=0.5$), (Gibson and Ashby, 1997).

The study presented by Gibson and Ashby (1997) on the mechanical behaviour of honeycombs was completed by presenting their findings on the effects of the variability of the geometry in the cellular structure. They concluded that the effects on the elastic modulus due to the micro-structural variability was limited, in agreement with previous studies by Kraynik *et al.* (1991) on 2D liquid froths and those of (Silva *et al.*, 1995) who confirmed the results for low density honeycombs ($0.05 < \rho/\rho_S < 0.30$).

The overall effects of geometrical factors on the mechanical behaviour of honeycomb loaded in compression (in-plane), can be seen in Fig. 2-26.

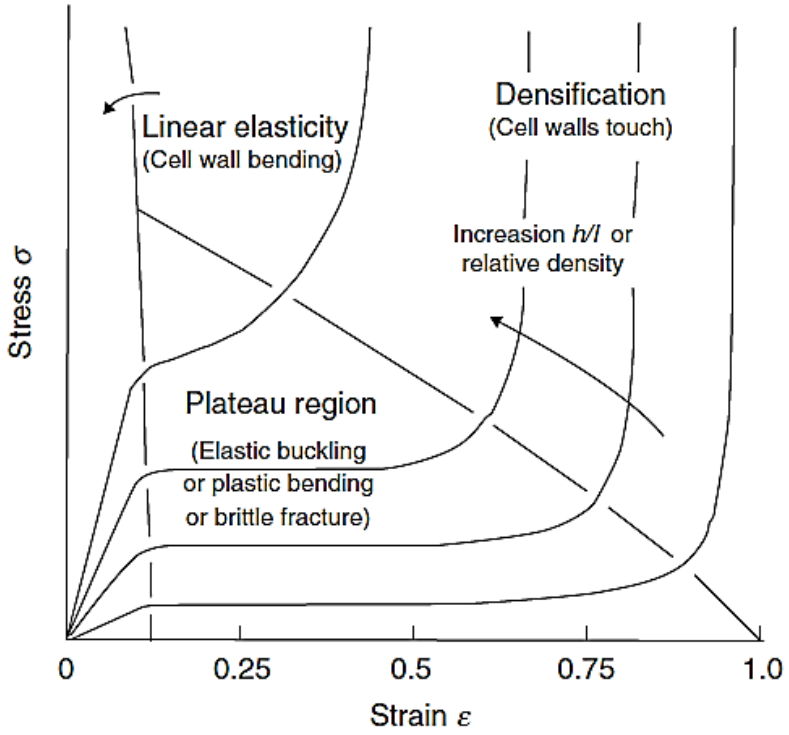

Fig. 2-26: schematic representation of stress-strain curve for a honeycomb loaded in in-plane compression. The three regimes and their characteristic mechanisms are shown, Linear elastic (left), followed by a *Plateau* (centre) and Densification (right), adapted from (Gibson and Ashby, 1997)

The most relevant effect of increasing density in honeycombs is the shortening of the *Plateau* region. Consequently the densification occurs at lower strains. The elastic behaviour, dominated by bending mechanisms occurs, as it should, approximately at the same strain. Beyond the elastic behaviour, the onset of the other collapse mechanisms is shown.

The fundamental mechanisms that govern the honeycombs will be transferred to the foams in order to study their behaviour.

2.4.3. Microstructure of foams

Although foams are much more complex than regular honeycombs, the main findings of the latter are useful to describe the behaviour of foams. Foams are made of polyhedral cells and have a 3D structure. A further distinction can be made by considering the cells as *open* or *closed*. Open cell implies that the solid material is concentrated on the struts (also referred as beams in modelling) while in closed cells the solid is present also on the faces by means of a thin membrane (Gibson and Ashby, 1982). Several examples of open or closed cells exist in Nature and nowadays almost any material can be foamed (Gibson, 1985; 1989; Gibson and Ashby, 1997; Gibson, 2000). Examples of natural and synthetic foams are shown in Fig. 2-27:

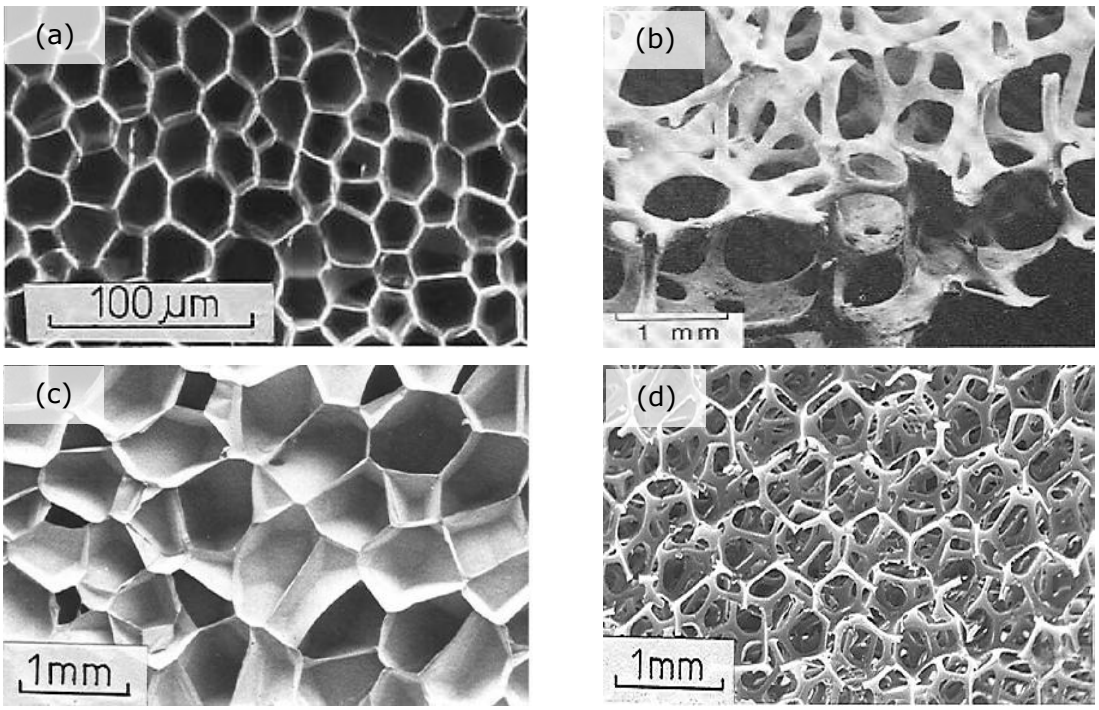

Fig. 2-27: images of closed and open cell natural and synthetic foams. (a) cork, closed cells, (b) cancellous bone, open cells, (c) polyethylene cell and (d) polyurethane open cell

A useful parameter used to distinguish between open and close cell is the ratio of volume of the material in the face V_f to that of the edge V_e:
$\phi = V_f/V_e = (t_f l)/t_e^2$. For open cell foams, $\phi = 0$ and $\phi = l/t$ for closed cell foams with wall and edges of the same thickness (Gibson and Ashby, 1982).

2.4.4. Mechanics of foams

It was anticipated in the study of honeycombs that the density is the most important property to measure. The geometry of regular honeycombs can, in fact, be related to the their density by recalling that: $\rho/\rho_S=(2/\sqrt{3})\,t/l$ (Eqn. 2-2). Such a relationship has been extensively used to model

the mechanical characteristics of foams. In their early studies on foams, Gibson and Ashby (1982) related the properties of the foam to those of the cell walls and equated them to the relative density elevated to an exponent $n \geq 1$:

$$\frac{Foam\ Property}{Cell\ Wall\ Property} = C\left(\frac{\rho}{\rho_S}\right)^n$$

The power-law relationship is used to determine several key mechanical properties such as: 1) the Elastic Modulus, 2) the Shear Modulus and can be used also to predict 3) the elastic collapse and 4) the plastic yield.

The model was demonstrated to effectively hold when written as a power-law whose fitting constants *C* were determined experimentally (Gibson and Ashby, 1982; Gibson, 1989; Gibson and Ashby, 1997). The fitting constants vary for each mechanical parameter being measured.

The original cubic model used by Gibson and Ashby to model both open and closed cells is shown in Fig. 2-28.

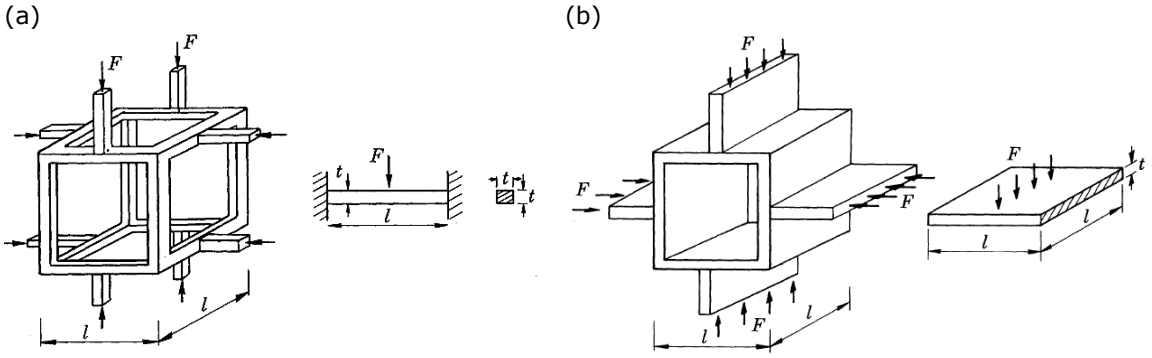

Fig. 2-28: schematic model of foams: (a)open cell and struts (b) closed cell and thin membranes covering the faces, adapted from (Gibson and Ashby, 1982).

The initial conditions for the analysis implied that the relative density would be proportional to the square of the dimension of the struts with length *l* and cross section *t* such that $\rho/\rho_S \propto (t/l)^2$ and that the second moment of area *I* of the strut member is related to its cross section ($I \propto t^4$). The former condition had been confirmed by the same authors for the modelling of honeycombs (Gibson *et al.*, 1982). As per the honeycombs, the cells were modelled as regular, so no variation in length or cross section was accounted for.

The deformation mechanisms were studied for compressive loadings and they parallel those for honeycombs.

2.4.4.1 Linear Elastic deformation

The initial *Linear Elastic* deformation - attributed to the *wall bending* for *open cells* or *wall stretching* for *closed cells* (Gibson and Ashby, 1982; Ashby and Medalist, 1983; Gibson and Ashby, 1997). This result was later confirmed by (Warren and Kraynik, 1988; 1991) who also accounted for the effects of increasing relative density $\rho/\rho_S > 0.1$. A useful representation of such mechanism is shown in Fig. 2-29.

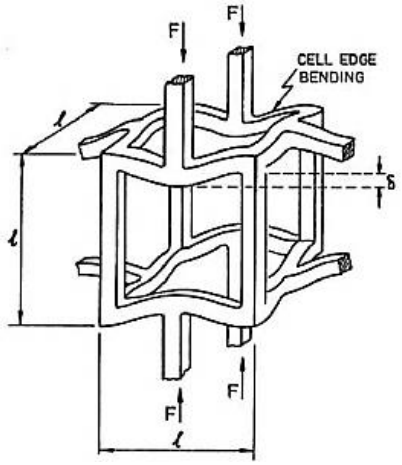

Fig. 2-29: open cell model subject to compression. Wall bending deformation occurs in the linear elastic region, adapted from (Gibson and Ashby, 1997)

The power-law relationships that describe the elastic behaviour of polymeric foams are Gibson and Ashby (1982):

$$\frac{E}{E_S} = C\left(\frac{\rho}{\rho_S}\right)^2 \qquad \text{for open cells} \qquad \textbf{Eqn. 2-36}$$

and

$$\frac{E}{E_S} = C'\left(\frac{\rho}{\rho_S}\right)^3 \qquad \text{for closed cells} \qquad \textbf{Eqn. 2-37}$$

The two constant were calculated by fitting several foams, made by different materials and it was found that $C \approx 1$ and $C' \approx 1$.

Closed cells with $\phi > 5$ behave as predicted by $\sigma_{pl}/\sigma_y \propto (\rho/\rho_S)^2$, but often $\phi < 1$ due to the fact that in synthetic foams, the solid tends to be concentrated on the edges of the cell rather than the face. In this case, their behaviour reduces to that of an open cell structure with $\sigma_{pl}/\sigma_y \propto (\rho/\rho_S)^{3/2}$. It was anticipated that for $1<\phi<5$ the experimental properties of the cell would be described by $2<n<3$ (Gibson and Ashby, 1982). For this case, the closed cell dependence of elastic modulus to ϕ, also accounts for the membrane stress:

$$\frac{E}{E_S} = \phi^2 \left(\frac{\rho}{\rho_S}\right)^2 + (1-\phi)\frac{\rho}{\rho_S} \quad \text{for closed cells} \qquad \textbf{Eqn. 2-38}$$

The shear modulus *G* for open and close cells also follows a power law with with relative density *n=2* and the *Poisson Ratio* $\nu \approx 1/3$ for both layouts.

2.4.4.2 Collapse by Elastic Buckling

Collapse by *Elastic Buckling* occurs similarly as in elastomeric honeycombs; the struts of the foam may buckle elastically if the buckling load is exceeded. A schematic representation of the elastic buckling of an open cell is shown in Fig. 2-30.

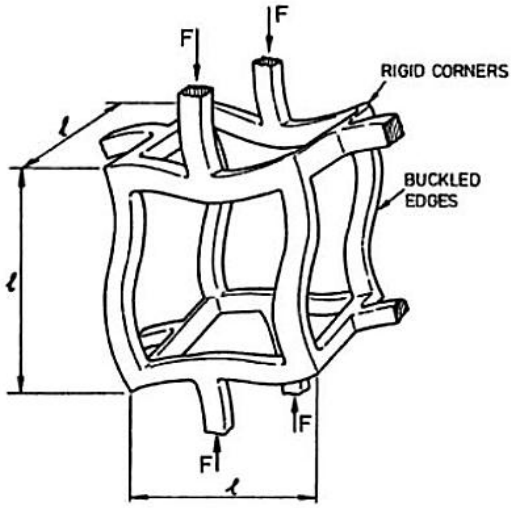

Fig. 2-30: cell wall deformation in compression due to elastic bending of an open cell foam, (Gibson and Ashby, 1997).

The collapse stress of an elastomeric foam σ_{el} due to buckling occurs after the initial elastic deformation of the cell walls. For open and closed cells again a simple power law applies:

$$\frac{\sigma_{el}}{E_S} \approx 0.05\left(\frac{\rho}{\rho_S}\right)^2 \quad \text{for open cells} \qquad \textbf{Eqn. 2-39}$$

and

$$\frac{\sigma_{el}}{E_S} \approx 0.05\left(\frac{\rho}{\rho_S}\right)^2 + \frac{(P_o - P_{at})}{E_S} \quad \text{for closed cells} \qquad \textbf{Eqn. 2-40}$$

Where P_0 is the actual pressure of the fluid in the cells and P_{at} is the atmospheric pressure.

It is commonly the case in which $P_0 = P_{at}$ so Eqn. 2-40 reduces to Eqn. 2-39.

2.4.4.3. Plastic Collapse

*In Plastic Collapse (*similarly to rigid honeycombs), plastic hinges develop at the cell corners when the moment on the cell walls exceeds the plastic moment. The

schematic representation of the plastic deformation mechanism is shown in Fig. 2-31.

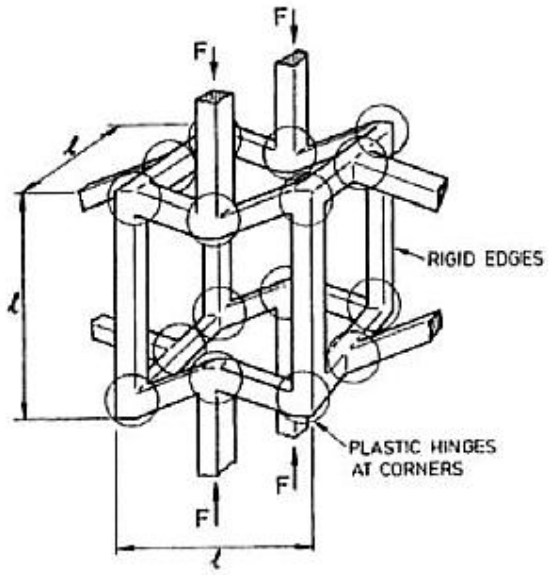

Fig. 2-31: cell wall plastic deformation of an open cell rigid foam and development of plastic hinges (circled) in compression, (Gibson and Ashby, 1997).

The plastic strength of the open and closed foam σ_{pl}, relative to the yield strength of the cell wall material (the fully dense solid) σ_{ys} can be expressed in terms of a power law with $n=1.5$. The closed foam relationship contains an additional term to account for the contribution of the material on the faces (Gibson and Ashby, 1997).

$$\frac{\sigma_{pl}}{\sigma_{ys}} \approx 0.3\left(\frac{\rho}{\rho_S}\right)^{3/2} \quad \text{for open cells} \qquad \textbf{Eqn. 2-41}$$

and

$$\frac{\sigma_{pl}}{\sigma_{ys}} \approx 0.3\left(\frac{\rho}{\rho_S}\right)^{3/2} + 0.4(1 - \phi)\frac{\rho}{\rho_s} \quad \text{for closed cells} \qquad \textbf{Eqn. 2-42}$$

2.4.4.4 Densification

Densification, similarly to honeycombs made of elastic or plastic materials occurs at large strains. Densification is recognised when the stress-strain curve shows a steep rise, indicating that the cell walls contact each other. The onset of densification strain ε_D can be predicted by $\varepsilon_D=1-1.4(\rho/\rho_S)^2$. The relationship correctly indicates that for increasing foam density, the densification occurs at lower strains.

2.4.4.5 Applicability of Gibson and Ashby Model

The analytical models reported herein that describe the deformation mechanisms were accurately re-developed and refined by Gibson and Ashby. Since their publication in the early '80s, they have been widely accepted as satisfactory

predictive tools for foam and honeycomb engineering purposes. Many foam and honeycombs handbooks written by experts in the industry (Landrock, 1995; Lu and Yu, 2003; Lee and Ramesh, 2004; Gendron, 2005; Lee *et al.*, 2007) refer to the work of Gibson and Ashby when mechanical performances of various foams (or honeycombs) are required.

Further analysis of the mechanical behaviour of cellular material has been conducted with the support of Finite Element Modelling (FEM) techniques and in recent years many refinements have been made. The main findings are presented in the next section.

2.4.5. Refinements of foam mechanics via Finite Element Method

As explained in previous sections, the applicability of the Gibson and Ashby (1997) model has many advantages including:

1. requiring basically one single parameter to be measured (usually with minor efforts, the actual density of the foam
2. being characterised by a power-law with a single constant which includes many of the irregularities of the cubic-model such as:
   2.1. non-uniform cell size
   2.2. non-constant section of the struts
   2.3. defects
3. Applies to a very wide range of materials and can be best fitted by actual experimental results

The effectiveness of the model to describe the deformation mechanisms and evaluate the mechanical properties of both honeycombs and foams has been acknowledged by many authors in the scientific community.

However, the major driving force more recently was to include analytically what Gibson and Ashby included semi-empirically in the fitting constants. In particular, studies on the effects of non-uniform cell size distribution were performed by Roberts and Garboczi (2001) and Roberts and Garboczi (2002a) and they concluded that the effect of cell size variation accounts for less than 10% of the mechanical performances. Roberts and Garboczi (2002b) also modelled random cell size distribution foams by using a *Voronoi Tessellation* FEM approach and the section of the struts was not imposed to be constant (as observed for real foams). The Voronoi tessellation is based on the principle that randomly placed seed-points in space are surrounded by surfaces that are closer to that point than any other surface (Roberts and Garboczi, 2001); and this technique is largely used for

modelling real foams. The results also confirmed that the Young's Modulus of the foams is independent of Poisson ratio of the material as had been anticipated by Gibson and Ashby (1982) and Gibson *et al.* (1982).

Grenestedt (1998) investigated analytically and via FEM perfectly regular models made of a) cubically symmetric-periodically arranged struts and compared them with b) randomly arranged struts, both with the same relative density. It was concluded that they behaved almost identically and that the power-law was adequate for prediction of mechanical properties. An overestimation of the properties was attributed to the deliberate absence of any defect in the model compared to what would normally occur in real foams.

Different and more realistic cell models were later investigated via FEM by many other authors, in order to better identify cell deformation mechanisms. Among them, Zhu *et al.* (1997a) and Zhu *et al.* (1997b) extensively used the FEM on Kelvin foams (known as the tetrakaidecahedron and shown in Fig. 2-11) with varying cell edges cross section and density and they calculated the Young's Modulus and Poisson ratio by bending, twisting and extension mechanisms. They concluded that the cell bending mechanism would be appropriately described by a power-law with n=2 and that the other mechanisms reduced this exponent by 3-5%. However, they argued that one of the assumptions that lead Gibson and Ashby (1997) to assume that $C_2 \approx 1$ (derived from the elastic model) was not justified and $C_2 \approx 0.33$ instead (Mills, 2007b).

FEM models were also used to account for the anisotropy of foams, a condition that determines large variation of the properties according to the loading directions and already discussed in earlier sections for wood and balsa.

The anisotropy of foams arises from the foam manufacturing method, particularly when the *Slabstock* process is used. In this process, detailed in a dedicated section, the polymer melt and the blowing agent are mixed together. Following the expansion of the gas, the voids are formed in the polymer melt. The foam is then left expanding unconstrained until the desired height is reached and later cooled. The overall effect is that the voids are elongated in the rising direction (Mills, 2007b).

Zhu *et al.* (1997a); Zhu *et al.* (1997b); Gong (2005); and Gong *et al.* (2005) investigated the effects of cells anisotropy by using again the Kelvin cell while Zhu and Windle (2002) used the Voronoi tessellation method to generate a random cell with constant strut cross section and found that its elastic modulus was almost

50% higher than its corresponding regular Kelvin cell. When circular cross section was instead used by Gan *et al.* (2005) the elastic modulus was found to be similar to that of Kelvin cells so irregularities/randomness have no effect on the linear elastic behaviour.

Further features of the overall behaviour of a foam under compression was modelled by Roberts and Garboczi (2001); Laroussi *et al.* (2002); Gong (2005); and Gong and Kyriakides (2005). Schraad (2007) investigated the effects of non-uniform cell size (also termed polydispersity of the foam) by a stochastic model and confirmed that the polydispersity has little or no effect on the initial elastic behaviour but, most notably, it increases the stability of the mechanical response in compression.

Even more recently, (Jang *et al.*, 2008) obtained an X-Ray digitalised image of a series of real polyester urethane foams with varying cell sizes. They used the *Surface Evolver Software* (Brakke, 1992) to model random foams with straight struts of non-uniform cross section (Fig. 2-32) and compared it with Kelvin cells (Fig. 2-11). The elastic modulus was found to be higher in the range of 5-10% for random foams.

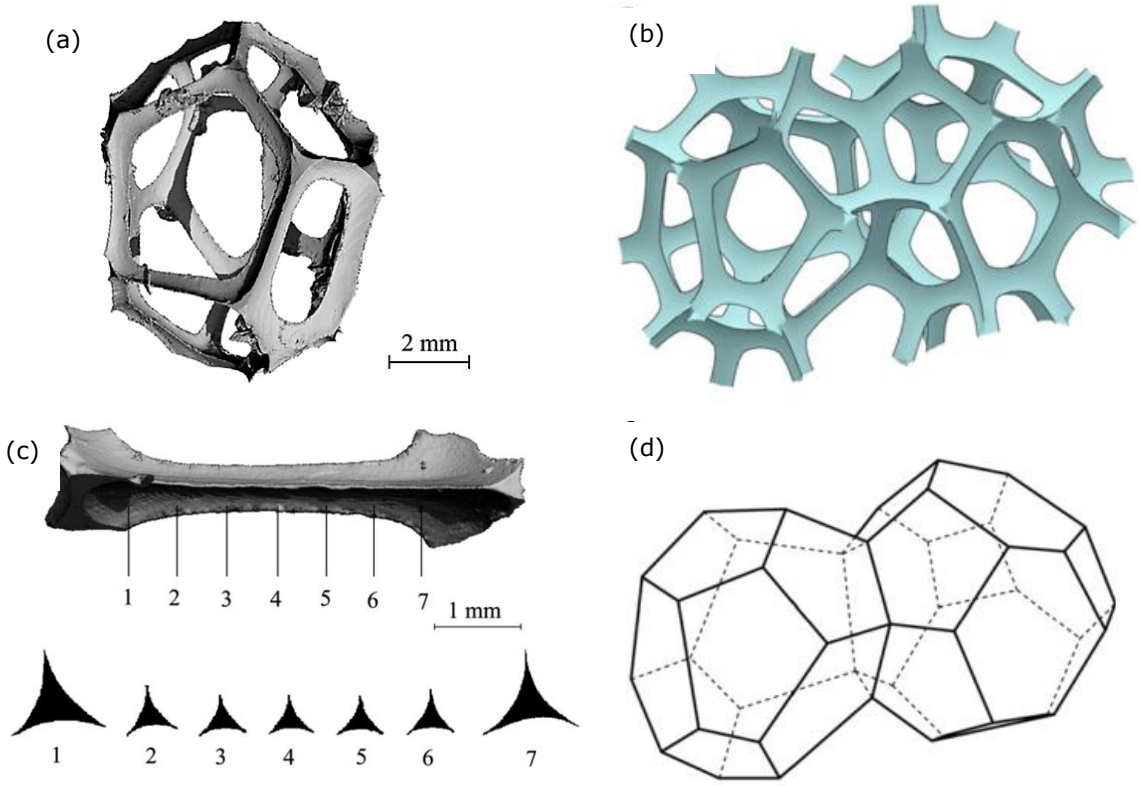

Fig. 2-32: digital image of polyester urethane foam (a) and Surface Evolver model (b). Cross section variation of foam struts(c). Skeletal drawing of modelled cell (d), adapted from (Jang *et al.*, 2008).

This section has shown the importance of foam modelling accuracy. The importance of the FEM method in capturing the morphology of the real foams is evident. Manufacturing processes and characteristics of the real foams are discussed in the next sections.

2.4.6. Processing of foams and effects on properties

Processing of foams is usually performed by two major techniques: 1) *Injection Moulding* and 2) *Continuous Slabstock* (Eaves, 2004). The injection moulding system basically consists of a screw where the polymer melt and the *Blowing Agent* (BA) are mixed together.

The BA can be a suitable gas or it can be a compound which produces the gas by two specific ways: 1) a chemical reaction (usually thermally activated decomposition at process conditions) with formation of gas, called chemical the blowing agent (CBA) or 2) a physical blowing agent (PBA) when a component such as a volatile chemical turns into a gas upon heating (Landrock, 1995) (Singh, 2004)).

In the injection moulding process, the polymer melt and the BA are typically thoroughly mixed in a high pressure extruder and further heated before being released through a die. The passage of the melt through the die causes a reduction of pressure which results in the melt expansion. The expanded melt is finally injected in the mould cavity which is later released. The mould serves multiple functions: a) distributes the melt into the cavities, b) shapes the part, c) cools the melt and d) releases the finished product (Osswald *et al.*, 2008). The process is then repeated to produce as many parts as required. An example of such process is shown in Fig. 2-33.

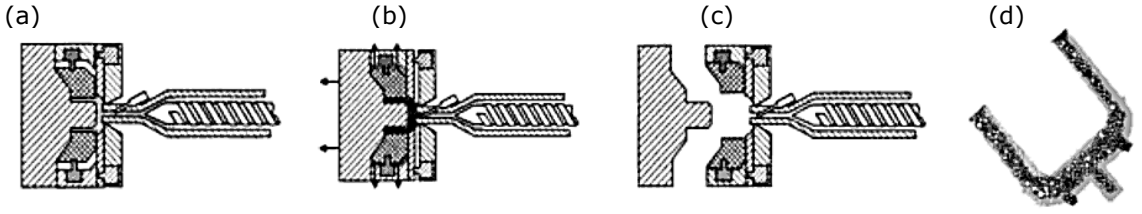

Fig. 2-33: mould filling process during injection moulding process. (a) injection of the polymer melt and BA in the mould by extrusion until designed volume is filled. (b) mould enlargement and starting of foaming process, (c) mould release and (d) final foamed part produced. Adapted from ((Pötsch and Michaeli, 2008)).

The mechanical details of a typical twin-screw extruder as wells as the extruder positions for optimal melt processing are shown in Fig. 2-34.

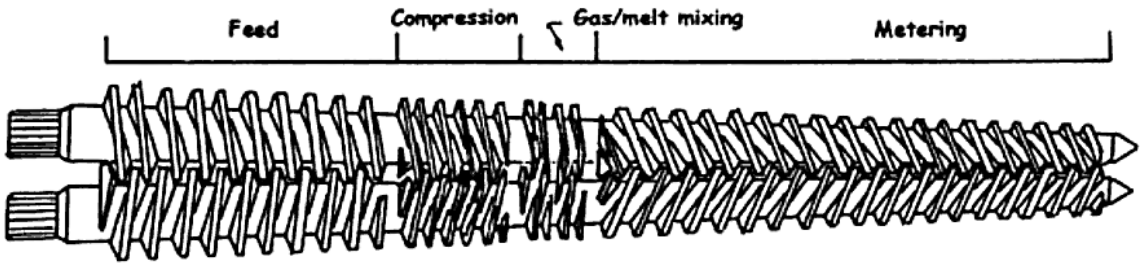

Fig. 2-34: details of a conical twin-screw used in injection moulding. Regions where different process steps occur are shown, (Throne, 2004).

The Slabstock process is a continuous process that differs for the Injection moulding by the fact that the foam is allowed to rise freely, unlike the confinement in a mould for injection process (Klempner *et al.*, 2004).

Another advantage resides in the process being continuous so large volumes of parallelepiped foams can be produced. The melt, in fact, is poured on a moving conveyor and is prevented from lateral expansion. This process, depicted in Fig. 2-35, enables the free rise but does not allow lateral expansion so, a degree of anisotropy is expected.

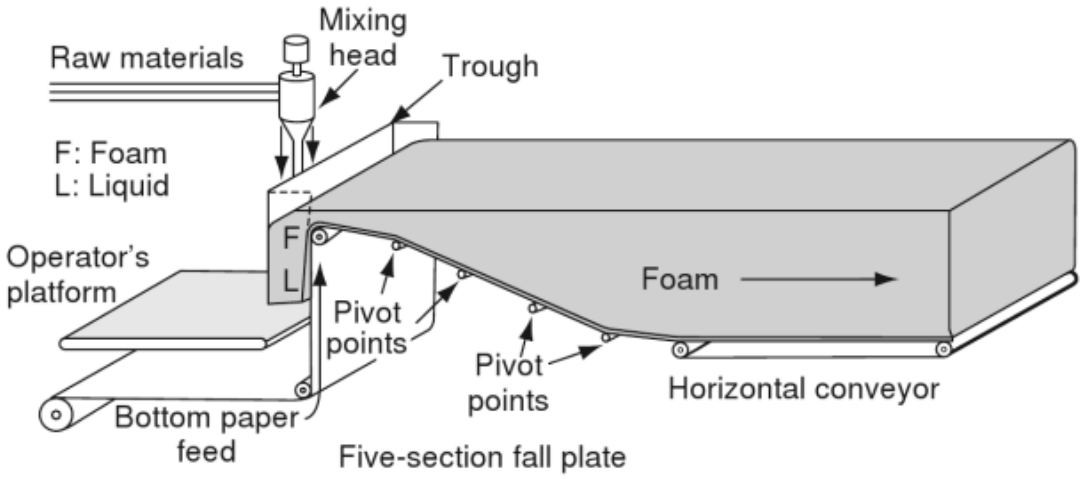

Fig. 2-35: Slabstok foam process (Maxfoam™). The compounds are mixed and poured onto a moving conveyor, (Mills, 2007b).

Anisotropy, as observed for natural materials affects the material properties and foam processing may have a relevant effect. Klempner *et al.* (2004) report a series of compressive test performed of several rigid polymeric foams with similar densities. The compressive strength σ_C was measured in two directions (perpendicular and parallel to the foaming direction) and showed and increasing trend with an increasing height-to-width (*h/d*) ratio. The highest σ_C always occurred in the direction parallel to the foaming direction.

In the light of the above mentioned manufacturing/processing processes which results in different structures, it can be anticipated that final product mechanical properties are related to the way(s) a foam is made. Simple evidence of such process-structure-properties relationship can be found by considering that a foam can be a) thermoplastic or thermoset, b) rigid or elastic, c) open or close celled, d) high density or low density (Lee, 2004). A schematic representation of foam performance (properties) dependency on process and structure is shown in Fig. 2-36 and it further highlights the different ways that can be used to obtain a product with specific characteristics.

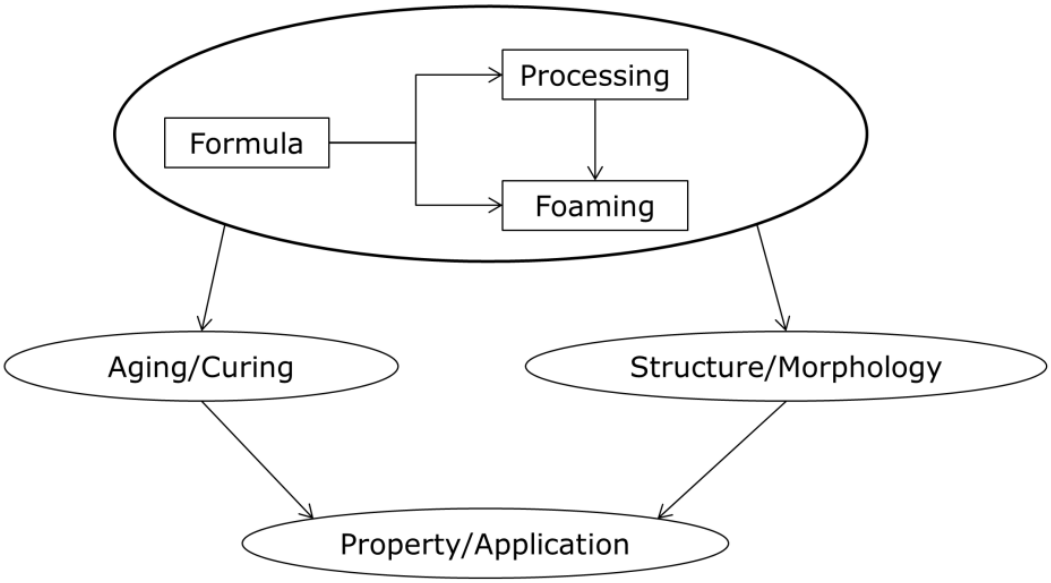

Fig. 2-36: Polymeric foam process-structure-properties dependency (Lee, 2004).

It can be seen that the final properties of a foam are initially related to the materials used. The foaming process can also be used as a variable if the polymer melt and gas system allows a wider range of foaming conditions. Foaming could then be adapted according to the desired morphology. An alternative, should the foaming process be limited to strict conditions, may include acting on post-foaming steps such as aging or curing under different conditions (Lee, 2004). Zhang and Xanthos (2004) extensively reviewed the material properties affecting the extrusion foaming of thermoplastic materials and schematised it based on the work of Khemani (1997). The process and material parameters relationships, all contributing to the foam characteristics are shown in Fig. 2-37.

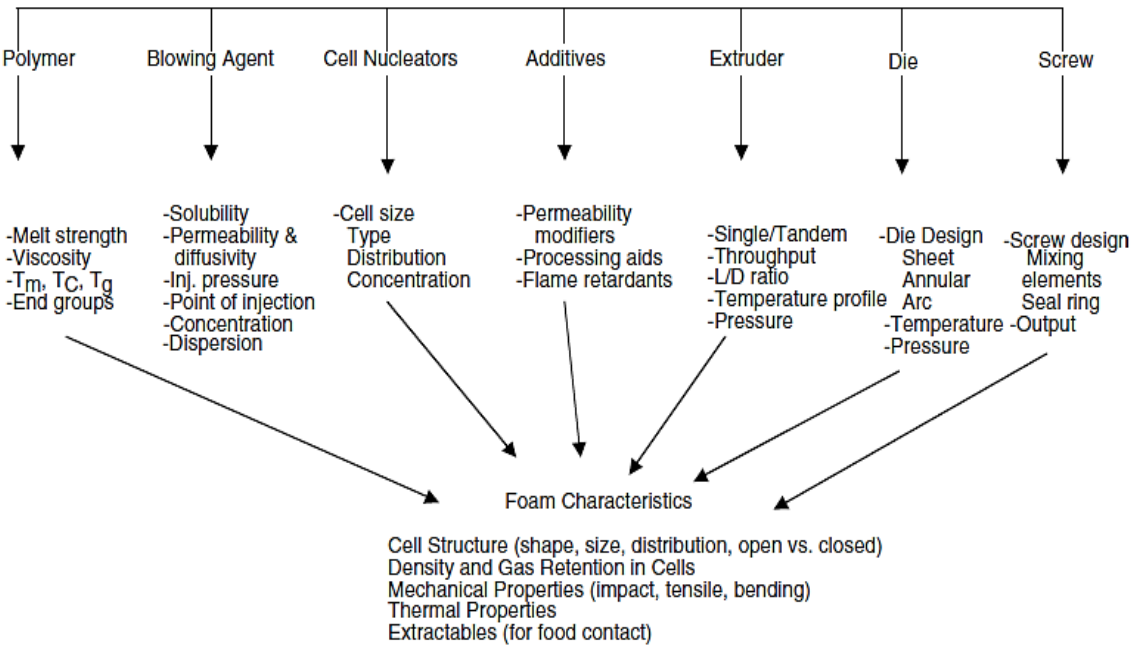

Fig. 2-37: parameters affecting the extrusion process of thermoplastic foams (Khemani, 1997).

It is evident that foam manufacturing is highly dependent on numerous parameters and this inevitably limits the flexibility. Once a foaming process and particularly its dedicated machinery are in place, little or no manufacturing variations are permitted.

2.4.7. Conventional and Microcellular foams

As presented in the previous section, different foams structures can be produced. Conventional thermoplastic foams are characterised by an average cell size between 100 and 500 μm and a rather narrow distribution. According to Throne (2004), a foam with an average cell size of 250 μm would present a Gaussian distribution with a standard deviation of ±100 μm. Foams made by cross-linked poly alkenes (i.e. Polyethylene – PE, Polypropylene – PP) are characterised by smaller cell sizes, 20-100 μm, (Throne, 2004). Their advantages reside in the increased toughness and better compression/energy absorption properties (Throne, 2004; Lee *et al.*, 2007).

The development of *Microcellular Foams* (MCF) which are characterised by an average cell size of 10 μm (Lee *et al.*, 2007) or slightly broader, between 5 and 20 μm (Throne, 2004), began in the early '80s by Martini-Vvedensky *et al.* (1984). The driving factor was the reduction of polymer content to be used without sacrificing mechanical properties (Eaves, 2004). The process for producing MCF involves the pre-saturation of the polymer with a uniform concentration of a gas (such as nitrogen or carbon dioxide) under controlled temperature and pressure condition to

prevent cell nucleation. After this pre-saturation stage, the material temperature is at or near its *Tg*. Nucleation then occurs when pressure is released. The developed microcellular structure is preserved by cooling the material (Martini-Vvedensky *et al.*, 1982; Martini-Vvedensky *et al.*, 1984). The MCF product currently commercially available is Polystyrene (PS) (Eaves, 2004).

2.4.8. Relationship between foam structure and properties

As reviewed earlier, the structure of a foam and accuracy of the model being used play a central role in the prediction of mechanical properties. When assessing the elastic properties of a foam, it was shown that the most important parameters are the density and the Young's Modulus of the un-foamed material. In this section, the case of materials with identical or similar densities but very different cells dimensions (i.e. average diameter) is reviewed.

The reduction of the cell size in MCF has resulted in improvements of many mechanical or thermal properties. For example, the creation of cells smaller than the typical critical defect size is a major advantage (Thomas, 2004; Bureau and Kumar, 2006). The pores would not compromise the toughness of the materials. With reference to thermal properties depending on the material cell size, smaller cells improve thermal insulation.

Although limited data exist on MCF, a review study conducted by Bureau (2005) reveals that the prediction of mechanical properties based only on the foam density (Gibson and Ashby model) may results in large inaccuracies, particularly when the same density can result from different cell diameters. The cell density is introduced to account for relative density correction and is defined as $N \approx (6\rho_p)/(\pi d^3 \rho)$. The foam density as a function of cell size is show in Fig. 2-38 for three different cell densities.

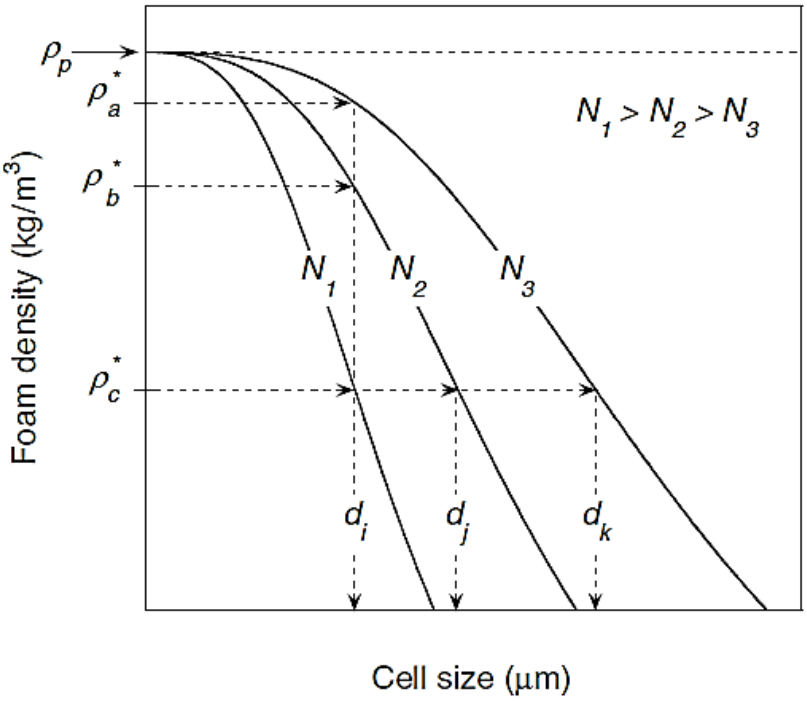

Fig. 2-38: foam density (ρ_1-ρ_3) as a function of cell size (d_i-d_k) for three cell densities (N_1-N_3), (Bureau, 2005).

The plot highlights the fact that a given bulk density can result from any of the three cell densities. For example ρ_c can be obtained by increasing *N* and its corresponding diameter *d*. However, the use of two independent parameters, 1) the foam density ρ^* and 2) the cell size has demonstrated to improve the applicability of the Gibson and Ashby method, (Bureau, 2005).

Further characterisation should include for example, a) wall thickness, b) number of cells per unit length and c) amount of material on cell edges. A more detailed set of parameters used to describe foams are summarised in Table 2-3.

Table 2-3: foam characteristics and their corresponding structural parameters, adapted from (Bureau, 2005)

Foam characteristics	Microstructural parameters
Amount of material	Density, relative density, void fraction
Foam structure	Fraction of open and closed cells
Cell size distribution	Number-average and Volume average diameters
Anisotropy	Cell size in orthogonal directions, cell aspect ratio

The review of the most significant studies on cellular materials behaviour has revealed a series of aspects. On the one hand, it confirms that the simple and effective analytical model developed by Gibson and Ashby forms the basis for understanding honeycombs and foams and has the advantage of being valid for almost any kind of porous material. On the other hand, when irregularities in the

structure are taken into account as in real foams, FEM provides further details which develop from the simple model. FEM methods offer a more detailed insight of a cellular structure, particularly with reference to the fact that the cell strut cross section is not square, as in the simple model, but varies along its length.

Conventional foams manufacturing processes have been discussed earlier. The limitations to manufacturing of foams are imposed mainly at the machinery level and this limits process flexibility to account for process-related structure modifications and their corresponding properties. All these processing limitations can be subverted and structural characteristics have been changed when polymeric foams are produced using polymeric emulsions as in this study. These novel techniques used for producing elastomeric foams are described in the next sections.

2.5. High Internal Phase Emulsion Polymers (PolyHIPEs) as bio-mimicking hierarchical polymeric foams

Synthetic porous materials are reviewed in this section; in particular, *Emulsion Template Porous Materials* are introduced and their origin, manufacturing and range of properties is discussed. Emulsions are defined as colloidal dispersions in which a liquid is dispersed in a continuous liquid phase of different composition (Schramm, 2005). The two main distinctive emulsions type are: 1) oil-in-water (O/W) for oil droplets dispersed in water and 2) water-in-oil (W/O) for water droplets dispersed in oil.

A further commonly used terminology refers to the dispersed phase (the droplets) as the *internal phase*. The continuous phase is also termed the *external phase*. The range of droplets spans between few microns to hundreds of microns (Schramm, 2005). The usual constituents of an emulsion are an oil based phase and a water phase. A schematic representation of W/O and O/W emulsions is depicted in Fig. 2-39.

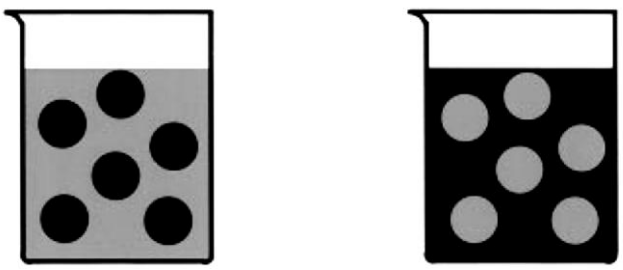

Fig. 2-39: schematic representation of emulsions. (a) Oil-in-Water (O/W) and (b) Water-in-Oil (W/O), adapted from (Schramm, 2005).

High Internal Phase Emulsions (HIPE) refer to emulsions in which the dispersed (or discontinuous) phase occupies more than 70% of the total emulsion volume (Lissant, 1966; Lissant *et al.*, 1974). The dispersed droplets have a relatively large contact area, are surrounded by the continuous phase and are stabilized by thin surfactant films. The continuous phase, which generally constitutes less than 26% of the final volume of HIPE, is usually composed of 1) a monomer, 2) a cross-linking agent, 3) a surfactant which enables the two phases to be stabilised and 4) an oil and/or water phase initiator.

A more precise figure of the maximum volume that uniform (non distorted) spheres can occupy accounts for 74.05% (Ostwald, 1910); not only HIPEs can be successfully produced at this value but also HIPEs reaching 99% of phase volume can be produced (Lissant, 1966; Williams, 1991). The latter compositions imply that the internal phase droplets are no longer uniform, but deformed into polyhedra (Barbetta, 2000; Cameron, 2005).

A 2D representation of the transition between circular to hexagonal shape is shown in Fig. 2-40.

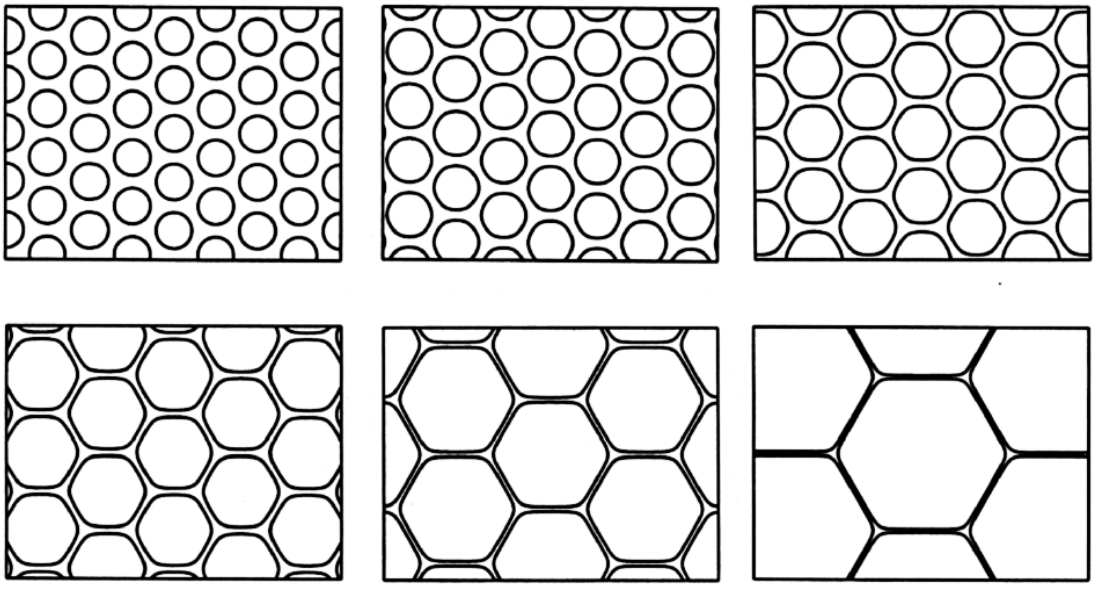

Fig. 2-40: 2D representation of an emulsion with circular droplets (upper figures) evolving into an hexagonal shape (lower figures) with increasing reduction of surrounding neighbouring walls, (Kraynik and Reinelt, 1999).

2.5.1. Development of PolyHIPEs and applications

HIPEs have been studied since the mid 70's, primarily by Lissant *et al.* (1974) and they were first called *High Internal Phase Ratio Emulsion* (HIPRE); they were later classified under the name of HIPEs. In particular, after Barby and Haq (1982) filed

a patent, the final product of polymerised HIPEs (a micro-porous solid material) was given the commercial name of PolyHIPE.

Proposed applications for the HIPEs and/or PolyHIPEs polymers (PHPs) due to their nature as emulsions and structure and morphology as polymers included (a) the production of petroleum gels as bulk liquid containment, (b) safe fuel transportation media, (c) detergents, (d) cosmetics and (e) oil recovery, that later were followed by (f) enhanced filtration (g) demulsification and (h) ion-exchange media (Barby and Haq, 1982; Small and Sherrington, 1989; Hainey, 1991; Bhumgara, 1995; Wakeman *et al.*, 1998; and Akay *et al.*, 2005c).

Additional applications include gas-liquid separation and removal of metal/softening from waste waters (Yildiz *et al.*, 2003). The areas of application further expanded when PHPs and their controllable porosity are used in biological related processes such as (a) support (scaffolding) for animal cells or microorganism growth as bioreactors and (b) for tissue engineering (Byron, 2000; Akay *et al.*, 2004; Barbetta, 2005b; and Bokhari *et al.*, 2005).

2.5.2. Interconnected and hierarchical structural layout

PHPs and EPHPs are characterised by a porosity that is commonly above 90% and may reach a remarkable 97% (Akay, 1990; Akay *et al.*, 1995a; b; Akay *et al.*, 2004). Although the porosity is large, the surface area of is rather limited, usually lower than the 5 m^2/g that is the common surface area for typical foams made of styrene and divinylbenzene (ST/DVD) (Cameron and Sherrington, 1997). Surface area is a typical characterisation of PHP especially when the micron and/or nano-sized pores and interconnecting pores are exploited in mass-transport, fluid-transport applications such as catalysis, membrane and tissue engineering. These applications are greatly enhanced when highly interconnected porous supports such as PHPs are used.

The surface area can be greatly increased by adding porogenic compounds (i.e. toluene, chlorobenzene (CB) and/or chloroethylbenzene (CEB)) in the oil phase that are able to create additional micro pores along the connecting edges of the droplets to reach values that exceed 350 m^2/g (Williams, 1991; Cameron and Barbetta, 2000; Barbetta and Cameron, 2004; Pakeyangkoon *et al.*, 2008). However, the introduction of the toluene porogenic compound to enhance the surface area resulted in severe degradation of the mechanical properties of the PHPs while CB and/or CEB had a limited effect (Barbetta and Cameron, 2004).

Two characterising dimensional parameters are used for Open Pores PolyHIPEs: 1) the (average) *Pore Diameter* (D) and 2) the (average) *Interconnecting Hole*

Diameter (d); the resulting highly open-porous tri-dimensional layout of the PHPs with *D* and *d* is highlighted in Fig. 2-41 his layout classifies the PolyHIPE as an "Open Pore PolyHIPE".

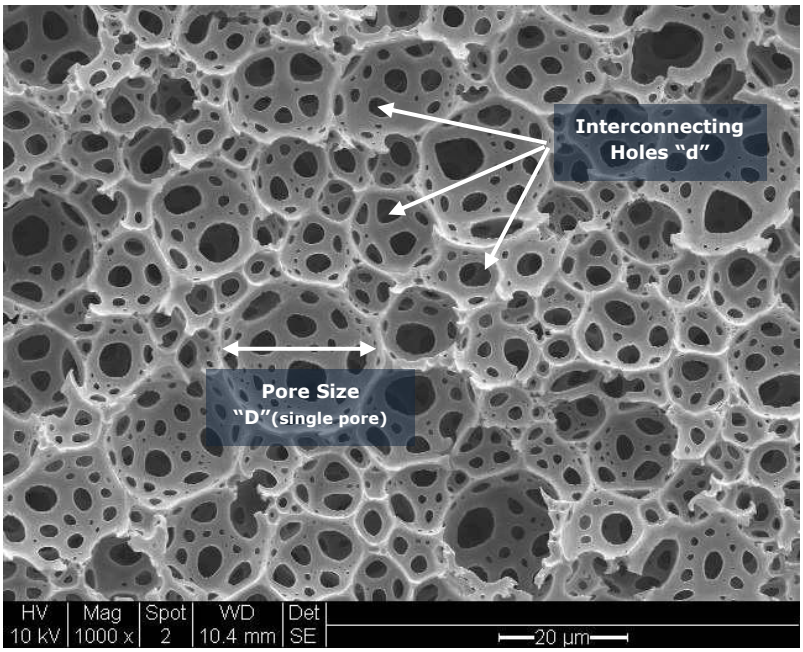

Fig. 2-41: Elastic PHP SEM Image (1000x magnification). A single Pore size "D" is shown, while 3 different Interconnecting Holes "d" are indicated by the arrows.

Fig. 2-41 shows the highly porous 3D structure of the PHP; the SEM picture reveals the fracture surface of a sample; broken pores can be recognised and the picture further reveals that the same tri-dimensional architecture is repeated beneath the surface. Although *D* is largely controllable by processing methods, such as 1) an increase of total mixing time reduces *D* as well as 2) an increase of HIPEs temperature (Akay *et al.*, 2005a), *d* is controlled by 3) the addition of surfactant concentration and 4) water soluble electrolytes (Hough, 1991), it has been observed that ST/DVB PHPs are further characterised by an almost constant average d/D ratio ($0.1 < d/D < 0.5$), with the most recurring ratio $d/D \cong 0.3$ (Hough, 1991; Akay *et al.*, 2000).

The effects of processing factors (mixing time *t* and temperature) on *D* were investigated by Akay *et al.* (2000) and they show that mixing time has a more pronounced effect at an early stage of processing and its influence becomes more moderate with increasing time (Fig. 2-42). Temperature influence has almost an opposite behaviour as its effect becomes more pronounced at values higher than the room temperature (Fig. 2-43).

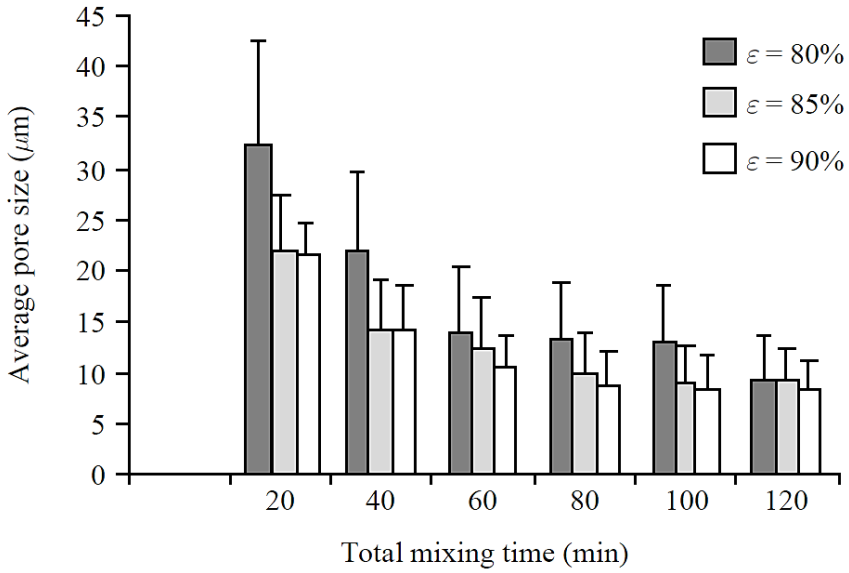

Fig. 2-42: variation of PHPs average Pore Diameter with total mixing time for 3 dispersed phase volume ratio ε (Akay *et al.*, 2005a).

As it can be seen from the picture of a conventional PHP and by taking into account that the average pore size can be modified by processing the emulsion, the mechanical properties of PHPs are influenced by both the structure and the processing route. The structure of PHPs has been exploited by many researchers and particularly where the hierarchy of pores plays an important role (i.e. tissue engineering or filtration) while a relatively limited number of research papers have been published on the manipulation of the mechanical properties of PHPs.

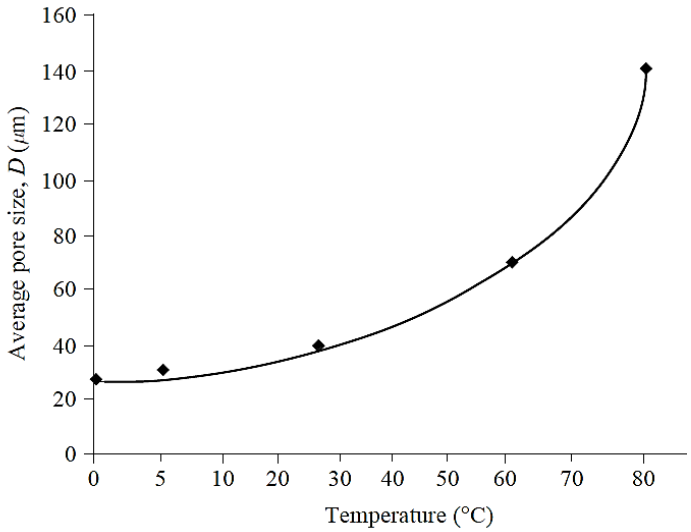

Fig. 2-43: variation of PHPs average Pore Diameter with the temperature. (Conditions: ε = 90%, t = 100 sec, from (Akay *et al.*, 2005a)).

The hierarchical layout of the PHPs is the results of the high degree of droplets' packing. As the concentration of the dispersed phase exceeds 74% the droplets start to deform to maximise the contacting points between neighbouring cells. The layout of PHPs shown earlier (Fig. 2-41) demonstrates that the cells are not

characterised by the same diameter. The diameter of the cells is hierarchically ordered to enable the highest degree of contacts between them. Recently, two studies by Wong *et al.* (2011); and Wong *et al.* (2013) focused on the hierarchical arrangement of PHPs and the benefits this has on load transfer mechanism (2013) and the mechanical strength (2011). The former investigation identified the hierarchical layout as an efficient arrangement that would be similar to the lattice girder as observed in bridges. In the latter investigation, the authors reported that it was inspired by Nature design, with its ability to maximise strength and toughness (as in wood, bamboo and bone). It resulted in the production of higher hierarchically ordered PHPs. In order to achieve this hierarchy, the presence of titania particles was necessary and the addition of the surfactant at the same time as the aqueous phase was identified to be another key factor.

It has now been confirmed that the ability to create hierarchical structures is important to achieve higher mechanical performances. The examples from Nature design offer then the material engineers an effective strategic design tool, thus these are layouts where the structure dominates over the basic material properties in dictating performance

2.5.3. Conventional applications

PHPs represent a new class of cellular micro-porous materials with several established applications. For instance in tissue engineering, where it was determined that the PHPs structure acted as an optimum scaffold that enhanced the adhesion and growth of cellular material (Akay *et al.*, 2000). Also, in ion-exchange and water softening active exchange sites are located and readily available within the PHPs structure (Wakeman *et al.*, 1998; Yildiz *et al.*, 2003). In tissue engineering applications, osteoblast growth and bone formation are facilitated by the inclusion of biocompatible materials onto the PHPs (Akay *et al.*, 2004). PHPs make it possible to produce highly porous filtration membranes with tuneable skin and core structures (Akay *et al.*, 1995b) and water in crude oil emulsion separation is further enhanced by the application of an electric field (Akay *et al.*, 2005c). Applications in agriculture were exploited by designing PHPs as controlled water release media (Akay and Burke, 2012).

While the applications range is wide, three main basic characteristics of PHPs are exploited: 1) the 3D connectivity of the pores (when open celled PHPs are produced), 2) the hierarchy existing between the pores and the interconnecting pores and 3) the chemical or biochemical functionalization of the pore walls. Such characteristics are sought after in the emerging technology of Process

Intensification and Miniaturisation – PIM (Akay *et al.*, 2005b). As chemical and biochemical processes are size dependent, the ability to control the size of the environment the processes takes place is an advantage both in terms of selectivity and optimisation of the intensified process.

2.6. HIPE Processing

The processing of HIPE has been initially described by Lissant (1966) who described the manufacturing procedure as 1) the external phase (vinyl chloride) is placed in a bowl and b) the internal phase (water, emulsifier and a water soluble reaction initiator) is slowly added while stirring. It was firstly shown that the freshly prepared emulsions were characterised by a higher viscosity compared to that measured after 24 hours. The viscosity was determined to increase with the internal volume content and decrease with the speed of the spindle being used, revealing a thixotropic behaviour (the viscosity decreases with increasing shear rate and time). It was also concluded that the behaviour was mainly related to the structure of the emulsion rather than its chemistry (Lissant, 1966). Further studies by Lissant *et al.* (1974) investigated the role of monomer to water phase ratio and confirmed that viscosity increases with monomer content. They also reported that an increasing emulsion viscosity resulted in less uniform droplets (polydisperse). Mixing conditions that would provide sufficient shear were found to contribute to higher uniformity of droplets (monodisperse). This factor highlights then the importance of an adequate and effective mixing method to achieve the desired droplets (mono or polydisperse). The fundamental description of HIPE processing has been described in the patents filed by Barby and Haq (1982) and many other authors (Aronson and Petko, 1986; Akay *et al.*, 2000; Akay, 2001a).

2.6.1. Oil and water phases

The preparation of HIPEs is made possible by preparing two distinct phases. Several authors have reported the preparation of various HIPEs with different components (Hainey, 1991; Akay *et al.*, 1995b; Cameron *et al.*, 1996; Cameron and Sherrington, 1997; Barbetta, 2000; Cameron and Barbetta, 2000; Tai *et al.*, 2001; Sergienko *et al.*, 2002; Akay *et al.*, 2004; Cameron, 2005; Krajnc *et al.*, 2005; Silverstein *et al.*, 2005) and the methodology can be summarised as follows: the oil phase usually consists of a monomer, a cross linker and a surfactant. The oil phase may or may not include an oil soluble initiator or a porogenic component. The water phase usually consists of deionised water and an initiator. If a water soluble functionalising component is desired to be incorporated in the PHP, it can be added in the water phase in a similar manner as with the soluble components.

Examples of water soluble component include hydroxyapatite, as reported by Akay *et al.* (2004) in the preparation of PHPs that support osteoblast and bone formation or hydrophilic 2-vinyl pyridine for water absorption and tar removal in flue gases produced from gasification process (Dogru and Akay, 2006). Water phase initiators are usually peroxides, with potassium persulphate as the most commonly used. The role of the initiator is that of promoting the radical polymerisation of the monomer and the cross-linker (Cameron and Sherrington, 1996b).

The oil phase monomer is S*tyrene* (ST), the cross-linking agent is D*ivinylbenzene* (DVB) and the surfactant that enables the formation of a stable emulsion with water containing a polymerisation initiator (potassium persulphate $K_2S_2O_8$), is Sorbitan Monooleate (SMO), best known under the brand name of Span80™.

PHPs can be created by using several monomers and cross-linking agents and the polymer obtained is usually a rigid one, unless a proper elastomeric co-monomer is introduced. Furthermore, the adopted co-monomer should be characterised by properties such as (a) being sufficiently hydrophobic to form stable HIPEs and (b) polymerise readily with ST (Cameron and Sherrington, 1997). According to the final usage temperature, that is usually room temperature, acrylate monomers have been employed to provide relevant elasticity to the PHPs (Cameron and Sherrington, 1997); the most used elastomeric co-monomers are *2-ethylhexylacrylate* (EHA) with a *Tg* of 263 K and *2-ethylhexyl(meta)acrylate* (EHMA) with a *Tg* of 223 K (Cameron and Sherrington, 1996a; Cameron and Sherrington, 1997; Akay *et al.*, 2005a; Barbetta, 2005b; Kovačič *et al.*, 2007). In this study, the EHA was used to produce elastomeric PHPs (EPHPs).

2.6.2. Flow Induced Phase Inversion method

The reversion of emulsions from *oil-in-water* (o/w) into *water-in-oil* (w/o) or vice versa depends on the stability of the emulsion itself, with thermodynamics dictating the most favourable final conditions. Although (uncontrolled) *Phase Inversion* may be seen as a phenomenon to avoid in certain cases, it may be highly favourable instead as it permits the control of the pore size of porous materials (Akay *et al.*, 2005a). The main advantages of controlled phase inversion are two: 1) the average pore size of the reversed emulsion is smaller and 2) the stability is higher (Shinoda and Arai, 1964; Shinoda and Friberg, 1986).

Flow-Induced Phase Inversion (FIPI) is a phenomenon that has been studied by Akay (1990) used in the preparation of Nano-Structured Micro-Porous materials

(NSMPMs) as well as in a wide range of chemical engineering processes such as 1) powder agglomeration (Akay, 1991; 1994a), 2) microencapsulation (Akay, 2001b), 3) detergent processing, 4) emulsification and others (Akay *et al.*, 2005b).

When two materials A and B are mixed without any relevant external energy input (chemical, surface energy), a dispersion of type A-in-B or B-in-A is dictated by thermodynamic variables as well as concentration, temperature, pressure, viscosity of each component and, in order to revert the emulsion e.g. A-in-B into B-in-A there are two possible approaches: 1) change the *Thermodynamics State Variables* (TSV) or 2) subjected to controlled *Deformation State Variables* (DSV). DSVs are shear, extensional (or combined) deformation fields that interact at emulsion's microstructure level and therefore should be confined into small processing volumes for optimal results (Akay, 1998; Akay *et al.*, 2005b).

Relevant features of the FIPI rely in the fact that it is possible to apply DSV to an emulsion with TSV kept constant and, the FIPI is 1) non catastrophic and 2) leads to a completely stable reversed emulsion with smaller droplet size (Akay, 1990; 1994b; 1998; Akay and Tong, 2000; Akay *et al.*, 2005b). The intermediate states that an emulsion undergoes before phase inversion are reported in Fig. 2-44.

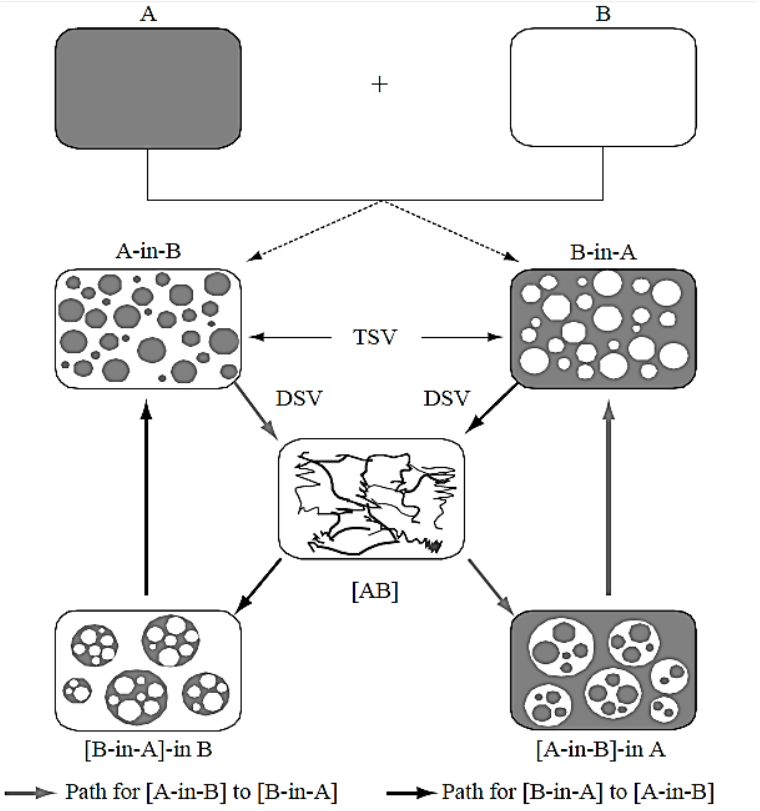

Fig. 2-44: isothermal FIPI path for the inversion of A-in-B or B-in-A emulsions through a co-continuous unstable emulsion phase [AB], adapted from (Akay *et al.*, 2005a; Akay *et al.*, 2005b).

The FIPI method has been used to produce all the PHPs for this study. Details of the FIPI processing method of the HIPEs, as described by Akay *et al.* (2005a) are given herein.

A schematic representation of the formation of PHPs is shown in Fig. 2-45, starting from: 1) a w/o emulsion containing less than 74% of dispersed phase (water), 2) a HIPE that is concentrated by adding more water so that the *dispersed phase volume fraction* (ε) exceeds 70% to 3) the final polymerisation process, with the creation of interconnecting holes in the droplets template walls, by curing the emulsion at 60°C for several hours.

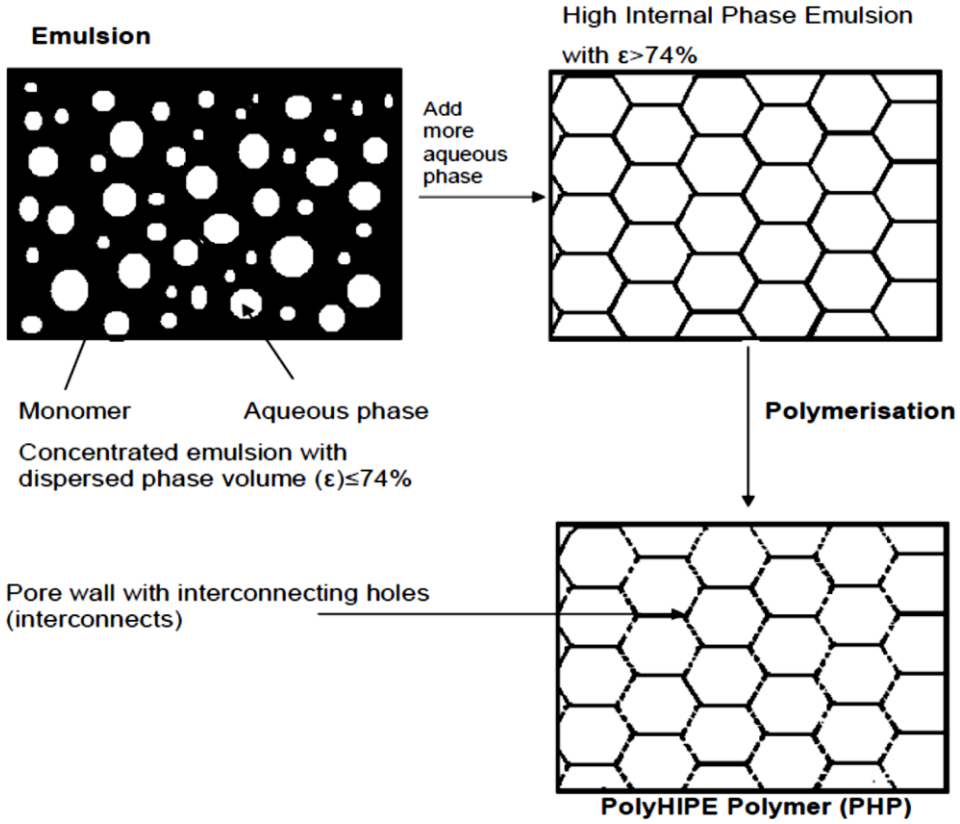

Fig. 2-45: schematic stages of preparation of PS and DVB PHP (Byron, 2000).

According to the procedure used for the preparation of ST/DVB/EHA PHPs, are mixed at given conditions to create a stable emulsion (Akay *et al.*, 2005a).

The key process parameters are:

- Relative Dosing Rate R_D (min.)
- Dosing Time t_D (min.)
- Homogenisation Time t_H (min.)

R_D has the dimension of the deformation rate [time^{-1}] and is given by:

$$R_D = \frac{V_A}{t_D\, V_O} \qquad \textbf{Eqn. 2-43}$$

with V_A (dosed over a period of time t_D) and V_O as the aqueous and oil phase volume, respectively.

The oil phase is already placed in the batch reactor so, T_d refers to the dosing time of the Aqueous phase under stirring conditions to create a stable emulsion; T_d is usually set to 5 minutes but can be increased if the oil phase content exceeds 30% (Akay *et al.*, 2005b).

t_H is the additional time required to homogenise the emulsion, once it has formed. The pre-set t_H values are usually in the range of 5, 10 and 15 minutes. Furthermore, the additional time t_H reduces the average pore size of the final PolyHIPE, so it is used to tailor the desired/required pore size (Akay *et al.*, 2005a).

There is, however, a limited homogenisation time not to be exceeded to prevent collapse of the aqueous phase droplet size and, eventually, HIPE emulsion breakdown due to Ostwald Ripening (Cameron, 2005). Ostwald ripening can be described as the disappearance of smaller droplets in favour of larger droplets. On one hand this is due to the higher solubility of smaller droplets into the continuous phase, on the other hand smaller droplets are characterised by a much reduced surface energy compared to larger ones. The net result over time is the creation of larger drops that have higher sedimentation (or creaming) rates (Schramm, 2005). The Total Mixing Time (t) is then defined as:

$$t = t_D + t_H \qquad \textbf{Eqn. 2-44}$$

When the HIPE emulsion has formed, it is then transferred into a mould or, for example a cylinder and polymerisation occurs in 8 hours in an oven at 60°C. The final solid polymer shape will be that of the mould or containing vessel. Some of the PHPs/EPHPs process parameters are reported in Table 2-4.

Table 2-4: EPHPs conventional process parameters.

Parameter	Description	Value	Units
R_D	Deformation Rate	$2.5 \cdot 10^{-3}$-$3 \cdot 10^{-2}$	sec^{-1}
V_A	Aqueous Phase Volume	225	ml
V_O	Oil Phase Volume	25	ml
t_D	Aqueous Phase Dosing Time	5 and 10	min
t_H	Emulsion Homogenisation Time	5, 10 and 15	min

2.6.3. Polymerisation route

A comprehensive study on the polymerisation of HIPE was initially done by Williams and Wrobleski (1988); Williams *et al.* (1990); Williams (1991) who identified the pivotal role of the surfactant content in determining the open or closed cell

structure of the PHP. With increasing surfactant content, not only do the droplets become smaller, but the oil phase layer that separates them becomes thinner, resulting in highly packed deformed droplets. Upon shrinkage due to polymerisation open cells are formed (Cameron and Sherrington, 1996c; Cameron *et al.*, 1996; Menner and Bismarck, 2006).

Polymerisation is usually achieved by placing the emulsion in a suitable mould and transferring it into an oven at 60-80°C with a time interval for completion that ranges from few hours (Cameron and Sherrington, 1996c; Akay, 1998; Akay *et al.*, 2000; Akay *et al.*, 2005a) to several days (Ceglia *et al.*, 2012) although γ-ray irradiation has also been successfully used for polymerisation at room temperature with a reduced amount of surfactant, as reported by Mao *et al.* (2013).

The schematic representation of the polymerisation and cross-linking of the styrene and divinylbenzene oil phase is shown in Fig. 2-46.

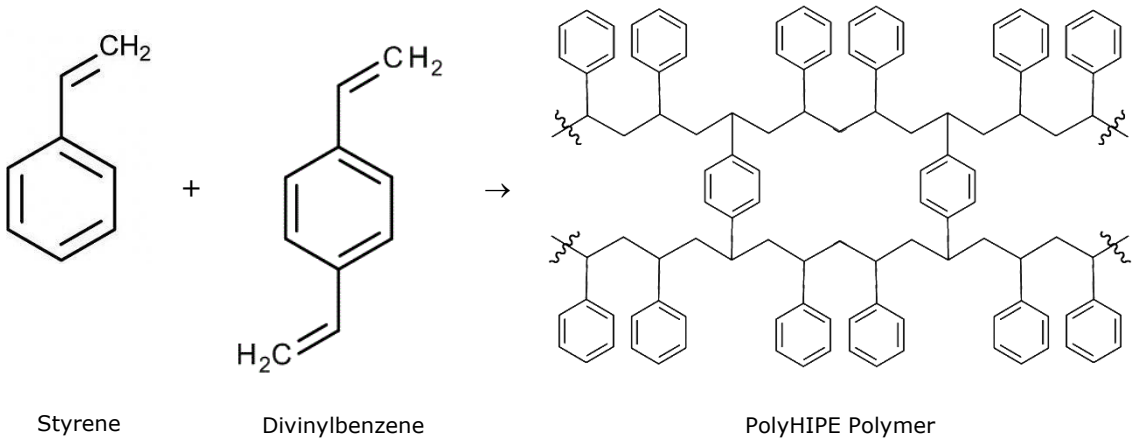

Fig. 2-46: schematic polymerisation of styrene (ST) monomer and divinylbenzene (DVB) cross-linker to produce ST/DVB cross-linked copolymers.

The cross-linking is performed by the DVB which acts as a bridging molecule between the chains formed by poly-styrene. This configuration renders the PHP capable of creating a stable 3D configuration.

2.6.4. Stability factors

The factors that affect the HIPE stability have been investigated primarily by Barby and Haq (1982), and later by many other authors (Lissant, 1966; Lissant *et al.*, 1974; Chen and Ruckenstein, 1990; Williams, 1991; Cameron and Sherrington, 1996a; Cameron and Sherrington, 1996c; Akay, 1998). The fundamental stability factors are the same as those for conventional emulsions. As emulsions necessarily need a surfactant to form, this plays a key role.

Early studies on identifying the chemico-physical characteristics that a surfactant should have to stabilise an emulsion were provided by Griffin (1946) and his development of the Hydrophilic-Lipophilic Balance (HLB) concept. In the intensive research on the determination of the most influential factors on HIPEs stability it was concluded that the most influential factors were: 1) the HLB of the surfactant, 2) temperature, 3) surfactant concentration and interfacial tension, 4) the relative viscosities and free energy between the two phases and 5) the salt presence in the dispersed phase.

1. HLB of the surfactant influences the stability of the emulsion; the higher the HLB Number, the smaller the amount of co-surfactant needed to form large dispersed phase droplets, thus stabilising the emulsion (Williams *et al.*, 1990; Williams, 1991).
   HLB is defined in terms of numerical values assigned to the chemical groupings in the surfactant, as follows (Boyd *et al.*, 1972; Goodwin, 2009):

$$\text{HLB} = 7 + \sum(\text{hydrophilic group number}) - \sum(\text{lipophilic group number}) \quad \textbf{eqn. 2-45}$$

   and the most effective surfactants that stabilise O/W emulsions have an HLB in the range of 3-6 while stabilisation of O/W emulsion is provided by surfactants with HLB in the 10-18 range (Schramm, 2005). The most used surfactant for the production of HIPEs is Span80™ whose HLB is 4.3 (Pakeyangkoon *et al.* (2008).

2. Temperature influences the stability as it is directly related to the HLB Temperature, also called *Phase Inversion Temperature* (PIT), of the surfactant that enables the formation of Oil-in-Water (o/w), or Water-in-Oil (w/o) emulsions; temperatures below PIT would enable the formation of o/w HIPEs while temperatures above the PIT would lead to w/o HIPEs. An increase in temperature reduces the emulsion stability as it positively contributes to the coalescence of the dispersed phase droplets (Cameron and Sherrington, 1996a).
3. Surfactant concentration and interfacial tension are two related parameters; as the former is increased, higher volumes of oil phase can be incorporated into the HIPE due to a reduced interfacial tension. Furthermore, the proper selection of a surfactant was suggested to be based on characteristics such as: (a) a strong interfacial film to be formed which prevents the coalescence of water droplets while permitting the coalescence of oil droplets, and (b) in cases where very rapid emulsification is required, the emulsifier should also be adsorbed rapidly at the interface (Ford and Furmidge, 1966; Williams and Wrobleski,

1988; Ruckenstein *et al.*, 1989; Williams *et al.*, 1990; Williams, 1991; Cameron and Sherrington, 1996a).

4. Viscosity and free energy between the two phases were found to be a stability factor for concentrated emulsions; increased viscosity of the continuous phase reduces phase mixing while a direct correlation between interfacial free energy and stability was identified: increasing interfacial free energy existing between the oil and water phase leads to higher stability (Ruckenstein *et al.*, 1989; Chen and Ruckenstein, 1990; Cameron and Sherrington, 1996a).
5. The salt added into the aqueous phase has a remarkable influence on the stability as it was considered that the interaction of surfactant molecules increases in the presence of salt. Particularly effective are the salts that decrease the cloud temperature of the water/non-ionic surfactant system (Kunieda *et al.*, 1989; Williams *et al.*, 1990; Cameron and Sherrington, 1996a).

The review of the factors that affect the stability of the HIPEs showed how many internal and external system's variables should be taken into account; however, it is the polymerisation route of the HIPEs that originates NSMPMs that has attracted increasing attention, in particular, the most studied system is the one that comprises the elements used by many authors (Barby and Haq, 1982; Williams, 1991; Akay *et al.*, 2005a; Barbetta, 2005a) and reported in the Oil and water phases section.

2.7. Mechanical behaviour of PHPs in compression

The mechanical testing of PHPs has been initially limited to the basic acknowledgment of their properties, with no particular exploitation of their related structure-properties. Early results on mechanical properties of rigid PHPs made with an oil phase comprising of 1 to 1 ratio of styrene (ST) to divinylbenzene (DVB) and sorbitan monooleate (SMO) Span80^{TM} as surfactant, were provided by Williams and Wrobleski (1988). They found that the main contributing factor to a stable microcellular foam structure was the surfactant to oil ratio.

A compositional phase diagram was plotted to highlight the water phase, oil phase and SMO concentration Fig. 2-47 to predict the outcome (i.e. open celled foam or the phase's separation).

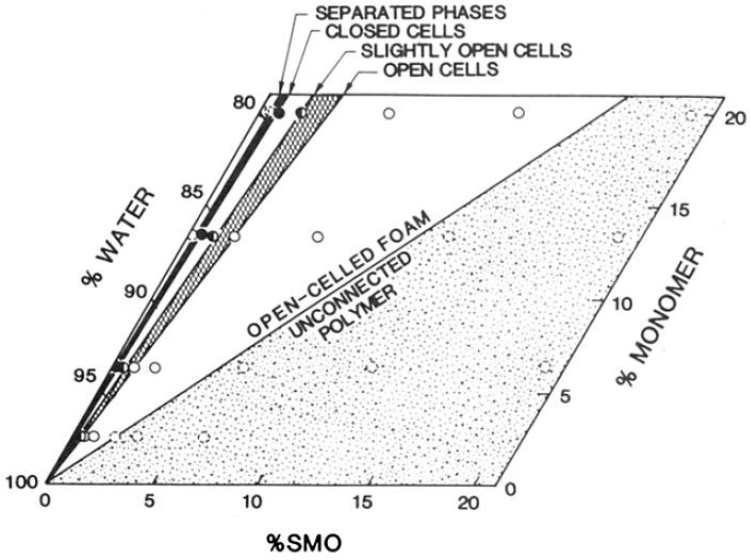

Fig. 2-47: phase diagram of rigid PHPs made with 1:1 ratio ST:DVB showing the effect on the stability and appearance of the foam as a function of the surfactant (SMO) and water phase % content, from (Williams and Wrobleski, 1988).

It can be seen that it is possible to produce open celled PHPs with a wider compositional window than that for closed cells. The instability of the emulsion is also highlighted by the widest area.

In terms of mechanical properties, several measurements were done and the Elastic Modulus was determined as a function of the surfactant content. As expected, the modulus largely decreased with increasing surfactant presence (Williams and Wrobleski, 1988). The authors attributed this mechanical behaviour to the fact that a higher content of surfactant has the effect of creating thinner oil layers in the emulsion, to a point at which the oil layer retracts and the water droplets start to touch. The effect is that foams with no walls but only struts are formed, thus the very low modulus (Williams and Wrobleski, 1988). The Young's Modulus was plotted as a function of the PHP density and showed an increasing value, as expected, with increasing density (Fig. 2-48a).

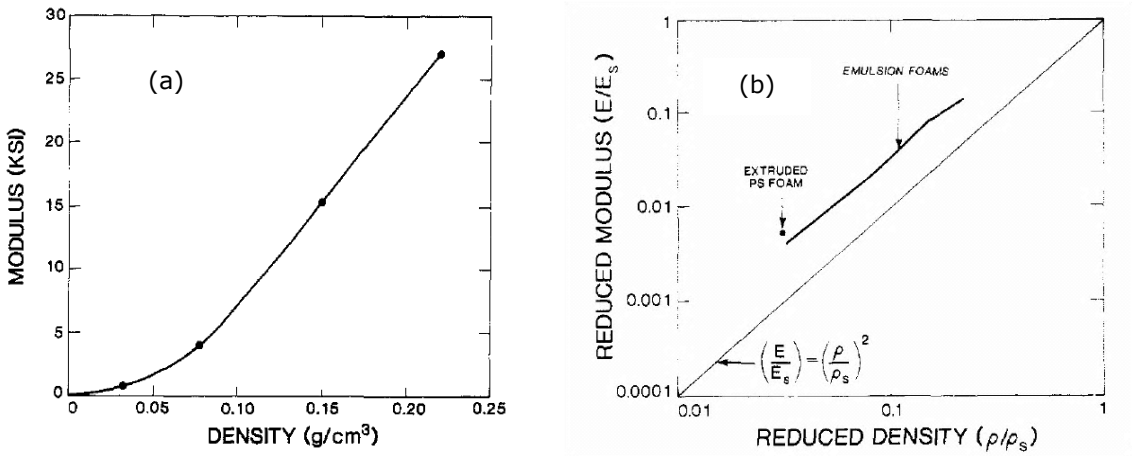

Fig. 2-48: plot of Young's Modulus as a function of PHP density (compression testing). 1 KSI = 6.89 MPa., (Williams and Wrobleski, 1988).

The fit would probably be described by two curves; a parabolic curve for the very low density values and a linear response from increasing densities. The experimental investigation of Williams and Wrobleski (1988) was also the first to use the Gibson and Ashby model $(E/E_S = (\rho/\rho_S)^2)$, as depicted in Fig. 2-48b. The power law with n=2 was used. The solid material from which E_s was taken was polystyrene (PS) although it does not account for the cross-linking features of PHPs. It was found that the values were slightly underestimated by the model, but they were in line with those of extruded PS.

More recent studies on the mechanical properties of PHPs have been performed by Haibach *et al.* (2006); Menner *et al.* (2006a); Menner *et al.* (2006b); Menner *et al.* (2008); Wu *et al.* (2010). One of the main focus of these studies is the toughening of the rigid PHPs by using silica particles (Haibach *et al.*, 2006). It was demonstrated that the Young's Modulus of silica reinforced PHPs doubled with respect to non-reinforced PHPs. Non-reinforced PHPs with increasing oil phase content up to 40% that also showed an increase in mechanical performances with oil phase content, were used as reference materials. Despite this interesting result, the methodology of preparing the PHPs included more than 10 sequential steps and it relied on the supply of nano-sized silica particles to be further processed with concentration of silica particles up to 60% (Wu *et al.*, 2010). The latter conditions could pose a limit with respect to increasing density of the final PHP. The inclusion of silica at such high levels may however eliminate or greatly reduce the advantages of the typical low density of PHPs.

Processing-Structure-Properties investigation on PHPs were even more recently investigated by Abbasian and Moghbeli (2010); 2011). Their investigation focused on the effects of stirring speed and rate of addition of the water phase on the morphology and mechanical properties of PHPs prepared by a 1 to 10 ratio of ST:DVB and a phase volume ratio of 85% (Abbasian and Moghbeli, 2010). A strong dependence of mechanical properties due to processing was observed. The highest elastic modulus was measured for the PHPs stirred at the highest speed, which resulted in the smallest cell diameter and the lowest water phase addition rate. The Young's Modulus ranged between 4 to 11 MPa and the behaviour of the materials upon compression showed the common three regions, elastic, plateau and densification. (Abbasian and Moghbeli, 2010).

Investigations on elastomeric PHPs with organo-modified clays were made by Moghbeli and Shahabi (2011). The elastomeric nature of open celled PHPs with 2HEA was retained by the inclusion of the clays (up to 5%). The elastic modulus was measured and it decreased with clay content but a maximum value, higher

than the reference material without clays was measured at 5% clay presence. It was also observed that the average pore size increased with clay content and a lower elastic modulus would be expected. This behaviour was explained by considering two facts: 1) the inclusion of clay reduced the cell wall thickness, rendering the wall easier to bend, thus the lower Young's modulus and 2) a narrower pore-size distribution was measured. The authors attributed the lower strain before deformation occurs to the latter condition.

One of the latest development in the structure-properties relationship for PHPs has been made by Ceglia *et al.* (2012). The authors reported the production of cellular materials based on various HIPE formulations to obtain PHPs with 1) varying cell size at constant density and 2) varying density. The first objective was achieved by formulating and processing various HIPEs. The second objective was achieved by controlled dilution of the emulsions (i.e. the pore size could be kept constant). The curing of the HIPEs was reported to be a function of the presence of the emulsifier and ranged between 5 days to a week. When plotting the Young's Modulus as a function of the cell size for a constant density, an increase of the modulus was determined which, according to the authors contrasts the independence of E from the cell size as know from the Gibson and Ashby model. Although this experimental conclusion seems to contrast with the established model, the authors do not specify whether the increase of the cell diameter was accompanied by the thickening of the cell walls. This condition can justify the increased modulus as the bending of thicker walls would be induced by higher stresses. An important contribution however was made by analysing the concentration of the emulsifier (surfactant) along the cell walls. It was concluded that the material behaviour can be justified by assuming that the walls are made of two different layers, each with a distinct Young's Modulus as a consequence of the emulsifier concentration gradient.

Further investigation on the influence of the cell size to the mechanical properties of foams was performed by Maheo *et al.* (2013), who produced an FEM based on the work of Ceglia *et al.* (2012). The cell model was compared to that of Gibson and Ashby and featured the struts as composed of two different materials with two different Young's Moduli (Fig. 2-49).

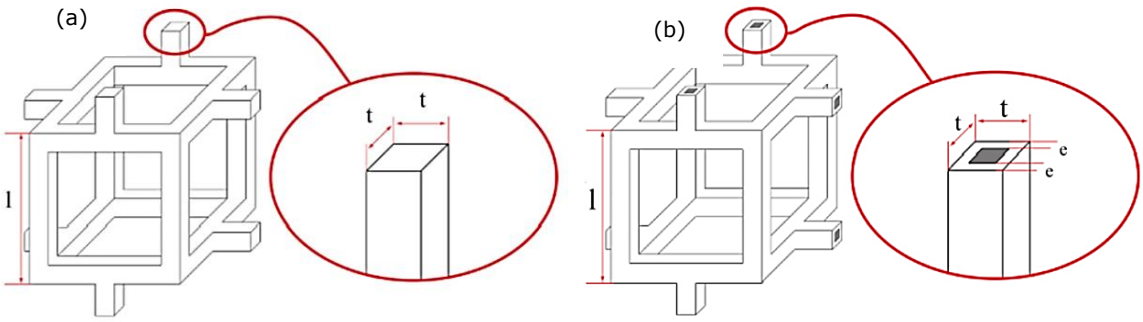

Fig. 2-49: cell models showing (a) the homogeneous struts, from Gibson and Ashby and (b) with heterogeneous materials (Maheo *et al.*, 2013).

The diversified approaches toward the understanding of the relationship between the processing, the structure and the properties of the PHPs have received increasing attention, as shown by the literature. Increasing interest is also dictated by the wide range of applications that the PHPs can offer. When referring to mechanical properties, little or no studies have been performed to investigate the effects of the temperature on the PHPs. Such an investigation has been performed in this work and the results will be presented in the dedicated section. It is worth mentioning that the majority of the literature refers to the rigid PHPs which are known to be brittle for the following reasons: 1) the main constituent, PS is a brittle material at room temperature as its *Tg* is approximately 100 °C (Gibson and Ashby, 1997), 2) the DVB provides the cross-links that further limits the sliding of the polymeric chains. However, the main characteristics of the stress vs. strain behaviours are always recognisable and they are discussed in the next section.

2.7.1. Stress vs. Strain curves

Stress vs. strain curves are used to identify the behaviour of a material. As reviewed in earlier sections, Gibson and Ashby (1997) have extensively studied cellular materials and identified typical regions, each is representative of a deformation mechanism. The initial linear response from which the Young's Modulus can be calculated is followed by a plateau region of varying length before densification of the cellular material occurs. The stress vs. strain curve for a cellular material is modified by the material density. With increasing density, the main effects are the increase of the elastic modulus and the shortening of the densification region. The latter is the result of a higher amount of solid on the cell wall that reduces the strain at which the walls contact each other (densification region). As already depicted in Fig. 2-26 and shown below again, each type of compressed material, whether elastic, plastic or brittle is still recognised by the three regions.

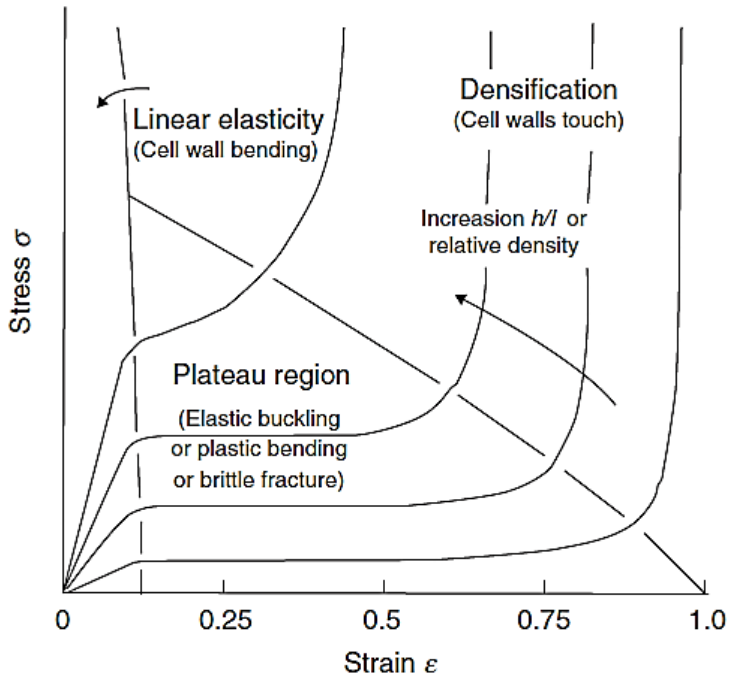

Fig. 2-50: schematic representation of stress-strain curve for a honeycomb loaded in in-plane compression, adapted from (Gibson and Ashby, 1997)

The cellular structures behaviour in the initial linear elastic region has been demonstrated to be bending-dominated (Gibson and Ashby, 1982; Gibson, 1989; Gibson and Ashby, 1997; Gibson, 2000). For this reason the elastic limit is the same for all the densities while the elastic stress increases with the material density.

With reference to PHPs, a relevant part of the studies on their mechanical response has been referred to rigid formulations, with a moderate level of interest in relating structure-properties relationships. Although in many cases the stress vs. strain curves resemble those of cellular materials, PHPs and also EPHPs are characterised by a much higher level of hierarchy among the pores. Such a feature is a fundamental aspect of the present investigation and will be analysed and discussed in details for the EPHPs in the dedicated sections. When the behaviour of elastomeric PHPs (EPHPs) is investigated, a distinctive change in the shape of the stress vs. strain curve is expected. The addition of 2EHA, as anticipated in the Oil and water phases section, has the role of lowering the *Tg* of the PHP. As a consequence of that, although the elastic modulus is reduced by a factor of 3, the brittleness of the rigid PHPs is avoided. Repeated compression loading is possible and the recovery of the EPHP is expected.

2.7.2. Time and Temperature Equivalence

The time and temperature equivalence principle was introduced in the 2.4.2.3 Viscoelastic behaviour section while analysing the mechanics of honeycombs as a function of temperature and strain rate. Williams *et al.* (1955) made it possible to identify that the plots of the elastic modulus as a function of temperature or time are almost identical (Fig. 2-51).

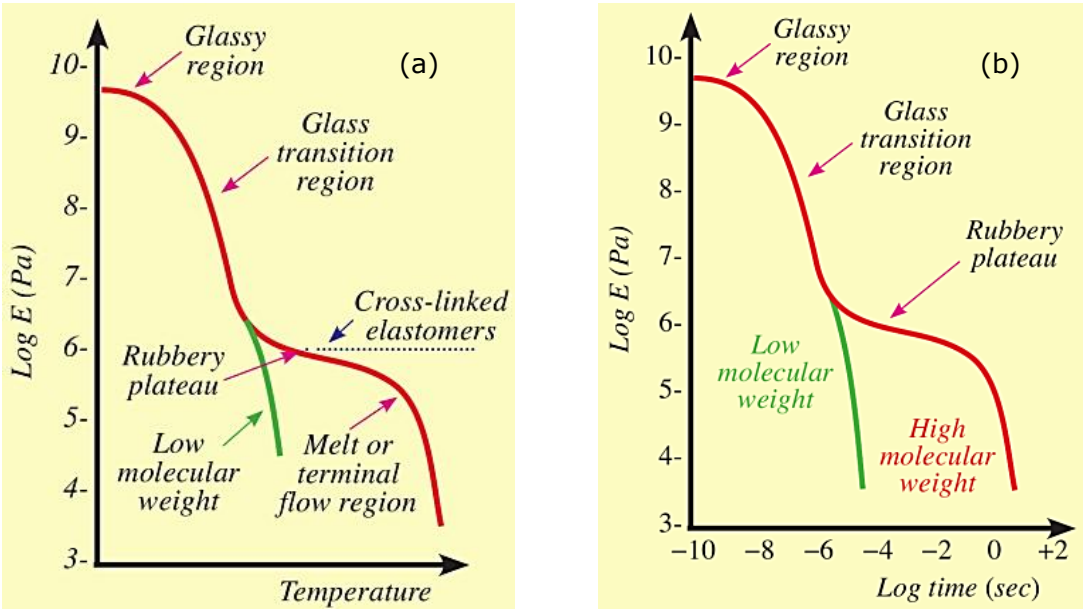

Fig. 2-51: plots of (Log) Young's Modulus with temperature (a) and (Log) time (b). The shape of the curves is almost identical, (Painter and Coleman, 2008).

A relevant property that can be depicted from Fig. 2-51a, is the practical absence of dependency of the modulus of cross-linked elastomers with temperature. In practice, the shift factor that exists between the curves was found to be related by two constants which are valid for a wide range of polymeric materials. When the modulus is known at a temperature (or at a given strain rate), it will be possible to calculate it at another temperature (or strain rate).

Studies on the effect of temperature on the mechanical performances of PHPs or EPHPs are not available. The only relevant work which however did not present any mechanical characteristics data, was performed by Cameron and Sherrington (1997). The effects of acrylate based copolymers content on the *Tg* of EPHPs were investigated and it was concluded that the correlation between *Tg* and copolymer content was not linear.

Chapter 3 – Methodology

"Science is the captain, and practice the soldiers".

- Leonardo da Vinci

This chapter describes the procedures that were developed and implemented for the manufacturing, structural characterisation and mechanical assessment of various classes of elastic PHPs.

In particular the following steps are presented and detailed herein:

(a) Procedure for the production of the elastic PHPs, with description of the apparatus and accessories required

(b) Preparation of HIPEs with varying ratio of oil and water phases

(c) Preparation of HIPEs with varying dosing and homogenisation processing times

(d) Curing (polymerisation) of the HIPEs in specifically designed moulds

(e) SEM imaging investigation technique

(f) Compression tests setting parameters for the evaluation of the EPHPs mechanical performance (Young's Modulus – *E* and Specific Absorbed Energy - SAE) at different temperatures and strain rates.

3.1. Preparation of HIPEs

Elastic PHPs were produced by following a well-established procedure developed by Akay *et al.* (2005a). The preliminary conditions that were kept the same for the preparation of all the HIPEs were the following:

1. The preparation of the HIPEs was performed at room temperature
2. Both phases were prepared independently by using the chemicals as received from the supplier (Sigma-Aldrich, UK)

While details of the varying aqueous to oil phase ratio ε and changes in dosing and homogenisation times are reported later, the procedure is valid for all the HIPEs that were prepared. The complete layout of the actual manufacturing equipment is shown in Fig. 3-1.

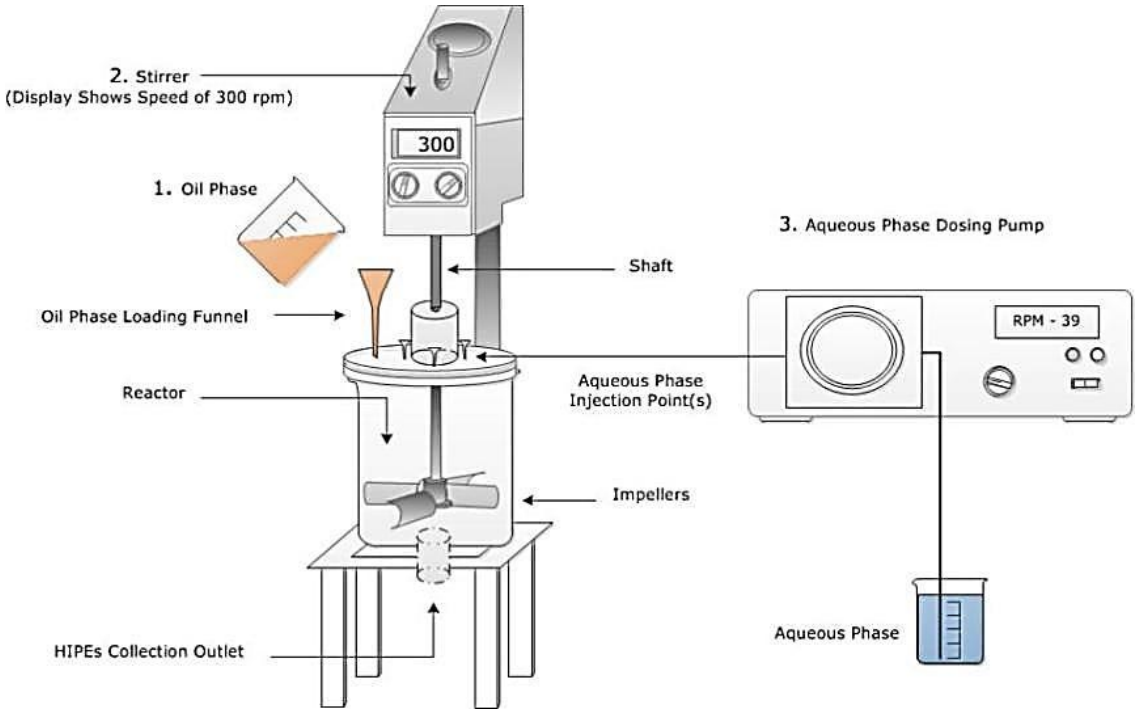

Fig. 3-1: HIPE manufacturing equipment: stirrer/impeller, reactor and aqueous phase dosing pump. Oil Phase loading funnel and aqueous phase injection point(s) are shown. Numbered items represent the sequential order of the manufacturing operations.

The procedure for preparing the HIPE is as follows:

1) A steel reactor with internal diameter of 12 cm and equipped with a heating jacket is placed on a support. The stirring shaft consists of two impellers at 90° to each other with a diameter of 8 cm.
2) The shaft is placed with the lower impeller as close as possible to the reactor surface to prevent the formation of no-mixing zones.
3) The reactor is covered by a lid that enables the shaft to rotate and prevents liquid spillage; the lid is also designed to enable 4 injection points for the aqueous phase. Only a single injection point was used throughout the EPHPs production to inject the water.
4) The reactor is filled with the oil phase volume by means of a flexible funnel mounted at the top of the lid. The stirrer is not rotating.
5) The aqueous phase pump is connected to the injection point and the pump rate is regulated according to the t_D. The objective of such a configuration is to add the aqueous phase drop wise.
6) The stirrer and the pump are switched on simultaneously. The t_d is accounted for.
7) At the end of t_d, which corresponds to the complete delivery of the aqueous phase into the stirring reactor, the homogenisation time t_H started and the pump was switched off.

8) Readings of the stirring speed were recorded at 5 minute intervals for a qualitative evaluation of increasing viscosity as the emulsion forms. Depending on the designed homogenisation time t_H, the stirring process was then halted, the shaft and the lid were lifted so that a visual inspection of the emulsion was possible.

All the previous steps contribute towards the formation and the structural modification of the HIPE as schematically shown already in Fig. 2-45 and presented again for ease of reading in Fig. 3-2 below.

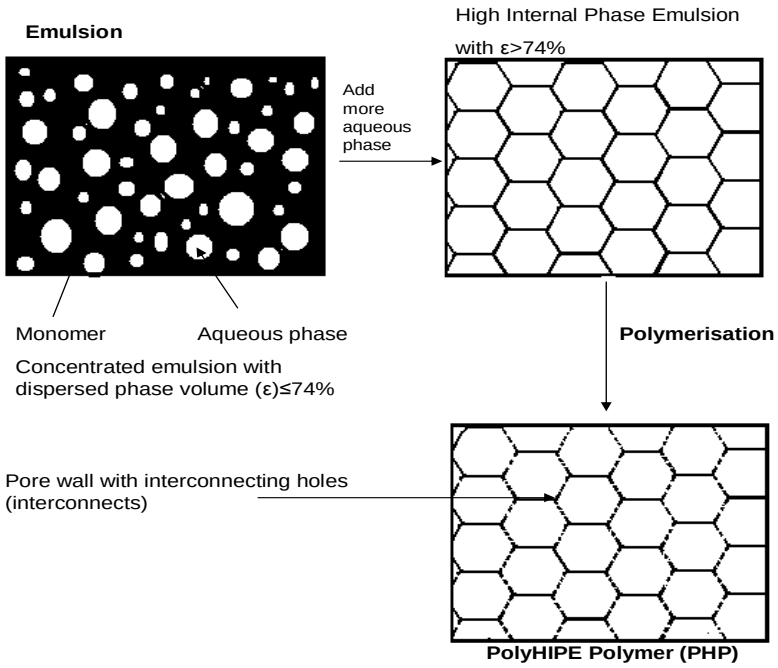

Fig. 3-2: Schematic illustration of PHP formation. An initial W/O emulsion is formed. Continuous addition of water exceeds maximum undistorted spherical packing (ε>74%) and structural modification into polyhedral geometry takes place. Polymerisation causes the formation of interconnecting holes in the cells' walls (Byron, 2000).

The initial conditions of water droplets dispersed in an oil phase (simplified in the picture with the term "monomer", change with time as more water is added to the oil phase. When the droplets reach the undistorted maximum packing (ε =74 %), additional water entering the system causes the droplets to distort and arrange themselves into the typical polyhedral (tri-dimensional) layout of HIPEs.

The formation of the wall interconnecting holes takes place during the polymerisation (curing) process (bottom right Fig. 3-2). The result is a, nano-structured micro-porous polymeric material in which the water droplets served as structural template.

9) The emulsion was withdrawn from the bottom of the reactor and, according to the required final shape it was transferred to three different moulds. Details of

transferring methods and shape of the moulds are reported in the dedicated sections.

10) The HIPEs were transferred into an oven at 60°C where polymerisation (curing) would occur for not less than 8 hours.

3.1.1. Water and Oil Phase components and varying phases ratio

The initial approach was that of producing EPHPs according to the most studied formulation with varying Water/Oil phase ratio ε. ε dictates the amount of dispersed phase (water) to be emulsified in an oil phase to produce HIPEs. The term *solid content* will be used throughout this thesis and it refers to the amount of polymerizable oil phase in the HIPEs. Increasing solid content can be referred to ε simply by the quantity of "1-ε".

The key factors to highlight for the preparation of HIPEs were the following:

1. The water and oil phase components, with each specific function reported in Table 3-1 were the same for all the HIPEs. The oil phase initiator was used in HIPEs with ε=0.65 and 0.6. The details are provided in the results' chapters.
2. Prior to starting the manufacturing process, it was required to set ε and derive the phase volumes.

Table 3-1: Oil and water phase HIPE components for the production of varying ε EPHPs.

Component	Phase	Function
Styrene (ST)	Oil	Monomer
Divinylbenzene (DVB)	Oil	Cross-Linker
2-ethylhexylacrylate (EHA)	Oil	Elastomer
Span80™ Sorbitan monooleate (SMO)	Oil	Surfactant
Lauroylperoxide (LPO)	Oil	Initiator
Potassium persulphate (KPS)	Water	Initiator
Water	Water	Emulsion Template

The different HIPEs phases' volumes for varying ε are summarised in Table 3-2. The total volume is 250 ml.

Table 3-2: Required volumes of aqueous and oil phase for varying ε series of EPHPs. Total volume 250 ml. (IN) refers to the presence of oil phase initiator LPO.

EPHP Series Name	"ε" (%)	Solid Content (1-ε)	Oil Phase Volume (ml)	Aqueous Phase (ml)
S10	90	10	25	225
S20	80	20	50	200
S30	70	30	75	175
S35(IN)	65	35	87.5	162.5
S40(IN)	60	40	100	150

The table also shows also the direct correspondence between ε and *solid content*. The EPHPs series with lower ε correspond to those where solid content (polymerizable oil phase) is higher.

3.1.2. HIPE with Water Phase volume ratio ε from 90% to 70%

HIPEs with ε of 90, 80 and 70% (S10, S20 and S30 series respectively) were produced with the initiator (KPS) present only in the water phase. The resulting emulsion was transferred into a) polyethylene tubes with 26 mm diameter, b) a square or c) a circular mould according to testing requirements. The transfer of the emulsion in the tubes was performed by opening the reactor's bottom outlet and as long as the emulsion was able to flow under gravity no pump was used. When the emulsion needed to be transferred at a controlled rate in the squared or circular mould a peristaltic pump was used. Changes in the qualitative appearance of the various series emulsions were noted and the identification of their rheological behaviour is reported in the dedicated section.

The tubes, filled up to 40 ml out of the nominal volume capacity of 50 ml were cured in an oven at 60°C overnight. Once cured the EPHPs monolith were removed from the tubes. Their homogeneous appearance of the sample was confirmed and they were then subjected to the following operations:

1. EPHs monoliths were cut in disks with a thickness that varies between 5 and 8 mm
2. Drying of disks at 40°C was performed for one day in a vacuum oven to enable residual water removal with reduced thermal induced mechanical stress

After the above operations, EPHP samples were ready for preliminary mechanical property measurements in the Mechanical Test Frame (MTF). Structural investigation of the EPHPs was performed by Scanning Electron Microscopy (SEM). Details of the MTF and SEM investigations are presented later.

3.1.3. HIPE with the lowest Water Phase Volume (ε=65 and 60%)

As stated in the previous section, HIPEs with ε up to 70% were processed with KPS initiator only and the EPHP monoliths and disks appeared homogeneous. HIPEs with lower ε, 65% and 60% (S35(IN) and S40(IN) series respectively), were processed with an initiator present also in the oil phase (LPO). Oil phase initiator (LPO) was added at 1% weight with respect to oil phase. The solution was prepared by mixing the solid LPO and the amount of oil phase needed for the production of the HIPE in a beaker and stirring for 10 minutes. The solution was later poured into the reactor according to the previously described procedure.

The addition of LPO in the oil phase was a consequence of the fact that when processing low ε emulsions (equivalent to higher solid content emulsions) with the initiator only present in the water phase, the polymerised EPHPs showed the presence of an appreciable amount of remaining liquid oil phase. Unlike in higher ε HIPEs where complete polymerisation was observed, only partial polymerisation occurred in higher solid content HIPEs. High solid content EPHPs produced with KPS and LPO initiators polymerised adequately, with a limited amount of residual oily liquid.

Partial polymerisation was justified by accounting for increasing viscosity of higher ε HIPEs. Higher viscosity is a direct indicator of the increasing mechanical energy dissipation (viscous effects) and reduced mixing efficiency for which details will be presented in the dedicated section. The addition of an oil soluble initiator (1% weight with respect to oil phase) resulted then in the availability of polymerisation reaction initiator in both phases. Even polymerisation of the EPHPs was obtained for S35 and S40 series which are referred to as S35(IN) and S40(IN) to account for the presence of the oil phase initiator.

3.1.4. Varying HIPE processing time

Each series was also prepared with different dosing and homogenisation times, t_D and t_H respectively, in order to assess the effects of processing on the structure of the EPHP as a porous material. The increased homogenisation time t_H reflects a higher mechanical energy input which aims at reducing the average size of the pores. The detailed processing times (dosing and/or homogenisation) of the entire EPHPs series are reported in Table 3-3.

Table 3-3: Dosing Time t_D and Homogenisation Time t_H for the complete EPHPs series. Water Phase Pump Dosing Rates (WPDR) are shown in the last column.

EPHP Series	Sub Series EPHP Sample	"ε" (%)	t_D (min)	t_H (min)	WPDR (ml/min)
S10	S10-05	90	5	5	45
	S10-10	90	5	10	45
	S10-15	90	5	15	45
S20	S20-15	80	5	15	40
	S20-20	80	5	20	40
	S20-25	80	5	25	40
S30	S30-15	70	5	15	35
	S30-20	70	5	20	35
	S30-25	70	5	25	35
S40	S40-15	60	10	15	30
	S40-20	60	10	20	30
	S40-25	60	10	25	30

As it can be seen from the table and anticipated earlier, the only relevant change for t_D occurred for EPHPs S40(IN) series. The doubling of t_D was implemented to enable the higher solid content to be mixed effectively over a longer time. With reference to homogenisation time, then all samples were subjected to 15, 20 and 25 minutes of mixing following the end of water phase dosing.

All the HIPEs were later polymerised in an oven at 60°C for a minimum of 8 hours and were characterised by a micro-porous hierarchical structure in which the water droplets provided the emulsion template.

3.2. Moulding of HIPE

The moulding of the HIPEs represents an integral step of the EPHPs production process. According to the manufacturing and/or investigation requirements, HIPEs were transferred in different moulds, each of which served specific functions, ranging from direct collection from the bottom of the reactor (cones), square shape with larger sample volume (square mould), to the controlled/adjustable width and thickness of the circular sample (circular mould).

3.2.1. Monolithic tubes

The moulding of monolithic EPHPs was performed by transferring the HIPEs from the bottom of the reactor into the cones. The polypropylene (PP) tubes with diameter of 26 mm and a screwable lid have a nominal maximum volume of 50 ml (Fig. 3-3L). HIPEs produced with different solid content and different processing times were characterised by distinct viscosities. It was possible to transfer HIPEs with higher solid content and low t_H, while those with lower solid content needed to be pumped at slow rates (5-10 ml/min).

The use of the cones also enabled a qualitative assessment of the EPHPs produced to firstly check whether the emulsion had formed then if the EPHP was homogeneous or contained visible defects (cracks, holes etc.). An example of a filled up cone and hand-cut disks of low solid content (high ε) is shown in Fig. 3-3.

Fig. 3-3: EPHP S10 series produced after polymerisation in cylindrical cone mould (L) and dried EPHP Disks, diameter = 2.6 cm and thickness = 5-7 mm (R).

With reference to the HIPEs manufacturing procedure, the use of cones as moulds would result in these two additional steps:

11) Transfer of HIPEs by free falling into PP cylindrical cones, with a volume of circa 50 ml and a diameter of 2.6 cm.
12) Once polymerised, remove the monoliths and cut them into several disks of thickness between 5 and 8 mm.

3.2.2. Square mould

A brass mould capable of producing (10x10) cm square sample with a variable thickness (5-7 mm) was designed and assembled. The drawings in Fig. 3-4 show the details of the mould and the various pieces it is composed of. The triangular shape of the inlet is meant to slow down the emulsion velocity and enable the filling of the whole available volume at low flow velocities. In addition to that, the outer end is symmetrically designed to reduce preferential pathways that would result in the uneven distribution of the emulsion. The emulsion is fed into the mould via a pump (5-10 ml/min flow rate) from one of the two sides. The mould is initially

placed in horizontal position, while after few minutes it is placed in vertical position to enhance the homogeneous distribution of the emulsion due to height gradients. The design of the mould implies that a sealing media be present along the perimeter (shown as the withe rectangle in Fig. 3-5). The sealing is obtained by screwing the lid onto the bottom by means of 8 screws.

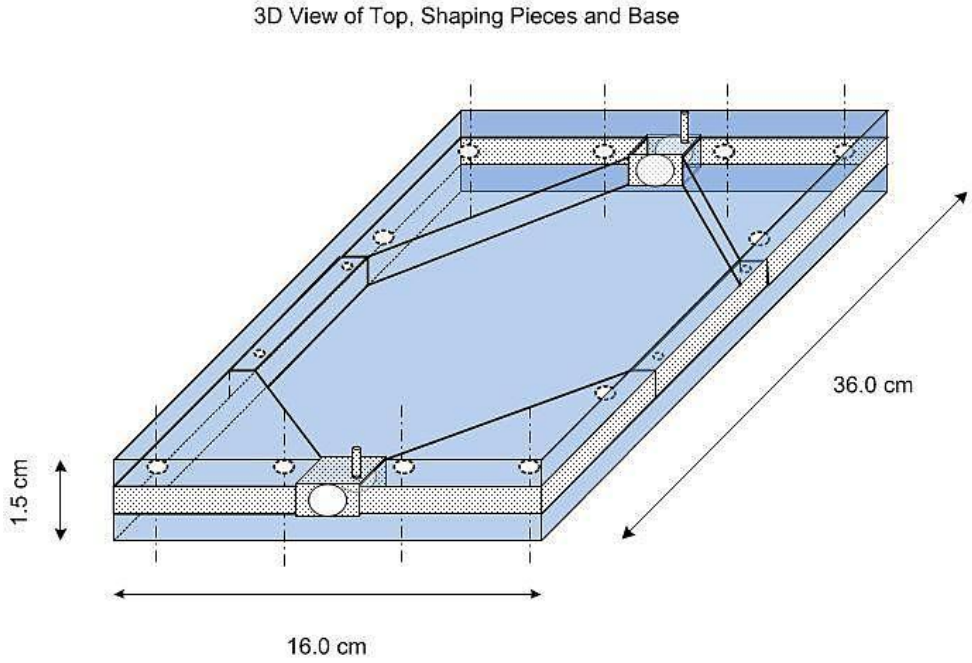

Fig. 3-4: Brass mould for EPHPs – 3D view. The injection point is located at the inlet of the mould (front or back of the picture). The emulsion was pumped in the mould at a rate of 5-10 ml/min. The injection process was operated with the mould in vertical position to enhance the compaction of the emulsion.

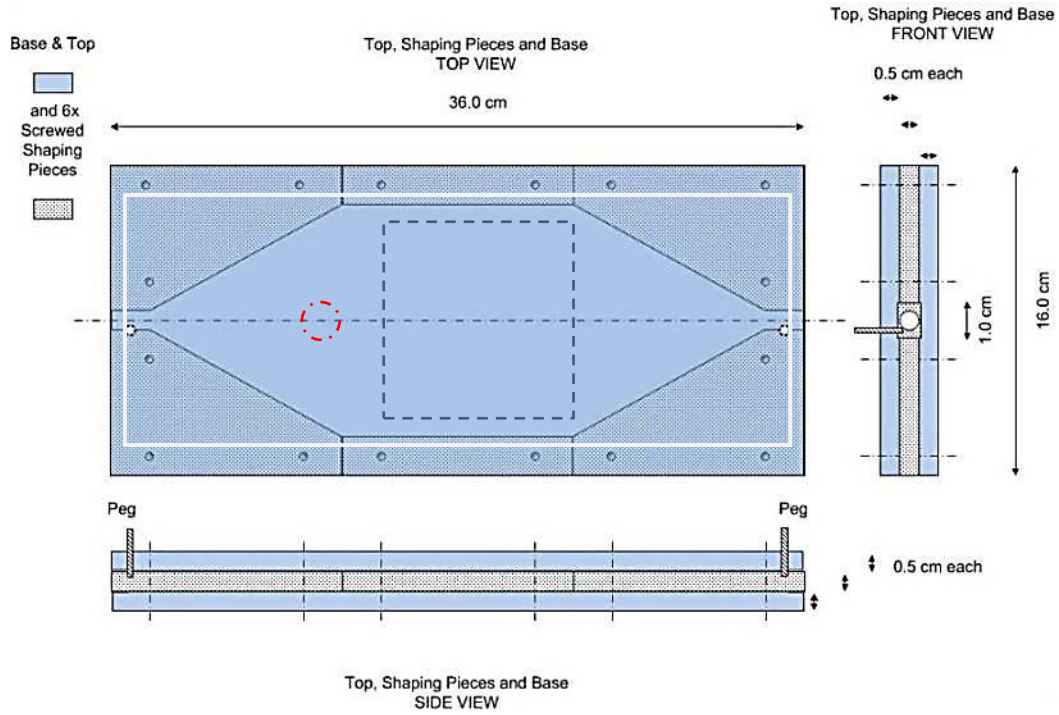

Fig. 3-5: Brass mould for EPHPs – top, side and front view. The central area (dashed square) of the mould was used to cut squares with 10 cm side. Disks of 26 mm diameter were taken to be tested for Mechanical Compression Testing (dash-dot circle cut, not in scale). The white solid line rectangle represents the sealing tape used between the mould base and lid.

Once the mould has been filled the following steps were taken:

- mould is placed horizontally
- pump is stopped and disconnected
- inlet and outlet connectors are sealed with plastic caps
- mould is transferred to the oven at 60°C for curing

The rectangular mould was used to produce EPHPs samples that were later tested to assess the effects of the flow direction (from the inlet towards the outlet) on the mechanical properties. Disks with a diameter of 26 mm (see Fig. 3-5, red circle) were cut by means of a tailor made steel cutter from different sections (inlet, central and outlet parts) and tested in structural and mechanical investigations.

3.2.3. Circular mould

A brass mould capable of producing circular samples with a diameter of 14 cm was designed and assembled. The drawings are shown in Fig. 3-6. With respect to the square mould, the design was simplified and only two pieces were used, a base and a lid. The sealing rubber ring is placed along the perimeter of the base and it does not affect the sample thickness. The two pieces are connected only by four spacers that dictate the thickness of the sample. The inlet and outlet connectors are placed on the lid and they are placed along the diameter to guarantee the maximum distance between them.

Several additional features were introduced with respect to the squared mould:

- All operations are performed with the mould in horizontal position only
- The sample thickness is better controlled and its value can be set at the mould assembling stage,
- slight variations of thickness due to sealing of the squared mould are eliminated
- Pumping at slow rate (5-10 ml/min) occurs from the top of the lid, which is easier in operation
- inlet/outlet connectors can be removed and replaced by screwable caps when the mould is completely full

After curing in the oven at 60°C overnight, the opening of the mould was facilitated by the removal of the inlet/outlet caps and spacers. This enabled the lid to be removed with minor directional stresses (i.e. the lid can only lifted vertically) compared to the squared mould where the opening needed to be performed by lifting the mould lid from one or multiple directions (i.e. either from the inlet, the outlet or one of the long sides).

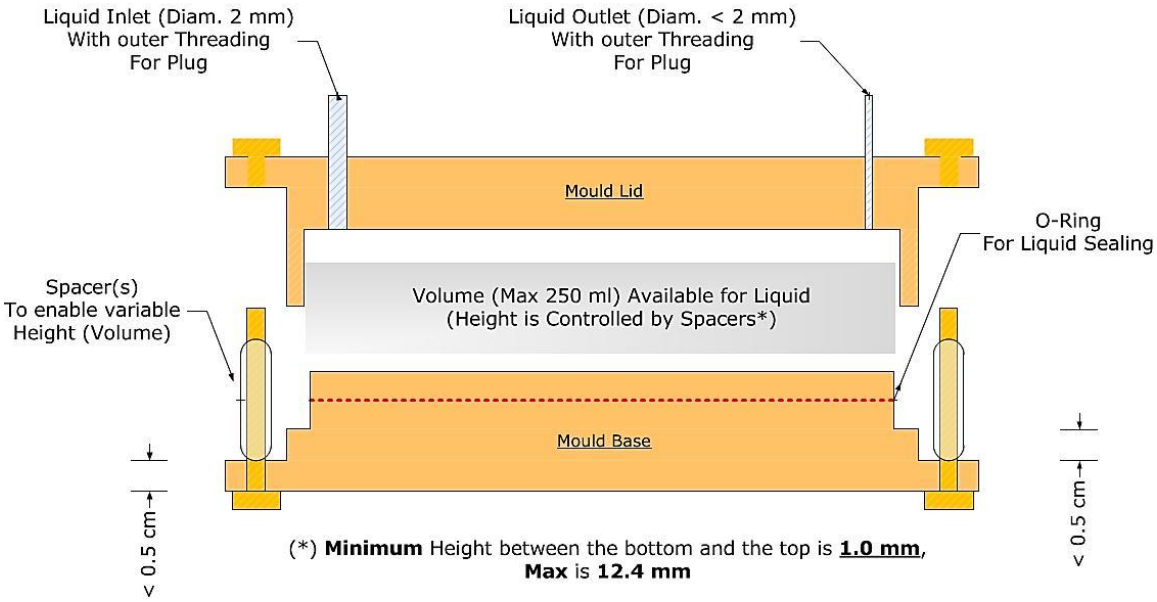

Fig. 3-6: Circular Mould made of brass. The mould consists of a Base and a Lid held in place by means of four spacers of different heights to provide the sample the selected thickness. An o-ring placed along the side of the mould base is used to obtain full contact of both parts and to prevent emulsion to leak before curing.

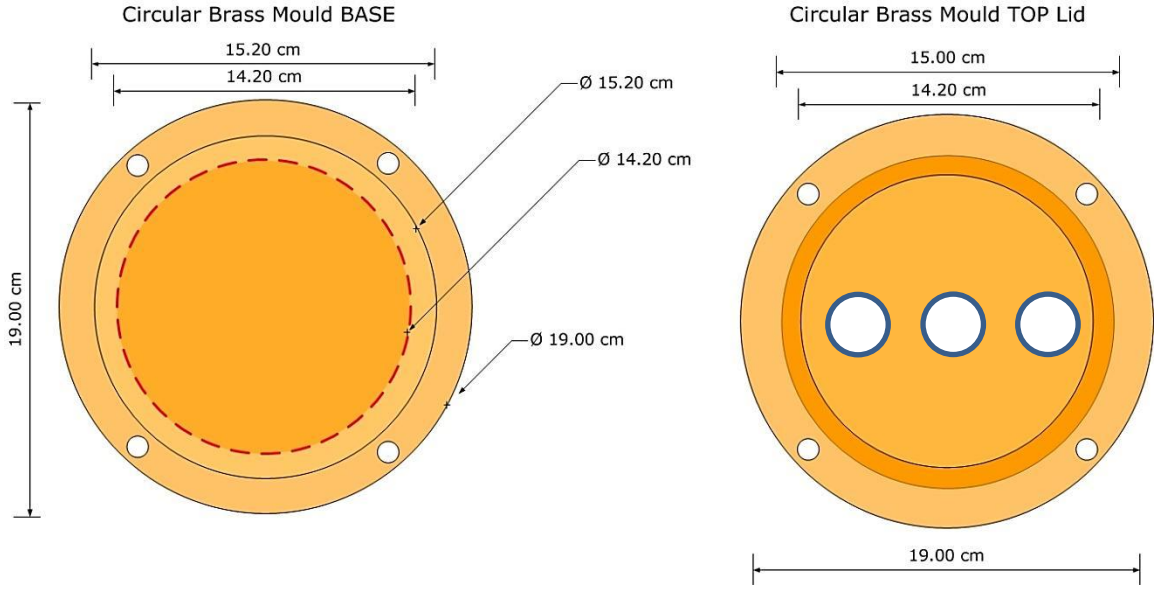

Fig. 3-7: Circular Mould parts. Base (L) and Lid (R). The O-ring is shown (red dashed line). The 3 circles on the right represent the 26 mm (not in scale) disks (inlet, central and outlet section) used for structural and mechanical investigation.

The 14 cm EPHP disks produced by the circular mould were removed from the base and transferred to a 40°C oven to enable the removal of watery excess and minimise thermal stresses during drying. The drying process was run for 24-36 hours.

Following the drying of the EPHP disk, three 26 mm diameter disks were cut and subjected to structural and mechanical characterisation. Similarly to the investigation of the flow conditions in the squared mould, the three disks were taken from the inlet, central and outlet mould sections.

The HIPEs were transferred into an oven at 60°C, where polymerisation (curing) would occur for not less than 8 hours.

3.3. Structural characterisation of EPHPs and orange skin

Porous materials are characterised by random or poorly organised geometrical arrangements. These factors and their importance in understanding and modelling the mechanical response have been introduced and described in the literature review. The structural characterisation of the EPHPs is particularly relevant for this study, as it focuses on the effects of HIPEs processing on EPHPs hierarchical, 3D structure. The structure of EPHPs is investigated in order to identify the following typical features:

- Open and/or Close cells/pores
- Presence of interconnected pores
- Presence of much larger/smaller pores
- Diameter of the pores, distribution and average value (*D*)
- Pore wall thickness (t_W) and intersecting vertexes thickness (*Tv*)

These geometrical parameters and EPHPs characteristics have been identified by means of the Scanning Electron Microscopy (SEM) technique. SEM is the most common technique used to acknowledge the structural features of PHPs thanks to its capability of producing highly detailed images ranging from mm to nm and a relatively easy preparation the samples. Further details on the SEM will be provided in the next sections. Fig. 3-8 shows two representative SEM images of EPHPS used to investigate the above mentioned features. The structural parameters, SEM imaging magnification and scale bare used are summarised in Table 3-4.

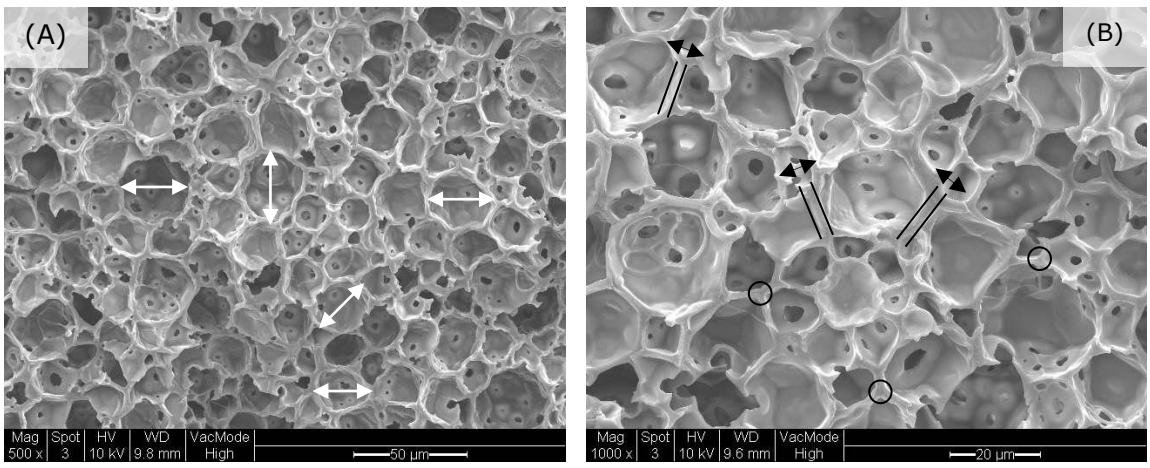

Fig. 3-8: SEM images of an EPHP. (A): magnification 500x and scale bar 50 mm used for the computation of average pore size/diameter *D*. Five double ended arrows with different length are shown. (B): magnification 1000x and scale bar 20 mm for computation of cell wall t_w and intersection vertexes thickness *Tv* (three of each are shown as lines and circles respectively).

Table 3-4: SEM magnification and scale bar reference for the identification and computation of EPHPs structural parameters.

Structural Parameter	SEM Magnification	SEM Image Scale Bar (μm)
Open and/or Close Pore	250	100
Pore Diameter	500	50
Wall and Vertexes Thickness	1000	20

The SEM investigation thus enables to obtain two types of information: 1) qualitative, to appreciate substantial differences among samples and 2) quantitative. The latter set of information analysis is performed by means of accurate statistical analysis, from which the parameters can be identified, measured and related to each other. The number of readings that were used to produce the statistical analyses of the various data is reported in Table 3-5. The data were analysed to derive an average value and the standard deviation has been used to acknowledge the scattering (shown as error bars) of the measurements.

Table 3-5: number of readings taken for the EPHPs structural parameters statistical analysis.

Structural Parameter	n° of readings	Error Bars determined by
Pore Diameter	80	± Standard Deviation
Wall and Vertexes Thickness	20	"

Structural investigations of the EPHPs cross sections were performed at the NACMA laboratories of Newcastle University by using a Scanning Electron Microscopy (SEM) manufactured by Philips (Fig. 3-9).

Fig. 3-9: typical SEM instrument facilities. The SEM is recognisable on the right, while the imaging and editing monitors are visible on the left.

The SEM used is capable of producing high resolution images on dry, conductive, non-conductive and wet samples. The latter characteristic, explained later on, proved to be useful when the outer skin of an orange was analysed.

3.3.1. Scanning Electron Microscopy (SEM) and Environmental-SEM (ESEM)

The use of the Scanning Electron Microscopy (SEM) in its Environmental-SEM (ESEM) version and its importance in the detailed study of EPHPs structures is presented in this section. SEM is the most common technique used to acknowledge the structural features of PHPs as already accounted for in the literature review chapter. It is worth mentioning that the main differences (and operational improvements) between SEM and ESEM reside in the fact that the instrument would operate in high vacuum, therefore vapours/gases from wet or biological samples would originate in the sampling chamber. These vapours and gases would disturb the electron beam pathway to the detector with poor imaging definition results in a conventional SEM. In order to overcome this factor, a second detector called Gaseous Secondary Electron Detector (GSED) , capable to operate in such conditions is added (ESEM). For a more detailed description of SEM and ESEM working principles and characteristics reference books by Michler (2008) and Sawyer et al. (2008) are particularly useful;

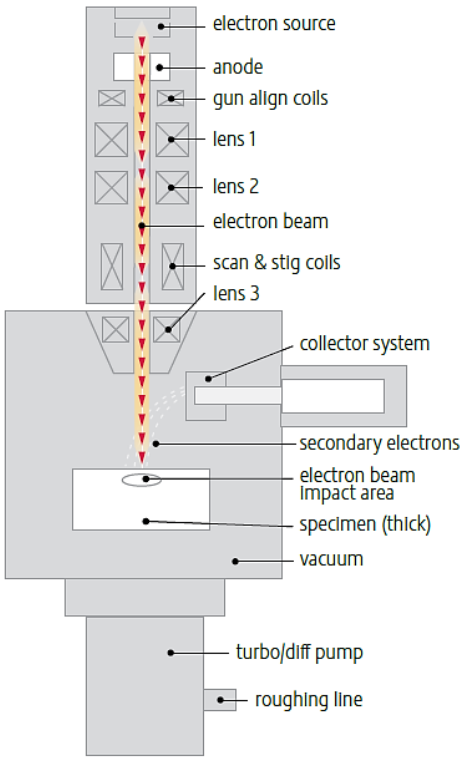

Fig. 3-10: schematic representation of the constituting element of an SEM; electron beam generation, focussing lenses, specimen chamber and detectors' system.

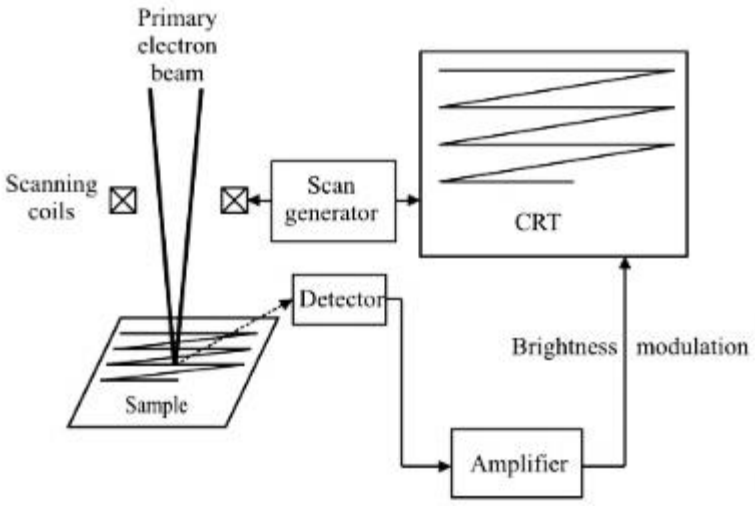

Fig. 3-11: schematic SEM principles; from scanning of the sample via electron beam to collection of signals and their conversion into an image.

The ESEM is capable of producing highly detailed images of EPHPs, ranging from mm to nm and this investigation focussed on the micrometre range making it possible to operate the instrument at optimal conditions.

The generation of the SEM image and its degree of resolution is due to a combination of signals generated by the interaction of primary electrons (generated by the electron beam) and the electrons generated by the specimen. Two kinds of electrons are detected: 1) secondary electrons (SE) and 2) backscattered electrons (BSE). X-Rays are also produced; they may be used for elemental chemical analysis. SE are originated in a thin layer on the specimen surface while the BSE originate at higher specimen depth. These two conditions provide different levels of image information and resolution: the SE provide the high resolution while the BSE provide the contrast.

3.3.2. Sample preparation for ESEM

An additional feature of ESEM is that the sample preparation is rather easy. The EPHPs cross-section (XS) structural layout is that of interest thus it is investigated. XS of disks were obtained as follows: a disk is bent until fracture occurs and the operation is repeated until an approximately 3x3 mm sample size is obtained.

The samples are then coated with gold to make them conductive with direct benefits on image resolution and contrast. This operation is performed by a dedicated machine and only takes 5 to 10 minutes. Once the sample is coated it is then placed on a metallic stub. The small sample is placed on the stub with the fracture surface exposed on the top surface as shown in Fig. 3-12. The stub is placed into the SEM chamber; the latter is closed and vacuum applied.

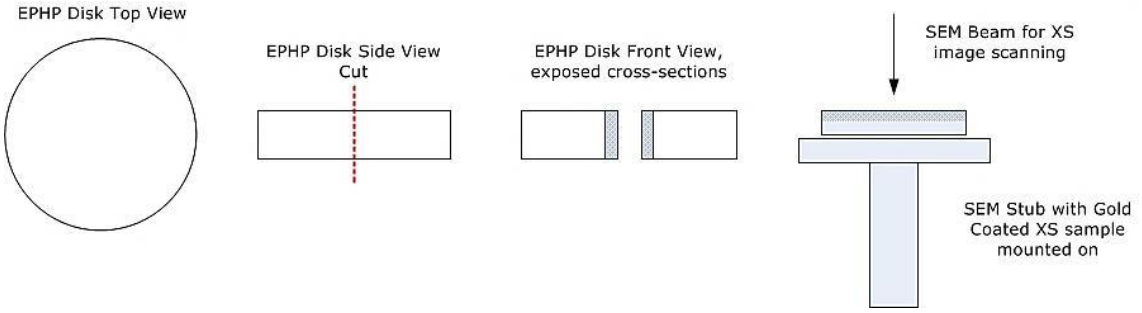

Fig. 3-12: EPHPs disk cross section cutting, gold coating and SEM stub preparation.

Once vacuum is applied in the specimen chamber, the imaging of the samples is obtained by the collection of signals produced by a scanning electron probe. The sample XS is then analysed at various points and at different magnifications according to the required level of details. The images produced are stored in the ESEM memory and can be edited by proprietary or generic image-editing software. Copies of the original or modified image files can also be exported.

3.3.3. Orange fruit skin

The ESEM characterisation of the orange skin was performed to assess how the pores diameter varies along the radial direction (i.e. from outer to inner skin). The orange fruit skin needed to be preconditioned before ESEM analyses. Due to its intrinsic moisture content, to prevent volume expansion during testing in ESEM vacuum conditions, the orange skin was placed into liquid nitrogen. The sample was kept in liquid N_2 for 2 minutes so that sample rigidity could be obtained. The SEM investigation was performed on two main parts of the orange skin: 1) outer XS and 2) inner skin, i.e. the exocarp and the mesocarp. The magnifications were selected according to the level of details required. Due to the nature of the sample, coating with gold for higher definition was not possible. Once the testing session was completed (45 minutes), it was acknowledged that the low vacuum conditions in the SEM chamber had been capable of causing a visible increase in pores diameter.

3.3.4. Statistical Analysis of structural data

All the relevant structural parameters obtained from the SEM images were subjected to statistical analysis. The average pore size *D* and its distribution on the three cross section surfaces (top, middle and lower region), were determined by means of an image editing software, *ImageJ* (ImageJ, version 1.44p, by W. Rasband, National Institutes of Health, USA, available from http://imagej.nih.gov/ij) and the data were then subject to statistical analysis. The pore size distribution was plotted to identify the most recurring diameter interval and to determine the effect of amount of solid and stirring time.

3.4. Rheological properties of HIPEs and mixing energy input

The rheological behaviour of HIPEs was studied to assess their stability at different processing conditions. Understanding how an HIPE behaves as stresses are applied to it is of primary importance. Most notably transferring (i.e. pumping) an emulsion from one place to another is a very common occurrence, thus knowing whether the pumping (i.e. shear stress) has an effect on its stability is necessary. Furthermore, the stability of an HIPE as a function of time is relevant. Moulding is a process whose extent (from seconds to tens of minutes) may be limited by the emulsion stability as stresses and time may combine their effects. HIPEs rheological behaviour was assessed by measuring their viscosity as a function of time with a Brookfield Viscometer (Fig. 3-13). The Brookfield viscometer is an instrument that measures the torque that is required to rotate a spindle immersed in a fluid. The viscosity is computed by considering that a given spindle would rotate at a given speed if not slowed down by viscous (frictional) forces of a given fluid.

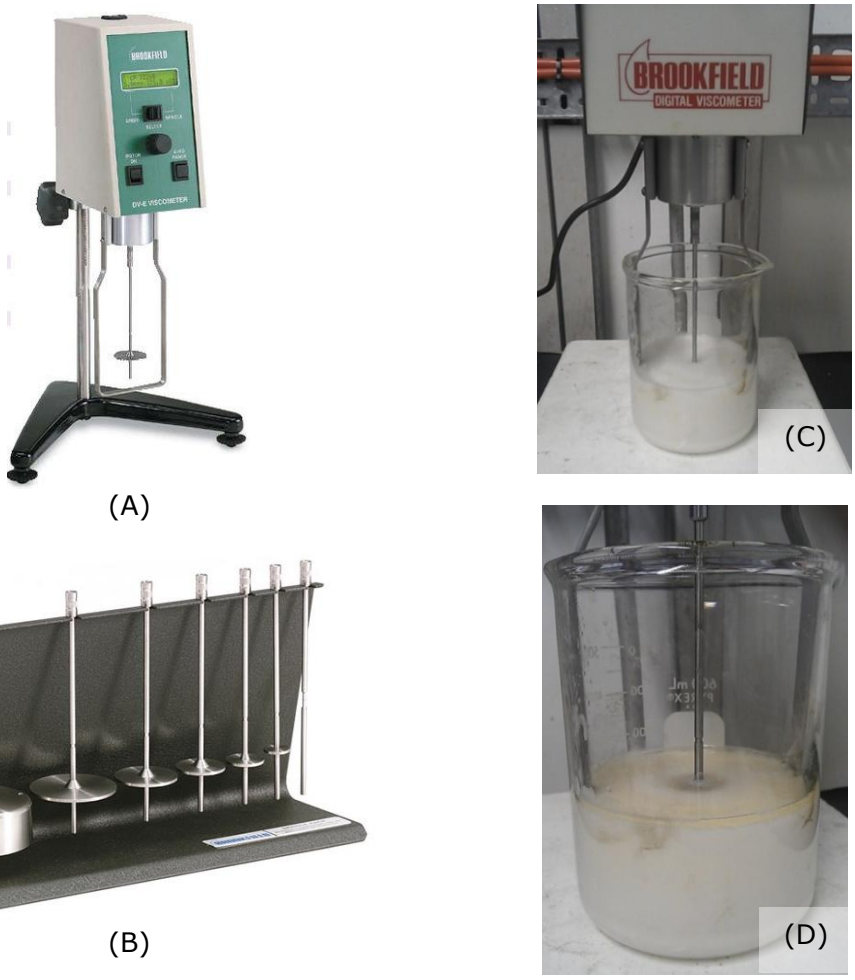

Fig. 3-13: a typical Brookfield digital viscometer and a set of spindles. Images (C) and (D) show an HIPE during the viscosity test. (C) few seconds after beginning and (D) at end of testing session.

It is worth noting that several spindles are available to offer both measurement accuracy and a wide viscosity operative range.
All the HIPEs were prepared according to the procedure highlighted in section 3.1., and the objective of the measurements was the determination of viscosity of the HIPEs as a function of time, from which two key process-related features could be identified:

1. Stability Transfer-Time (STT): the time range within which the emulsion shows a relatively constant viscosity. STT provides an indication of the overall transfer time (i.e. moulding time) an HIPE can sustain.

2. Instability Region Time (IRT): the time (after the STT) at which the viscosity drops and indicates continuous changes in stability. This region is also usually associated with visual evidence of early signs of phase separation.

All the HIPEs tested were firstly prepared according to required dosing and homogenisation times and then transferred into a beaker of suitable diameter (Fig. 3-13C and D). The spindle was slowly submerged in the HIPE and the instrument motor was switched on. Minor adjustments were necessary to obtain a valid reading. Display readings were taken over time at intervals of 1, 5 and 10 minutes and later converted into viscosity values (units are cP converted into mPas). The duration of the test exceeded 1 hour in order to simulate long emulsion transferring times and visual observations were recorded (an example is shown in Fig. 3-13D as an oily layer floating at the top of the emulsion is visible).

The stirring/mixing process used to produce the various HIPEs was also investigated. The stirring conditions (i.e. rotations per minutes and reactor assembly) were kept the same throughout the study and their effectiveness in producing the various HIPEs was determined. The theoretical amount of energy per volume that the stirring system would be able to produce was calculated and it was later related to the EPHPs structure. This theoretical Mixing Energy Input (MEI), provided by the system to produce the various HIPEs, was computed by considering key factors such as the Pumping Number N_Q and Power Number N_P. These numbers are a function of several geometrical and physical characteristics of the mixing system. The most relevant factors include: 1) the shape of the stirrer, 2) its rotational speed and 3) stirring time, 4) the emulsion density and viscosity, as well other geometrical factors such as 5) the reactor diameter and 6) the stirrer's blade diameter (Paul *et al.*, 2010). The effects of the MEI on EPHPs structure are shown in the results section.

The actual MEI transferred to the emulsion is inevitably lower than the nominal (theoretical) amount as the emulsion are inherently viscous hence energy losses due to viscosity are expected.

3.5. Mechanical Compression Testing of EPHPs

Mechanical Compression Tests (MCT) were performed in order to assess the effects of EPHPs structural changes imparted due to a) the difference in solid content and b) the various HIPE processing routes. The relationship between processing and structure was then supported by investigating the mechanical properties of the EPHPs. Hence, the process-structure-properties relationships are combined.

MCT sessions of EPHPs samples were performed using a Mechanical Test Frame (MTF) manufactured by Tinius Olsen, Ltd. The bench top test frame is a Dual Column model, shown in Fig. 3-14 (L), equipped with a 5 kN load cell. The machine is also equipped with testing Software "Horizon", a screenshot of which is depicted in Fig. 3-14 (R).

Fig. 3-14: Mechanical Test Frame (L) manufactured by Tinius Olsen, dual column model HK-S. Screenshot of the Testing Software "Horizon" (R) used to set up test conditions, taken from Tinius Olsen website.

The Horizon software enables the following features: 1) setting up the test conditions, 2) live plotting the graphs and 3) exporting of the data for further analyses and processing of data. MCT were performed on EPHPs disks. For samples moulded in the cylindrical cones, the cutting of cylinders into disks of a given thickness was done manually by a metal blade cutter. There was an intrinsic variability of thicknesses (between 5 and 8 mm) for such a reason. The EPHPs samples moulded in the rectangular mould had a narrower thickness range as it was set by the mould itself and by the additional sealing tape between the base and

the lid (see Fig. 3-5). The variability was limited to 5-5.5 mm and the disks were cut by means of a purpose-made metal cutter with a circular shape and a diameter of 26 mm. EPHPs Samples moulded in the circular mould were given different thicknesses according to the mould spacers. The most recurring thicknesses were 4 and 6 mm. The disks were cut from the larger moulded samples again by the circular cutter.

3.5.1. Mechanical test frame setup and testing parameters

The geometrical parameters of the EPHPs samples input in the Horizon Software were the diameter and the thickness, from which the area and volume of the EPHPs disk could be calculated. Following the geometrical values, the *Travelling Distance* of the cell was input. The downward travelling distance of the cell was set to correspond to half the sample thickness. By doing so, 50% compression of each sample was obtained. Furthermore, the speed at which the cell would move downwards, thus the *Strain Rate*, was set at 1 mm/min for tests at room, low and high temperatures. The strain rate $\dot{\varepsilon}$ is defined according to the following equation $\dot{\varepsilon}=\frac{d\varepsilon}{dt}=\frac{d}{dt}\left(\frac{l-l_0}{l_0}\right)=\frac{1}{l_0}\frac{dl}{dt}=\frac{v(t)}{l_0}$ and it accounts for the velocity at which a sample of initial thickness (length l_0) is compressed.

Before starting each test, the sample was pre-loaded with a force of circa 1N in order to ensure an even contact between the cell and the sample. Each sample was tested three times in order to determine an average value for *E* and *SAE* and at intervals of 2 minutes, in accordance with good practices for IRMs testing procedures. The tests were performed at an initial strain rate of 1 mm/min before increasing it up to 50 mm/min when the effects of strain rate and temperature were investigated.

A typical MCT session procedure is provided here below:

1) The specimen is loaded and the cell is lowered until even contact is attained and a pre-compression force of 1N is measured
2) Geometrical parameters, travelling distance and strain rate are input
3) The compression test is started and the curves of force vs. position and stress vs. strain are plotted automatically
4) When the requested compression distance (50% of the initial thickness of the sample) is reached, the cell returns to the original "zero" position
5) After 2 minutes, the test is repeated; three tests are performed in total
6) All data and graphs are exported for further analysis

This time enabled the samples to fully recover the original shape in case of viscoelastic behaviour influence and according to recommended good practice.

Chapter 4 - Results and discussion

"Wisdom is the daughter of experience".

- Leonardo da Vinci

This chapter presents and discusses the project results. Many EPHPs structural and mechanical parameters have been investigated and they vary according to the study performed.

The results are presented according to the following main studies:

1. Preliminary identification of structural similarities between low solid content EPHPs and orange fruit skin. It aims to recognise the importance of the hierarchical pore size feature of orange skin and its bio-mimicking approach by means of EPHPs.
2. Structural changes of EPHPs as the results of different processing conditions. This is aimed at presenting and identifying the Process-Structure relationship.
    2.1. Structural parameters include the average pore diameter D, the wall thickness t_W as well as the intersecting vertex thickness T_v.
    2.2. Structural identification of reference/benchmarking materials
3. Mechanical behaviour characterisation of EPHPs. This study aims at presenting and identifying the Structure-Properties Relationship. Parameters such as Young's Modulus E and Specific Absorbed Energy SAE were determined for EPHPs that were produced by:
    3.1. An increasing amount of polymerizable oil phase (solid content) at constant processing time conditions (t_D and t_H)
    3.2. An increase in the processing time conditions at constant solid content
    3.3. Evaluation of Gibson & Ashby Model prediction capabilities
4. Rheology of HIPEs with varying solid content and homogenisation time
5. Effect of temperature on EPHPs mechanical performances and time-temperature equivalence
6. Comparison with reference/benchmarking IRMs
7. EPHPs as a novel class of materials in a Material Selection Chart (Ashby Charts)

Hence, the Process-Structure-Properties relationship (shown in Fig. 4-1), have been investigated in the light of the above research results.

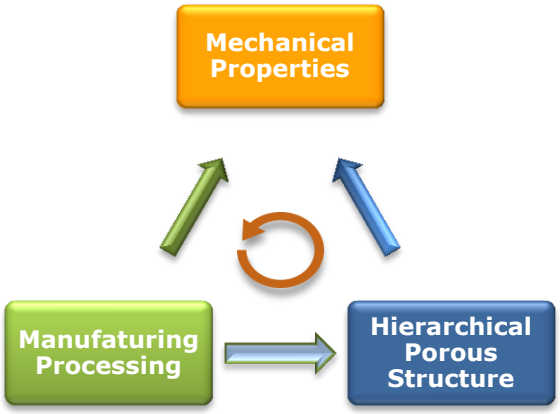

Fig. 4-1: EPHPs Processing-Structure-Properties relationship cycle.

The cyclic symbol in the centre of Fig. 4-1 means that the approach of Process-Structure-Property needs to be constantly used as an EPHP design guideline. In fact, modifications in the EPHPs solid content were driven firstly by measuring their mechanical properties (via MCT) with reference to the comparison materials. Solid content was then increased until preliminary satisfactory results were obtained. Once reviewing and comparing mechanical properties, mechanical behaviour changes were observed.

In the light of these changes, the identification of the EPHPs structure (via ESEM imaging) became critical to provide a Structure-Property relationship.

The modification of EPHPs manufacturing process by increasing the dosing and homogenisation time (t_D and t_H respectively), focused at identifying to what extent the hierarchical pore structure, i.e. the distinctive feature of EPHPs, could be taken. This approach hence, focussed towards the Process-Structure relationship.

Changes in the manufacturing of a product, for example by changing its formulation to obtain a set of desired mechanical properties, without assessing the role and influence of the structure, can generally be termed as a *"Trial and Error"* scheme. When the structure is considered and placed at the centre of the investigation, the approach is termed as *"Knowledge Based"*. Such two approaches are schematised in Fig. 4-2.

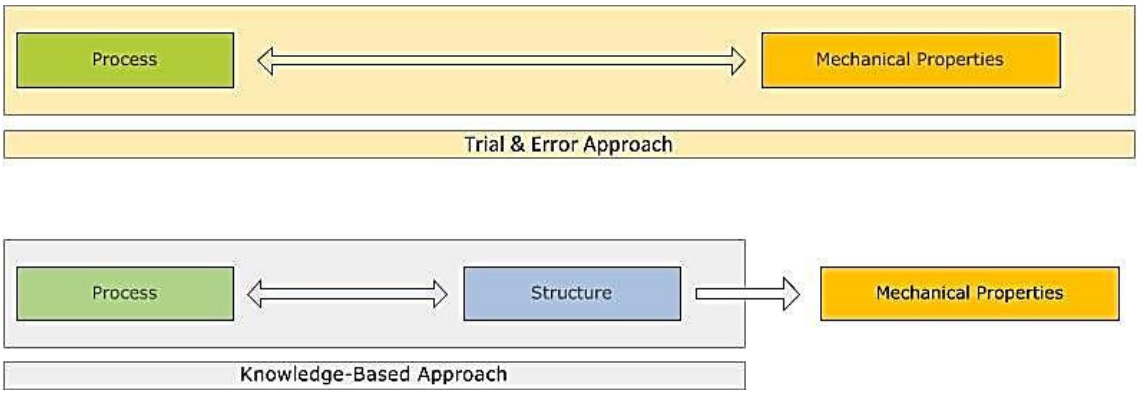

Fig. 4-2: Approaches to meet mechanical properties targets. Trial & Error (top drawing) may include changes in the formulation and different manufacturing processes. Knowledge-based approach (bottom) focuses on the structure of the material and its role in generating mechanical properties.

Throughout the next sections, the latter approach will become evident as it is determined that the manipulation of the EPHPs structure produces more remarkable results in terms of higher elastic modulus and energy absorption than an increase of solid content alone.

Mechanical performances of the various series of EPHPs are presented by means of stress vs. strain curves, from which the mechanical behaviour description can be obtained. Typical elastomeric, foam and composite-like behaviours are recognised throughout the study of EPHPs, as well as by testing the two reference materials. Once a detailed presentation and interpretation of the results has been provided, the EPHPs will be inserted into the Modulus vs. Density Material Charts, also known as Ashby Charts. EPHPs locate themselves into an empty space (an envelope), where no other existing materials are found.

4.1. Structural similarities between orange fruit skin and low solid content EPHPs

The orange fruit skin has been found to be particularly effective in absorbing energy. The reason for such a remarkable capacity lies in the hierarchy of the cells/pores that form its skin. The hierarchy makes it possible for the impact load to be initially dealt with by the smallest pores followed by larger ones toward the inner part of the skin.

The ESEM investigation was used to 1) characterise the degree of the pores hierarchy in the orange skin and in the lowest density EPHPs (series S10) and 2) compare them to identify similarities in pores hierarchical distribution.

4.1.1. Hierarchical structure of orange fruit outer skin

The porous and hierarchical structures of the orange outer and inner skin were recognised and identified via SEM images. The full view of the outer cross section (XS) sample is shown in Fig. 4-3 and it is further divided in middle (Fig. 4-4) and lower region (Fig. 4-5).

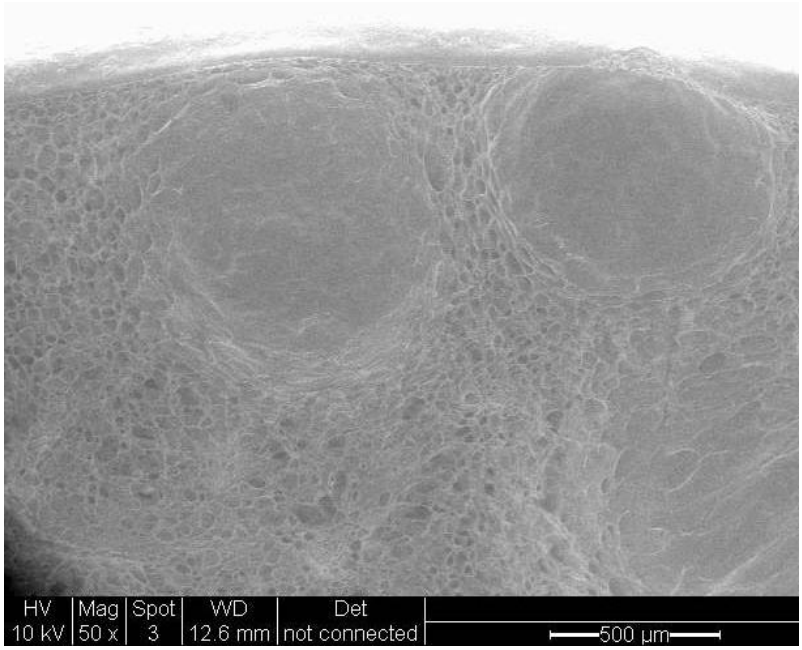

Fig. 4-3: SEM orange outer skin XS (50x). Full view, outer top.

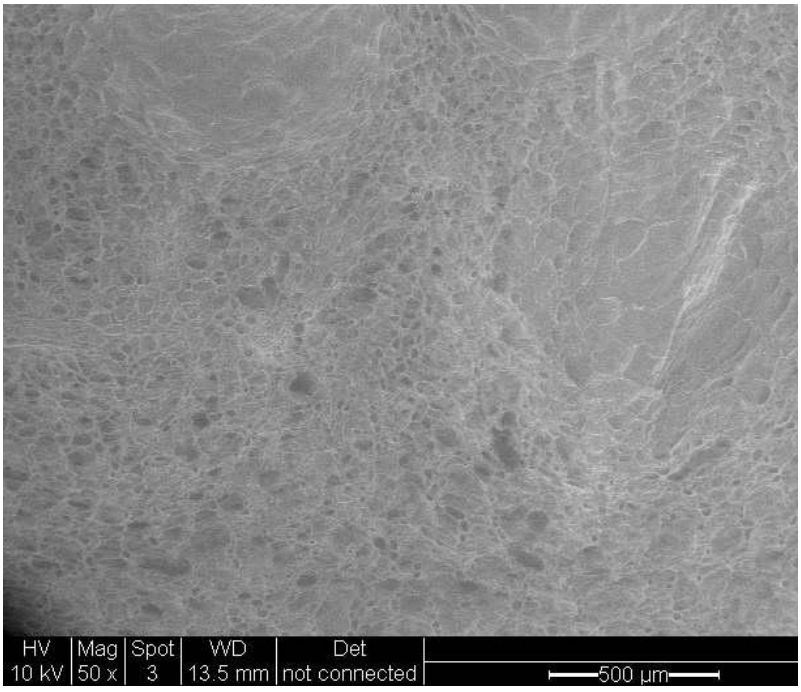

Fig. 4-4: SEM orange outer skin XS (50x). Middle Region.

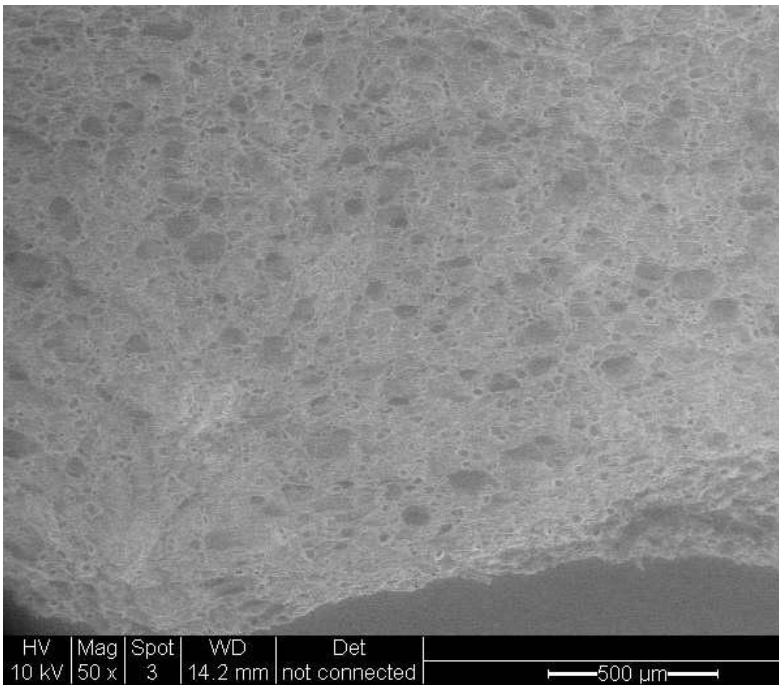

Fig. 4-5: SEM orange outer skin XS (50x), Lower Region.

The SEM images reveal that the orange skin is characterised by pores with varying diameter when moving from the outer top toward the inner bottom. In order to precisely assess such variation, higher magnification images were taken. The orange skin XS was further magnified (500x) at the top between the two large pores, as well as at the middle and the bottom region (Fig. 4-6A-C respectively).

It can be observed that the skin structure keeps the same layout along the radial section; an open tubular-layers that resembles that of an open pore foam. These open, elongated tubular-pores are constantly present and they increase in diameter towards the bottom region as expected.

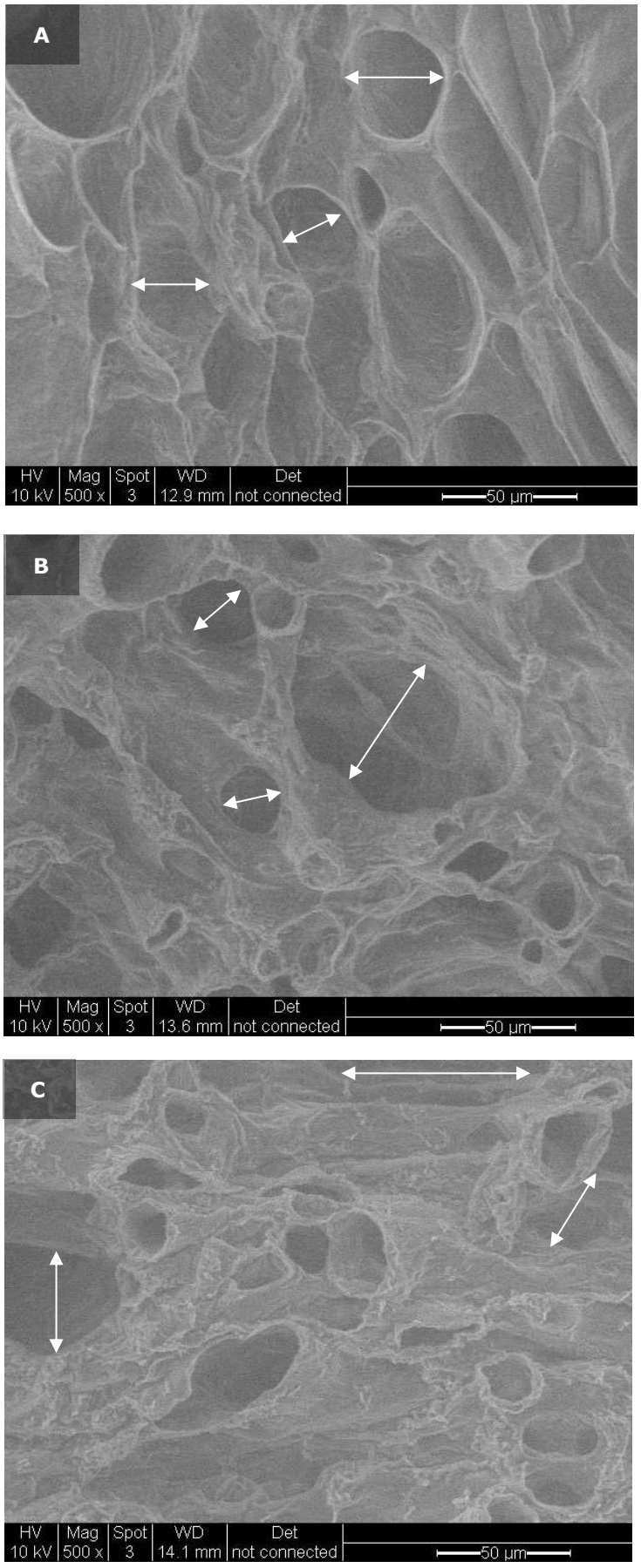

Fig. 4-6: SEM orange outer skin XS (500x), Top region (A), middle (B) and lower (C). Doubled arrow lines represent the pores for which the diameter is measured. The diameter can be seen to increase from A to B and C.

Before presenting the detailed statistical analysis of the pore diameter variation along the XS, it is worth comparing the pictures of the orange skin at the beginning and at the end of the SEM session. As anticipated in the methodology and due to the vacuum conditions that exist in the ESEM, it was noticed that the sample had lost its frozen status. As a consequence of that, Fig. 4-7A shows larger inner pores when compared to Fig. 4-7B (which is a duplicate of Fig. 4-3).

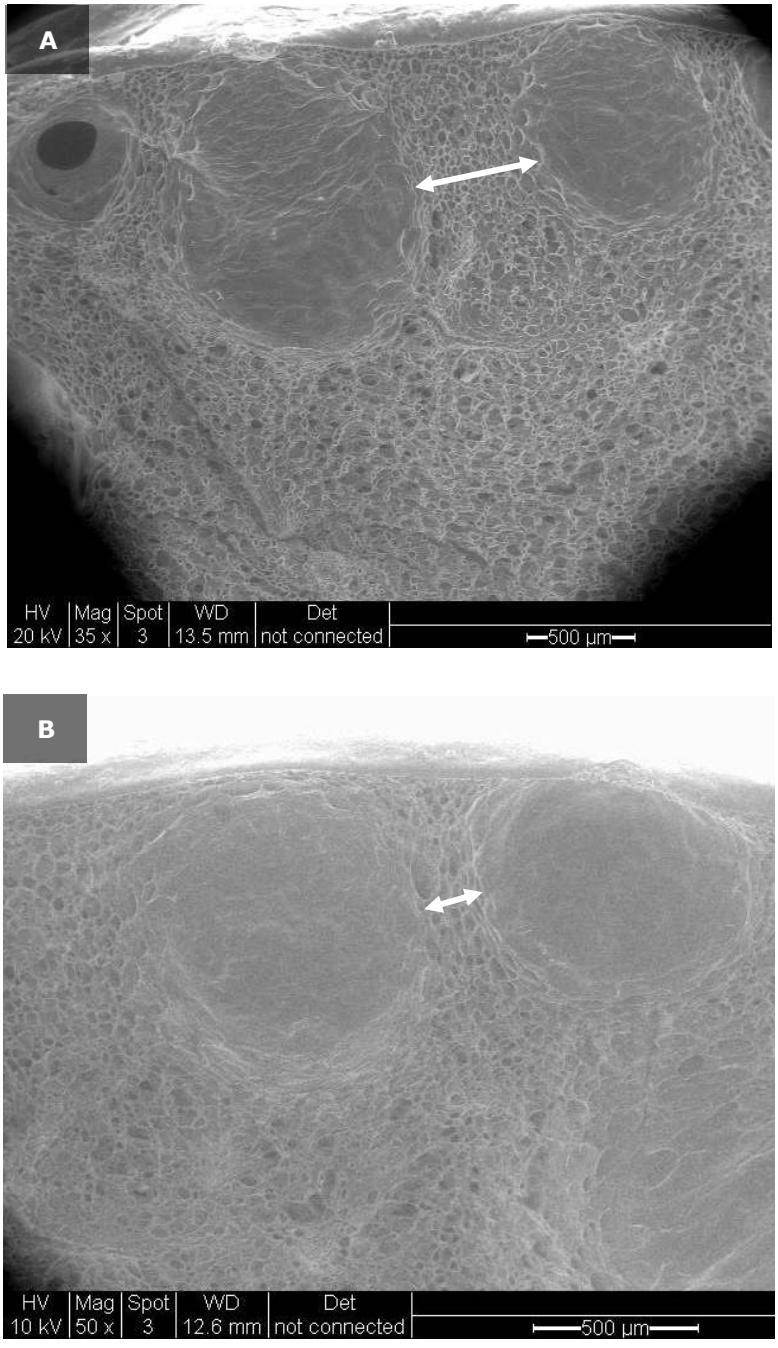

Fig. 4-7: SEM orange outer skin XS. (A) full view at end of session (35x) and (B) beginning of session (50x, copy of Fig. 4-3). The two double arrow lines show the distance between the two large pores. Changes occurred for the distance at the end of the SEM session (the sample expanded its volume). The effect of expansion is exaggerated by the two different magnification factors.

The average pore size *D* and its distribution on the three cross section surfaces (top, middle and lower region), were determined and the data were then subject to statistical analysis.

With reference to the orange outer skin (top region XS, Fig. 4-6A) the average pore size is 29.2 μm based on 10 readings. The distribution histogram is shown in Fig. 4-8 and the relevant statistical data are reported in Table 4-1.

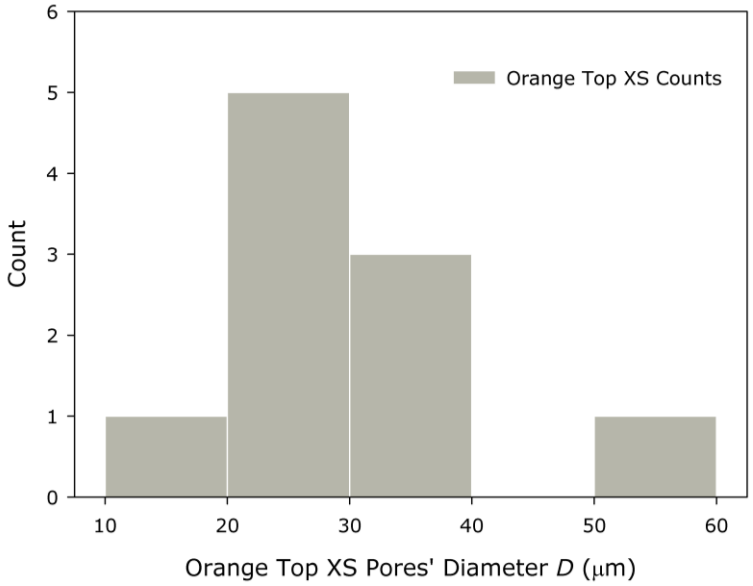

Fig. 4-8: Pores diameter distribution of orange outer skin XS top region (total readings 10, diameter interval 10 μm).

The graph shows that 5 out of 10 readings had a pore size between 20-30 μm, followed by 3 recurrences in the 30-40 μm intervals.

Table 4-1: Orange outer skin (Top Region) XS pore size *D* statistical data summary (based on 10 readings).

Orange Top Region *D*	Value (μm)
Average	29.2
Std. Deviation	11.6
Interval	44.4
Min	11.8
Max	56.2

The orange outer skin middle region XS (Fig. 4-6B), has an average pore size of 56.2 μm and the value is based on only 5 measurements. The distribution histogram is shown in Fig. 4-9 and the relevant statistical data, although limited to only five readings, are reported in Table 4-2.

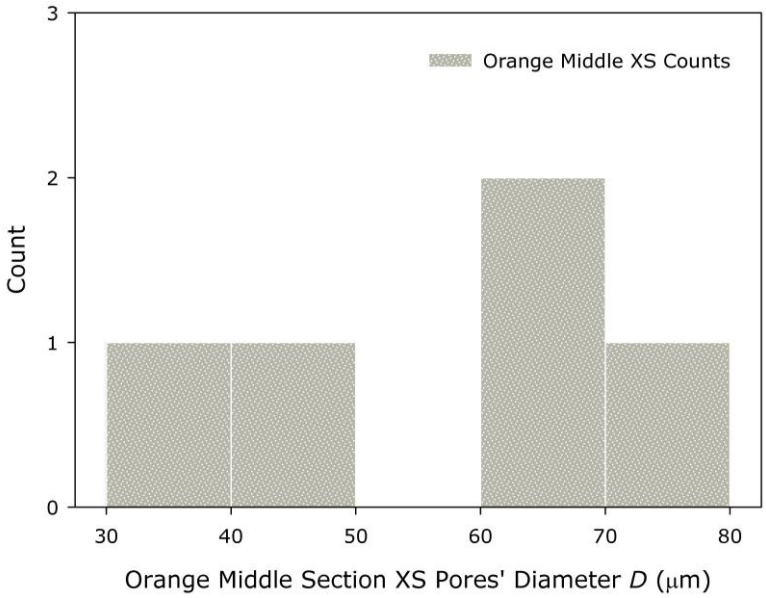

Fig. 4-9: Pores diameter size distribution of orange outer skin xs middle region (total readings 5, diameter interval 10 μm).

The histogram shows that the diameters from 60-70 μm occurred 2 times out of 5, while the remaining intervals were counted once, with no counts between 50 and 60 μm.

Table 4-2: Orange outer skin (Middle region) xs pore size *D* statistical data summary (based on 5 readings).

Orange Middle Region *D*	Value (μm)
Average	56.2
Std. Deviation	13.2
Interval	33.8
Min	36.7
Max	70.5

The Bottom region of orange cross section surface, has an average pore size of 72.2 μm and the value was based only on 3 measurements from Fig. 4-6C. The distribution histogram is not shown due to the very limited amount of readings, three and their basic statistical data are reported in Table 4-3.

Table 4-3: Orange outer skin (Bottom Region) XS pore size *D* statistical data summary (based on three readings).

Orange Bottom Region *D*	Value (μm)
Average	72.2
Std. Deviation	20.5
Interval	36.9
Min	58.9
Max	95.8

The overall results for the average pore size of the orange cross section surfaces, Top, Middle and Bottom, are summarised in Table 4-4.

Table 4-4: Orange outer skin (Bottom Region) XS Pore Size *D* Statistical Data Summary (based on three readings).

Material	Sample	Average Pore Size *D* (μm)
Orange XS	Top "	29.2
"	Middle "	56.2
"	Bottom Region	72.2

A plot of average diameter as a function of orange skin XS is shown in Fig. 4-10. These data were later compared to those from EPHPs series S10.

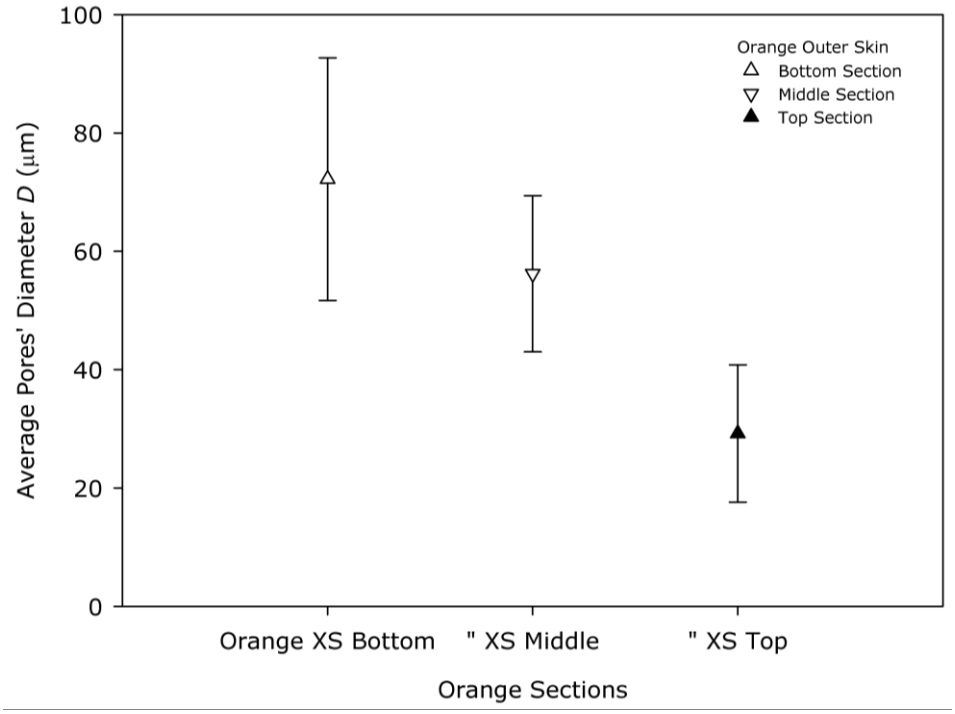

Fig. 4-10: Orange outer skin average pore diameter *D* as a function on skin section (from bottom to top).

It can be seen that the average pore size *D* decreases when moving from the bottom XS region of the orange skin towards the top region. These results confirm those that had been found for the outer skin of the *Citrus maxima* pummel (Fischer *et al.*, 2010; Seidel *et al.*, 2010). Hence, the hierarchy of the pore size with respect to the position is established and it is this hierarchy that enables the orange skin to be highly effective at resisting high and repeated impacts.

4.1.2. Hierarchical structure of orange fruit inner skin

Further evidence in the similarity of orange skin and EPHPs was found by investigating the layout of the orange fruit inner skin. This skin layer connects the outer skin with the fruit. Its function is that of spreading the residual impact load.

The inner skin is shown in Fig. 4-11A-B and resembles the EPHPs structure (shown in Fig. 4-12 and Fig. 4-13) as it appears like an open-pore foam; the pore size ranges from circa 50 to 100 μm. The structure also shows tubular-shaped interconnecting walls.

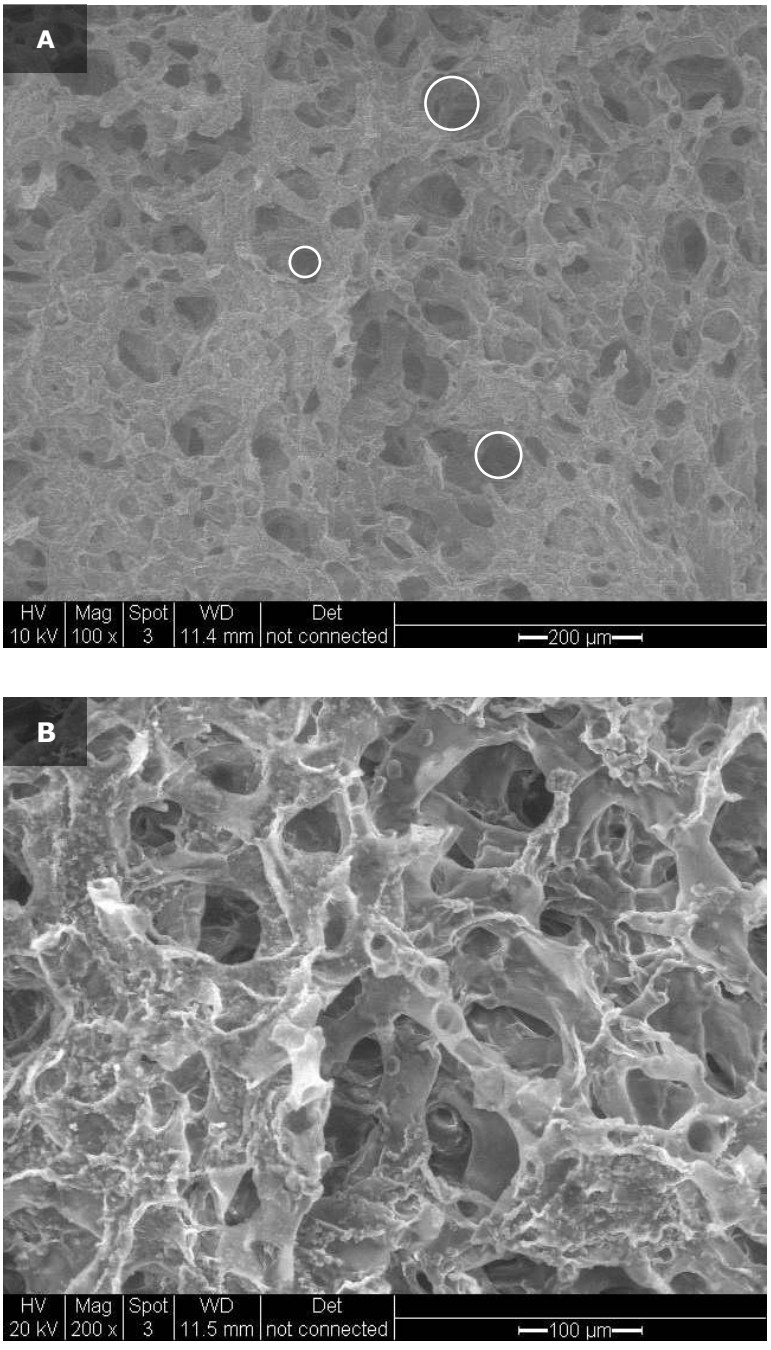

Fig. 4-11: SEM orange inner skin. (A) cellular foam-like structure (100x) and (B) more detailed (20 kV Beam) view of Cellular/Tubular structure (200x). Circles represent the pores' diameter readings (only 3 with different diameters are shown).

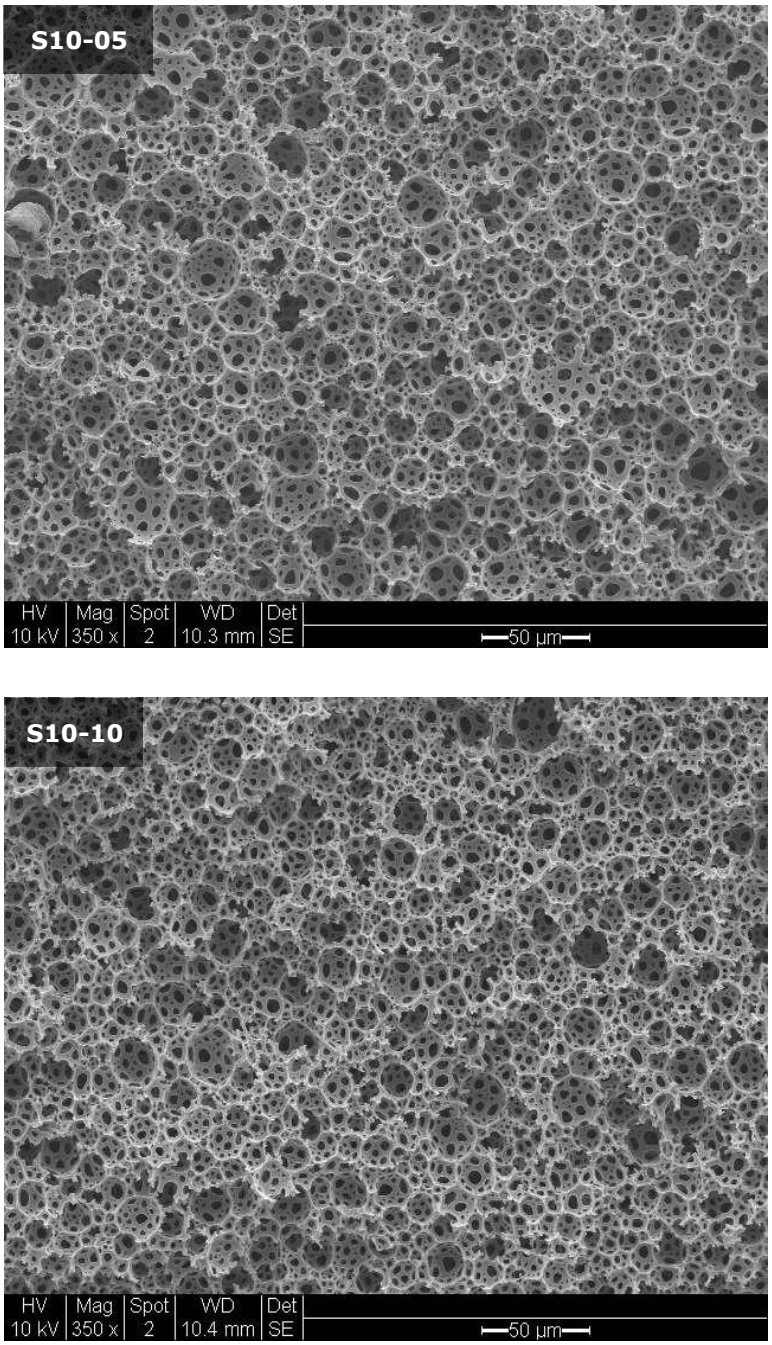

Fig. 4-12: EPHP Series S10. S10-05 and S10-10 SEM images (350x). Note the hierarchical porous structure with *interconnecting holes* inside each pore.

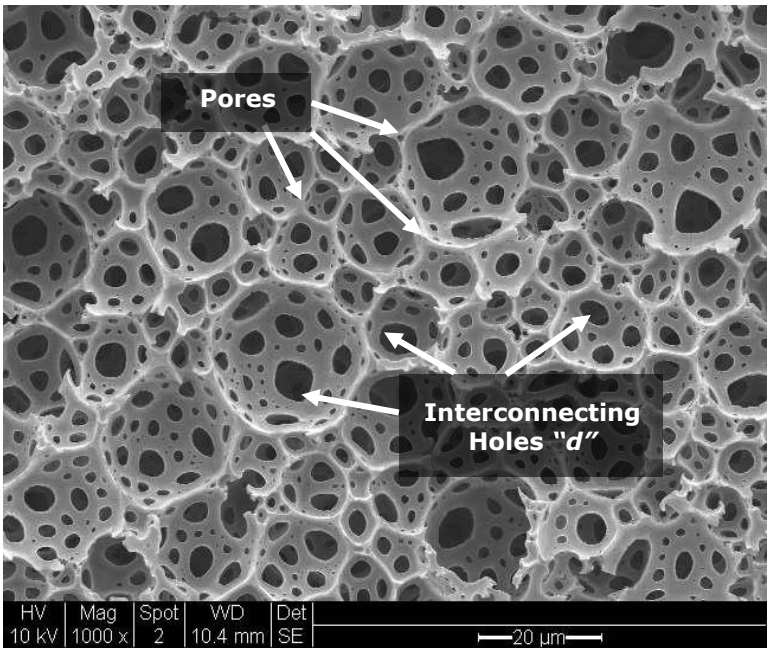

Fig. 4-13: SEM Image of EPHP S10-10 (350x). Detailed view of hierarchical pores and *interconnecting holes* (indicated by the arrows). Note the similarities with the orange inner skin as depicted in Fig. 4-12 (200x).

The pore size distribution of the orange inner skin was measured and 50 readings were recorded by using Fig. 4-11A. The average pore size *D* for the orange inner skin sample is 75.0 μm; the distribution histogram is shown in Fig. 4-14, while all the statistical data are summarised in Table 4-5.

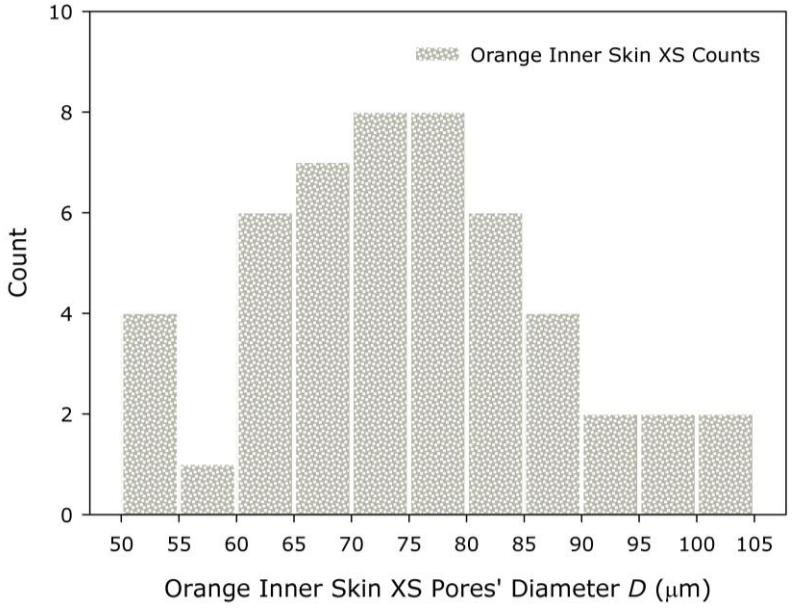

Fig. 4-14: Pores diameter size distribution of orange inner skin (total readings 50, diameter interval 5 μm).

Orange inner skin pores diameter distribution, shows that the interval spans between 50 and 105 μm, with the highest recurrence for pores whose diameter is

from 70 to 80 μm, followed by 65 to 70 μm intervals and, as third most recurring almost symmetrical intervals 60-65 and 80-85 μm.

Table 4-5: Orange inner skin pore size statistical data summary.

D - Parameter	Value (μm)
Average	75.0
Std. Deviation	12.7
Interval	53.8
Min	50.9
Max	104.7

This results section provided the structural and geometrical characterisation of the natural material layout that inspired the present study. The bio-mimicking of the structure, thus the hierarchical arrangement for the orange skin, was compared to the average pore size and distribution of low solid content EPHPs whose processing conditions (homogenisation time) were varied to better mimic the orange skin pore distribution.

4.1.3. Low solid content EPHPs (ε=90%) hierarchical structure

The hierarchical structure of the EPHPs with the lowest solid content (ε = 90%, equivalent to 10% solid content) is presented, analysed and compared to that of the orange skin by means of SEM imaging. As shown earlier (Fig. 4-12) the similarities in the structure between the two materials are many. Both are characterised by an open-pore structure with varying diameters.

All the EPHPs S10 series were characterised by the same dosing time t_D (5 mins) while the homogenisation time t_H was diversified per single batch by incremental intervals of 5 mins. EPHPs samples with total stirring time t = 10, 15 and 20 mins were referred as EPHP S10-05, S10-10 and S10-15 respectively. The S10 series manufacturing details are provided in Table 4-6.

Table 4-6: EPHPs S10 series dosing time t_D, homogenisation time t_H All samples prepared with 25ml oil phase and 225 ml water phase.

EPHP Series	Sub Series EPHP Sample	t_D (min)	t_H (min)	t (min)
S10	S10-05	5	5	10
	S10-10	5	10	15
	S10-15	5	15	20

EPHP S10-05 SEM images are shown in Fig. 4-15A at 350x magnification with a scale bar of 50 μm which revealed an open porous layout. Fig. 4-15B shows a

higher magnification (1000x) SEM picture. The scale bar of 20 μm further reveals the highly interconnected pores.

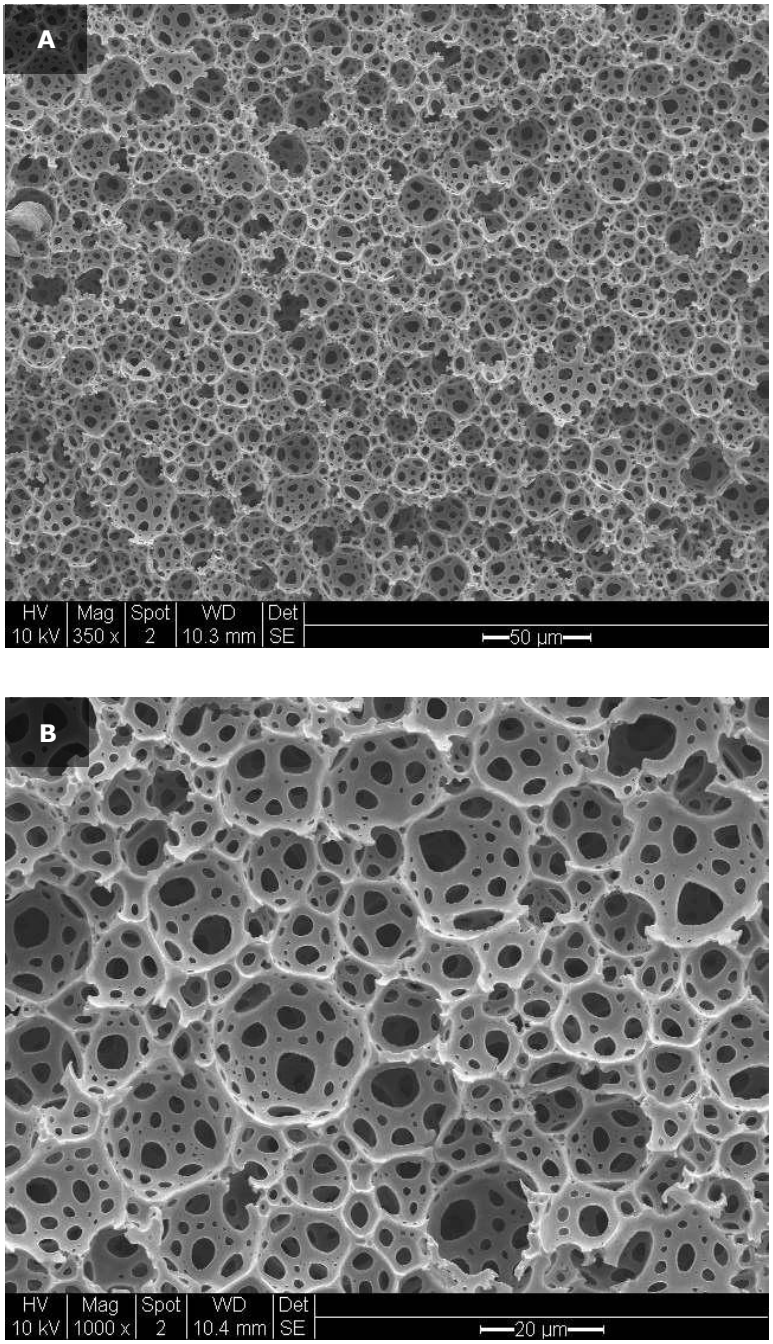

Fig. 4-15: EPHP S10-05, SEM images (A-350x) and (B-1000x).

As expected, the openness of the structure resulted from the oil and water emulsion polymerisation. During the polymerisation, in fact, the water acted as the emulsion template and, once polymerisation completed, the water was able to leave the system, leaving interconnected pores with hierarchical diameters in the solid polymer.

The evaluation of *D* was performed by measuring 50 pores on the 1000x (scale bar 20 μm) image. The data were then subject to statistical analysis and the pore size distribution was plotted.

EPHP S10-05 (*t*=10 mins) is characterised by a *D* of 13.1 μm; its distribution is shown in Fig. 4-16, while all the statistical data are summarised in Table 4-7.

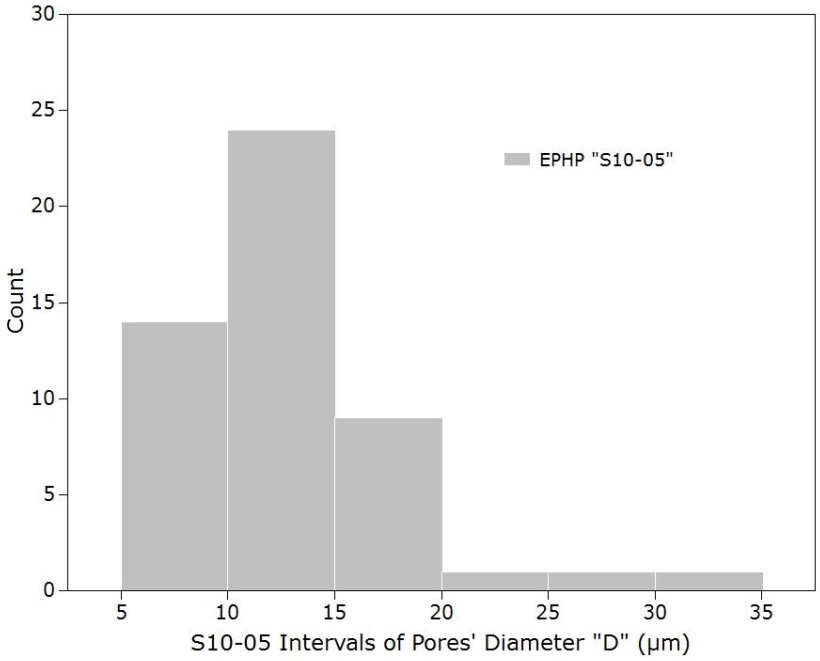

Fig. 4-16: Pores diameter size distribution of EPHP S10-05 (total readings 50, diameter interval 5 μm).

EPHP-S10-05 diameter distribution shows that the interval spans between 5 and 35 μm, with the highest recurrence for pores whose diameter is from 10 to 15 μm, followed by those with 5 to 10 μm and 15 to 20 μm interval. The diameter distribution is not symmetrical but it is located more towards the left of the average interval. The hierarchy of pores' diameter can be seen mainly in the 5 to 20 μm interval with limited occurrences above 20 μm.

Table 4-7: EPHP S10-05, pore size statistical data summary.

S10-05 "*D*"	**Value (μm)**
Average	13.1
Std. Deviation	5.4
Interval	27.8
Min	6.0
Max	33.8

The effects of an increase in total stirring time on *D* are shown for EPHP-S10-10 samples. For such samples, the homogenisation time was increased from 5 to 10

minutes. The SEM images of S10-10 samples (Fig. 4-17A-B) show again an open porous layout.

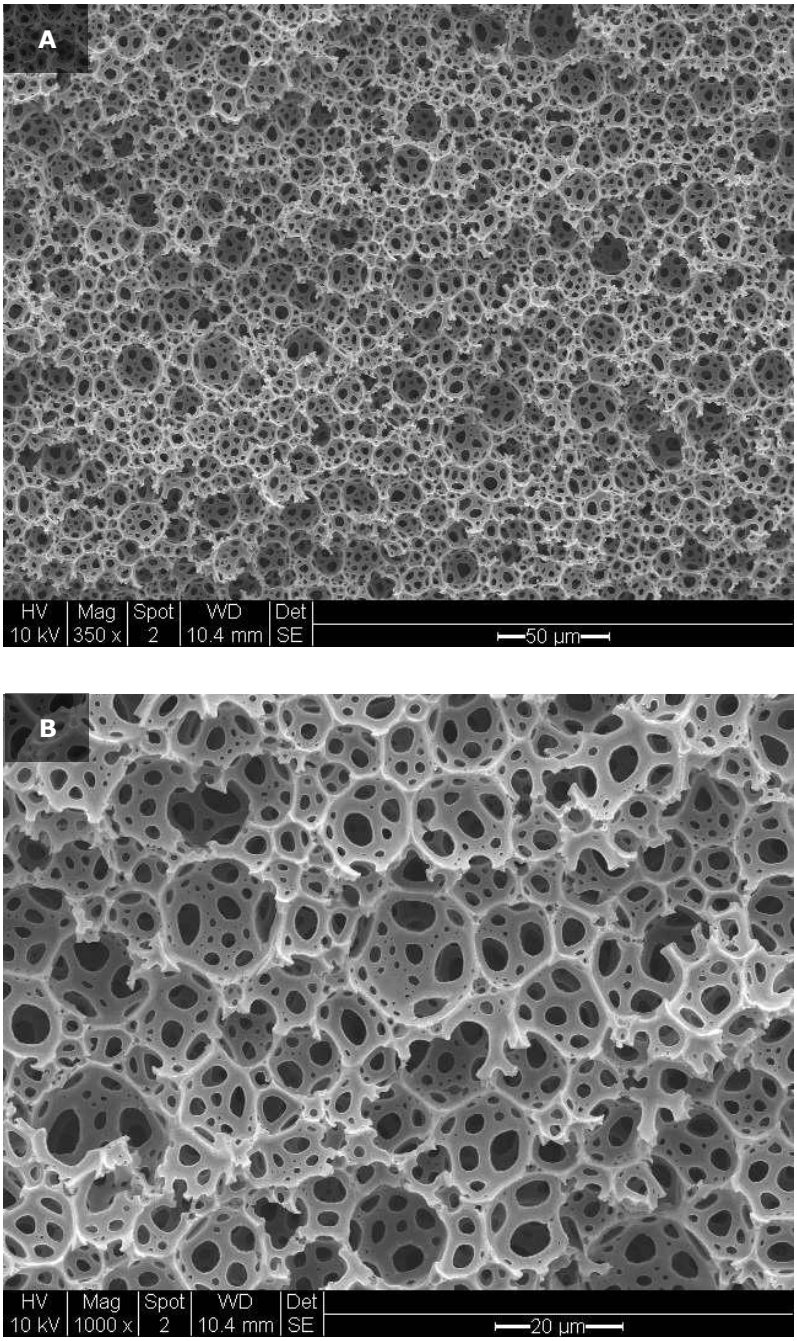

Fig. 4-17: EPHP S10-10, SEM images (A-350x) and (B-1000x).

The evaluation of *D* was performed by measuring 50 pores on the 1000x (scale bar 20 μm) image. The data were then subject to statistical analysis and the pore size distribution was plotted.

EPHP S10-10 (*t*=15 mins) is characterised by a *D* of 11.2 μm; its distribution is shown in Fig. 4-18, while all the statistical data are summarised in Table 4-8.

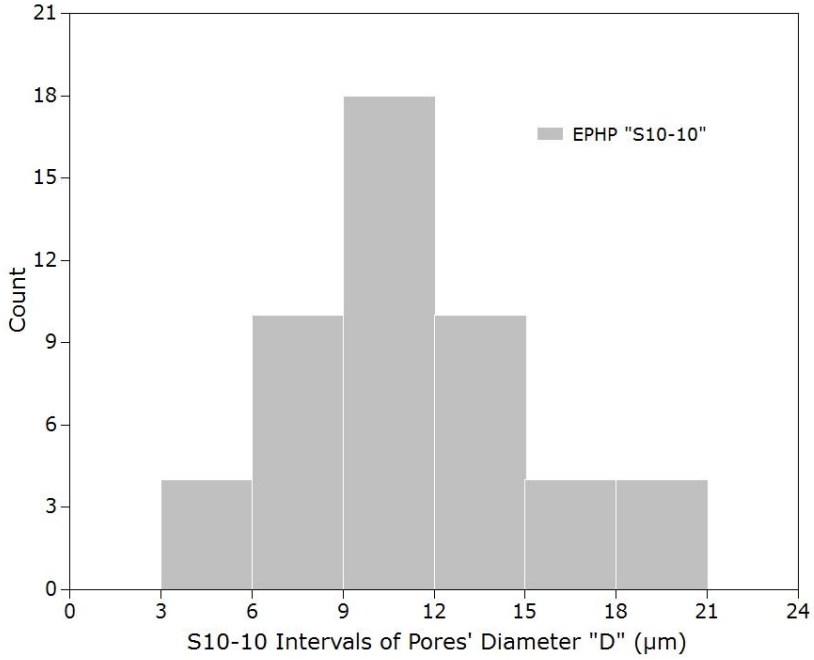

Fig. 4-18: Pores diameter size distribution of EPHP S10-10 (total readings 50, diameter interval 3 μm).

EPHP S10-10 diameter distribution shows that the interval spans between 3 and 21 μm, with the highest recurrence for pores whose diameter is from 9 to 12 μm followed, symmetrically, by those from 6 to 9 μm interval on the left of the central value and from 12 to 15 on the right side. A higher degree of hierarchy of the pores' diameter can be seen with respect to EPHP-S10-05; in fact, a more uniform occurrence of intervals from initial to final ranges was recorded.

Table 4-8: EPHP S10-10, pore size statistical data summary.

S10-10 "*D*"	**Value (μm)**
Average	11.2
Std. Deviation	3.8
Interval	15.0
Min	4.6
Max	19.7

EPHP S10-15 is the last sample of the EPHP S10 series with the highest total stirring time (t=20 min). It completes the investigation for the lowest water phase volume EPHPs. Its SEM images are shown in Fig. 4-19 and they reveal an open porous layout as expected.

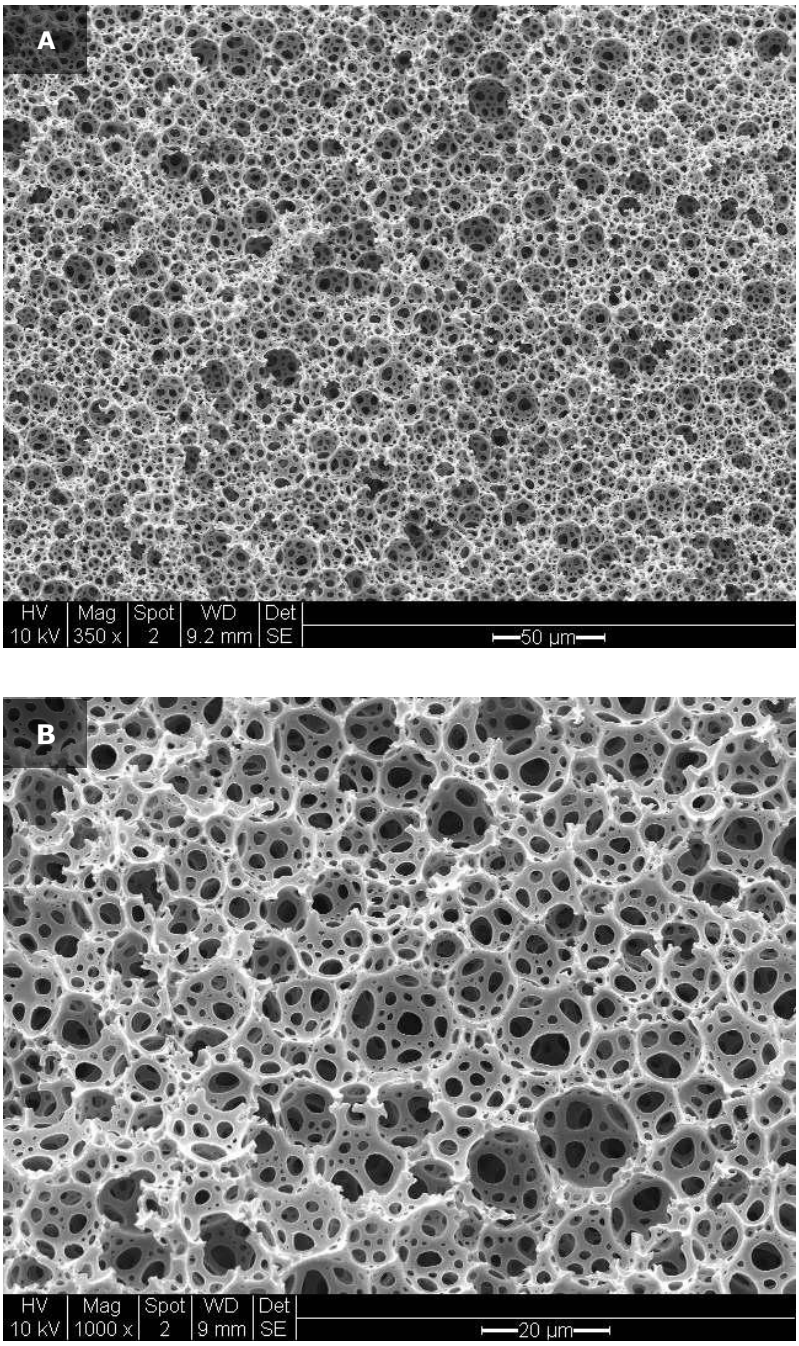

Fig. 4-19: EPHP S10-15, SEM images (A-350x) and (B-1000x).

EPHP S10-15 (t=20 mins) was characterised by a D of 9.8 μm; its distribution is shown in Fig. 4-20, while all the statistical data are summarised in Table 4-9.

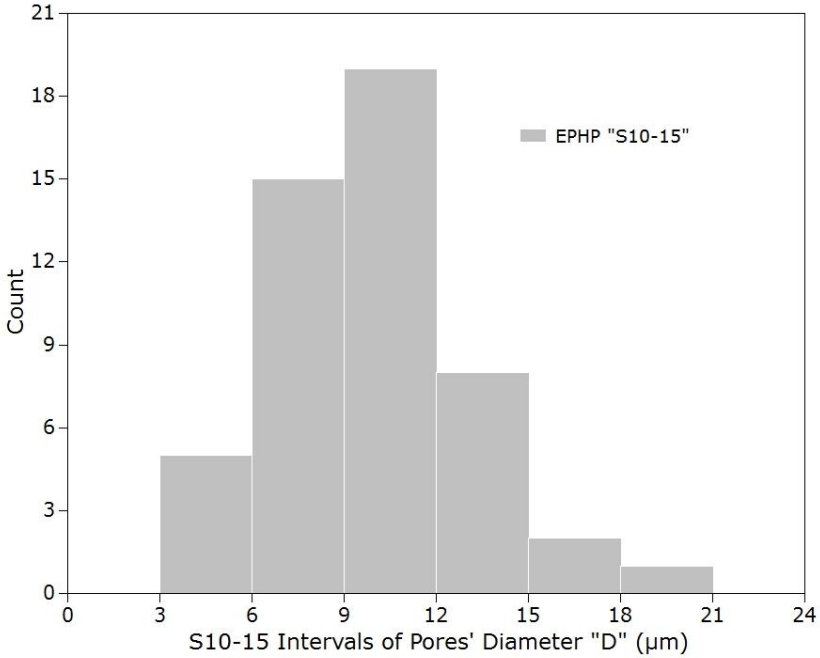

Fig. 4-20: Pores Diameter size distribution of EPHP S10-15 (total readings 50, diameter interval 3 μm).

EPHP S10-15 was characterised by a less symmetrical pore diameter's distribution with respect to sample EPHP-B; it is, however more evident that the frequency of smaller diameters increased. Moreover, the histogram shows that the interval spans between 3 and 21 μm, with the highest recurrence for pores with a diameter between 9 and 12 μm. These are followed, in recurrence, by those from 6 to 9 μm interval on the left of the central value and those from 12 to 15 mm on the right. The average pore diameter is the smallest of the S10 series due to the longest stirring time.

Table 4-9: EPHP S10-15. Pore size statistical data summary.

S10-15 "*D*"	**Value (μm)**
Average	9.8
Std. Deviation	3.1
Interval	14.0
Min	4.6
Max	18.5

The EPHP S10 Series average pore size diameter *D* is plotted in Fig. 4-21 with Standard Deviation (SD) error bars. The distinctive feature in the EPHP S10 series is the increasing homogenisation time t_H with constant solid content (ε=90%) and dosing time (t_D=5 min).

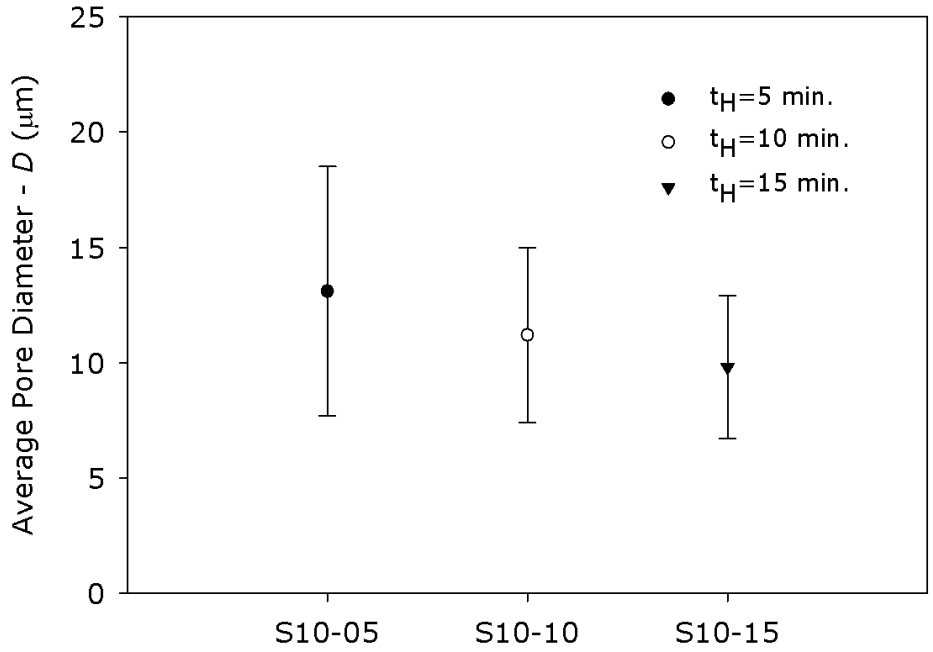

Fig. 4-21: Average pore size *D* of EPHP S10 series with standard deviation error bars. All samples with water phase volume ε=90% and dosing time t_D=5 min.

By considering the EPHP S10 series average pore size diameter *D* (Fig. 4-21), as well as the diameters' distribution, it can be seen that an increase of t_H led to 1) a reduction of the average diameter of the pores and 2) an increase of the hierarchical layout. The first condition is clearly recognised: a smaller D is obtained when moving from S10-05 to S10-15. The second is reflected by an increase of occurrences of diameter intervals, although the overall extent of diameter intervals is reduced. This behaviour is better depicted when considering the SD error bars. The bars become narrower with increasing stirring time.

It can also be observed that the lowest measured diameters are quite close one another. These low values may represent the minimum attainable droplets diameters according to the mixing energy input. The results obtained, in particular their trends and the order of magnitude are in line with those produced by Akay *et al.* (2005a) although rigid PHPs were examined.

The average pore size *D* results for the EPHP S10 series and those for the orange skin are presented together in Fig. 4-22. Furthermore, details of EPHP S10 series manufacturing process characteristics are summarised in Table 4-10.

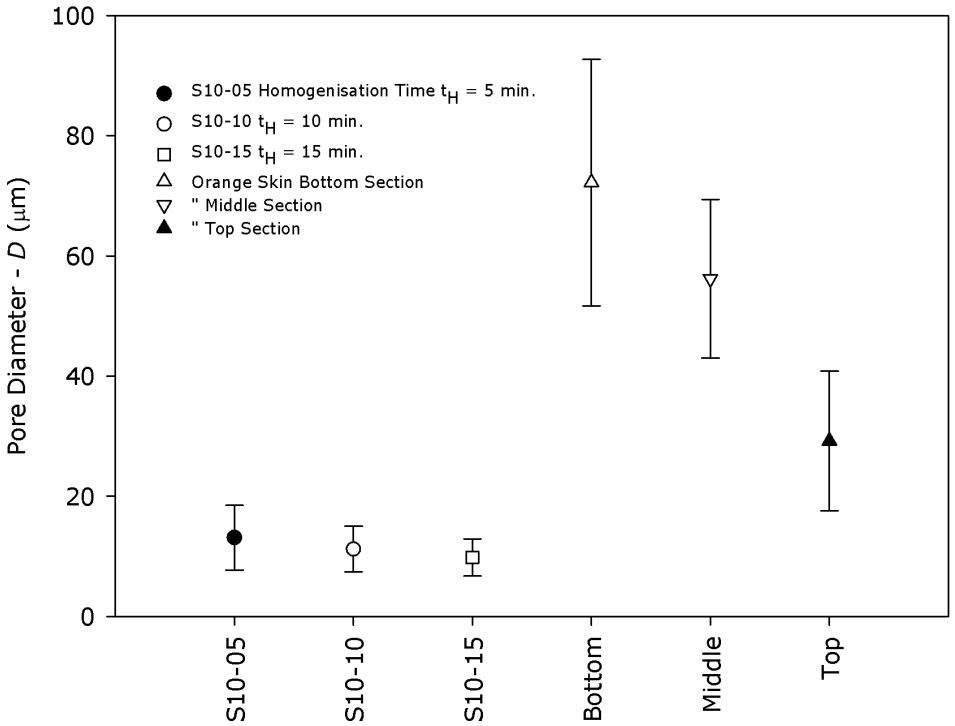

Fig. 4-22: Comparison between EPHP S10 series and orange outer skin average pore diameter *D*.

The comparison of the average pore diameter supports the expected similarities between the orange skin and the EPHPs. It is clearly seen that the orange skin is characterised by a higher average diameter which, in turn decreases rapidly as it moves from the bottom to the top of the cross section. In addition to that, the orange outer skin is a continuous media (a single material) which is capable of reducing its average diameter to nearly 2.5 times (from bottom to the top) in a thickness as little as 1.5-2.5 mm.

With reference to the EPHP S10 series with the lowest solid content (ε=90%), the results confirm that the variation of the average pore diameter is dictated by the homogenisation time, which accounts for the mechanical energy provided, thus reduces the emulsion droplets size.

Table 4-10: Average pore diameter *D* of EPHP S10 Series and orange outer skin sections (bottom, middle and top). Homogenisation time t_H and total mixing time *t* for EPHP S10 Series, with dosing time t_D 5 min.

Sample	Average Pore Size *D* (μm)	Homogenisation Time t_H (min)	Total Mixing Time *t* (min)
EPHP S10-05	13.1	5	10
EPHP S10-10	11.2	10	15
EPHP S10-15	9.8	15	20
Orange Skin XS - Bottom	72.2	-	-
Middle	56.2	-	-
Top	29.2	-	-

4.2. Effects of processing time on EPHPs porous structure

In the previous section, the effects of increasing the total stirring time have been introduced and analysed for the lowest solid content EPHPs. It was determined, as expected, that a longer stirring time resulted in smaller average pore size and narrower range of diameter distribution. These mixing vs. structure changes are in fact directly related to the total mixing time because it also represents the amount of mechanical energy that is theoretically input into the system.

In this section, the effects of the mechanical energy input (MEI) on the structural layout of the entire EPHPs series, from S10 to S40(IN) and sub-series (given series with increasing mixing time *t*), are presented and discussed to assess the Process-Structure relationship. The macroscopic structural parameters are again the average pore diameter and its distribution. In addition to that, the wall thickness t_W as well as the intersecting vertex thickness T_v for each EPHPs sub-series are presented and detailed in the next sections.

The dosing and homogenisation processing times for the entire EPHPs series are summarised in Table 4-11.

Table 4-11: Complete EPHPs series dosing time t_D, homogenisation time t_H and total mixing time *t*. (IN) indicates the use of oil phase initiator.

EPHP Series	Water phase ratio - ε (%)	Sub Series EPHP Sample	t_D (min)	t_H (min)	t (min)
S10	90	S10-05	5	5	10
		S10-10	5	10	15
		S10-15	5	15	20
S20	80	S20-15	5	5	10
		S20-20	5	10	15
S30	70	S30-15	5	15	20
		S30-20	5	20	25
		S30-25	5	25	30
S40(IN)	60	S40-15	10	15	25
		S40-20	10	20	30
		S40-25	10	25	35

The data, as introduced in the methodology section, show that with the exception of the S40(IN) series the dosing time was 5 minutes while the homogenisation time was initially set at 15 minutes and later increased to 20 and 25 minutes.

The importance of accounting for the total mixing time becomes evident when it is appropriately converted into the amount of energy per unit volume that the system is theoretically capable of producing. Although this amount of energy is ideally available for the formation of the emulsion and its droplets diameter reduction as mixing proceeds, only a fraction of it is actively involved in this process. Many frictional losses are in fact expected, particularly from the viscous nature of the HIPE itself.

The theoretical MEI is plotted for all the EPHPs in Fig. 4-23 and it can be clearly seen that the energy increases proportionally to the amount of time each sample was stirred for.

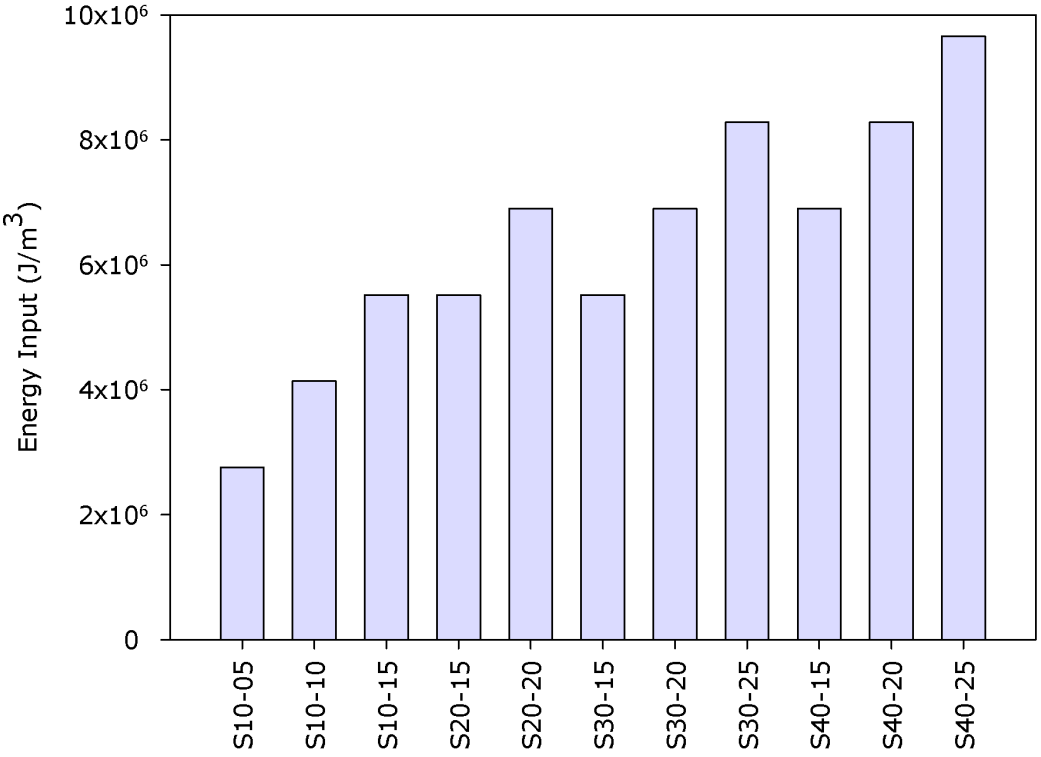

Fig. 4-23: Energy per volume input (J/m^3) due to mechanical stirring of the various EPHPs.

It is worth noting that for the S40(IN) series, the amount of energy is higher due to the fact that the dosing time was increased from 5 to 10 minutes. This change, as already anticipated in the methodology, was introduced to enable a lower amount of water phase to be properly emulsified with a correspondingly higher amount of oil phase.

In order to evaluate the effectiveness of the MEI at reducing the average pore diameter of the HIPEs with various amounts of solid content, the structure of the entire EPHPs series has been analysed. As with reference to the low solid content EPHP S10 series, the results in terms of average pore size diameter and distribution for all the other EPHPs have been obtained by SEM imaging.

The EPHP S20 series is characterised by twice as much the solid content of S10 series and its manufacturing comprised samples S20-15 and S20-20 (Table 4-11). The SEM images are shown in Fig. 4-24 and Fig. 4-25 for S20-15 and S20-20 respectively, while their pore diameter distribution is shown in Fig. 4-26. Each sample distribution statistical analysis is reported in Table 4-12.

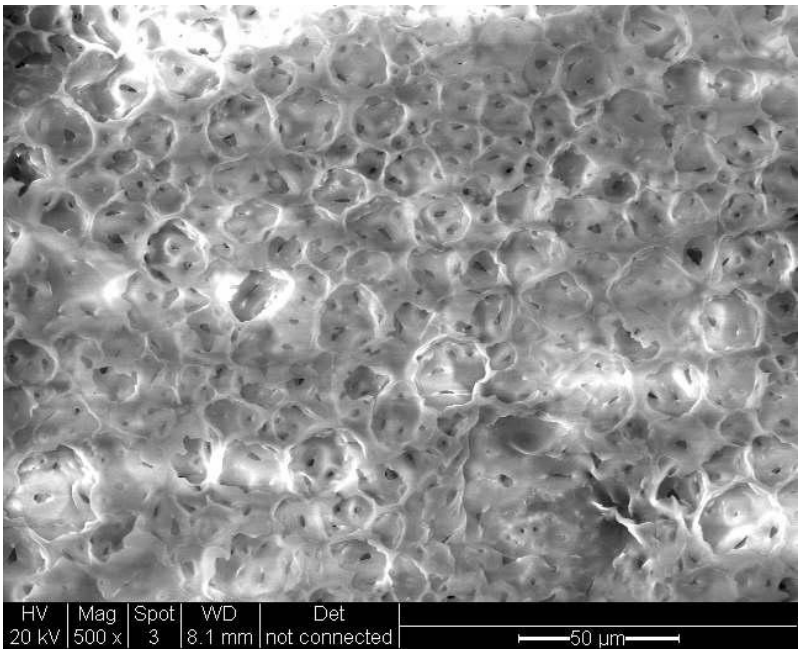

Fig. 4-24: EPHP S20-15 SEM image, 500x magnification, scale bar 50 µm. The white areas are the result of early signs of electric charging of the sample due to exposure to SEM electron beam.

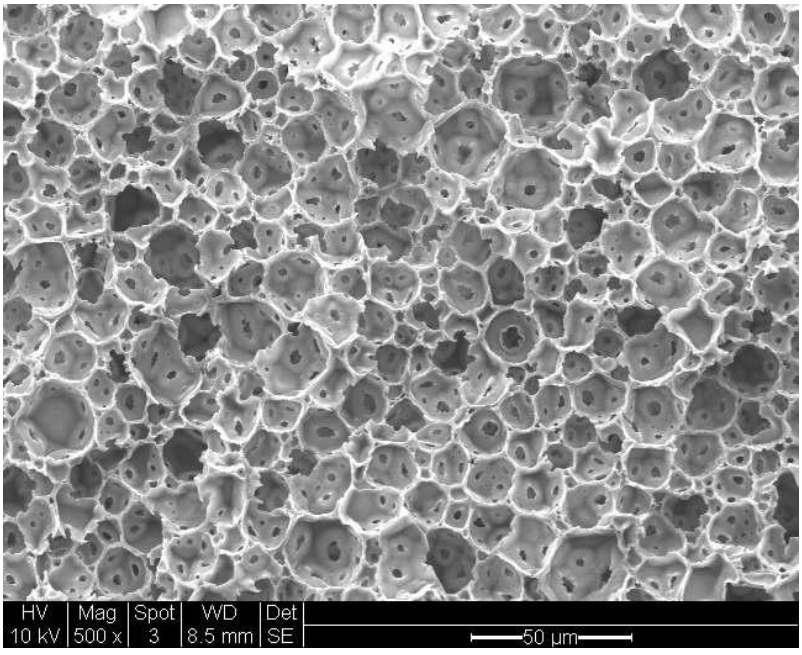

Fig. 4-25: EPHP S20-20 SEM image, 500x magnification, scale bar 50 µm.

The SEM investigation revealed that the structures were both recognised as open pores with interconnecting holes, however, it can be seen that the interconnecting holes within a pore are much less that those observed for the S10 series.

The average pore diameters *D* for S20-15 and S20-20 are 16.1 and 11.3 μm respectively. The pore size distribution further confirms the narrowing of the overall pore size intervals and an increased symmetry with respect to the central interval values. The details from the statistical analysis are reported in Table 4-12.

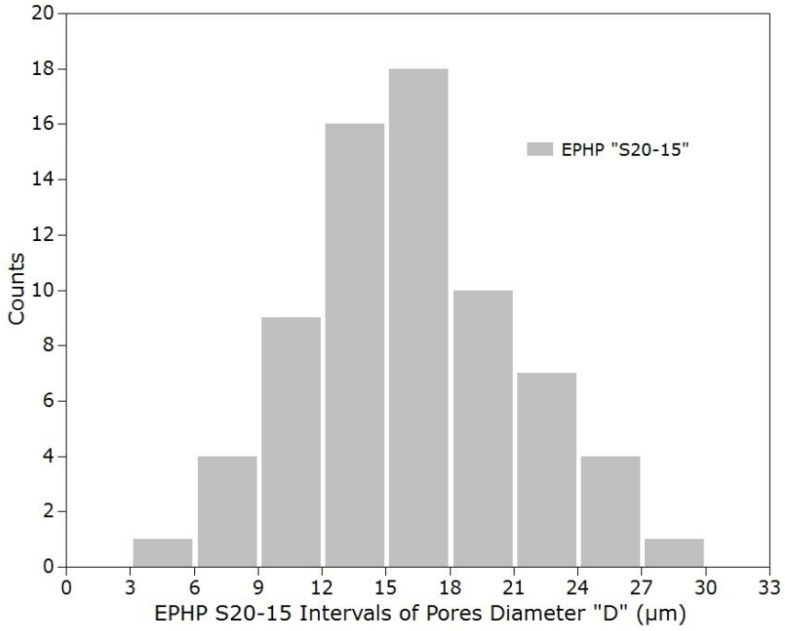

Fig. 4-26: Pores diameter size distribution of EPHP S20-15 (total readings 70, diameter interval 3 μm, Average pore diameter *D*=16.1 μm).

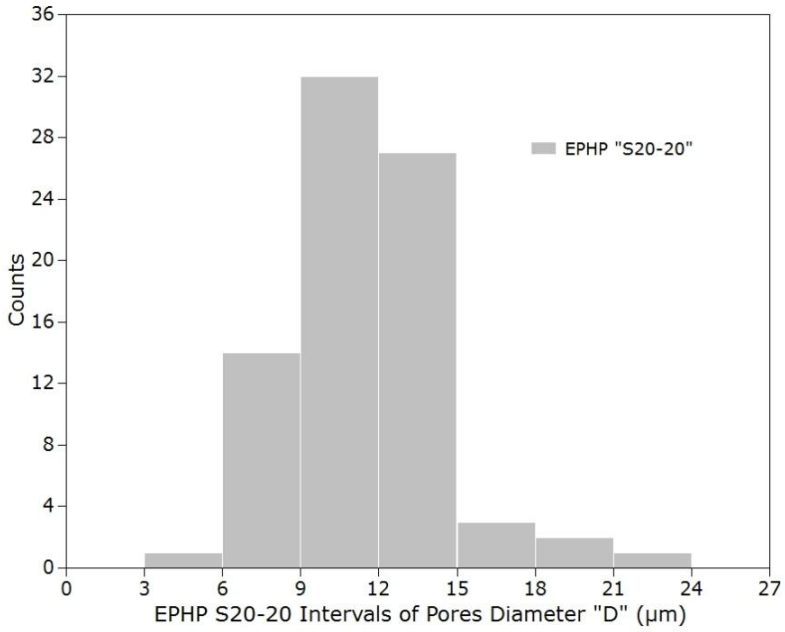

Fig. 4-27: Pores diameter size distribution of EPHP S20-20 (total readings 80, diameter interval 3 μm, Average pore diameter *D*=11.3 μm).

The most notable result due to an increase of *t* is that the average pore size of sample S20-20 is nearly 30% smaller than that of S20-15. Its largest measured value reduction (from 30 to 24 μm) is also in line with the *D* reduction, showing that a higher MEI is more effective at reducing the largest droplets diameter.

Table 4-12: EPHP S20 series pore size statistical data summary. Total mixing time *t* for S20-15 and S20-20 is 20 and 25 minutes respectively.

***D* – Parameters**	**Units**	**S20-15**	**S20-20**
Average	μm	16.1	11.3
Std. Deviation	"	5.0	2.8
Interval	"	23.9	15.4
Min	"	5.3	5.9
Max	"	29.2	21.4
Number of Readings	-	70	80

The EPHP S30 and S40(IN) series are characterised by three and four times as much the solid content of the initial S10 series respectively. Both high solid content EPHPs series samples were manufactured according to the specifications given in Table 4-11, hence three sub-series samples were manufactured. These three sub-series samples are S30-15, S30-20, S30-25 and S40-15, S40-20, S40-25. The average pore diameters for S30 and S40(IN) EPHPs series have been determined by using SEM images. The SEM images for EPHP S30 series are shown in Fig. 4-28 - Fig. 4-30, together with the pore size distribution (Fig. 4-31 - Fig. 4-33) and the statistical analysis of the data (Table 4-13).

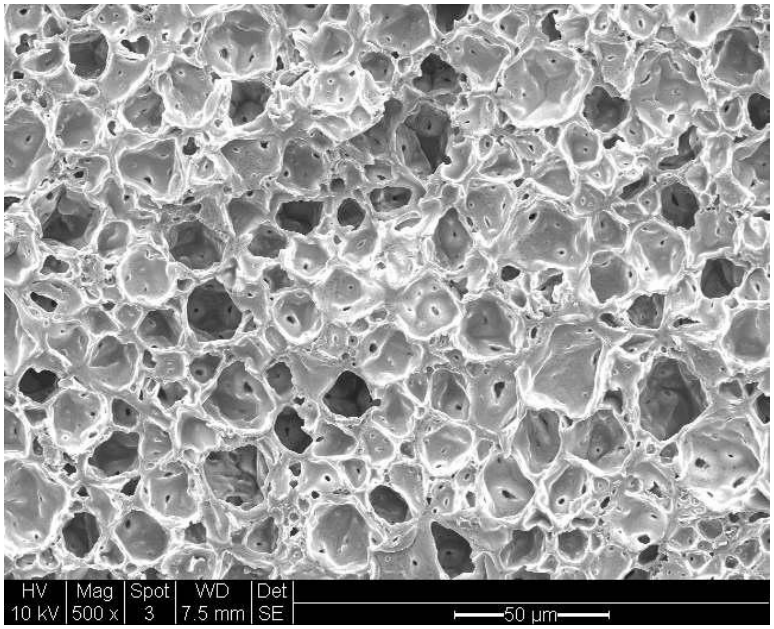

Fig. 4-28: EPHP S30-15 SEM images, 500x magnification, Scale bar 50 μm.

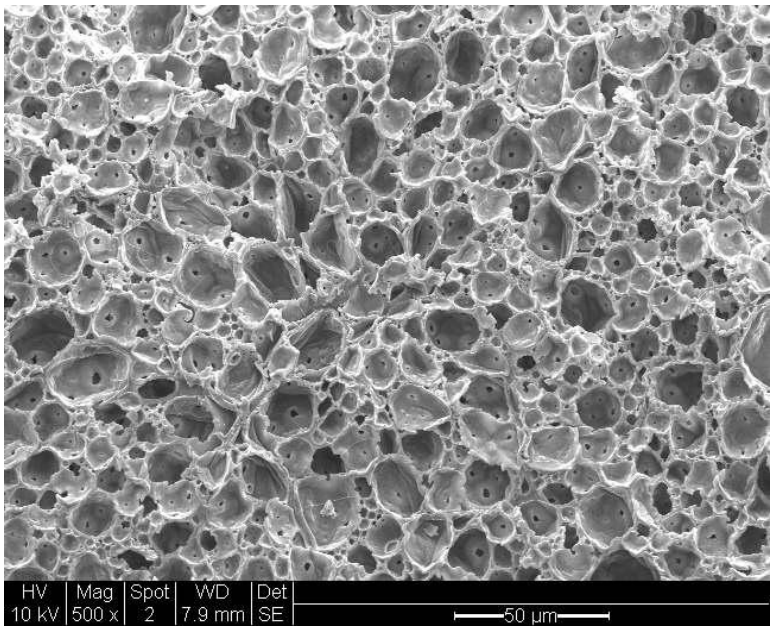

Fig. 4-29: EPHP S30-20 SEM images, 500x magnification, Scale bar 50 µm.

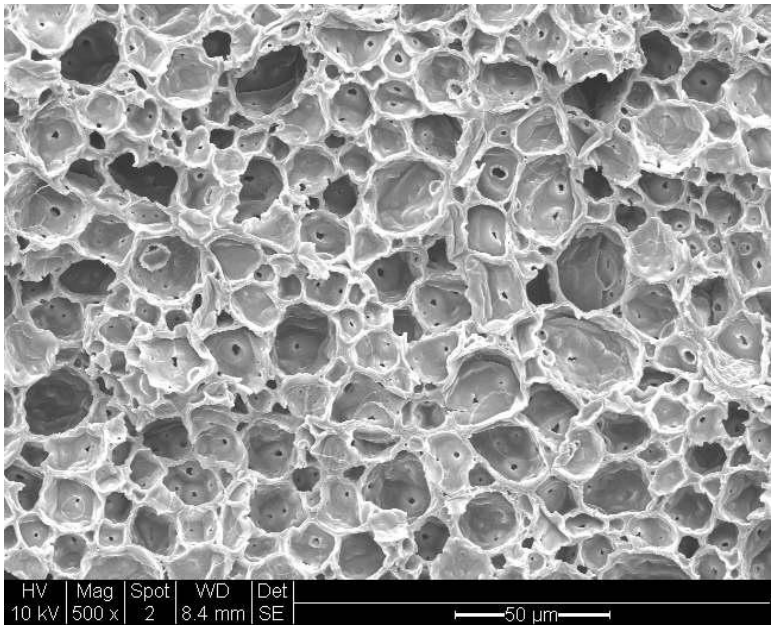

Fig. 4-30: EPHP S30-25 Series SEM images, 500x magnification, Scale bar 50 µm.

The SEM investigation reveals that the structure of the S30 series is still recognised as open pores with few interconnecting holes. The average pore diameters and their distribution plots (shown in Fig. 4-31 to Fig. 4-33) confirm the narrowing of the overall pore size intervals for samples S30-15 and S30-20 but a reverse of trend was observed for S30-25 sample instead.

The details of statistical analysis of data for the complete EPHP S30 series are shown in Table 4-13.

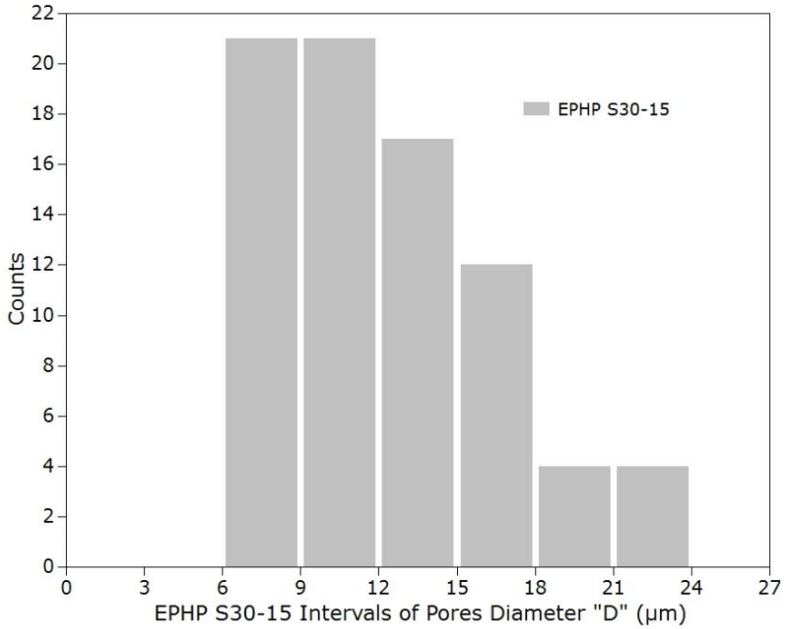

Fig. 4-31: Pores diameter distribution of EPHP S30-15 (total readings 80, diameter interval 3 μm, Average pore diameter *D*=12.1 μm).

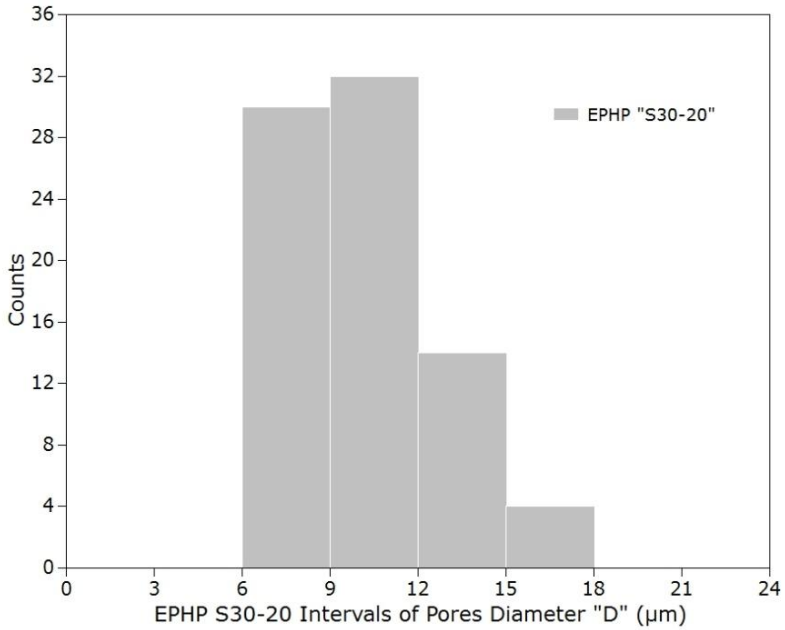

Fig. 4-32: Pores diameter distribution of EPHP S30-20 (total readings 80, diameter interval 3 μm, Average pore diameter *D*=10.1 μm).

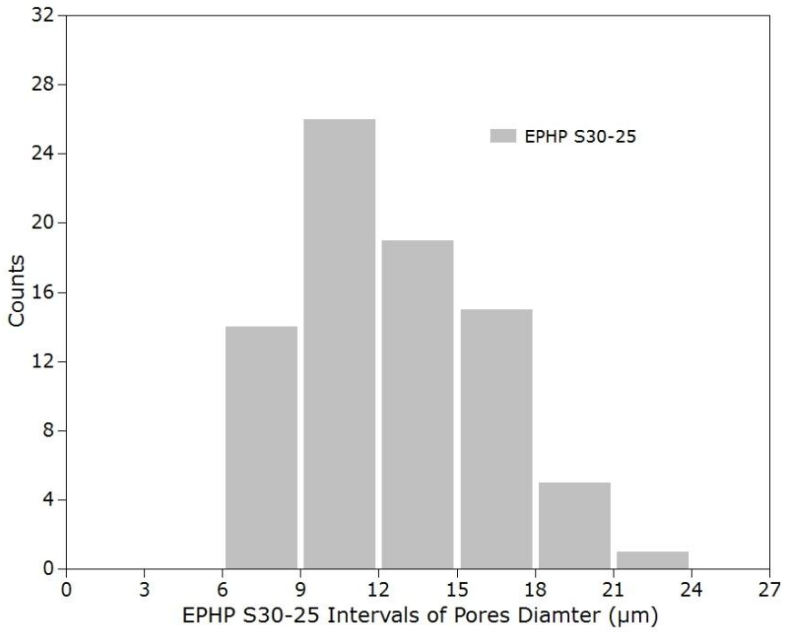

Fig. 4-33: Pores diameter distribution of EPHP S30-25 (total readings 80, diameter interval 3 μm, Average pore diameter *D*=12.4 μm).

Sample S30-15 interval ranged between 3 and 21 μm and that of S30-20 from 6 to 18 μm only; both showed that occurrence (i.e. number of counts) for the central interval values increased. However, the inversion of the decreasing of *D* with increased homogenisation time was observed for sample S30-25. Its average diameter is in fact, higher than that of S30-15 which is the sample with the lowest mixing time of the series. Moreover, sample S30-25 has a diameter interval which is almost the same as that of S30-15, as well as similar minimum and maximum values.

These results, both in terms of *D* and variation in distribution, may indicate that initial phenomena of pore coalescence (i.e. smaller pores collapse and form larger pores) occurred indicating a limit in the stability of the surfactant film that separates the water and oil droplets in the emulsion.

Table 4-13: EPHP S30 series pore size statistical data summary. Total mixing time *t* is 20, 25 and 30 minutes respectively.

D – Parameters	Units	S30-15	S30-20	S30-25
Average	μm	12.1	10.1	12.4
Std. Deviation	"	4.0	2.5	3.5
Interval	"	15.6	9.6	15.2
Min	"	6.0	6.2	6.7
Max	"	21.6	15.8	21.8
Number of Readings	-	80	80	80

The SEM images for EPHP S40(IN) series are shown in Fig. 4-34 - Fig. 4-36, together with the pore size distribution (Fig. 4-38 - Fig. 4-40) and the statistical analysis of the data (Table 4-14).

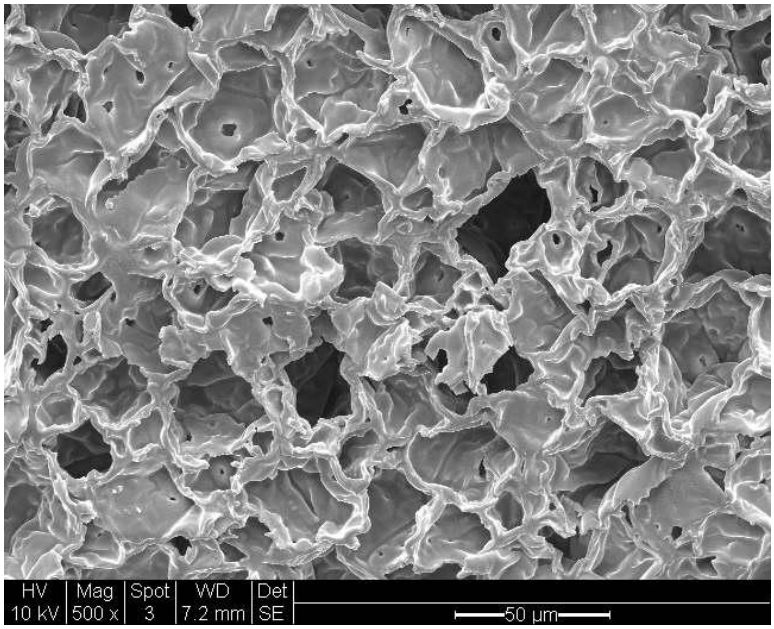

Fig. 4-34: EPHP S40-15 SEM images, 500x magnification, Scale bar 50 µm.

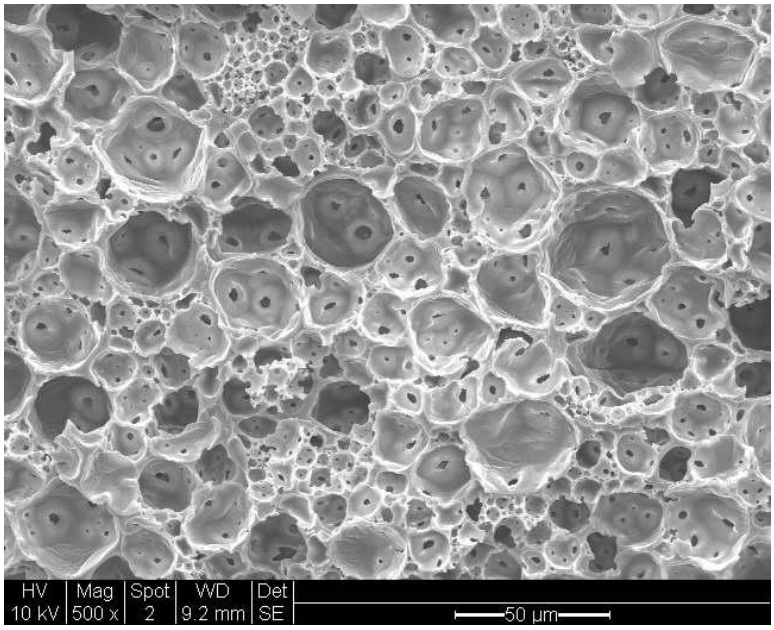

Fig. 4-35: EPHP S40-20 SEM images, 500x magnification, Scale bar 50 µm.

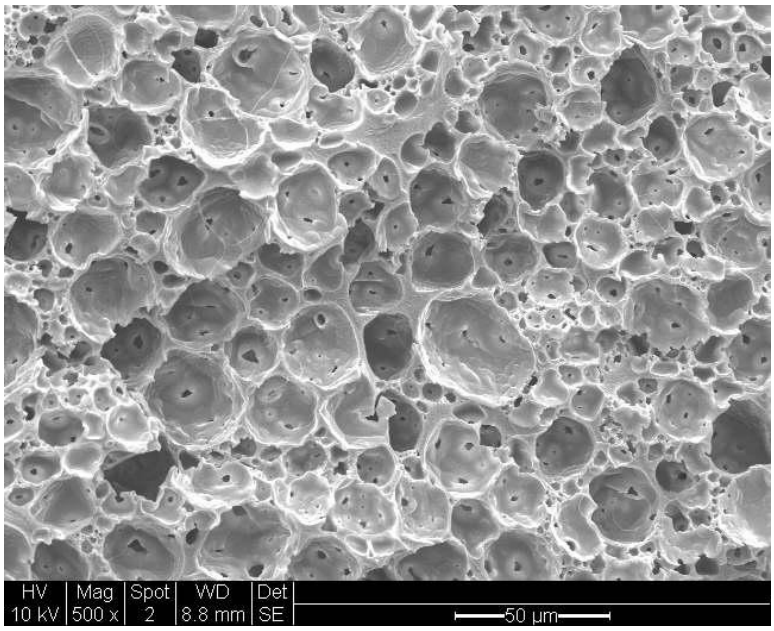

Fig. 4-36: EPHP S40-25 SEM images, 500x magnification, Scale bar 50 µm. All samples coated with gold for optimal image definition. Open Pores with interconnecting holes structure. The pore walls of S40-15 are distinctively thick.

The SEM investigation of EPHP S40(IN) series reveals that the structure is still recognised as open pores with few interconnecting holes, similarly to what has previously observed for S30 series. The S40(IN) series is the only one that includes the additional oil phase initiator, and it appears that it contribution has been valuable.

The HIPEs with ε=40% S40-15, formulated without oil phase initiator, lauroylperoxide - LPO, were relatively stable but their polymerisation was not satisfactory. In fact, as already presented in the methodology section, the EPHPs without LPO were characterised by an appreciable amount of non-polymerised oil phase excess. An example of such an occurrence for moulding it in the cylindrical cones and rectangular mould is shown in Fig. 4-37.

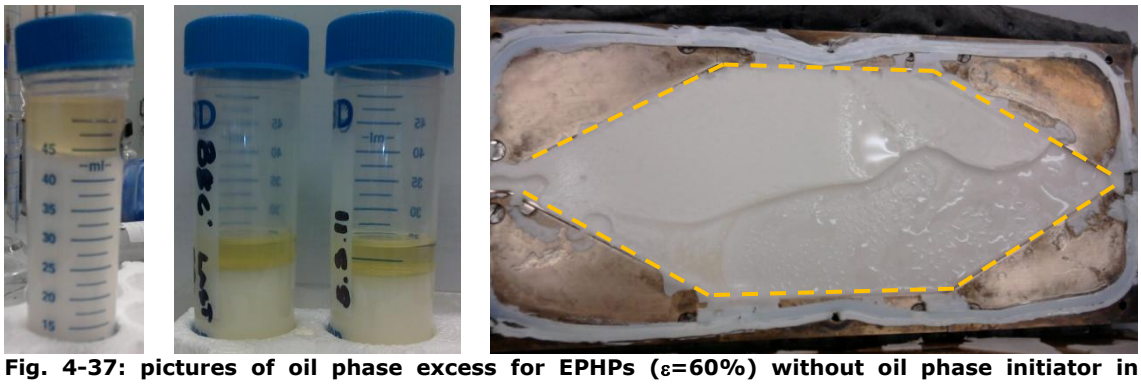

Fig. 4-37: pictures of oil phase excess for EPHPs (ε=60%) without oil phase initiator in cylindrical cones mould (left) and partial polymerisation in the rectangular mould (right) Original shape of mould is enhanced by the dashed lines.

With reference to the EPHP S40(IN) series with LPO, the average pore diameters and their distribution plots (shown in Fig. 4-31 to Fig. 4-33) confirm the narrowing

of the overall pore size intervals for all the samples. The details of statistical analysis of data for the complete EPHP S40(IN) series are shown in Table 4-14.

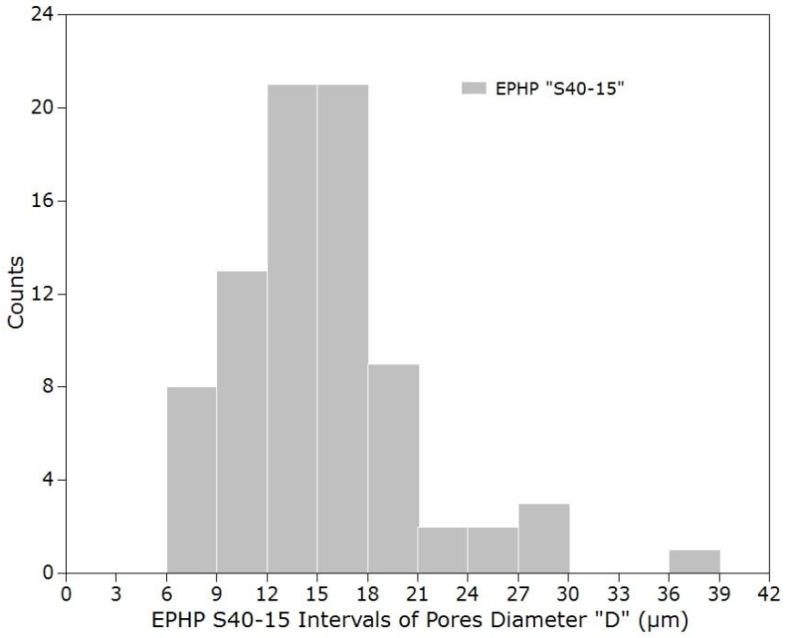

Fig. 4-38: Pores diameter distribution of EPHP S40-15 (total readings 80, diameter interval 3 µm, Average pore diameter *D*=15.2 µm).

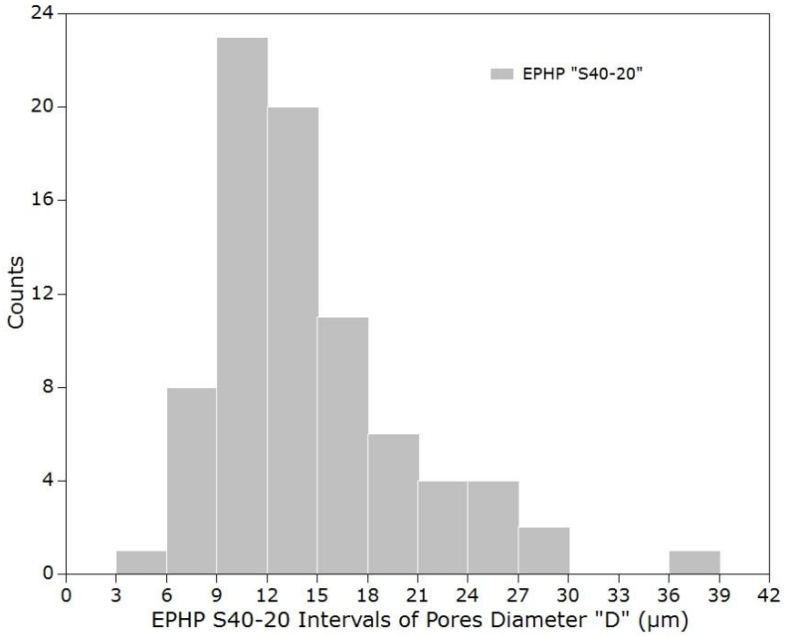

Fig. 4-39: Pores diameter distribution of EPHP S40-20 (total readings 80, diameter interval 3 µm, Average pore diameter *D*=14.5 µm).

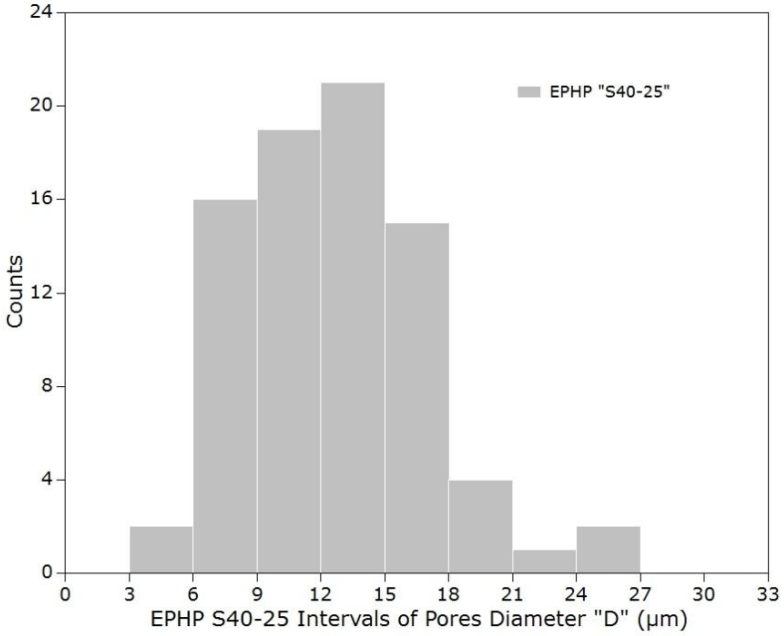

Fig. 4-40: Pores diameter distribution of EPHP S40-25 (total readings 80, diameter interval 3 μm, Average pore diameter *D*=12.7 μm).

The most notable results following an increase of mixing time on the S40(IN) series is that the average pore size *D* of each sample decreased steadily. The largest *D* is that of S40-15 (15.2 μm), followed by S40-20 and S40-25, with 14.5 and 12.7 μm respectively. Their diameter distribution also follows the expected trend; with S40-15 and S40-20 sharing a very similar interval, its average value shifted toward a lower value for the latter sample. The longest mixed sample, S40-25 indeed is characterised by the smallest *D*. Furthermore, it distribution is narrower and satisfactorily symmetrical.

Table 4-14: EPHP S40(IN) Series pore size statistical data summary. Total mixing time *t* is 25, 30 and 35 minutes respectively.

***D* – Parameters**	**Units**	**S40-15**	**S40-20**	**S40-25**
Average	μm	15.2	14.5	12.7
Std. Deviation	"	5.4	5.8	4.1
Interval	"	28.9	30.9	20.2
Min	"	6.3	5.5	5.7
Max	"	36.2	36.4	25.9
Number of Readings	-	80	80	80

The analysis and determination of the average pore diameter for the entire EPHPs series enables to account for the effects the mechanical energy input, which is proportional to mixing time, has on producing emulsion with smaller pores and narrower distribution.

The MEI and the average pore diameter for the entire EPHPs series are plotted together with in Fig. 4-41.

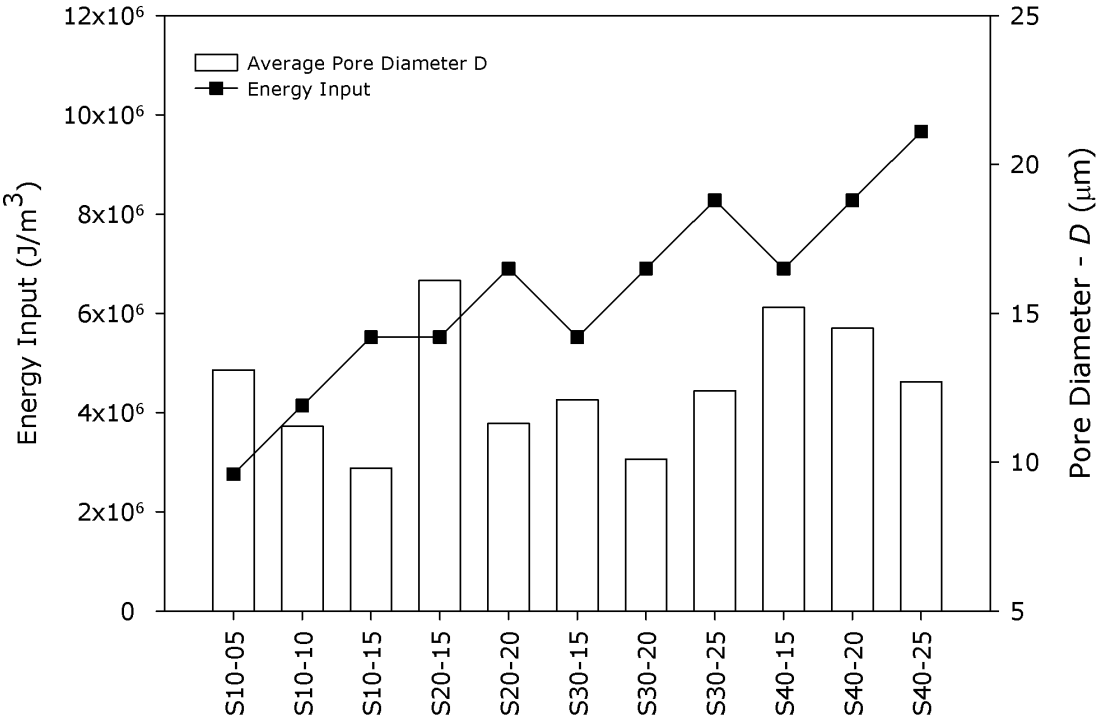

Fig. 4-41: pore size as a function of mechanical energy input for all EPHPs series.

It can be seen that the effect of providing a higher MEI is that of reducing the average pore size. Each individual series, with the exception of S30-25 clearly shows a proportional decrease of *D* with increasing MEI.

However, another valuable piece of information can be obtained by looking at the graph when each EPHPs series is considered as an averaged result. Moving from lower (S10) to higher solid contents (S20 up to S30 series), appears to result in a relatively constant average pore diameter despite a higher MEI.

On the other hand this result confirms the importance of thoroughly investigating each series for which a relevant change in D is determined. Further evidence is provided when considering the S40(IN) series. Despite the highest MEI the average diameter is the largest if seen as a whole but, once again, the marked reduction of *D* with MEI is indeed obtained.

4.2.1. Pore wall thickness and vertex modification

The effects of mixing on the pore presented in the previous section have shown that in increase of energy input reduces the average pore size. In this part, further structural/geometrical modifications are presented. These energy input induced modifications focus on pore wall thickness t_w, intersecting vertex thickness *Tw* and their ratio *t/T*. These three parameters also provide an indication of how the pore structure changes (adjusts itself), upon mixing.

The pore wall thickness was measured in the middle of each cells' strut, where its thickness is at its minimum (Mills, 2007a) by SEM images. A higher magnification, 1000x and 2000x, with a scale bar of 20 and 10 μm respectively were used. Only 20 measurements were possible due to the limited number of cells that fit into the highly magnified image.

An example of the appearance and the measurement performed onto two samples, S20-20 with the lowest value of *t* and S40-15(IN) with the highest is shown in Fig. 4-42 and Fig. 4-43 respectively.

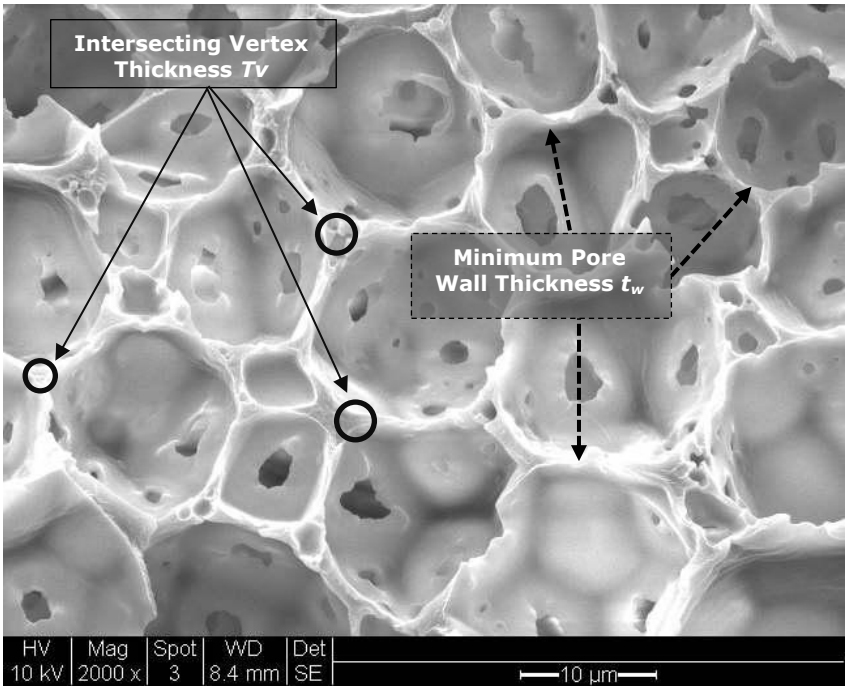

Fig. 4-42: EPHP S20-20 SEM image, 2000x magnification, Scale bar 10 μm used for the identification of minimum pore wall thickness *t*, intersecting vertex thickness *Tv* and *t/T* ratio.

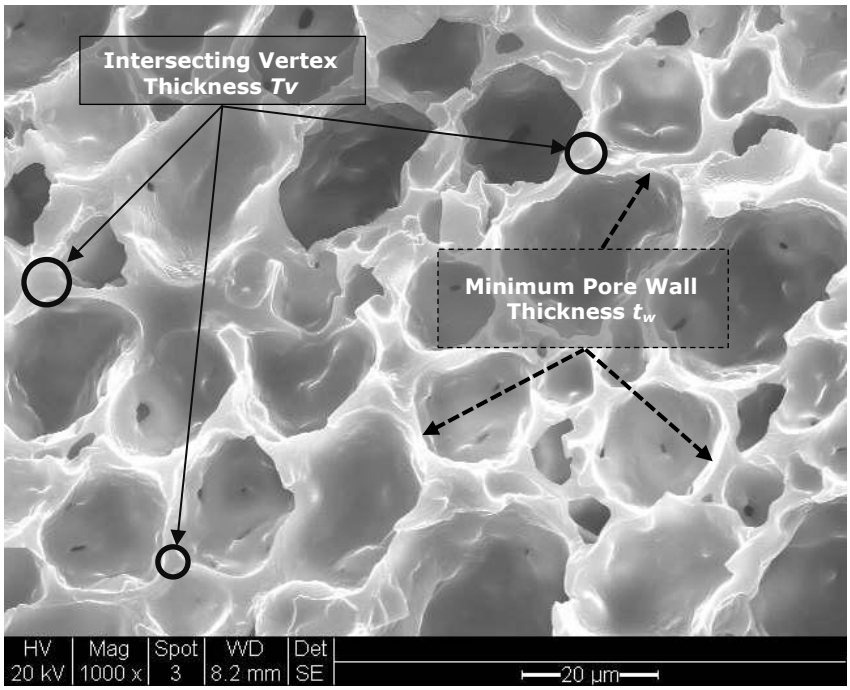

Fig. 4-43: EPHP S40-15 SEM image, 1000x magnification, Scale bar 20 µm used for the identification of minimum pore wall thickness *t*, intersecting vertex thickness *Tv* and *t/T* ratio.

The changes in terms of t_W, T_v and their ratio t/T that occurred on each EPHPs sample are shown in Table 4-15 and are all plotted for a more effective visual comparison in Fig. 4-44.

Table 4-15: EPHPs pore wall thickness t_w, intersecting vertex thickness *Tv* and their ratio *t/T* as a function of total mixing time. (IN) indicates the use of oil phase initiator.

EPHP Sample	Average Pore Diameter *D* (µm)	t_w (µm)	*Tv* (µm)	*t/T*
S10-05	13.1	0.90	1.74	0.52
S10-10	11.2	1.00	1.70	0.59
S10-15	9.8	0.55	0.93	0.59
S20-15	16.1	1.63	3.34	0.49
S20-20	11.3	0.75	1.78	0.42
S30-15	12.1	1.15	2.20	0.52
S30-20	10.1	0.94	1.52	0.62
S30-25	12.4	0.98	2.36	0.42
S40-15	15.2	2.07	4.21	0.49
S40-20	14.5	1.50	3.14	0.48
S40-25	12.7	1.96	3.87	0.51

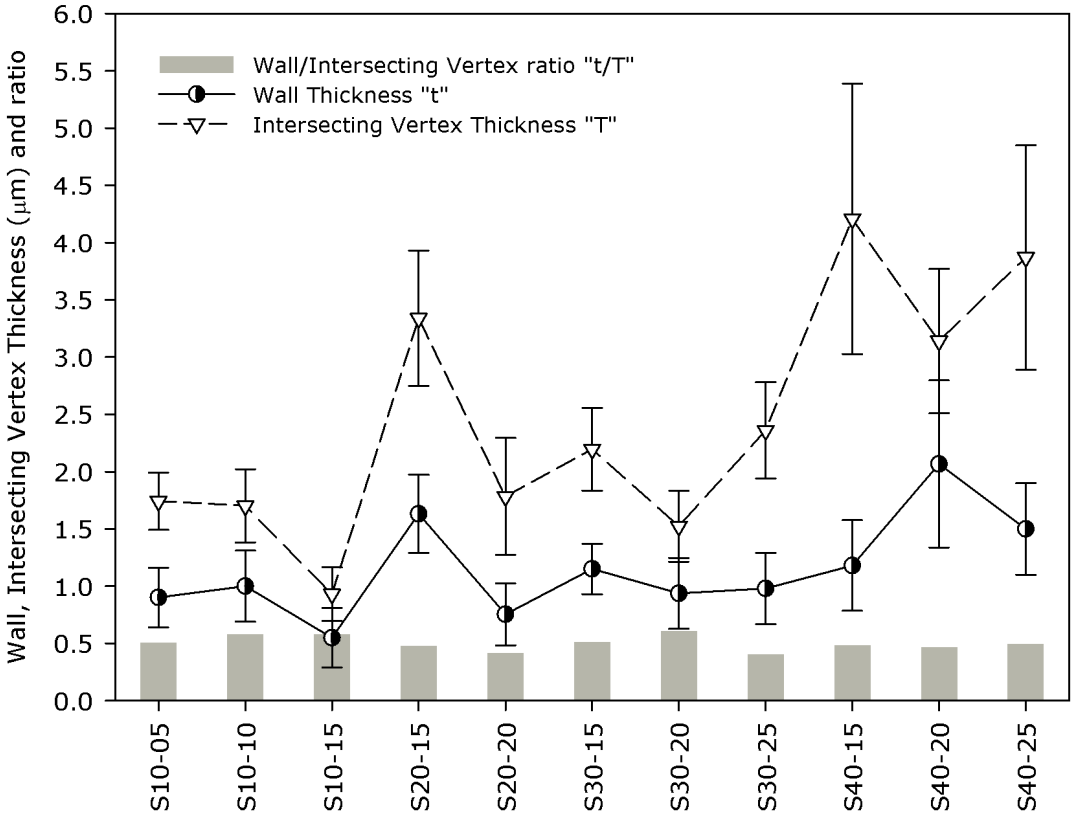

Fig. 4-44: Pore wall t_w, intersecting vertex thickness *Tv* and their ratio *t/T* of complete EPHPs series. The polymeric content increases towards the right, with S40(IN) series containing 40% oil phase volume.

The variation of the pore wall and intersecting vertex also indicates how the solid content is distributed. It can be seen that for all the series, with the exception of S40, both wall and vertex thickness follow the same trend. In S10, S20 and S30 EPHPs series, in fact, the parameters are closely related one another.

An increase in wall thickness is accompanied by a much more pronounced increase in vertex thickness. This behaviour can be explained by considering that with increasing solid content, the MEI is less effective at reducing the droplets size hence, with less smaller droplets formed, and the majority of solid content tends to accumulate at the vertex. This phenomenon is particularly evident in S40 series which is characterised by the highest value of intersecting vertex thickness and solid content.

Moreover, a substantial confirmation of the mutual trend of the two thicknesses is provided by their ratio. It follows both parameters when compared within the same series and its value fluctuations are very limited. Furthermore, when the ratio of the thicknesses is extended to the entire EPHPs series it appears to remain almost constant, regardless of the increasing solid content.

This result indicates however that the investigation should consider all the series without the S40 series, as it is produced by twice as much the dosing time and, as a consequence of that, has the highest energy input. By considering only EPHPs S10, S20 and S30 series and by also adding the average pore diameter (Fig. 4-45), it can be seen that the *T/t* ratio tends to become smaller as the solid content increases so, a relationship between the thicknesses and the solid content can be established.

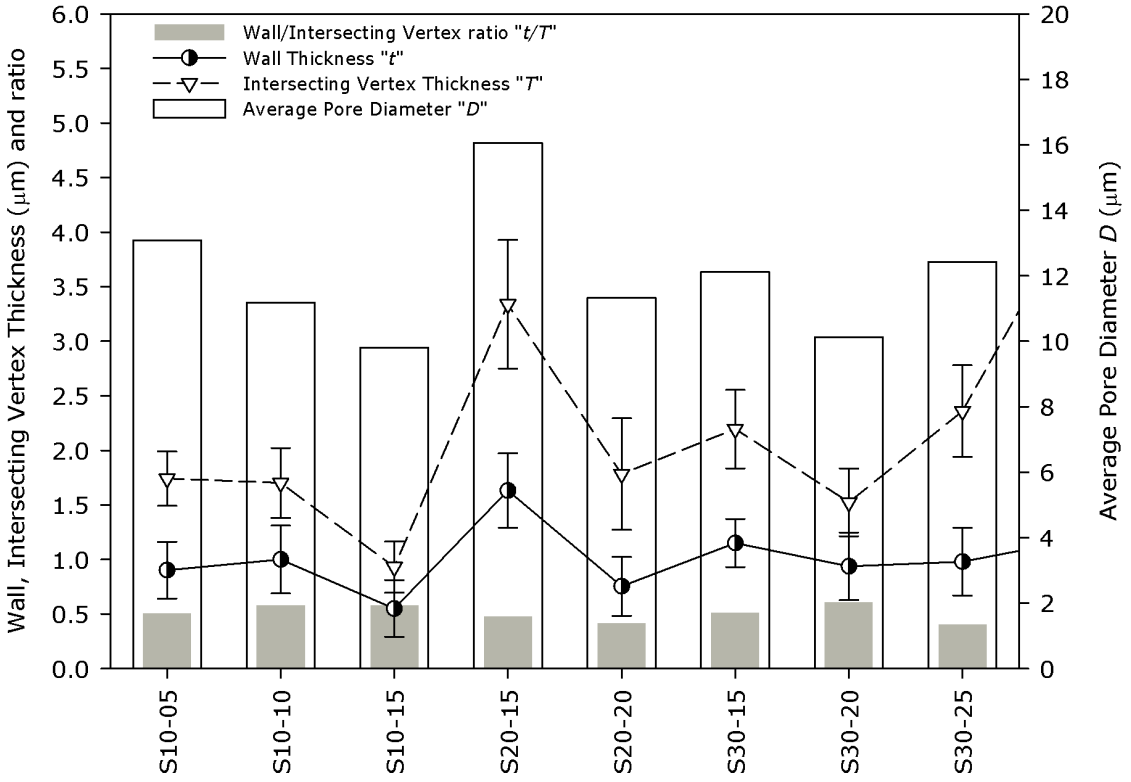

Fig. 4-45: Average pore diameter *D*, pore wall t_w, intersecting vertex thickness *Tv* and their ratio *t/T* of EPHPs S10, S20 and S30 series.

The trends of the parameters presented in the figure can be used to further support and confirm the considerations of the influence of homogenisation time and solid content on the average pore size.

While a longer mixing time produces a higher number of pores with thinner walls, an increase of solid content (or coalescence phenomena) produces a lower number of pores with consequently thicker vertexes. Sample S30-25 is the one which has experienced coalescence of the pores. This occurrence can be supported by observing that its vertexes thickness is the highest of the series.

A visual schematic representation of the effects of solid content and mixing time on the wall and vertex thickness is presented in Fig. 4-46.

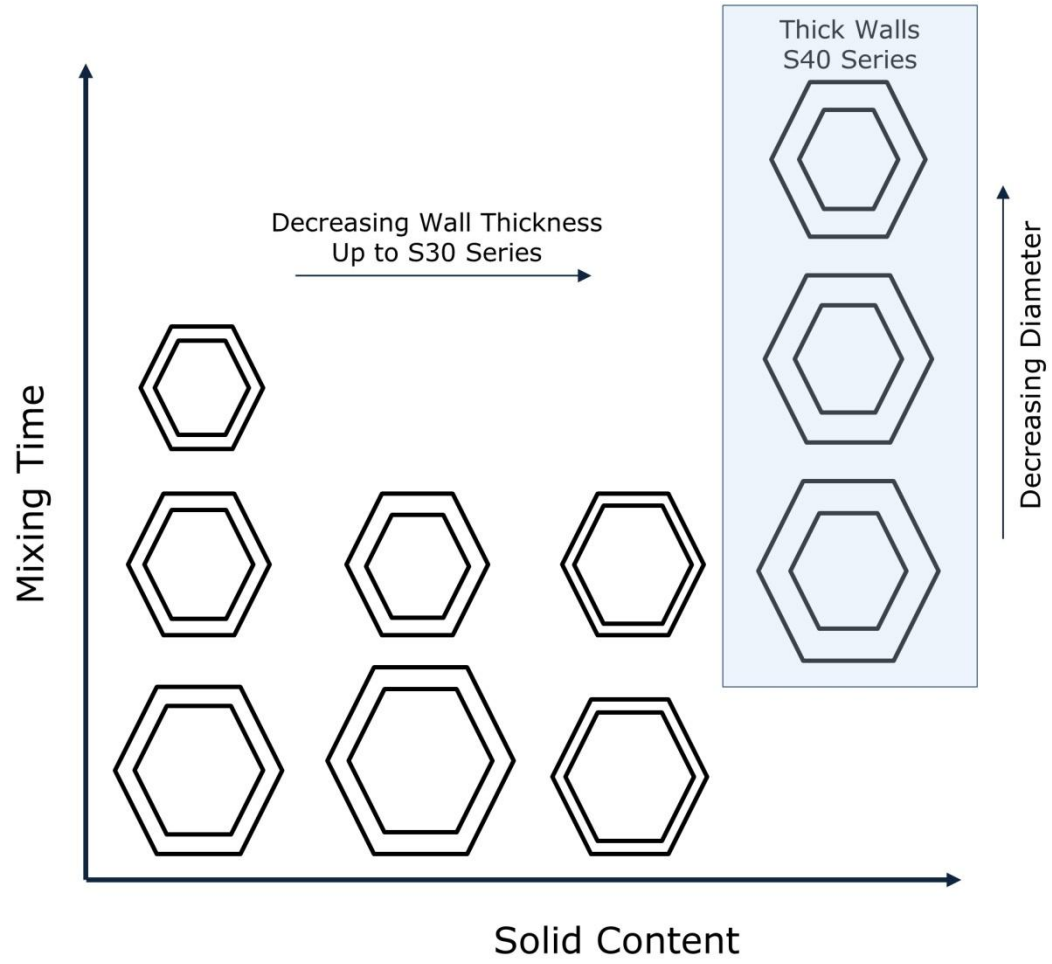

Fig. 4-46: schematic representation of the effect of missing time and solid content on pore diameter, wall and vertex thickness.

The results and the discussion provided in this section represent the basis of the effects of increased mixing time (or, equivalently increased mechanical energy input). It has been assessed that the EPHPs structure can be modified and, in particular, the average pore size and its distribution can be made smaller and narrower, respectively.

Moreover, a more detailed analysis of the changes that the processing time produces on the pore wall and intersecting vertexes confirms that longer mixing produces smaller pores and smaller vertexes. At the same time, the influence of increasing solid content has been studied and identified when the entire EPHPs series were considered. However, higher details will be provided in the dedicated section particularly when describing the stress vs. strain curves.

Although the manipulation of the rigid PHPs structure has been studied recently by few authors and some interesting results have been produced, the relationship between actual Process/Manufacturing and Structure has not been investigated. Not only for the elastomeric version of PHPs but also for EPHPs whose solid content and energy input is varied, as performed in this study.

The studies already presented in the literature review focussed on modifying the structure by combining different HIPEs with no reference to the possibility of using mixing, or energy inputs to obtain significant structural changes.

In this work, it has instead been demonstrated that an acceptable degree of control on the EPHPs structure can be achieved.

The variation of average pore diameter and other cell parameters will be related to mechanical properties in the next section. By doing so, the Structure-Properties relationship will be assessed by the Young's Modulus (elastic modulus) and the Specific Absorbed Energy.

4.2.2. Young's Modulus

In the light of the Process-Structure findings presented and discussed in the previous sections, each EPHP was mechanically tested to assess the influence of the structure on the properties of the material (i.e. Structure-Properties relationship). As already presented in the methodology, a series of Mechanical Compression Testing (MCT) sessions were run to obtain the fundamental mechanical parameters.

Two parameters, in particular were determined: 1) *Young Modulus E* (also known as elastic modulus or modulus of elasticity), which measures a material stiffness and 2) the *Specific Absorbed Energy SAE* that indicates the capacity of a given material to absorb energy without fracture. Full details of MCT are presented in the next sections.

The Young's modulus of the various EPHPs series is calculated by using the stress vs. strain curves generated by the MCT equipment at room temperature. The elastic modulus is the initial region of the curve where proportionality between stress and strain exists. The whole stress vs strain curves are shown for each EPHPs series to highlight the effects of increased mixing time and the structural changes presented earlier.

The stress vs strain curves obtained from room temperature measurements are shown in Fig. 4-47-49 for S10, S20, S30 and S40 series respectively.

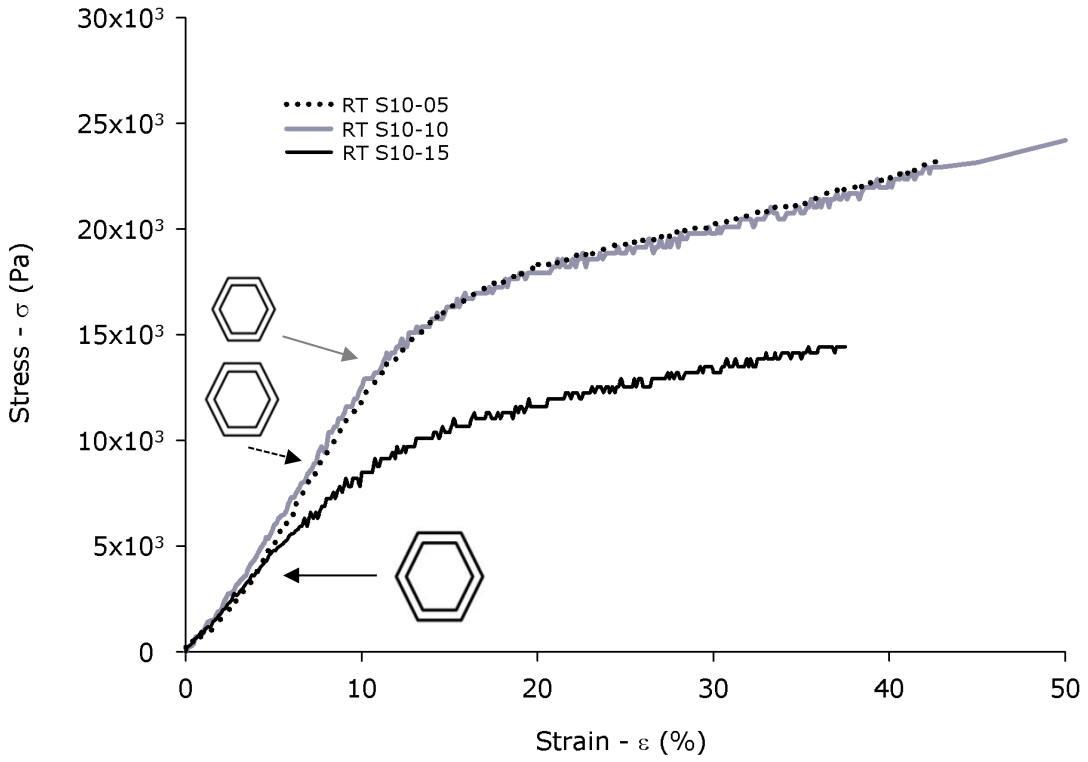

Fig. 4-47: Stress vs. Strain curves at room temperature (RT) of EPHP S10 series. S10-05, S10-10 and S10-15. Idealised hexagonal average pore diameter shown to illustrate the pore size vs elastic modulus effect.

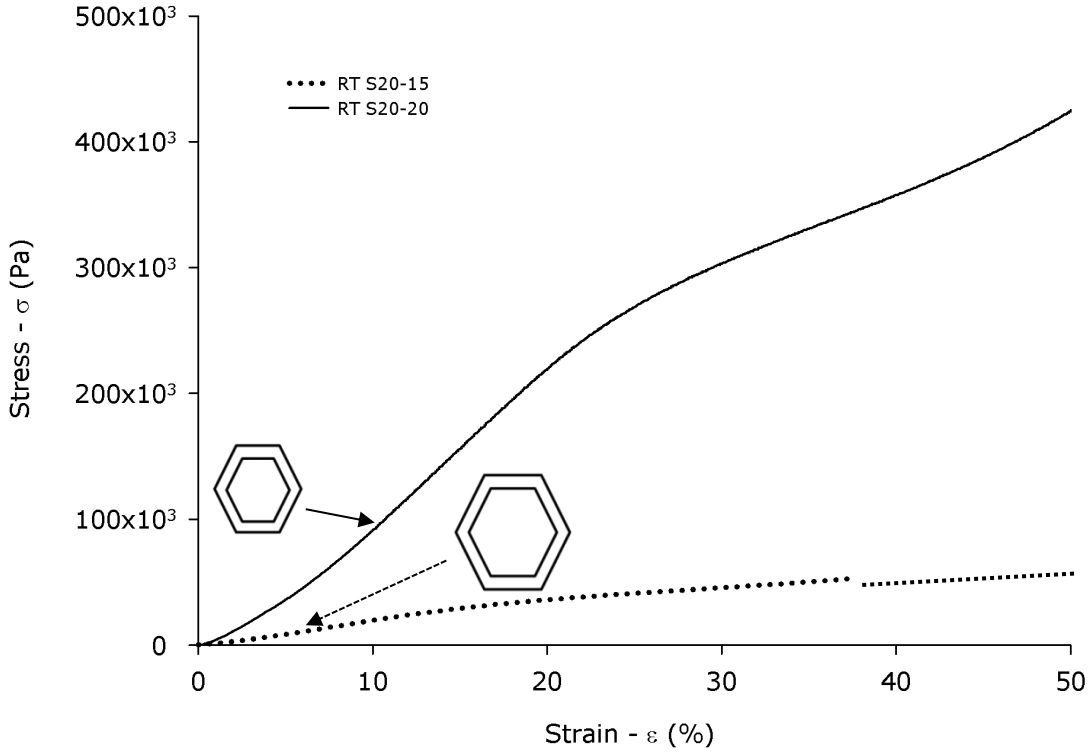

Fig. 4-48: Stress vs. Strain curves at room temperature (RT) of EPHP S20 series. S20-15 and S20-20. Idealised hexagonal average pore diameter shown to illustrate the pore size vs elastic modulus effect. Higher elastic modulus for S20-20 results from a higher wall thickness / Pore diameter ratio.

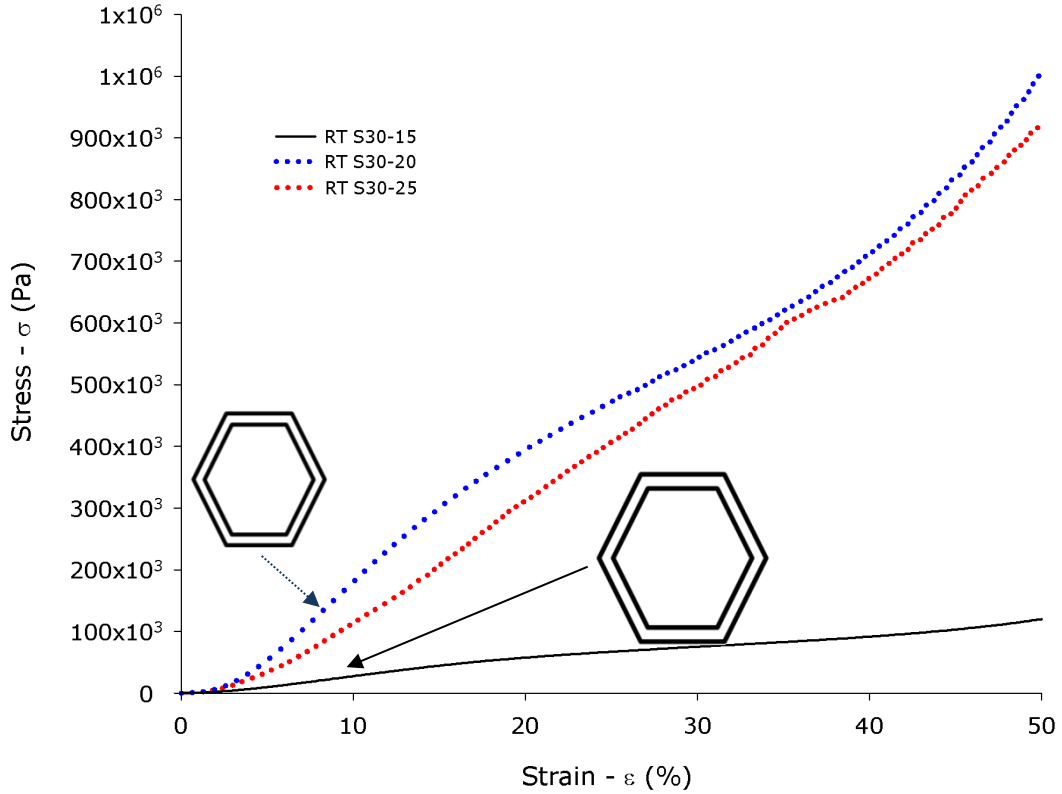

Fig. 4-49: Stress vs. Strain curves at room temperature (RT) of EPHP S30 series. S30-15, S30-20 and S30-25. Higher elastic modulus for S30-20 results from a smaller pore diameter with a narrower distribution.

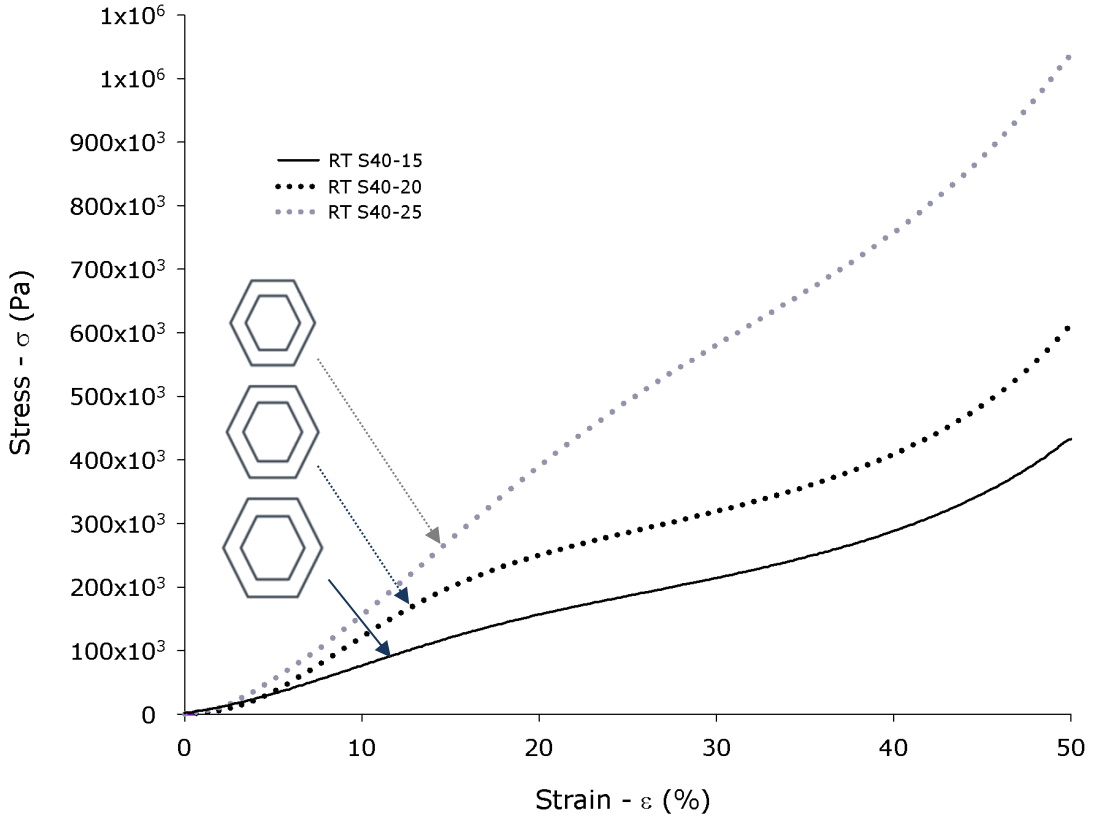

Fig. 4-50: Stress vs. Strain curves at room temperature (RT) of EPHP S40 series. S40-15, S40-20 and S40-25. Higher elastic moduli of the S40 series are due to thick walls. Narrow distribution of pores determines an almost linear response.

A direct increase in elastic modulus as a function of longer mixing time (and corresponding energy input) is clearly shown by the stress vs. strain curves. Hence, as determined earlier, each EPHP series is characterised by a higher stiffness as the average pore diameter decrease.

A confirmation of such behaviour is provided by the plot of Young's modulus as a function of pore diameter as shown in Fig. 4-51.

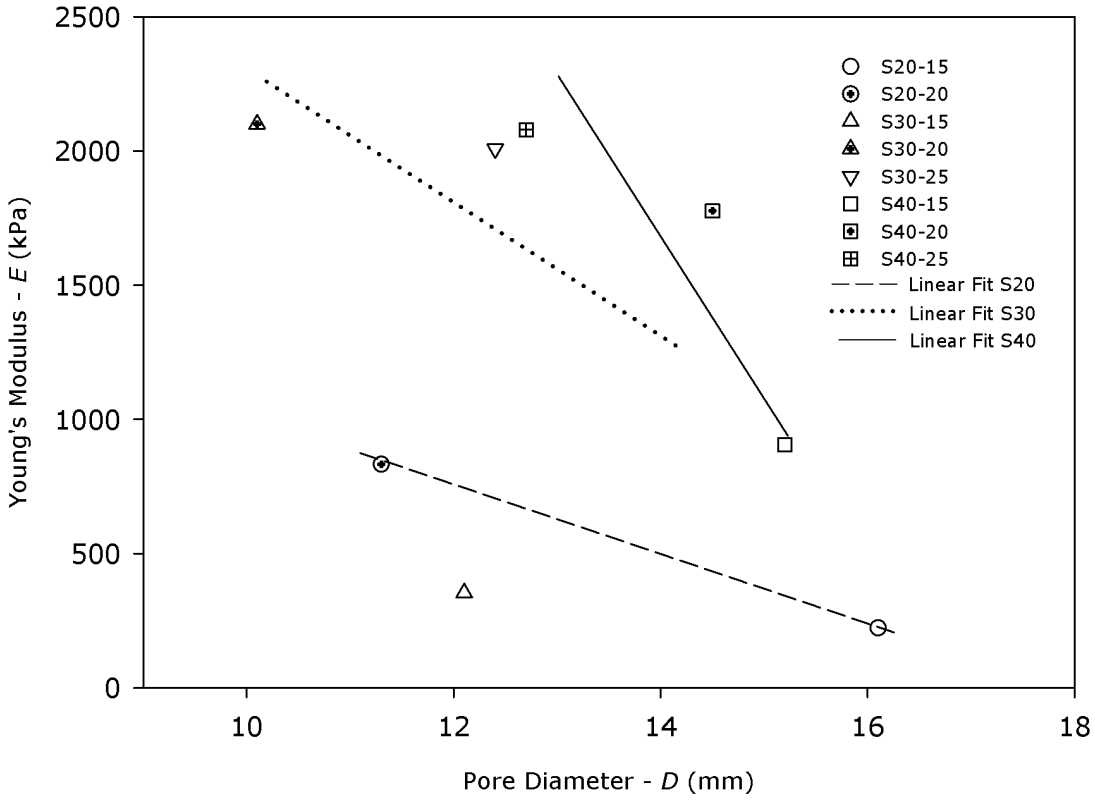

Fig. 4-51: Young's modulus as a function of average pore diameter *D* for S20 and S40 EPHPs series.

The plot highlights several interesting results: 1) the higher values of Young's Modulus are given by the EPHPs with the smallest pore diameters and 2) smaller pores can be produced for any EPHPs, regardless the solid content.

These two conditions can be verified by considering that, for example, the modulus of S30-15, which contains 30% of solid content, is lower than that of S20-20 with 20% solid content. However, the average pore size and wall thickness of S20-20 is smaller due to a longer mixing time (higher energy input).

A global linear fit-curve that accounts for both mixing energy input and solid content shows a marked inverse proportionality, thus confirms the structure-property relationship. Before analysing this aspect in more details, it is worth noting how large the variation of Young's modulus for the various series of materials is. The complete series of data for Young's modulus (and absorbed energy), calculated

by the stress vs strain curves at room temperature, are reported in Table 4-16, along with the density of each EPHP.

Table 4-16: Young's Modulus and Specific Absorbed Energy *SAE* at Room Temperature of the entire EPHPs Series. Density of EPHPs samples is shown in the last column.

EPHP	Solid Content (1-ε) (%)	Young Modulus *E* (kPa)	Specific Absorbed Energy (mJ/mL)	Density (mg/mL)
S10-05	10	139	7.8	0.09
S10-10	10	126	7.5	0.09
S10-15	10	120	8.0	0.09
S20-15	20	223	15.3	0.19
S20-20	20	833	118.5	0.20
S30-15	30	354	30.8	0.26
S30-20	30	2100	229.7	0.25
S30-25	30	2008	202.5	0.25
S40-15(IN)	40	628	77.0	0.36
S40-20(IN)	40	1777	138	0.29
S40-25(IN)	40	2079	237	0.36

As the data take into account both solid content (i.e. the various EPHPs series) and mixing time, the two contributions can be assessed independently. The plot of *E* vs homogenisation time, shown in Fig. 4-52, enables to effectively identify the effects of these two parameters for the various EPHPs series.

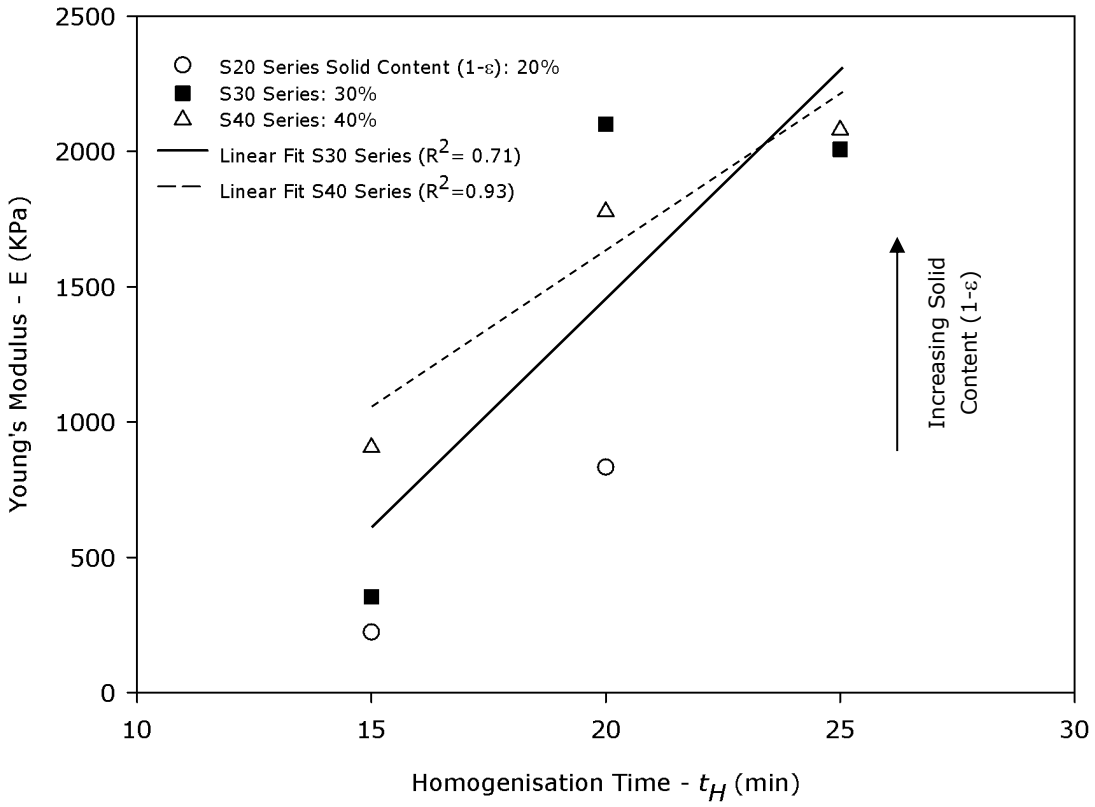

Fig. 4-52: Young's modulus as a function of homogenisation time for S20, S30 and S40(IN) EPHPs series. Linear best-fit lines shown only for S30 and S40 series. Error bar is removed for clarification.

The plot confirms that an increase in mixing time results in higher elastic moduli. Moreover, the graph shows that by increasing the homogenisation time, the modulus of lower solid content samples can be increased to values similar (or even higher) to those with higher solid content samples.

An example of this remarkable result is the Young's modulus of samples S30-20; it is higher than that of S40-20 and very similar to that of S40-25. Despite the two EPHPs series are characterised by a different amount of solid content (30 and 40%), the average pore size of S30-25 is very close to that of S40-25 (12.4 and 12.7 μm respectively); hence the dominating parameter is the pore size.

4.2.3. Specific Absorbed Energy

The specific absorbed energy of a material can be physically interpreted as the energy that is stored in a given volume of that material. Whether this energy is elastic, plastic or a combination of the two behaviours is directly related to the properties of the material. Two additional behaviours, visco-elastic and visco-plastic also depend of the material itself.

The SAE is also analytically defined as the area under the stress vs. strain curve. A dimensional analysis confirms that it represents an amount of energy per volume. The computation of the SAE (J/m^3) was performed by integrating the stress vs. strain curve numerically. This technique not only allows calculating it as a single value, but it is also possible to calculate SAE values at different, incremental strains. Summing up this interval would indeed produce the total SAE. The reason for such a choice resides in the fact that the SAE is directly related to the stress vs. strain curve.

Any change in the shape of the curve is in fact reflected by a different shape of the corresponding SAE curve when this is plotted as a function of the strain. The SAE of the entire EPHPs series is plotted in Fig. 4-53 and the incremental SAE is shown in Fig. 4-55.

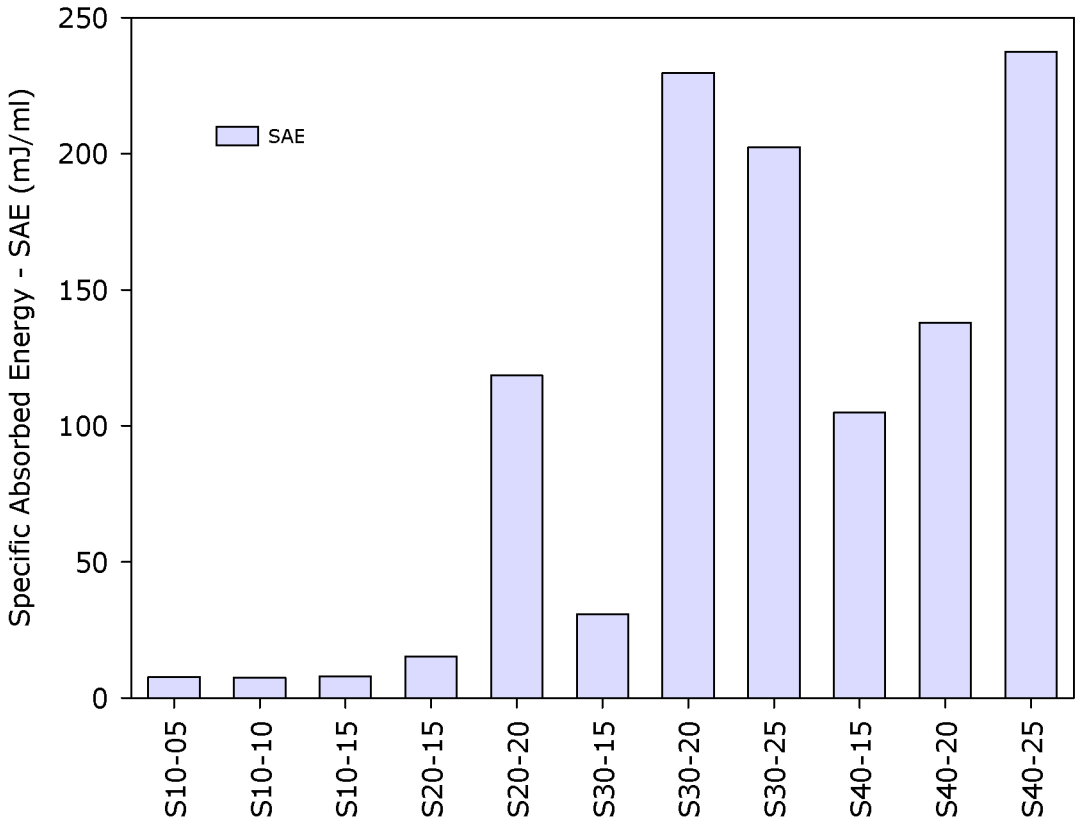

Fig. 4-53: Specific absorbed energy of complete EPHPs series measured at room conditions.

The trend of increasing SAE as a function of increased energy input/mixing time and (consequent) reduction of pore size is recognised. With the exception of the lowest solid content series EPHPs (S10), whose elastomeric behaviour is more pronounced, the SAE markedly increases.

For example, samples whose solid content is constant, i.e. S30 and S40(IN) series, show a pronounced increase of SAE with mixing time. More importantly and similarly to what already observed and discussed for Young's modulus, S30-20 and S30-25 samples exceed the SAE of two out of three S40(IN) samples.

Such a result can further be supported when the various EPHPs samples SAE is plotted as a function of homogenisation time (Fig. 4-54).

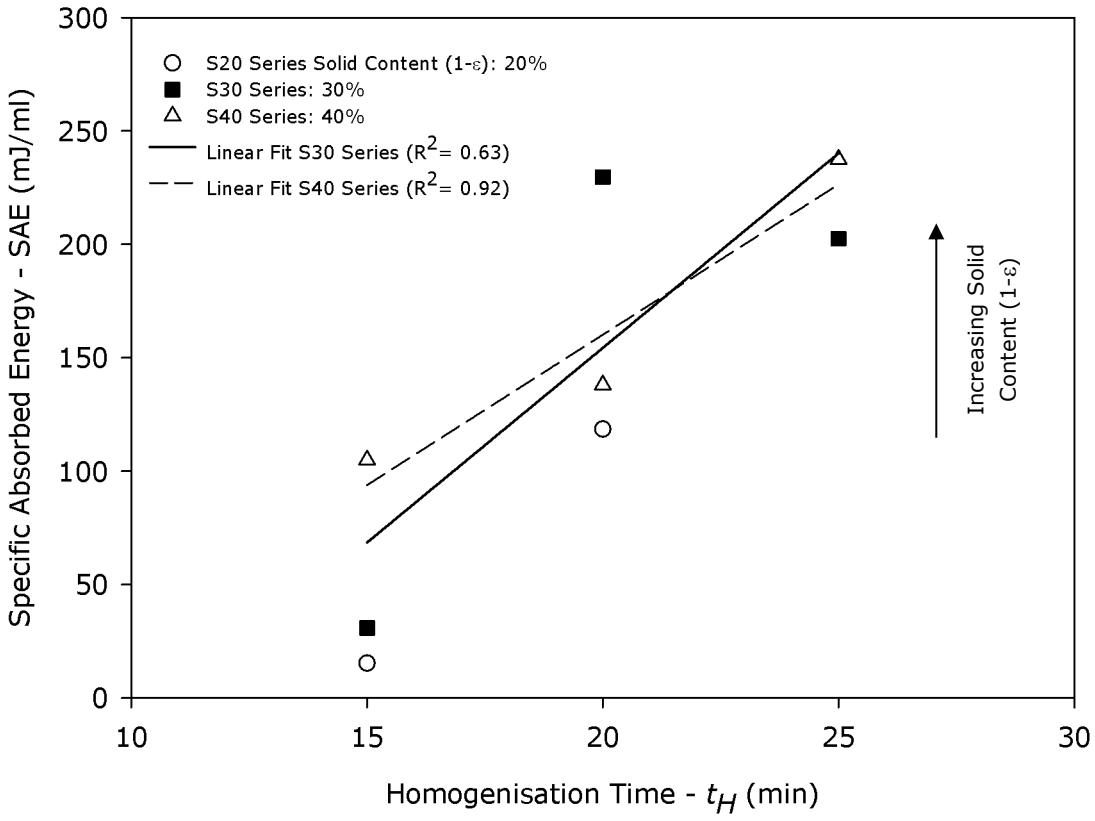

Fig. 4-54: Specific absorbed energy as a function of homogenisation time for S20, S30 and S40(IN) EPHPs series. Linear best-fit lines shown only for S30 and S40(IN) series. Error bar is removed for clarification.

The overall effects of S30-20 and S30-25 reduced pore size diameter, wall and intersecting vertex all contribute to these interesting process-properties relationship.

The incremental SAE plot shown below provides, as anticipated, a more detailed view on how each EPHP behaves under compression.

Two main trends can be recognised from the plot: the EPHPs with lower SAE and those with much higher SAE. However, the distinction goes beyond the final value. In fact, it is the shape of the curve that reveals how the material behaves. This assumption is better supported if the definition of modulus of resilience U_r is provided.

According to Callister (2000), the area below the stress vs strain curve represents a measure of the degree of elastic deformation that has been sustained by a material (before or at fracture). Therefore, whenever a material is subject to a stress and it does not exceed the elastic behaviour the *Modulus of Resilience* (U_r) is obtained by integrating the Stress vs Strain curve within the elastic limit.

Hence, the modulus of resilience "*represents the capacity of a material to absorb energy when it is elastically deformed*".

Its mathematical expression is:

$$U_r = \int_0^{\varepsilon_y} \sigma d\epsilon \qquad \textbf{Eqn. 4-1}$$

where the integration is performed between the unloaded state $\sigma=0$ and σ_y as the upper elastic strain. The integral can be solved analytically by substituting $\sigma=E\varepsilon$ twice to give U_r as a function of Young Modulus E:

$$U_r = \frac{\sigma^2}{2E} \qquad \textbf{Eqn. 4-2}$$

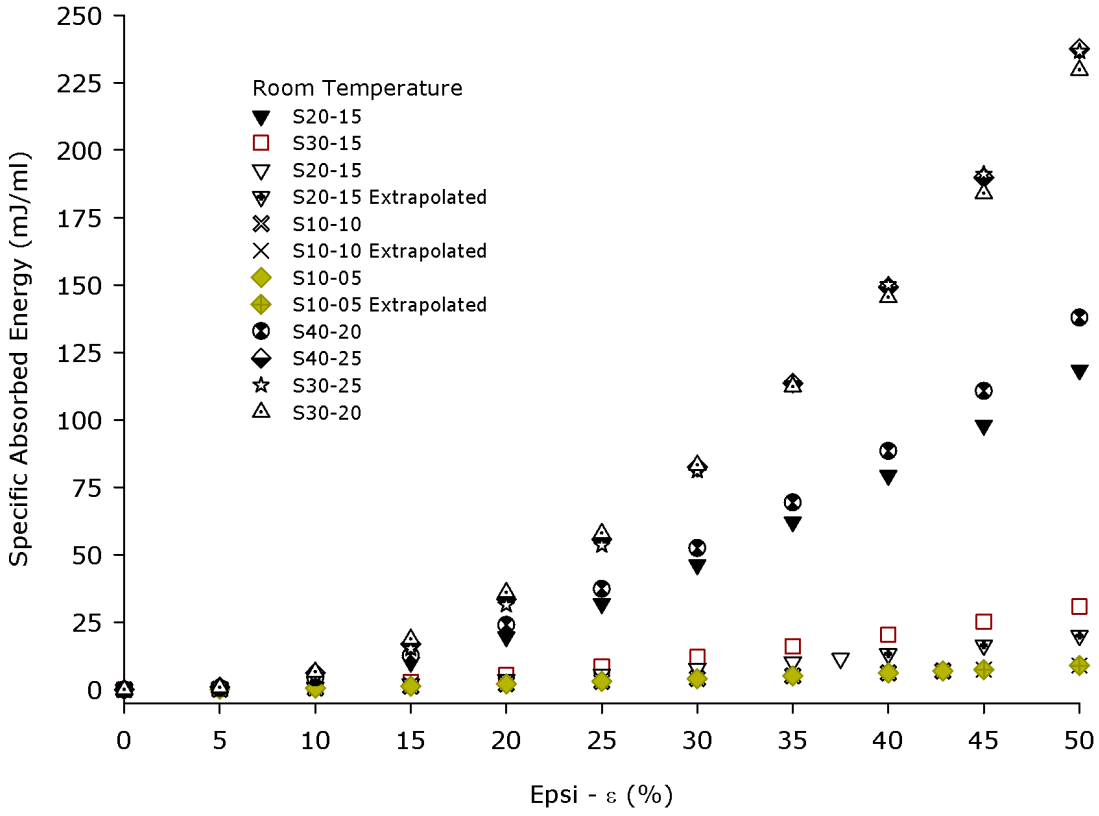

Fig. 4-55: Incremental specific absorbed energy for all EPHPs series at room temperature.

Although a more detailed analysis of the EPHPs curves will be provided in the following sections, those of S10 series are characterised by a limited initial slope (i.e. the definition of *E*) and a relevant, large strain with low stresses.

When considering S30 series, S30-15 sample is characterised by a behaviour which still resembles that of foam (Fig. 4-56). An initial relatively low *E*, followed by an increasing slope plateau and a further but gentle increase in slope only near the end of the strain interval are recognised.

However, if considered as a whole, the curve shows a close stress vs strain proportionality. This is related to its pore (cell) diameter distribution. It appears as if its structure overall behaves as that of a spring.

A spring is in fact an idealisation of proportional (elastic) force, needed to obtain a given strain deformation. Fig. 4-56 also compares the SAE of S30-15 with that of S10-10 where the two different behaviours (shape of the each curve) are highlighted.

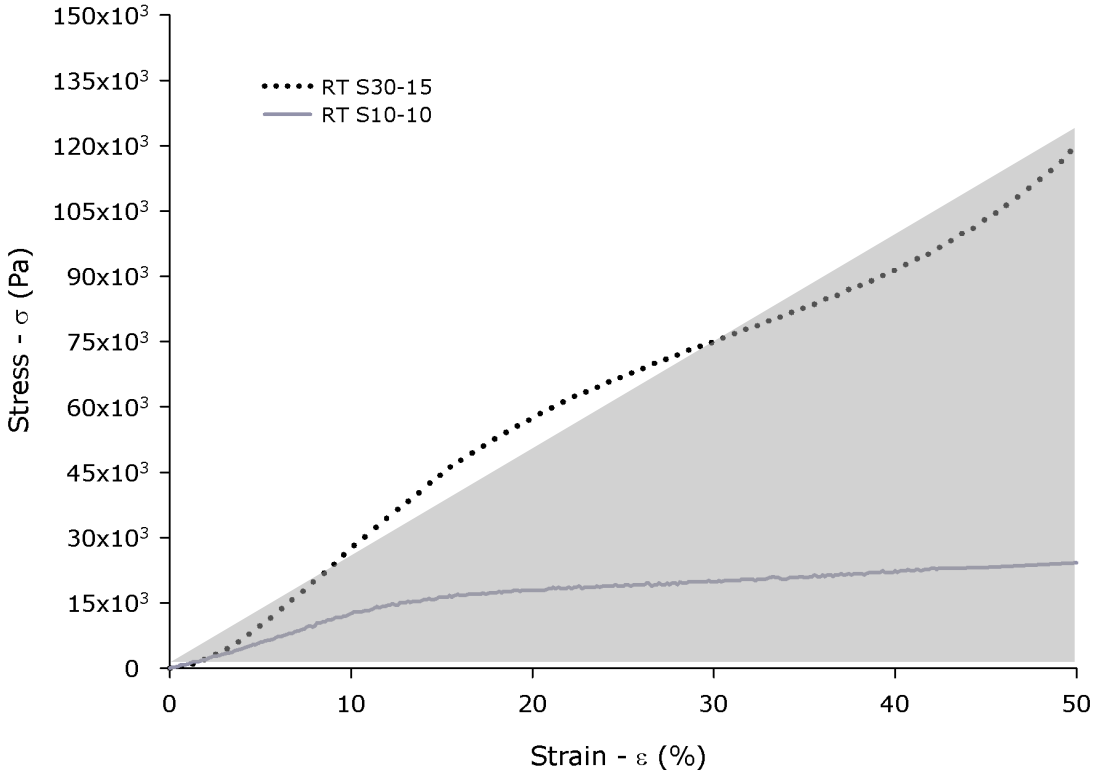

Fig. 4-56: Stress vs strain curves at room temperature (RT) of S10-15 and S30-15 EPHPs samples. The greyed area approximates the area under the curve of S30-15, thus its SAE.

A combined plot of *E* and SAE is shown in Fig. 4-57 and it substantially confirms that an increase of the modulus is also accompanied by an increase in SAE. Both the effects of increased mixing time (energy input) and higher solid content are visible.

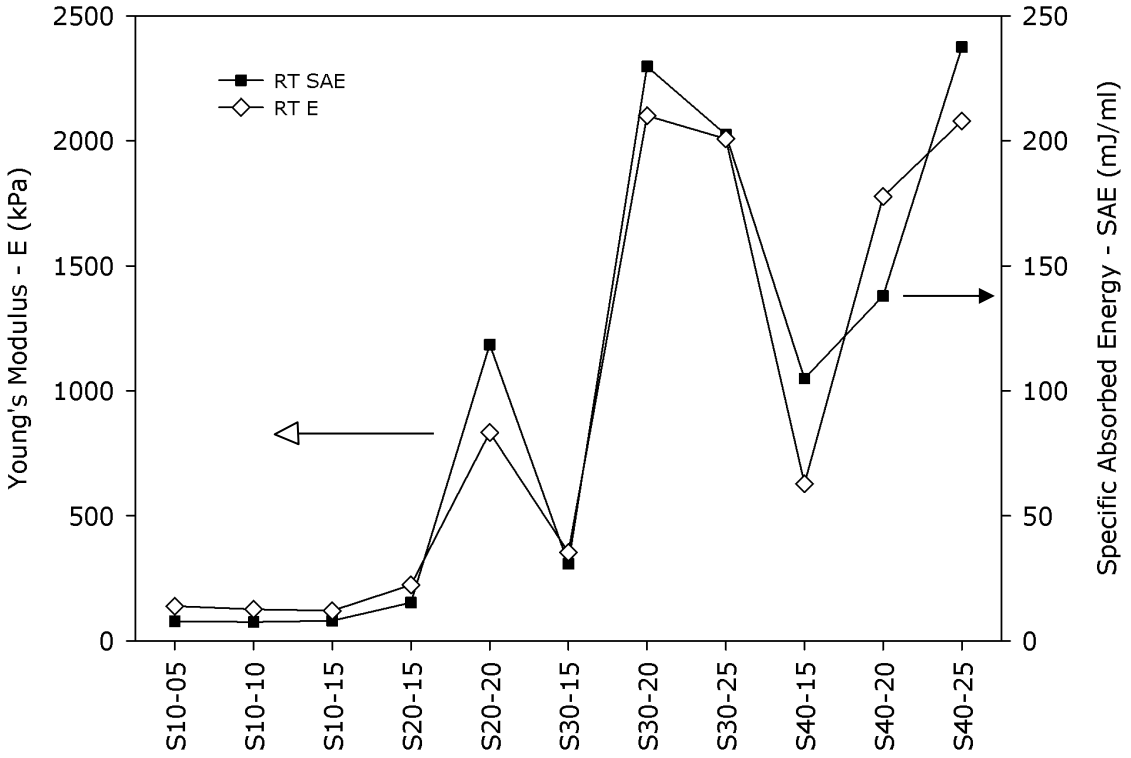

Fig. 4-57: Young's modulus and specific absorbed energy of the entire EPHPs series.

By considering the latter first, i.e. by moving from the left to the right of the plot, the expected trend of higher elastic moduli and absorbed energy is evident. With reference to the effect of increased energy input for every series of EPHPs, it can be seen that its effect are much greater than those of the increased solid. For example, S20 and even more pronounced S30 series experience a remarkable increase in both mechanical parameters.

A particular feature is that the modulus of S20-20 (20% solid content) is in line with that of S40-15, a sample which contains twice as much its solid content (40%). Furthermore, S30-20 (30% solid content) modulus is actually in line with the highest value measured for the longest mixed S40-25. These remarkable results are indeed a consequence of the structural arrangement that the EPHPs can be given by manipulating their manufacturing processes.

Further details in terms of mechanical response of EPHPs, thus the changes in shape of their stress vs strain curves, will be provided in the following sections.

4.2.4. Stress vs Strain curves: overall mechanical behaviour modification

The stress vs. strain curves presented in the previous sections highlighted the changes that occurred to any given series of EPHPs processed with increasing

mixing time. The shape of the curves changes quite distinctively as the mixing time increases.

By looking at the S20 series, with only two different processing times (S20-15 and S20-20 with t_H=15 and 20 minutes respectively), a change in the shape from the foam-like to the composite-like is noticeable (Fig. 4-48). The initial linear elastic response for both samples is described by the Young's Modulus and the Plateau Region is clearly recognisable only in the S20-15 sample. This sample is characterised by a fairly symmetric distribution of pore diameter (Fig. 4-26).

With this pore distribution, the structure response to compression beyond the linear elastic behaviour of S20-15, would be that of enabling the largest pore to buckle first, rapidly followed by smaller pores. The largest pores are limited in number and are prone to buckle due to their higher ratio of length to width. Once this deformation occurs, the load is transferred to a higher number of pores with relatively smaller diameter but also with a high length to width ratio. As the pore diameter interval is rather close, these pores also buckle, producing an almost flat curve.

The sequential elastic buckling collapse from larger to smaller pores is typical of foam-like materials and, in particular, EPHPs. Another interesting feature of EPHPs is that the smaller pores also contribute to the overall behaviour under compression. Their presence provides further deformation of the material prior densification. With smaller pores, thus, an intrinsic increase of material stiffness is provided. Should much smaller pores be not present, the densification of the material, as a result of contact among the collapsed cell would occur at an earlier stage (lower strain).

The behaviour of S20-20 instead is driven by a different structural arrangement. Pore distribution is indeed shifted towards smaller pores. Larger pores occur less frequently while the intermediate and smaller pores are many more and occur with comparable frequency. Not only does this make the material stiffer, but the buckling collapse (i.e. the Plateau Region) is less likely to occur due to a lower length to width ratio.

The mechanism during compression loading appears to be dealt sequentially by the sample structure. The intermediate size pores are deformed under compressive load first and, before buckling occurs (i.e. simultaneous collapse), the load is transferred to smaller pores which are stiffer.

Overall, the shape of the stress vs strain curve resembles the behaviour of a spring. The absence of a Plateau Region indicates that the compression mechanism is borne by the structure in a progressive way. Narrower pore distribution shifted toward smaller pores as the result of longer stirring time, behave in this way.

This load bearing progressive sequence appears to be rather consistent also for the higher solid content EPHPs. In fact, the EPHPs series S30 also shows these mechanical behaviour changes due to increased process time.

Most notably, S30-15 sample with t_H=15 minutes still behaves as a foam material. Although the Young's modulus is, as expected, higher that the other lower solid content EPHPs processed for the same time, the Plateau Region exists and extends up to 50% strain without signs of densification. By referring to the S30-15 average pore size and distribution, it shows that a wider and rather symmetrical distribution of pore diameter results in a typical foam behaviour. On the other hand, samples S30-20 and S30-25 are characterised by a narrower distribution, once again shifted towards smaller pores.

In addition to that, it is worth noticing that when comparing S30-20 and S30-25 their overall behaviour is very similar but the slightly wider distribution of pore diameter for S30-25 results in a lower elastic modulus and SAE.

As anticipated in earlier sections, the slightly wider pore distribution, coupled with a higher average pore size can be attributed to early signs of pore coalescence. This phenomenon indicates that the emulsion is close or has reached its stability limit and further energy input would lead to phase separation.

The last series of EPHPs, S40(IN) has a distinctive behaviour: it does not present the typical behaviour of foam, at any of the mixing times Fig. 4-50). Its overall behaviour can be described as a spring-like, particularly well when at the lowest t_H. As t_H increases the spring-like (proportional) behaviour slightly differs but it is also accompanied by a dramatic increase of the elastic modulus and, above all the SAE (i.e. the much larger area under the curve of S40-25).

By referring to the average pore size and distribution of the EPHPs S40(IN) series, it is possible to support the spring-like behaviour. For S40-15, although an almost symmetric pore distribution exists, it is also coupled by a relatively large pore wall thickness. This characteristic may contribute to effectively reduce the buckling that would produce the typical Plateau region.

The pore wall thickness further increases for sample S40-20; such a feature is coupled with a pore size distribution shifted towards lower values due to higher mixing energy input. Consequently both features provide S40-20 with a higher modulus and higher degree of stress vs strain proportionality (i.e. the approximation of linear behaviour). The last sample, S40-25 further exploits the effects of mixing on the structure. The average pore size is the smallest of the series; therefore the modulus is the highest. The fairly symmetrical pore size distribution shifts towards smaller values and results in a steeper slope of the curve.

This section has analysed and discussed the overall mechanical behaviour of the entire series of EPHPs. The structural changes induced by processing the emulsion for longer homogenisation (mixing) time are reflected by the different mechanical behaviour. As supported by the stress vs strain curves, the most appreciable result is the shift from foam behaviour to solid-like (almost linear, spring-like response between stress and strain) due to reduction of pore diameter and narrowing of its distribution.

While EPHPs series with the same density but different average pore size and distribution have shown to behave in the two distinct ways, lower solid content samples can exceed the mechanical properties of higher solid content EPHPs.

The next section focuses on the mechanical performances of EPHPs with increasing solid content.

4.3. Effect of polymeric content on PolyHIPEs structure

The previous sections, which focussed on mixing energy input and average pore diameter and distribution modifications (Table 4-15 and Table 4-16), have provided valuable insights in the process vs. structure relationship. The overall effects of increasing mixing time were thus studied. Similarly, in these sections the results in terms of structural changes, Young's modulus and specific absorbed energy will be presented as a function of EPHPs solid content.

The solid content has several effects on the EPHPs. As depicted in the SEM picture of the various EPHPs series in the previous sections, the increase of solid content is reflected by a change of EPHPs appearance. The highly open-cell interconnected layout of 10% solid content (S10 series samples, Fig. 4-12) shifts towards an open but less interconnected structure for all the remaining series (S20-15, S30-15 and S40-15 shown in Fig. 4-24, Fig. 4-28 and Fig. 4-34 respectively). Although the structure still presents a more limited number of interconnecting holes, it resembles

a closed-cell layout. As the manufacturing equipment (i.e. the reactor and the mixing device) remained unaltered for all the increasing solid content EPHPs, the changes in appearance may be attributed to a sub-optimal equipment configuration. However, the manufacturing equipment and procedures enabled the successful production of EPHPs whose solid content was beyond the original value of 10%. Furthermore, the EPHPs formulation was kept unchanged. The only difference was the use of the oil phase initiator for S40(IN) series.

4.3.1. Cell, walls' thickness and vertex modification

The solid content contribution to changes in cell diameter, thickness and intersecting vertex is presented and discussed here. Although the complete data have been presented in the section that studied the effects of processing time, a more refined analysis of the data reveals additional details.

When considering the volume of an emulsion formed by adding two phases, water and oil phase (solid content), a higher amount of the latter results predictably in the formation of, ideally, a cell with either thicker walls or vertexes. A larger amount of solid (in a lower amount of water) would thus occupy a larger volume. This assumption can be made because the total volume of the two phases remains constant although the ratio changes. Under this condition, the plots shown in Fig. 4-58 and Fig. 4-59 confirm that this is the case for EPHPs.

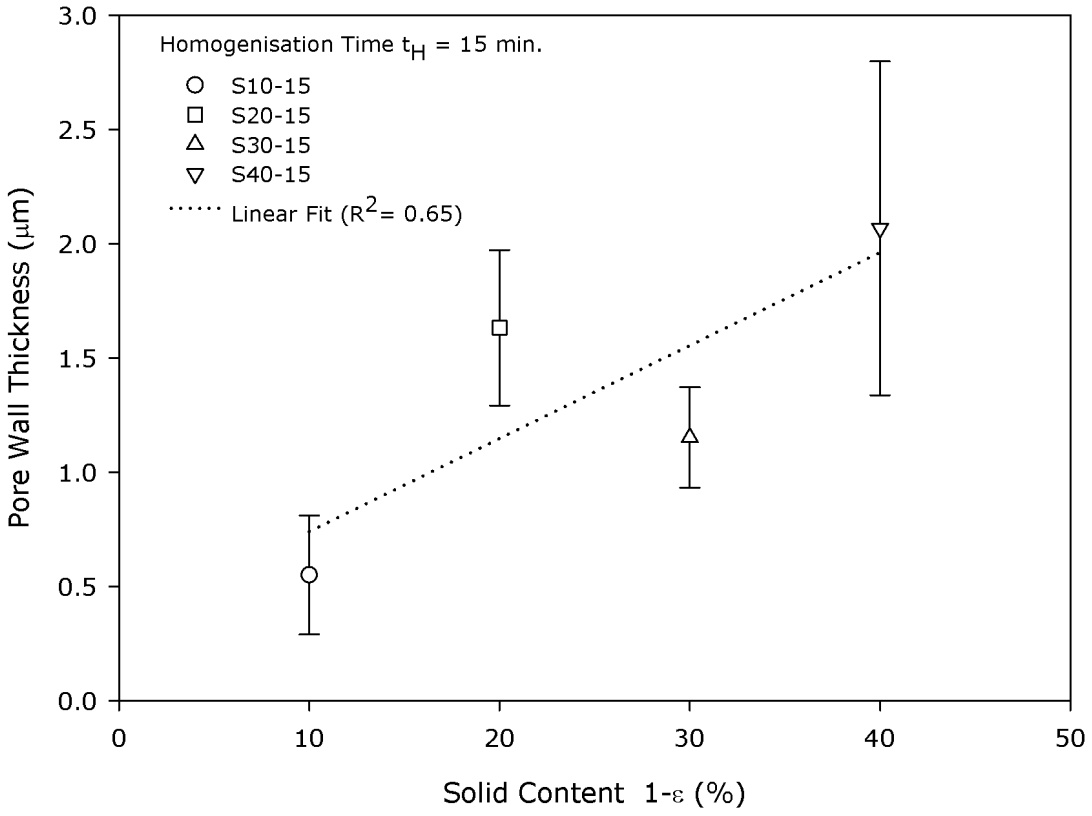

Fig. 4-58: Pore wall thickness as a function of solid content for S10-15, S20-15, S30-15 and S40-15 EPHPs .

While the pore wall thickness clearly increases when moving from 10% to 40% solid content (i.e. at the two extremes of the plot), the values for S20-15 and S30-15 appear to behave in an opposite way. However, when the scatter of the value is considered this fluctuation is minimised.

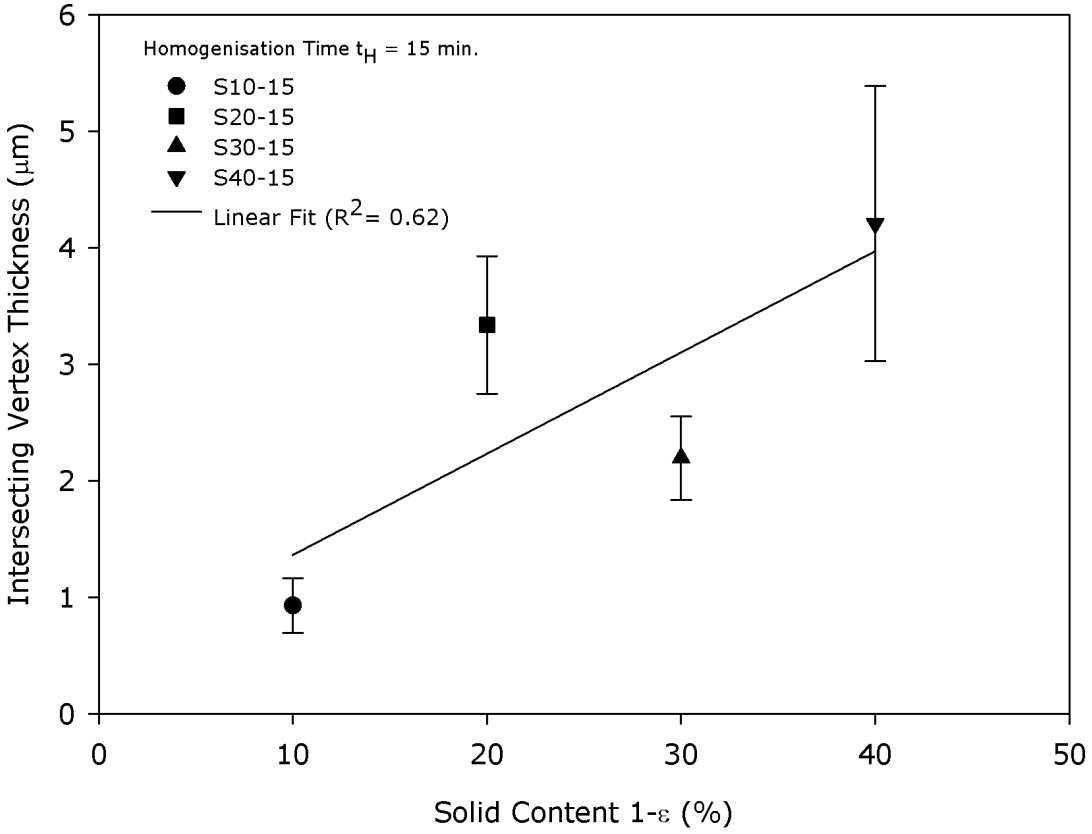

Fig. 4-59: Intersecting vertex thickness as a function of solid content for S10-15, S20-15, S30-15 and S40-15 EPHPs series.

Similarly to what has been observed for the pore wall thickness, the amount of solid that accumulates at the intersecting vertexes increases. The best-fit line shows that a linear relationship exists and similar comments for the behaviour of samples S20-15 and S30-15 can be made.

The pore wall thickness as a function of the solid content for all the EPHPs series, (shown in Fig. 4-60) supports the trend described earlier for (t_H=15 minutes).

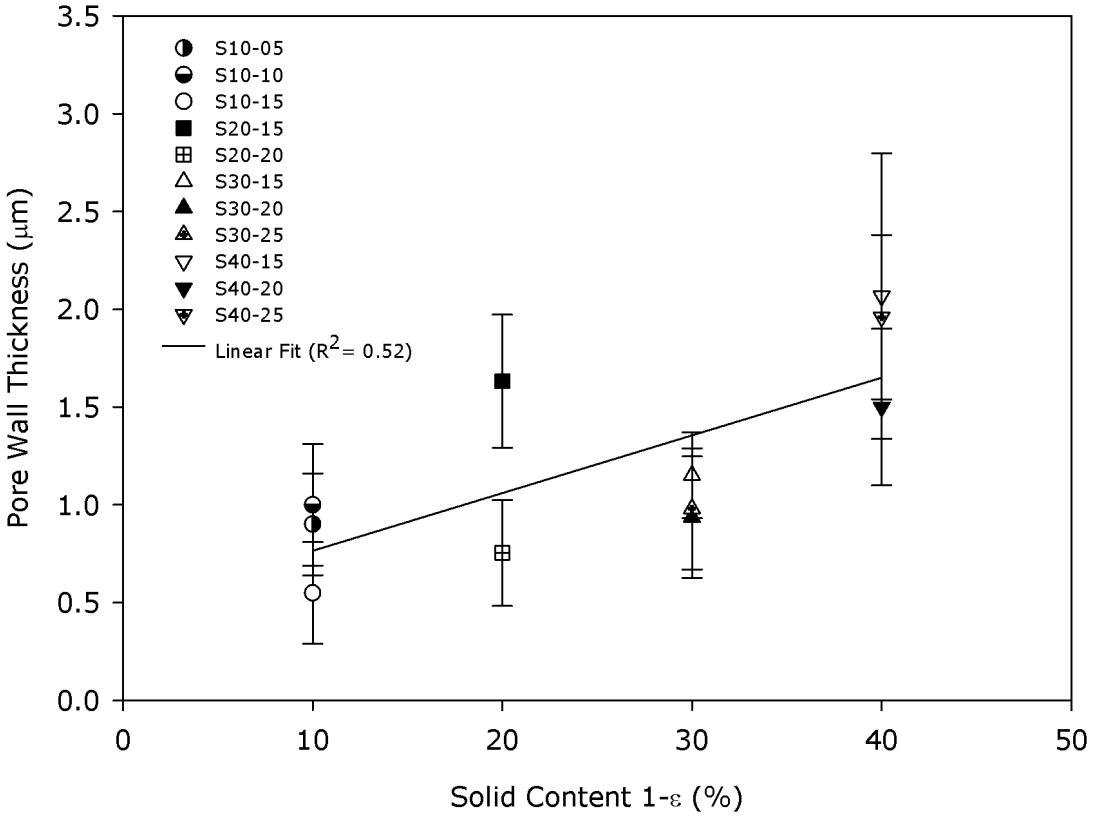

Fig. 4-60: Pore wall thickness as a function of solid content for all EPHPs series. Linear best-fit line for all data.

The measurement of the wall and intersecting vertex thickness thus highlighted that once the (ideal) cell has been created, an increase of solid content results in cells which are characterised by: 1) smaller pore (i.e. reduced pore diameter), 2) thicker walls (ideally a thicker column with a lower slenderness ratio) and 3) more solid accumulates at the vertexes. The latter characteristic may also contribute to the overall stiffening of the material.

In particular, a higher amount of solid at the vertexes increases the bending moment, therefore making the material more resistant to bending. This feature has been observed and discussed with reference to EPHPs with a more pronounced spring-like behaviour, such as S40-15 and others with higher value of intersecting vertex thickness.

In conclusion, the effects of the solid content on the pore size can be summarised and effectively represented by analysing the changes of the ideal hexagonal cell depicted in Fig. 4-61.

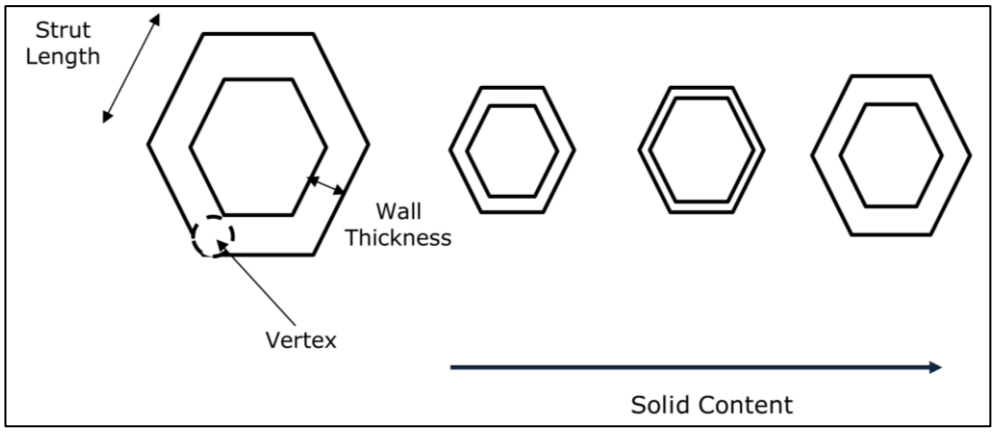

Fig. 4-61: Structural parameters of an idealised hexagonal cell. Strut length, wall thickness and vertex thickness dictate the mechanical behaviour. The ratio between length and thickness varies more than the ratio with the vertex and is found to have a greater effect on stiffness.

4.3.2. Young's Modulus and Gibson and Ashby Model

The Young's modulus of increasing solid content EPHPs is analysed in details in this section. Moreover, the Gibson and Ashby model will be used to assess its prediction capabilities. As already discussed in the literature review, the Gibson and Ashby model has been widely used for predicting the elastic modulus of many porous materials.

The model's most important parameter is the density of the porous material and that of the bulk material ($E/E_s=(\rho/\rho_s)^2$). The additional difference between open and closed-cell layout tends to be very limited and for this reason the moduli are represented both by the same equation.

The Young's modulus of EPHPs processed with increasing solid content, at 15 minutes homogenisation time, is shown in Fig. 4-62. The Gibson and Ashby model as well as a modified version of the model and a linear fit are plotted.

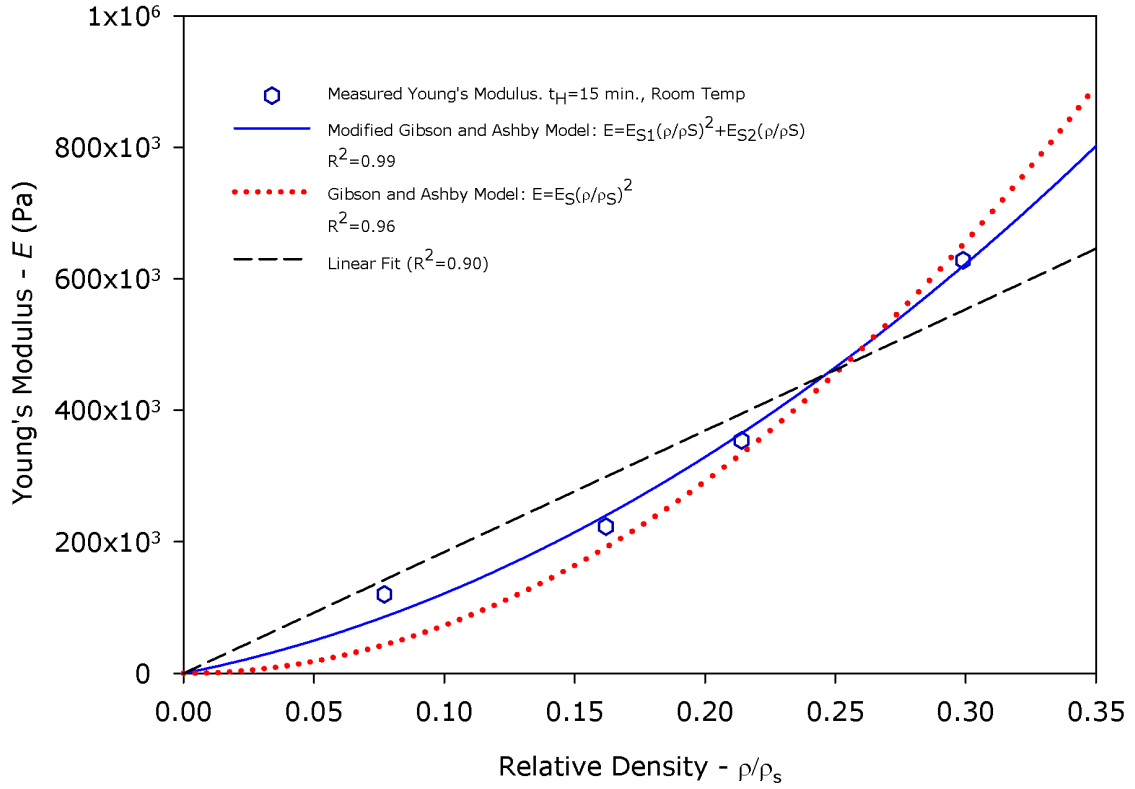

Fig. 4-62: Young's Modulus of EPHPs series with homogenisation time t_H=15 min as a function of relative density ρ/ρ_S . Modified Gibson and Ashby Model (solid line), original model (dotted line) and linear fit of data (dashed line). Data measured at room temperature. Solid content increases from left to right: 10, 20, 30 and 40% respectively.

The original Gibson and Ashby model fits the experimental data satisfactorily for EPHPs with solid content higher than 10%; a relevant scatter for the low solid content EPHPs is observed. A significant improvement in data fitting is provided by a modified Gibson and Ashby model. This model uses a quadratic expression with two constants (Es_1 and Es_2) as they originate from the equation shown in the plot. The original model instead uses a single parameter that represents the bulk material modulus E_S. Further useful information can be obtained by a linear fit of the data. Although the model slightly overestimates the measured value for solid content <40% (or density ratio < 0.30), it can be anticipated that a very good agreement with low solid content data exists.

The implications of the linear fit and the Gibson and Ashby model (original and modified) are remarkable. Different structures are described by different models. The open-cell structure which is the distinctive feature of low solid content EPHPs (Fig. 4-19) is retained in all the other EPHPs series. Although the higher solid content EPHPs may seem to resemble closed-cell structures (Fig. 4-25, Fig. 4-28 and Fig. 4-35), the presence of even just a few interconnecting holes in almost all the pores still enables the structure to act as an open-cell material.

This change in structural appearance is also reflected in an overall change in mechanical behaviour.

The model(s), whose equations have been plotted with measured data, are used to assess the validity of two parameters: the bulk material density and the bulk modulus. The latter parameter is further exploited due to a series of ways by which it can be determined. The bulk material elastic modulus was in fact initially computed by the rule of mixture, thus the moduli of both the main constituents (styrene and 2EHA) were weight-averaged (data are reported in Table 4-17). As reported in the literature by Sergienko *et al.* (2002), such an approach has been successfully used but very few details are available.

Table 4-17: Young's Modulus, density and weight % ratio of EPHPs oil phase components.

Oil Phase Component	Young's Modulus -*E* (MPa)	Density – ρ (kg/dm^3)	Weight % ratio in Oil Phase	Weighted Average *E* (MPa)	Weighted Average ρ (kg/dm^3)
Polystyrene (PS)	$2.7 \cdot 10^3$	1.05	1	570	1.17
Poly2EHA (P2EHA)	38	1.2	4		

Following the computation of the Young's modulus by weight-average, the bulk material modulus of the EPHPs has been measured by polymerising the oil phase only. All the bulk material elastic moduli are presented in Table 4-18.

Table 4-18: measured, weight-averaged and Gibson and Ashby Model values of bulk material Young's modulus.

	Measured	Weight-Averaged (calculated)	Gibson and Ashby Model *Es*	Modified Model (Es_1 and Es_2)	Linear Fit
Young's Modulus –*E* (MPa)	0.610	570	7.29	4.3 and 0.78	1.85

The values obtained by the measurements, the rule of mixture and the models appear with different orders of magnitude. The measured value obtained by oil phase polymerisation is by far the lowest. This may indicate that the polymerised oil phase alone does not represent the EPHPs bulk material and s shown in previous sections, the unique hierarchical porous structure created by the emulsion manufacturing process is responsible for the remarkable mechanical properties of the EPHPs.

The weight-averaged modulus is three orders of magnitude higher than the measured value. This may be intrinsically due to the assumption that the bulk material properties are retained by the emulsion and they scale down according to the density only.

The moduli that the models use to best-fit the measured data should be the most significant. As they are built on measured data they should provide a more accurate

description of the various EPHPs. The Gibson and Ashby model is rewritten in a more compact form [$E=c(x)^2$], with $x=\rho/\rho_S<1$. C represents then the bulk material modulus. The results show that the value of C is one order of magnitude higher than that of the measured value but, more importantly, two orders of magnitude smaller than the weight-averaged value. Therefore, although the model predicts a higher modulus than the measured values it confirms that the rule of mixtures for the modulus may not be valid.

However, the polymerised oil phase may be considered representative of an EPHP bulk material even though it cannot be regarded as an emulsion-template porous material.

The modified model which uses two moduli is capable of fitting the data more accurately. Furthermore, the two moduli are to the measured value. Although the modified model uses a quadratic regression (the quadratic equation is used as $y=a\cdot x^2+b\cdot x$) a particularly accurate value of the modulus is provided by the linear coefficient ($b=Es_2$=0.78 MPa).

The validity of the modified Gibson and Ashby model may also be confirmed when considering that it accounts for two distinct structure-related behaviours. As anticipated earlier, in fact the EPHPs with lower solid content are best fitted by a linear curve and a marked deviation from linear behaviour is observed only at the highest solid content. Therefore, the two moduli model should be considered.

According to the results shown for EPHPs prepared with t_H=15 minutes, it can be concluded that the more reliable model is the modified model, however this conclusion is not definitive as the variation in Young's modulus of EPHPs processed with increasing mixing time yet is not fully captured, as shown for the Young's modulus data of EPHPs processed for longer time (Fig. 4-63).

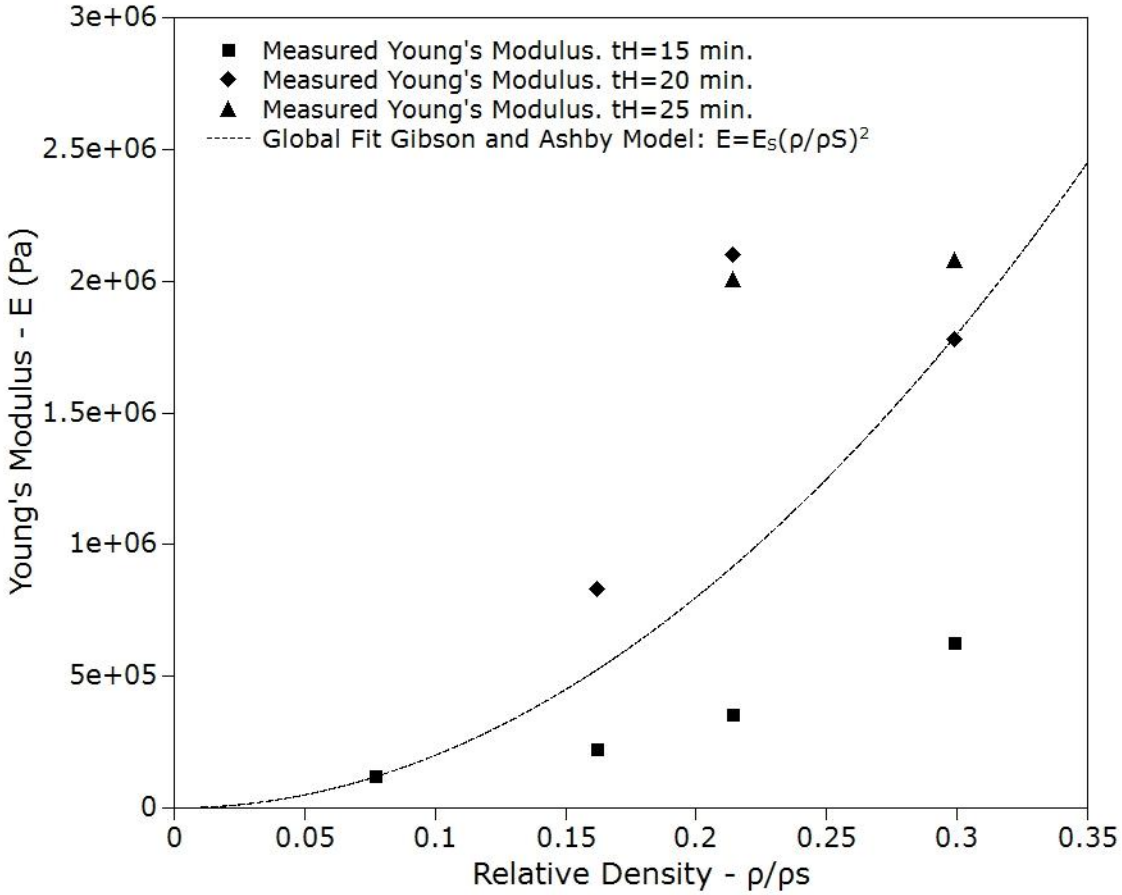

Fig. 4-63: Young's Modulus of all EPHPs series as a function of relative density ρ/ρ_s . All data fitted with Gibson and Ashby Model (solid line). Data measured at room temperature.

The global fit of Young's moduli data with the Gibson and Ashby model confirms its limitations as it only accounts for the relative density of the material (and its bulk modulus). Keeping the porous materials density constant and processing it for longer time modifies its pore diameter and distribution.

These modifications in turn result in higher elastic moduli and this not only demonstrates that the model is not adequate but also that the bulk material modulus, as reported earlier, is not a reliable parameter to use.

Although a rather wide scattering of data is a well acknowledged by the Gibson and Ashby model, the data tend to appear better represented (closer to the fit curve) when they are plotted on logarithm scale. This representation is useful for a rather initial estimation of the porous material properties. The typical appearance of a log scale plot is shown in Fig. 4-64.

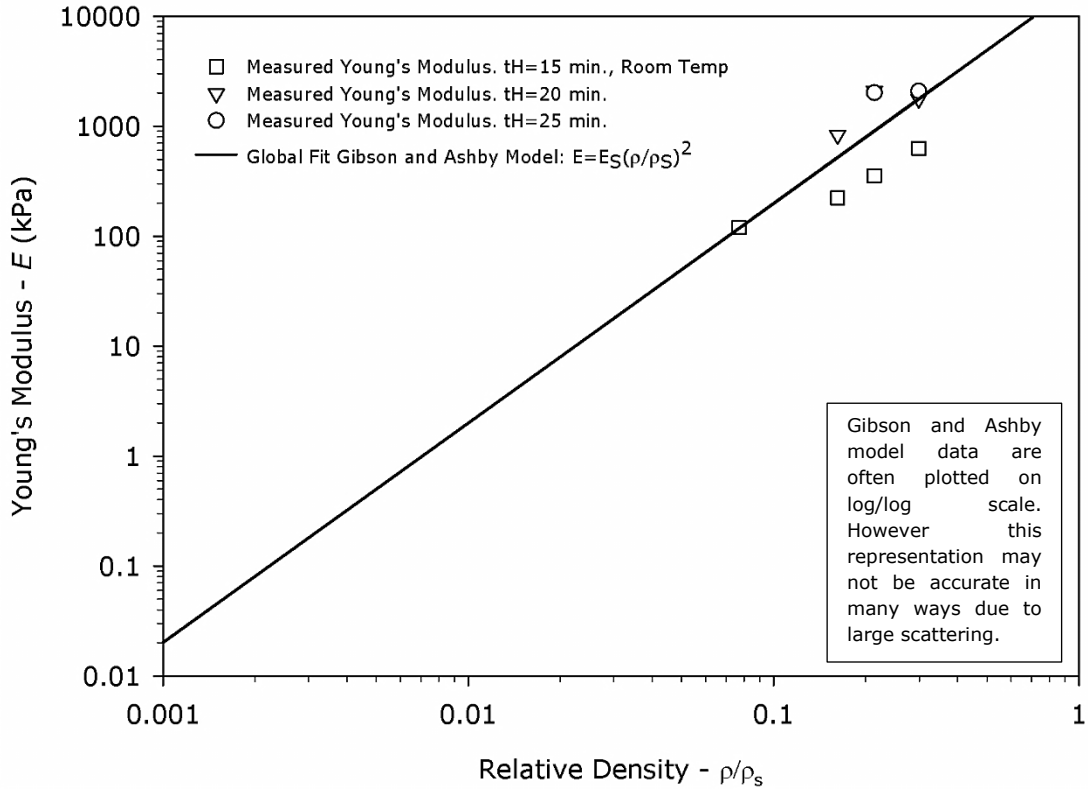

Fig. 4-64: Young's Modulus of all EPHPs series as a function of relative density ρ/ρ_s plotted on double logarithm scale. All data fitted with Gibson and Ashby Model (solid line). Data measured at room temperature.

The plot of Young's modulus as a function of relative density, both on logarithmic scale appears to fit well the whole set of EPHPs data, regardless the large variation due to increased homogenisation time.

Furthermore, the plot resembles quite accurately the common Gibson and Ashby plots (Fig. 2-19) and the triangle at the bottom of the graph is also a common feature of such plots. The triangle indicates graphically that the plot on both logarithm scales is fitted by a an equation with an exponent of 2 (i.e. $log(E/E_S)=2log(\rho/\rho_S)$), basically supporting the suitability of the model.

On the other hand a logarithmic scale may result fairly difficult to provide adequate data when read. Minor errors in locating the relative density points may result in rather large modulus readings as they are also reported on a logarithmic scale.

4.3.3. Specific Absorbing Energy

The SAE of EPHPs with higher solid content follows the same trend of Young's moduli. Both properties are in fact enhanced. The data for SAE of EPHPs with increasing solid content are shown in Fig. 4-65.

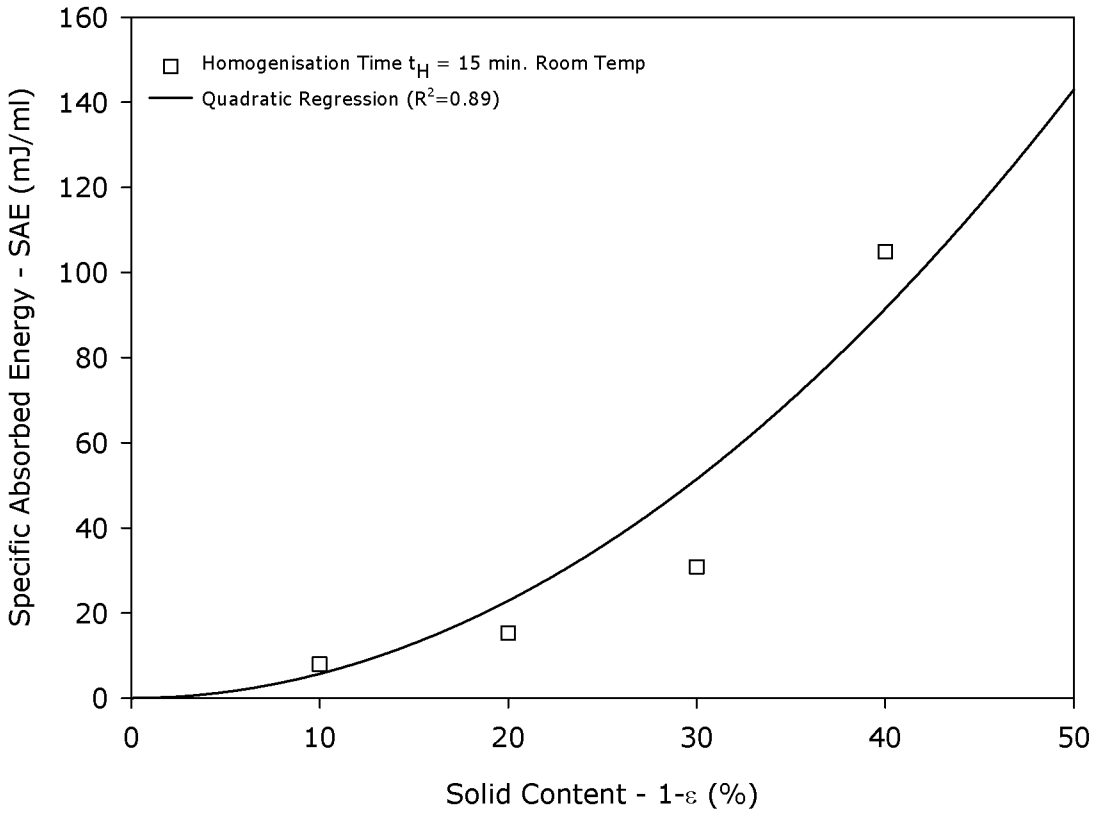

Fig. 4-65: Specific absorbing energy as a function of solid content for S10-15, S20-15, S30-15 and S40-15 EPHPs series. Data at room temperature.

The quadratic regression resembling the Gibson and Ashby model (Eqn. 2-36) describes the SAE trend for homogenisation time t_H=15 minutes properly, and similarly to Young's modulus.

However, when the whole series of EPHPs SAE is plotted as a function of increased solid Fig. 4-66, the quadratic trend does not adequately represent (i.e. capture) the positive effects of longer homogenisation time.

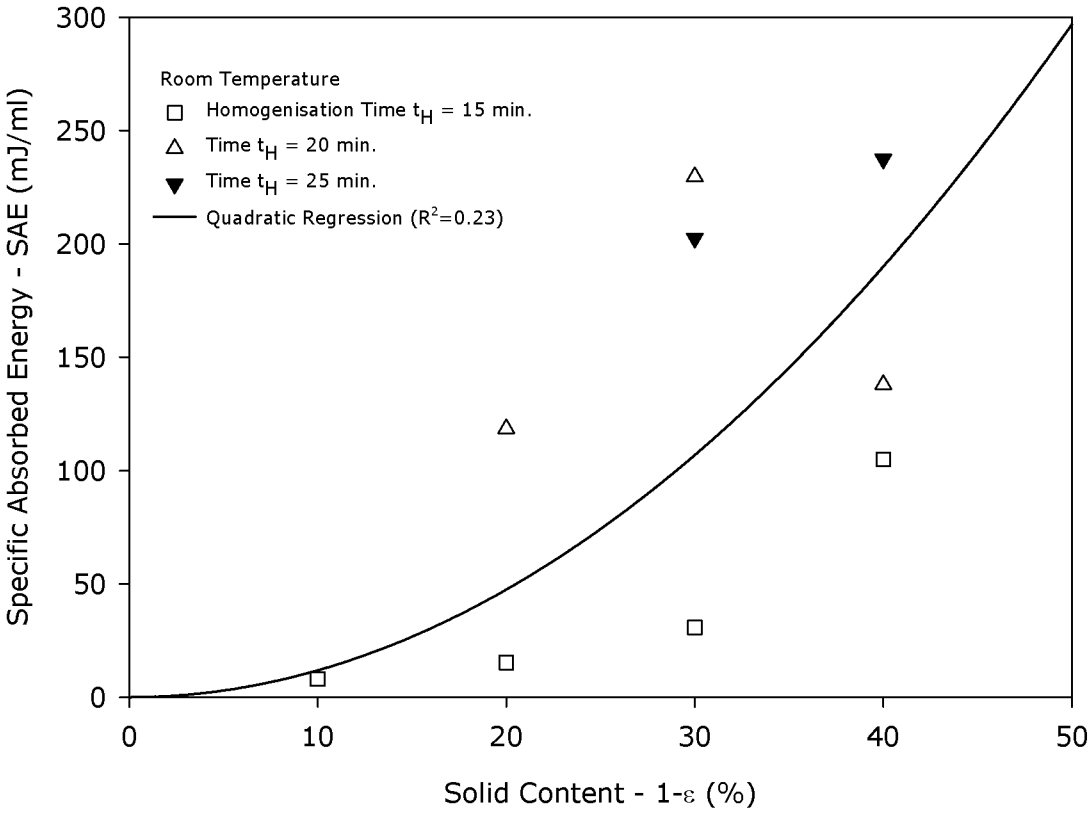

Fig. 4-66: Specific absorbing energy as a function of solid content for all EPHPs series. Homogenisation time t_H=15, 20 and 20 minutes. Data at room temperature.

This apparent lack of adherence between the SAE and the simple quadratic model is not unexpected. As discussed in earlier sections, longer homogenisation time provides a remarkable effect on the EPHPs structure and its consequent mechanical behaviour.

The SAE in fact, accounts for the variation of the stress vs. strain curves, thus from foam to spring-like behaviour. This latter behaviour starts to be observed when the solid content is 20% or higher with $t_H \geq$ 20 minutes.

The overall SAE plot further highlights the importance of t_H with respect to the solid content increase. It can be seen that the solid content is not the most important parameter to obtain EPHPs with higher SAE.

On the contrary, it can be seen and confirmed that t_H can substantially modify (i.e. increase) the SAE value of a given solid content EPHP, making the EPHPs a material whose properties can be tailored according to the required level of performances.

4.4. Effect of solid content and homogenisation time on HIPEs rheology

The preparation of the EPHPs relies on the properties of its originating high internal phase emulsion (HIPE). The rheological properties of various HIPEs have been investigated at room temperature by means of viscosity. The viscosity is a key parameter in processing emulsions as it contributes to energy input losses, with less energy available for homogenisation and structural modification.

Higher viscosities in fact, make the processing more expensive and may limit the stability of the emulsion. The measurements of viscosity aim at understanding the flow properties of the HIPEs (soon after being prepared according to the procedure), with particular reference to their stability with time when transferred into the mould(s).

4.4.1. Viscosity of HIPEs with increasing solid content

The variation of viscosity with time of increasing solid content HIPEs is shown in Fig. 4-67.

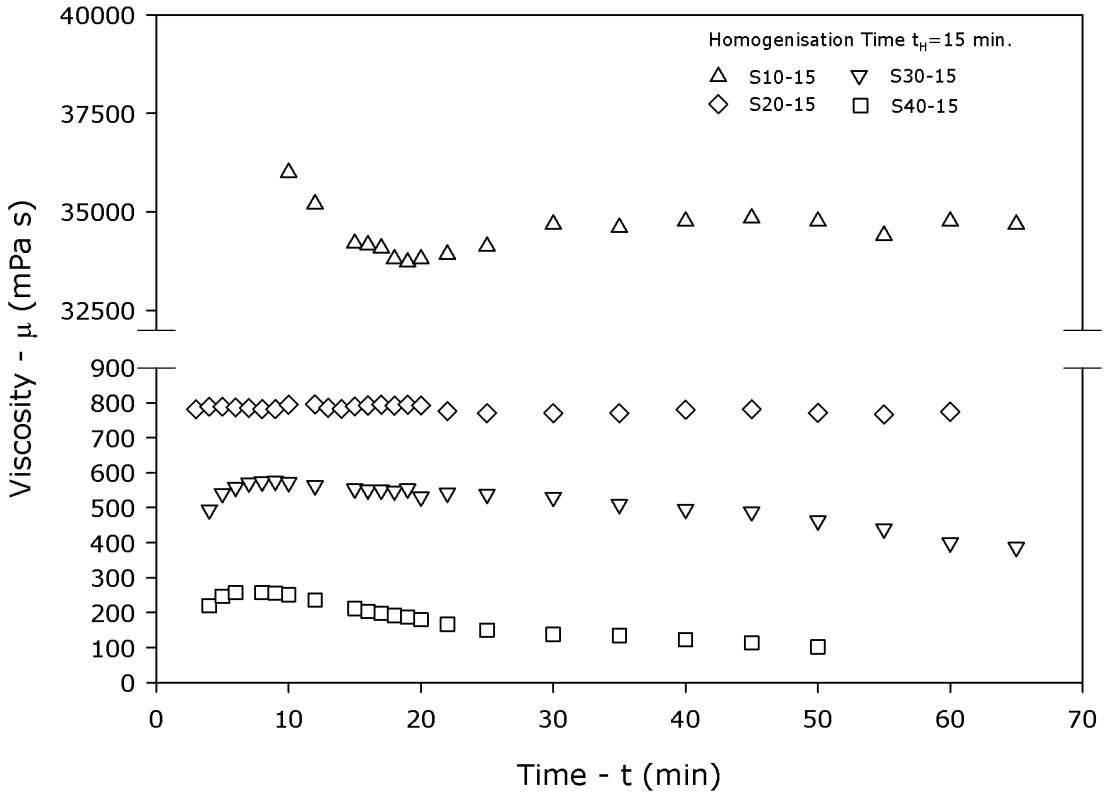

Fig. 4-67: Viscosity of increasing solid content HIPEs as a function of time. Homogenisation time t_H=15 minutes for all the HIPEs. Solid content for S10, S20, S30 and S40(IN) is 10, 20, 30 and 40% respectively.

The first characteristic of the various HIPE viscosities is the remarkably high value for the 10% solid content emulsion. This is, however a typical characteristic of a proper HIPE; 10% oil phase content is, in fact, what generally defines a HIPE.

Moreover, being the emulsion an inverted emulsion, its viscosity is remarkably high. In non-inverted emulsions, the low amount of oil would contribute little to a mainly water-based emulsion.

On the other hand, the inversion of the emulsion and the small average size of the droplets results in high viscosity. Similarly, but with two order of magnitude smaller figures, the viscosity of increasing solid content HIPEs follows a similar trend. As more oil phase is added in the HIPE the lower the viscosity. This behaviour is in line with that of inverted emulsions.

In a non-inverted emulsion, a higher amount of oil phase (in an inverted emulsion) would contribute largely to a higher viscosity. As an extreme example, an HIPE with almost 100% solid content would have a viscosity identical to that of the oil phase, hence much higher than that of water.

The phase inversion actually reverses the properties of the HIPE. The lowering of viscosity for HIPEs with increasing oil phase is consistent and supports the contribution of the resulting pore size and distribution.

The changes in HIPEs viscosity with time, simulating the transferring into a mould, provide an insight for an optimal transfer-time window. Should the viscosity rapidly drop, then an HIPE stability issue would be anticipated and this should be avoided.

A more detailed trend is shown in Fig. 4-68 where the drop in viscosity with time is more evident, particularly for S30-15 and S40-15 samples.

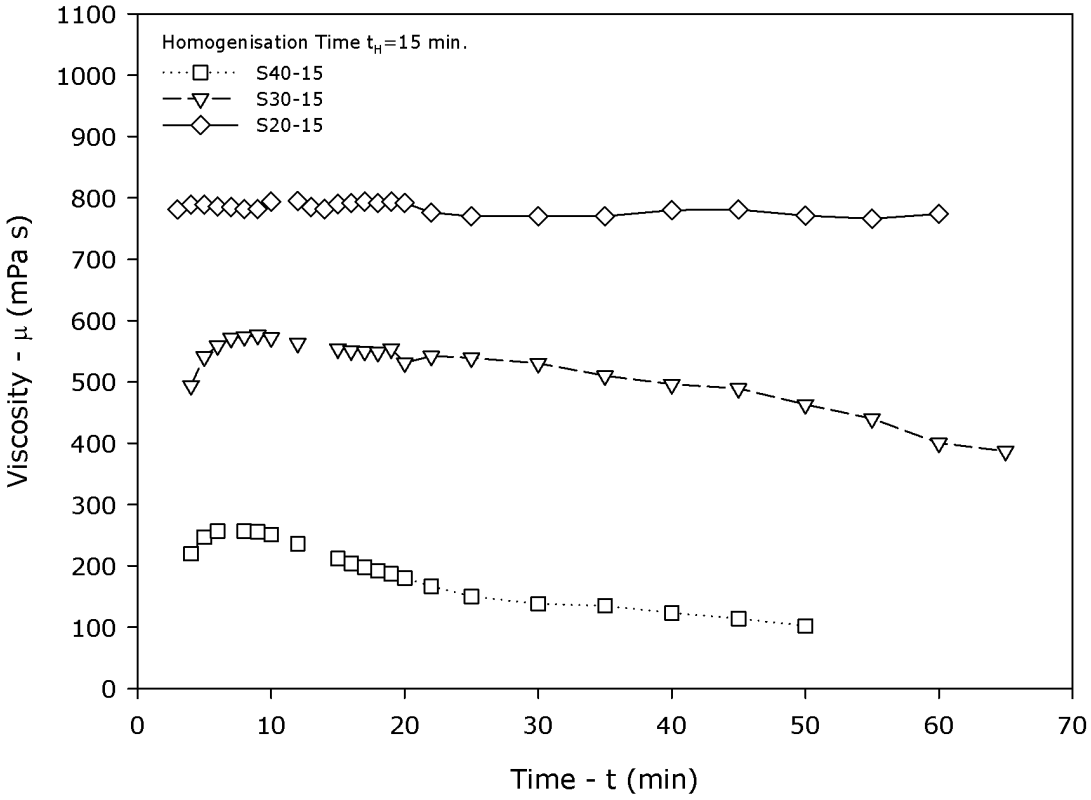

Fig. 4-68: Viscosity of increasing solid content HIPEs as a function of time. Homogenisation time t_H=15 minutes for all the HIPEs. Solid content for S10, S20, S30 and S40(IN) is 10, 20, 30 and 40% respectively.

The drop in viscosity is more evident for sample S40-15; this is particularly marked in a narrower time interval. Sample S40-15 viscosity stability window is likely to be satisfactory for no longer than 10 to 15 minutes. Although S30-15 also shows a similar decease of viscosity with time, the stability window is wider. Transferring time up to 25-30 minutes does not cause an appreciable change in the emulsion rheological behaviour.

Both stability time-interval windows can be considered as indicators of manufacturing process effectiveness. When the same process is applied to substantially different emulsions (i.e. HIPEs with higher oil phase ratio), limitations occur.

On the other hand, a much wider almost time-insensitive behaviour is observed for S20-15 HIPE. Unlike the other HIPEs with higher oil phase ratio, it does not show any change in viscosity with time. This remarkable feature reflects the effectiveness of the manufacturing process in stabilising the emulsion.

The overall rheological behaviour therefore helps understating practical post-processing properties such as the emulsion transferring/moulding stability time and process manufacturing effectiveness. The latter characteristic is particularly useful to implement changes such as reactor/mixing equipment.

4.4.2. Viscosity of HIPEs with increasing homogenisation time

The processing of emulsions has a remarkable effect on their final properties, whether rheological or mechanical. For the rheological case, the viscosity of the highest oil phase HIPEs (S40(IN) series) as a function of increased homogenisation time has been examined (Fig. 4-69).

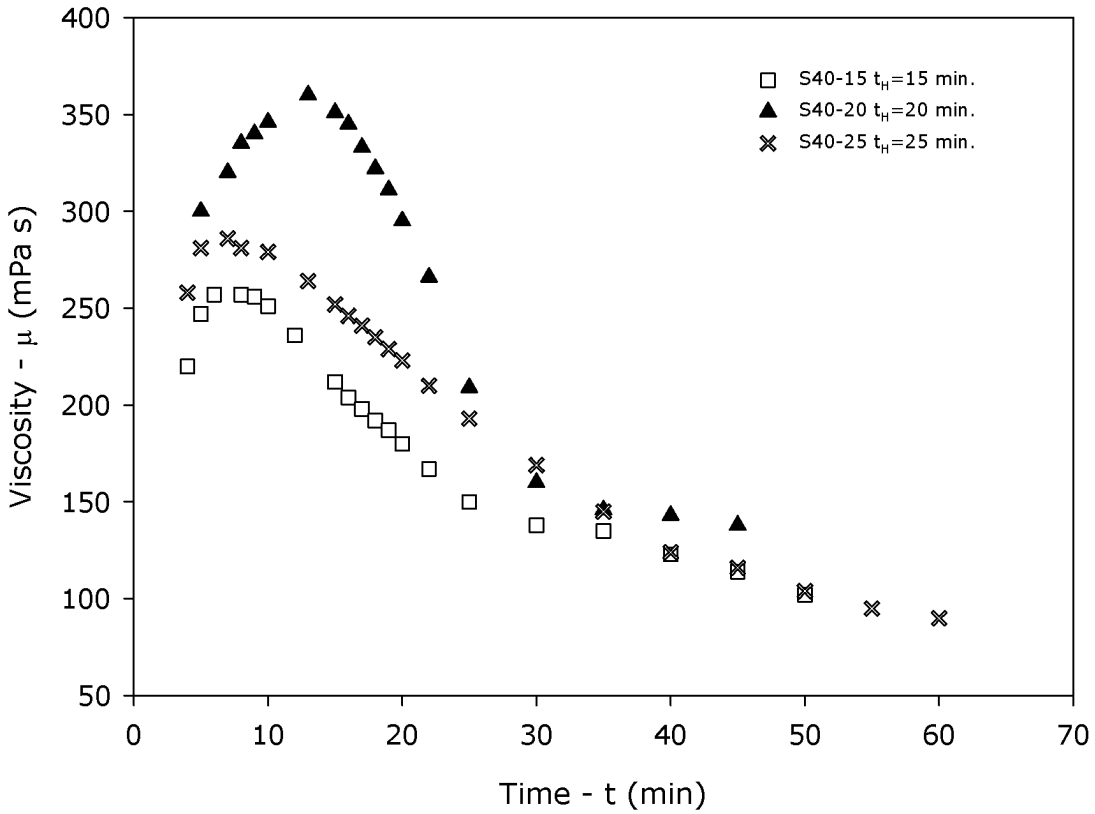

Fig. 4-69: Viscosity of S40(IN) HIPEs series as a function of time. Homogenisation time t_H=15, 20 and 25 minutes for S40-15, S40-20 and S40-25 respectively.

The effect of increased t_H can be seen to be particularly marked during the initial time interval (from 5 to less than 10 minutes). The data follow the same trend: from an initial reading to a maximum, before a more pronounced and almost steady drop occurs as a typical shear-thinning behaviour.

Sample S40-15 and S40-25 are characterised by similar values while S40-20 show a higher maximum which, however drops at a faster rate.

This behaviour can be considered satisfactory because, despite the slightly higher maximum of S40-20, all data tend to approach the same value as time increases. Sample S40-15 and S40-25 viscosity actually overlaps when exceeding 30 minutes. S40-20 viscosity approaches the other samples value after 25 minutes and resembles the same limit value after 30 minutes.

The rheology of HIPEs provides precious insights; not only has it confirmed that HIPEs viscosity is largely influenced by the oil phase ratio but also by the pore size and distribution.

Further knowledge of the HIPEs stability can be derived by analysing the viscosity when moulding/transferring time is accounted for. Stability with time is related to the capability of the system in creating homogeneous emulsions.

4.5. Effect of temperature on PoyHIPEs mechanical performance

All the results presented in the previous sections are referred to data taken at room temperature. The effects of lower and higher temperatures on the mechanical performances of EPHPS are presented and discussed here.

The two temperatures at which the EPHPs were tested reflect conditions at which an IRM may be subjected to work. Cold temperatures slightly above 0°C are not rare in Northern European Countries in winter while high temperatures in the range of 45±5°C may be a common occurrence Northern African and Middle East Countries summers.

The effect of temperature on mechanical properties of polymeric materials is well known. Operating temperatures close to the glass transition temperature t_g should be avoided; under this circumstance a polymeric materials starts to soften and its properties, with the elastic modulus above all, dramatically decrease making it no longer suitable for the original purpose.

Low temperatures cause the material to become brittle with energy absorption properties severely affected.

4.5.1. Young's Modulus

The modulus of EPHPs at low, room and high temperature is shown in Fig. 4-70.

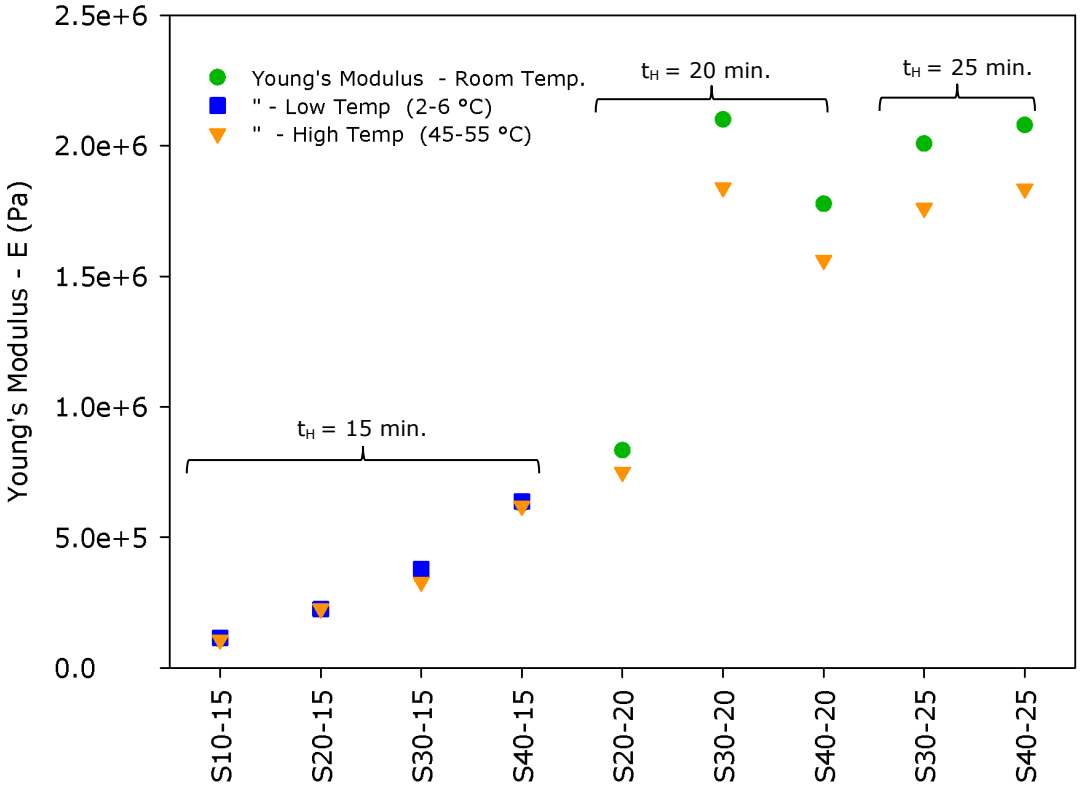

Fig. 4-70: Complete EPHPs series Young's modulus at low, room and high temperature.

It can be seen that the variation of the elastic moduli with temperature is limited. This interesting result is particularly relevant for samples with t_H=15 minutes, and it appears to be independent from solid content.

Young's modulus of higher solid content EPHPs starts to be slightly affected by higher temperatures when tH≥ 20 minutes instead. However, the variation between room and high temperature values is moderate (±10% variation with reference to room temperature). The difference seems to reach a maximum value for sample S30-20, compared to almost no difference for S30-15. A similar trend is observed when examining S40(IN) series: from practically no difference for S40-15, to almost identical ranges for S40-20 and S40-25.

The latter results indicate that the structural modification of the EPHPs due to longer t_H plays a more important role on Young's modulus change with temperature. In addition to that, the difference tends to remain constant for t_H=20 and t_H=25 minutes, hence the effects can be controlled.

The variation of elastic moduli is limited by the cross-linking of the monomers. As already presented in the dedicated section and effectively depicted in Fig. 2-51a, a

cross-linked polymeric network is much less susceptible to temperature variations. The (idealised) polymer chains are prevented from sliding paste each other by the cross linker component; therefore the effect of temperature is greatly reduced.

4.5.2. Specific Absorbing Energy

The effects of temperature on Young's modulus have determined the important role played by the cross-linked structure of EPHPs. As the SAE represents the energy per volume that is stored in an EPHP sample upon compression, all the structural characteristics beyond Young's modulus are also accounted for.

The SAE of EPHPs at low, room and high temperature is shown in Fig. 4-71.

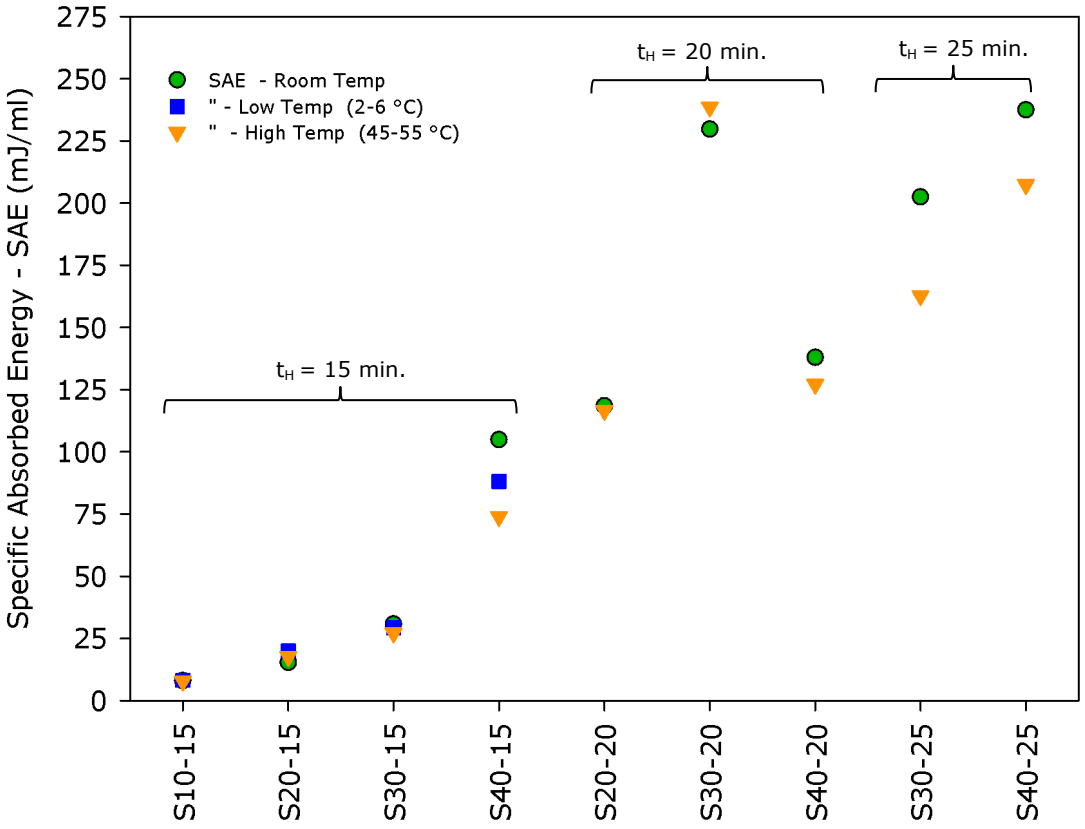

Fig. 4-71: Complete EPHPs series specific absorbing energy at low, room and high temperature.

Similarly, but to a greater extent for the SAE, the effect of temperature on EPHPs is related to their structure. For EPHPs with t_H=15 and 20 minutes, the variation of SAE with temperature is very limited. An exception to this is represented by sample S40-15 (40% solid content).

The reason for such a slightly different result is probably related to the sample compression testing accuracy. In fact, support to this is provided by the low temperature SAE value to be lower than that at room temperature; the opposite behaviour would be expected instead.

Further support is given by analysing the results for samples with t_H=20 minutes (i.e. S20-20, S30-20 and S40-20). All samples present close values at room and high temperatures conditions.

A more marked trend though, is observed for sample with t_H=25 minutes (S30-25 and S40-25). The two samples present a larger difference between room and high temperature compared to lower solid content and homogenisation time EPHPs. The reasons for such results can be related to the fact that the SAE represents the area under the whole stress vs. strain curve, not only the initial proportional region that determines the elastic modulus.

Furthermore, the changes in the curve shape are due to solid content and/or structural modifications due to mixing. As the wider changes in SAE occur for samples with high solid content and higher t_H, such a behaviour can be attributed mainly to the amount of solids in the EPHPs and how this solid content is distributed in the (idealised) cell. Both these physical characteristics make the EPHPs more sensitive to temperature variations.

4.6. Effect of strain rate and temperature on PolyHIPEs mechanical performance

The effects of temperature discussed in the preceding section have confirmed the importance of the cross-linked structure of the EPHPs. It is in fact this feature that is largely responsible for the EPHPs fairly stable mechanical performance, particularly in the high temperature conditions.

This section presents the stress vs strain curves of two selected EPHPs (S20-15 and S40-15) obtained by varying the strain rate at two different temperatures (room and high). The strain rate is the rate at which the EPHPs disks are compressed. Its effects may become particularly important as the properties of polymeric materials may be seriously affected.

Comparing the combined effects of temperature and strain rate is also common. It is worth recalling the concept of time-temperature-equivalence as it states that the effects of temperature are equivalent to those of strain rate (which is a time dependant quantity), hence their effects are interchangeable. The stress vs. strain curves of S20-15 and S40-15 at various strain rates and temperatures (room and high) are shown in Fig. 4-72 and Fig. 4-73.

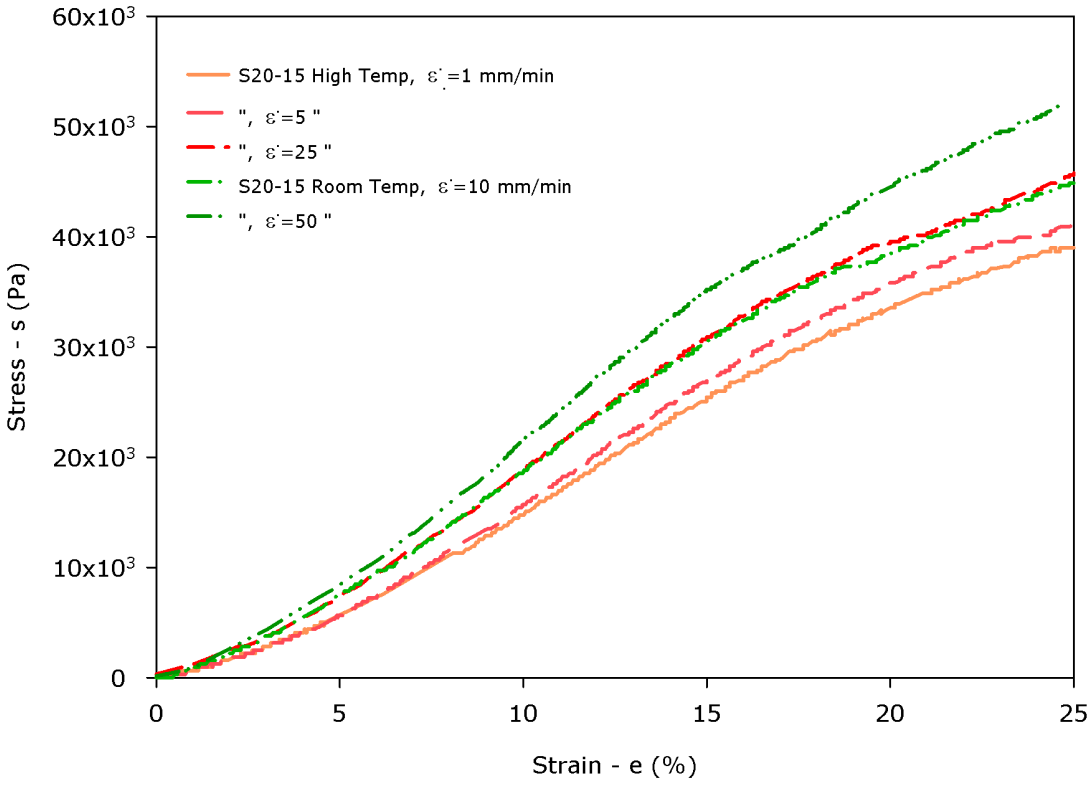

Fig. 4-72: stress vs strain curve for S20-15 sample at various strain rates and temperatures. High temperature range: 45±5°C.

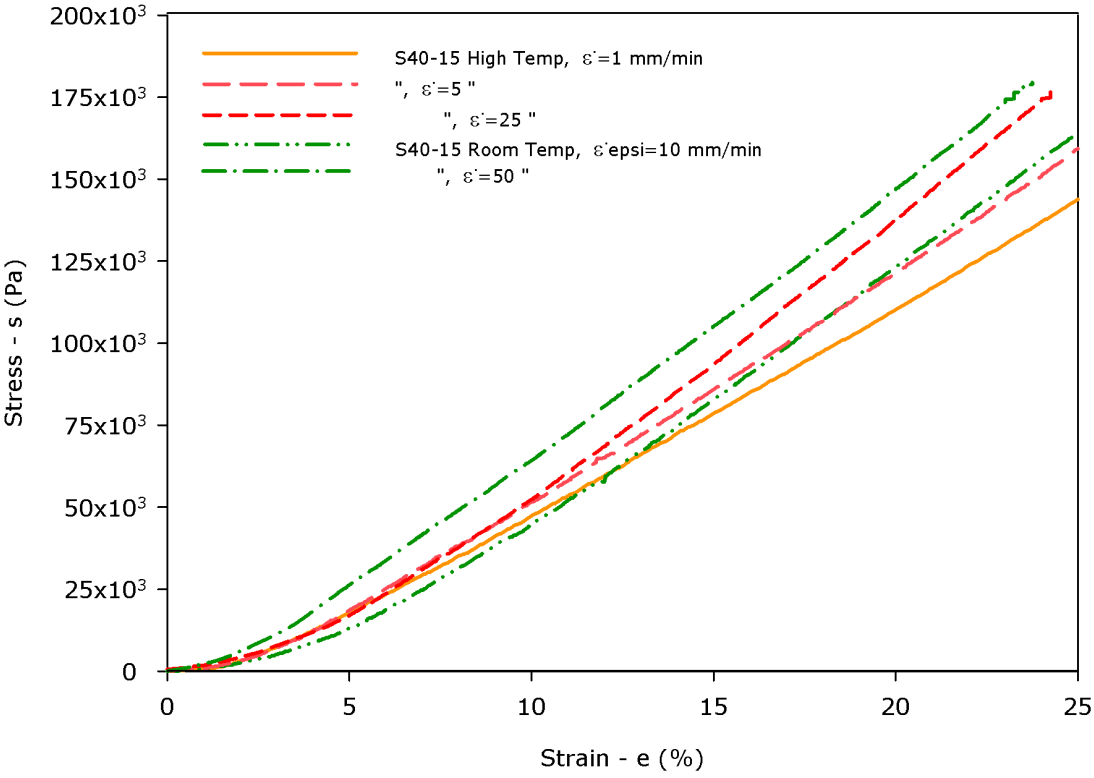

Fig. 4-73: stress vs strain curve for S40-15 sample at various strain rates and temperatures. High temperature range: 45±5°C.

The EPHPs subjected to both strain rate and temperature variation show that the EPHPs depend moderately on both parameters but follow the time-temperature equivalence principle.

Consequently, the lowest and highest stresses are given by the slowest strain rate at the highest temperature, while the opposite result is given by the fastest strain rate at room temperature.

The behaviour at intermediate strain rate conditions follows the expected trend. Just as when S20-15 is compressed at high temperatures its SAE (area under the curve) is slightly lower than that at room temperature, however, an equivalent curve is obtained when the strain rate is 25 mm/min at high temperature.

S40-15 behaves in a rather similar way: the lowest stresses are obtained by compressing the sample at high temperature and the lowest strain rate. Conversely the highest strain rate ($\dot{\varepsilon}$=50 mm/min) at room temperature produces the highest stresses. An almost equivalent stress vs. strain curve is obtained when the strain rate is 10 mm/min at high temperature.

Although S20-15 and S40-15 respond similarly to combined strain rates and temperatures, it appears that S40-15 variations are more limited. With a higher amount of solid content S40-15 tends to behave like a solid more than S20-15 (less amount of solid content) consequently, density and cross-linking play an important role. With higher solid content and with the use of an additional oil phase initiator, S40-15 is less susceptible to strain rates and temperature changes.

Nevertheless, both EPHPs behave according to the time-temperature-equivalence principle and this important result can be used to predict their behaviour at design stage.

4.7. Mechanical performance of two commercial IRMs and comparison with PolyHIPEs

The investigation of the mechanical behaviour of the various EPHPs at different temperatures and strain rates has demonstrated that they maintain their properties almost unaltered. The effects of solid content and structural modification due to energy input (increased homogenisation time) have also demonstrated that the mechanical of the EPHPs can be modified significantly. As a result, the typical foam curve of low solid content EPHPs can become a solid-like (spring-like) curve under a combination of homogenisation time and solid content increase.

However, these remarkable results would be of limited significance if not compared to existing impact resistant materials. The EPHPs have been benchmarked against two different materials whose properties resemble those of the EPHPs.

However, despite substantially different structural characteristics and main material composition, their performances are comparable.

The two materials, *GPhlex* and *D3O*, characteristics are summarised in Table 4-19.

Table 4-19: Benchmarking materials main characteristics. *E* and *SAE* measured at room temperature.

Material	Density (kg/dm^3)	Porosity (%)	*E* (kPa)	*SAE (mJ/mL)*	*SAE by Weight (mJ/mg)*
GPhlex	0.26	20-30	1910	78.5	301.9
D3O	0.59	0	1330	136(*)	230.5

(*) extrapolated value from 42.8% to 50% Strain.

The stress vs. strain curves at room temperature, plotted in Fig. 4-74, highlight the behaviour of both benchmark materials.

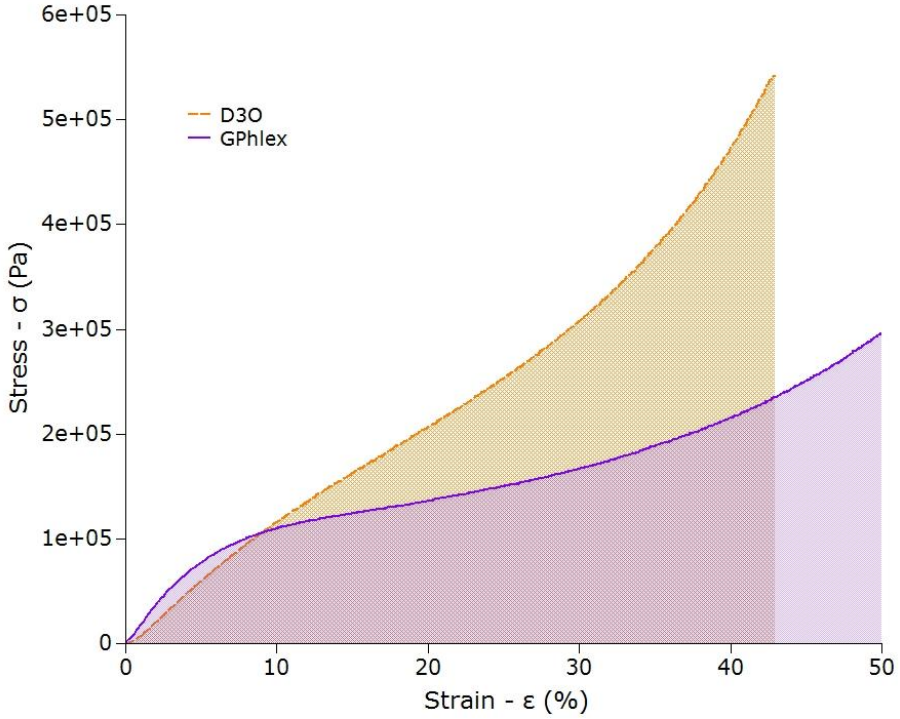

Fig. 4-74: Stress vs. strain curves for reference materials GPhlex and D3O at room temperature. Strain rate: 1 mm/min. Shaded areas represent the specific absorbed energy – SAE (in mJ/mL).

GPhlex material is porous and it behaves like a foam when compressed. A linear response region due to the elastic bending of the pores is followed by a wide Plateau region, with early signs of densification when strain exceeds 40%.

The D3O material characteristics are also well described by the shape of a rather different curve. An almost linear proportionality between stress and strain is

observed up to 30% strains. As compression continues, the material enters the densification region without any intermediate *Plateau region*. In addition to that and unlike GPhlex, densification is clearly manifested when $\varepsilon \geq 30\%$.

4.7.1. Benchmark materials structure

The structures of the GPhlex and D3O materials are shown in Fig. 4-75 and Fig. 4-76 respectively.

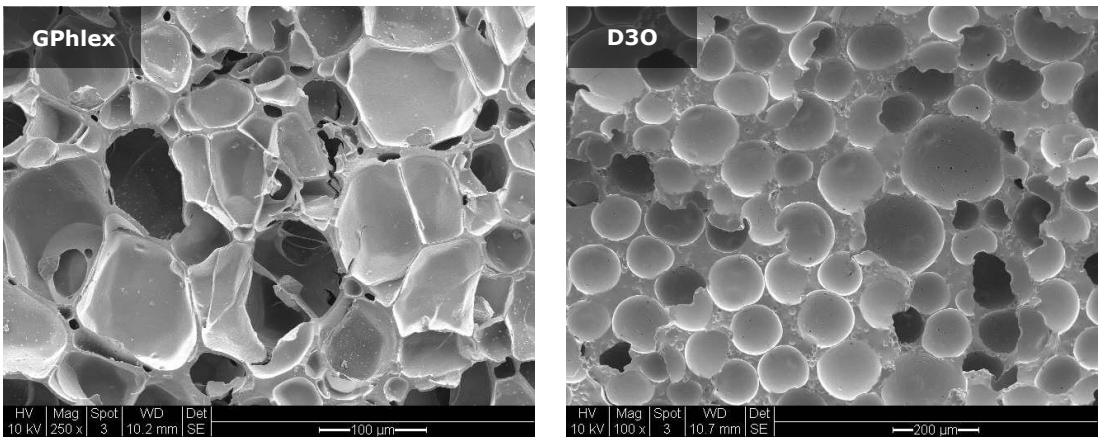

Fig. 4-75: GPhlex and D3O materials SEM images at 250x and 100x magnification, Scale bar 100 and 200 μm respectively. Closed-cell, porous layout of GPhlex and non-porous matrix-embedded spherical particles structure of D3O.

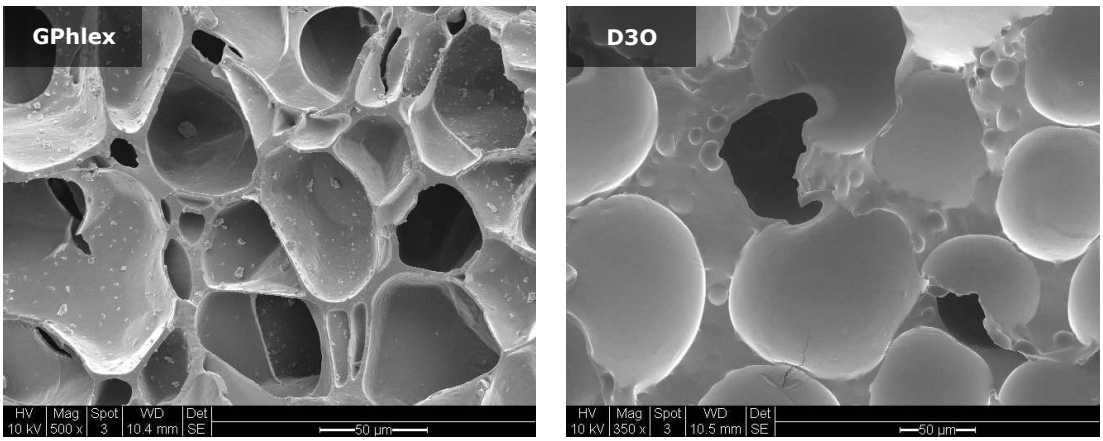

Fig. 4-76: GPhlex and D3O materials SEM images at 500x and 350x magnification, Scale bar 50 μm. Details of Closed-cell, porous layout of GPhlex and non-porous matrix-embedded neighbouring spherical particles structure of D3O.

The SEM imaging reveals that GPhlex is composed of a closed-cells porous structure, with an average pore size of 57 μm and an almost symmetrical, rapidly decreasing distribution around the central value (Fig. 4-77).

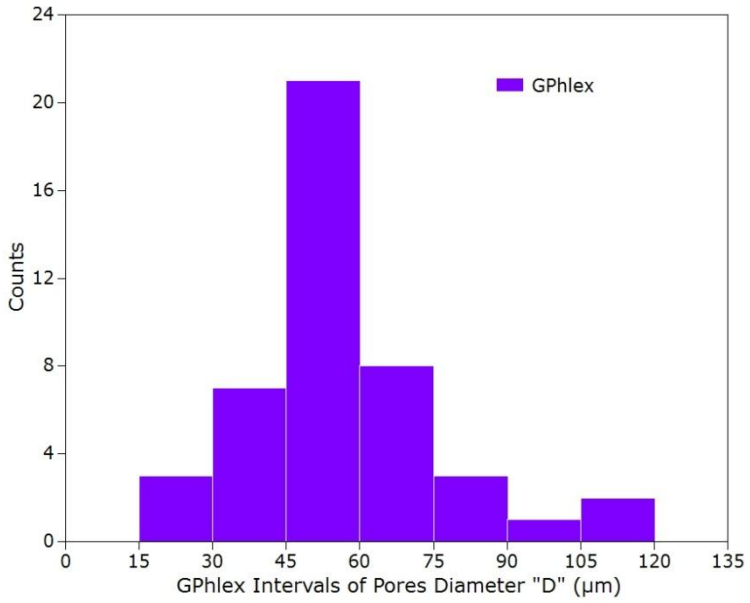

Fig. 4-77: Pores Diameter size distribution of GPhlex (total readings 45, diameter interval 15 µm, Average Pore size *D*=57.0 µm).

The D3O material is instead made of a less stiff elastic matrix (reflected by a lower *E*) with dense-solid spherical particles. The much harder spheres are likely to cause the densification when the softer matrix has been almost fully compressed. The average size of the spheres is 111 µm with rapidly decreasing occurrences at higher values, as shown in Fig. 4-78.

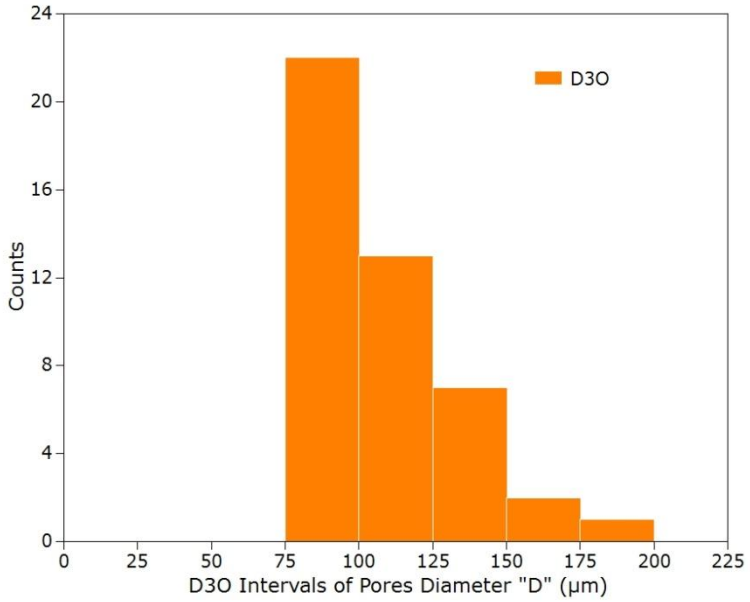

Fig. 4-78: Spherical Particles Diameter size distribution of D3O (total readings 45, diameter interval 25 µm, Average particle size D_P=111.0 µm).

The details of the porous and non-porous structure of the two materials then explain their different behaviours, particularly for the initial linear-elastic response.

While GPhlex is a porous material and D3O is a composite, it is expected that the composite material comes with a higher energy absorption capability. The area

under the stress vs. strain curve also confirms this. However, it is the density of the materials that plays a relevant role when comparing the *SAE*.

The porous structure of GPhlex makes it much lighter than D3O; 0.26 mg/ml instead of 0.59 mg/ml respectively. The density ratio is 2.27 and this feature provides a distinctive advantage for GPhlex. In fact, the SAE of GPhlex with reference to its density reaches a value of ~310 mJ/ml, while that of D3O is only 230 mJ/ml despite its stiffer spherical particles matrix.

4.7.2. Effect of temperature on mechanical behaviour

The mechanical performances of both benchmarking materials have been also assessed at low and high temperatures. A material that performs satisfactory at room temperature may not perform equally well in temperature is changed. The stress vs strain curves at low, room and high temperature of GPhlex and D3O are shown in Fig. 4-79.

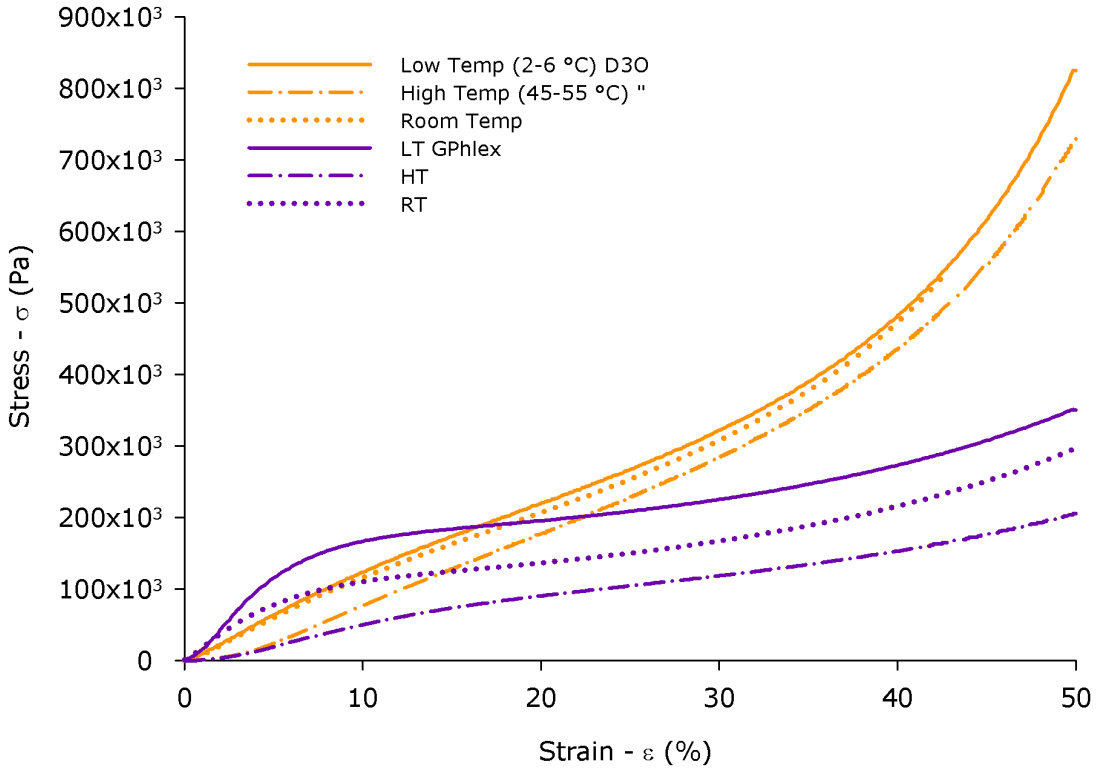

Fig. 4-79: Stress vs. strain curves of GPhlex and D3O materials at low, room and high temperature.

As can be seen, the effects of temperature are quite significant. GPhlex material Young's modulus is particularly sensitive as it becomes much smaller at high temperature. In the same way, its value increases at low temperature. This behaviour clearly results from the constituent material: nitrile-based with an approximate t_g range between -38 and -2 °C.

The low t_g results in a high sensitivity of material properties. The elastic modulus and the *SAE* are inversely proportional to the operating temperature. Although an increase of SAE is observed at low temperatures, the value drops significantly when operating at high temperature. Furthermore, the structure still has an important impact on the material properties: the foam like behaviour is retained.

The D3O material also is affected by variations of temperature, but to a much more limited extent. It is worth noting that the difference between low and room temperature is very limited. Similarly, the high temperature curve is only slightly different, with an elastic modulus that is almost unaffected. All these properties can be related to the T_g of the material that is likely to be in the range of 5-25 °C. Such a hypothesis must be made as the material is a patented and very little amount of technical information is available from the supplier.

4.7.3. Young's Modulus and Specific Absorbed Energy

The comparison of benchmarking materials and EPHPs is presented and discussed. The Young's modulus and the SAE as a function of temperature are shown in Fig. 4-80 and Fig. 4-81 respectively.

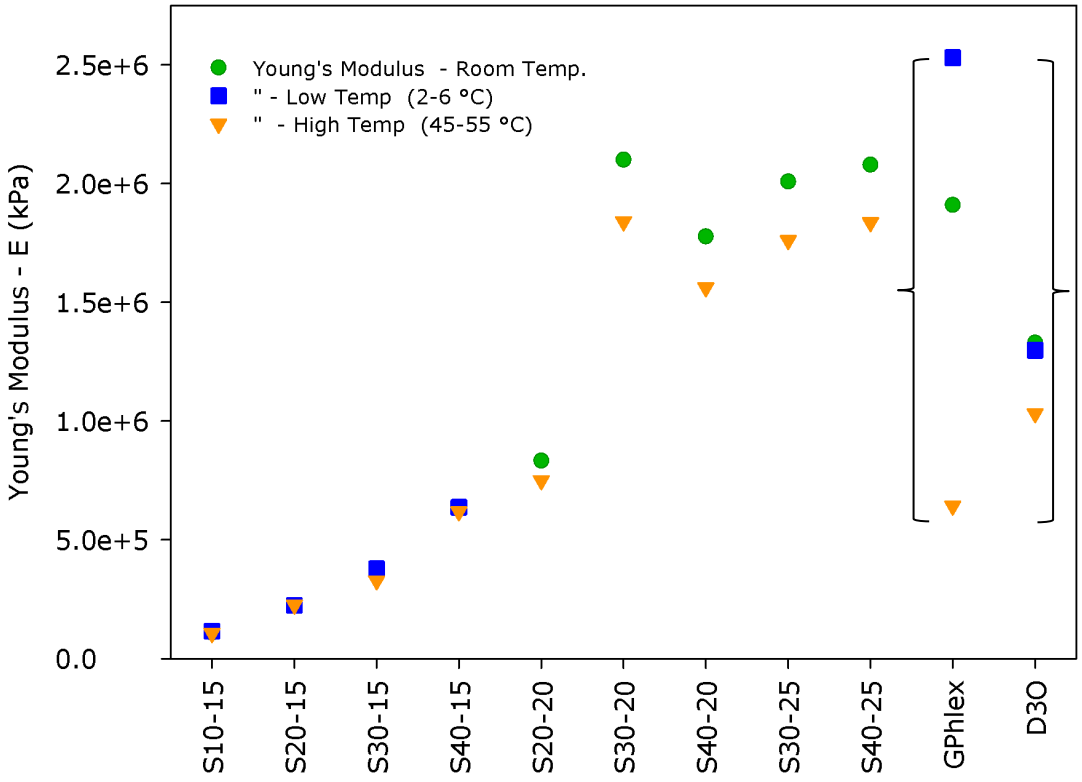

Fig. 4-80: Young's modulus of complete EPHPs series, (sorted by increasing solid content and homogenisation time) and benchmark materials GPhlex and D3O at low, room and high temperature. The parentheses highlight the benchmark materials results.

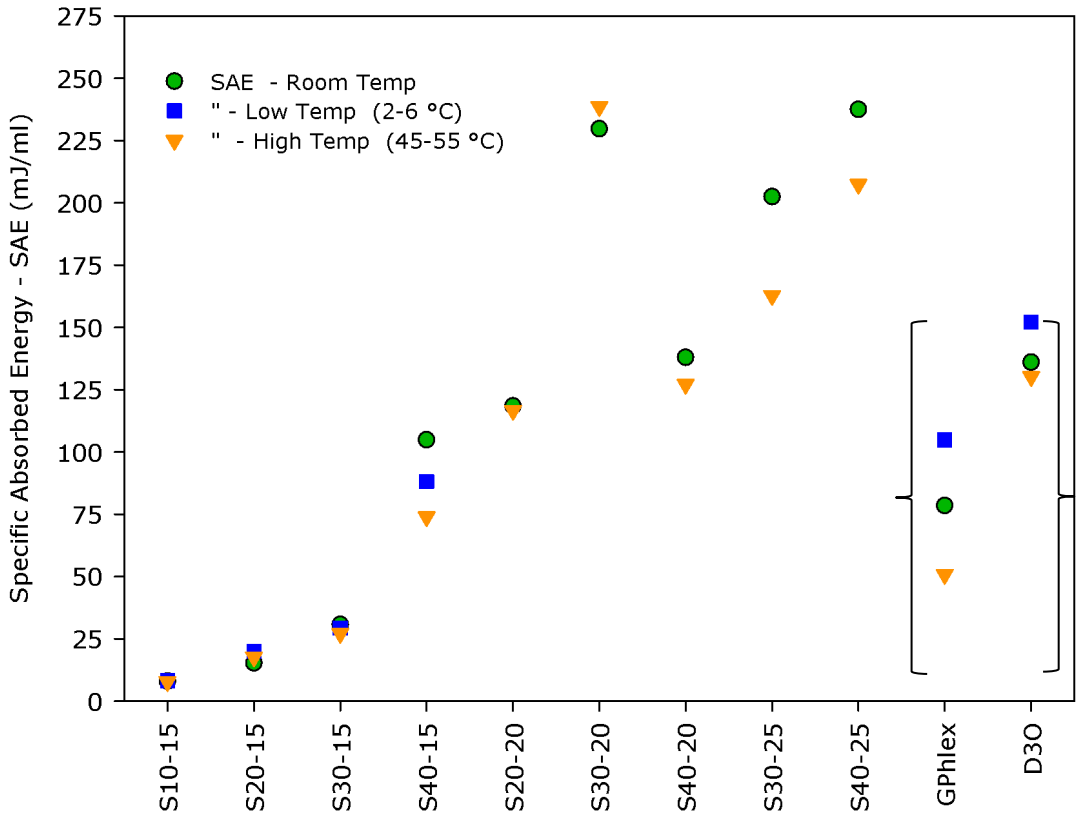

Fig. 4-81: Specific absorbed energy of complete EPHPs series (sorted by increasing solid content and homogenisation time) and benchmark materials GPhlex and D3O at low, room and high temperature. The parentheses highlight the benchmark materials results

The plots effectively highlight the influence of the temperature on the benchmark materials. Most notably, GPhlex high temperature Young's modulus drops by 65% compared to room temperature. Furthermore, this value is in line with that of low solid content EPHPs which are, in turn, practically insensitive to temperature variations.

In addition to this, it can be observed that all the EPHPs samples with t_H>15 min. have a higher modulus and SAE of GPhlex, regardless of the temperature.

D3O material also is compared to the complete EPHPs series. Similarly to GPhlex, its modulus and SAE are matched and in many cases exceeded by EPHPs. The modulus of D3O is systematically lower than EPHPs with solid content higher than 30% and t_H≥20 min. The same results have been observed for D3O *SAE*.

These important results further support the concept of EPHPs process-tailored properties. Lighter (less dense) EPHPs can have higher *E* and *SAE* than GPhlex and D3O. Even more importantly, their properties are more stable when the operating temperature changes.

4.7.4. EPHPs property plan

The variety of mechanical properties and structural layouts that have been observed for EPHPs and the two benchmarking materials can be grouped into a "Structure-*Property Plan*". Such a schematic representation, shown in Fig. 4-82, aims at providing an immediate property and structure reference tool where the tailorable properties of EPHPs are exploited.

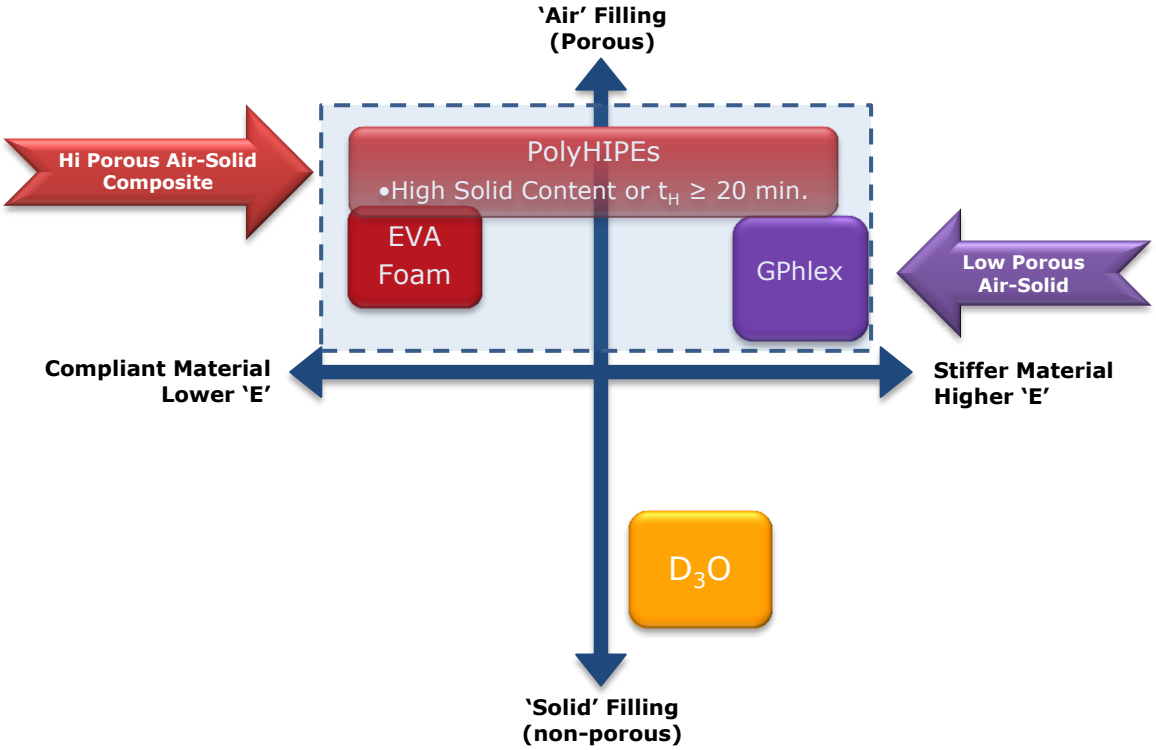

Fig. 4-82: Structure-Properties Plan. The materials are located according to their filling component, either solid or air (vertical axis) and stiffness (Young's modulus) on the horizontal axis. The Specific Absorbed Energy (dashed rectangle) among various EPHPs series and *GPhlex* is equivalent at room temperature.

The *Materials Structure-Property Plan* shows qualitatively where each material class would fall according to stiffness and porosity. The vertical axis ranges from solid to air filling and mainly exploits the structural properties of the materials.

The non-porous fully dense D3O material is located at the bottom. Conversely, porous materials such as EPHPs and GPhlex are located toward the top end of the axis, with the EPHPs above due to their higher porosity.

As the horizontal axis highlights the stiffness of the materials, compliant materials are located on the left while stiffer materials are located on the right. The horizontal axis thus refers qualitatively to the Young's modulus and it can be seen that GPhlex is the material with the highest elastic modulus.

The particularly interesting structure-property of the EPHPs can be seen effectively in the plan and even in higher details as depicted in Fig. 4-83 where the Young's modulus is plotted as a function of homogenisation time and oil/water phase ratio.

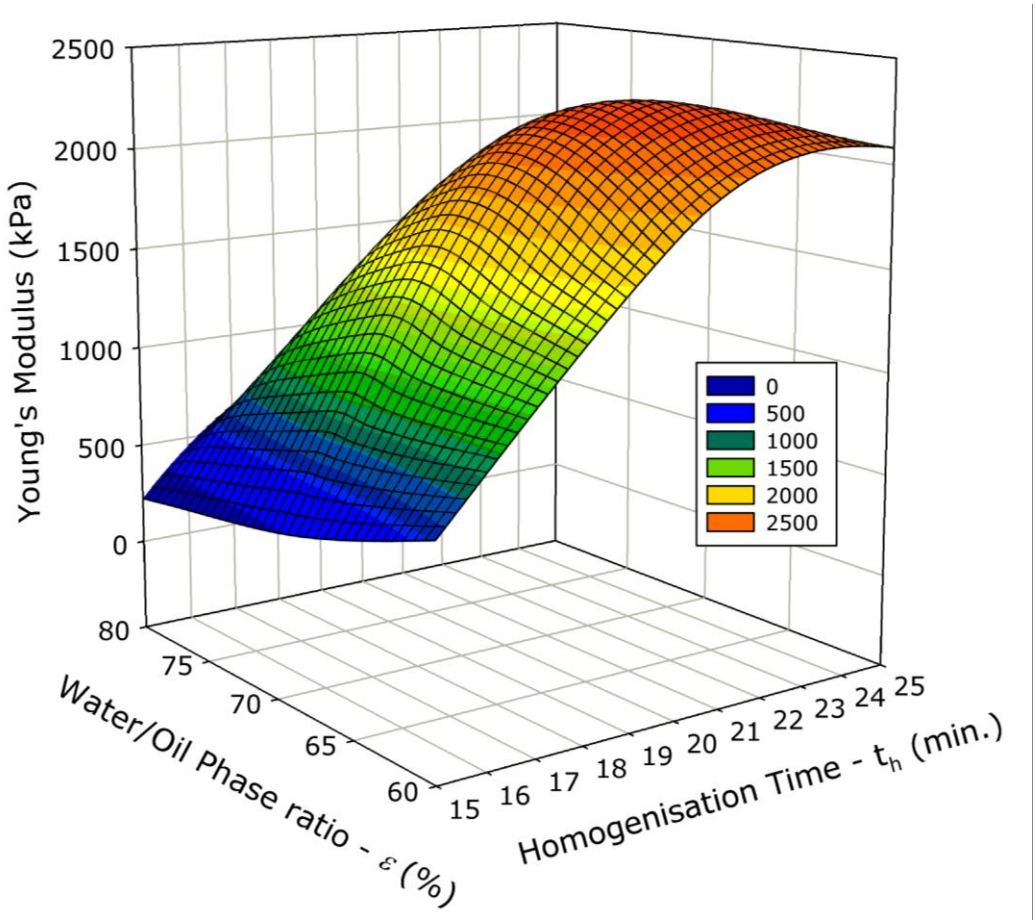

Fig. 4-83: EPHPs Young's modulus as function of Water/Oil phase ratio and homogenisation time.

The EPHPs, in fact, can be formulated and/or processed to be characterised by a wide range of elastic modulus. The upper quadrants of the plan are occupied by both compliant (e.g. 10% solid content) and stiffer EPHPs (higher solid content). Such a remarkably wide range can be obtained by either increasing solid content or homogenisation time for various EPHPs. The latter processing property has demonstrated to be even more relevant to improve the elastic modulus and absorption energy.

When EPHPs and GPhlex materials are compared in terms of energy absorption capability, the EPHPs properties envelope is rather wide (the dashed rectangle). Hence the structure-properties plan highlights the equivalence of *SAE* among many EPHPS and GPhlex at room temperature. The comparison is even more effective when the porosity of both materials is considered. EPHPs with higher porosity (i.e. lower solid content) match and/or exceed the SAE of GPhlex. Such a condition

further confirms that the tailorability of the EPHPs is a fundamental advantage toward achieving desired properties.

EPHPs are materials that can behave like foam and also like solid materials; they are structure-dominated materials whose mechanical properties can be set and controlled at the design and processing stage. Evidence of such an invaluable set of properties is provided by the EPHPs capability to absorb an equivalent amount of energy as do GPhlex and D3O, while being characterised by neither of their properties.

4.8. Modulus vs. Density Charts

In the previous section, the mechanical properties of EPHPs have been compared with those of two commercially available materials. For more generic purposes though, it is interesting to provide these properties with a wider context. For such a purpose, the well-known *Material Selection Charts* (also known as *Ashby Charts*) are used. The *Material Selection Charts* are capable of representing classes of materials according to a combination of properties. The charts usually present two properties from which it is possible to effectively group materials in envelopes. By plotting for instance the Young's modulus vs. density (Fig. 4-84), it is possible to identify the materials, or class of materials, that are stiff and light.

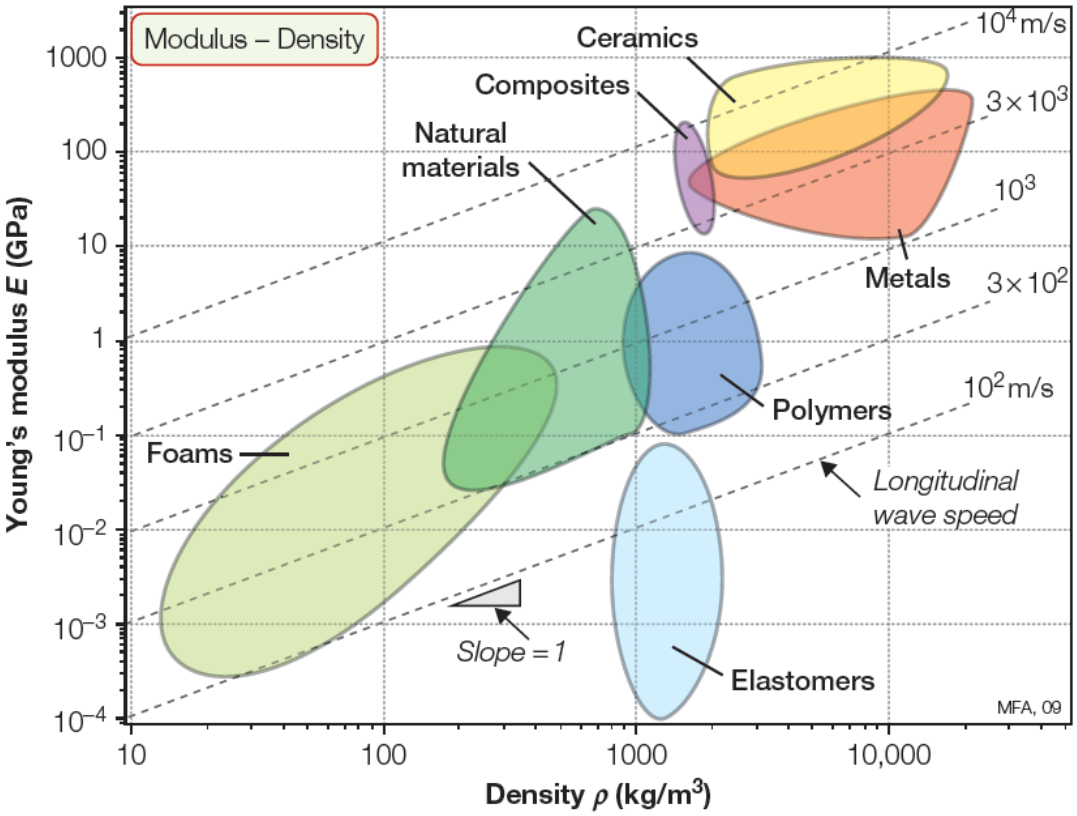

Fig. 4-84: Young's modulus plotted against the density on log scales. The dashed lines show the longitudinal elastic wave speed $v=(E/\rho)^{0.5}$. Different classes of materials can be linked by the same wave speed.

The elastic modulus against density chart shows further useful parameters that provide additional insights. For instance, the longitudinal elastic wave speed v is added on the chart and, as it is related to both parameters ($v=(E/\rho)^{0.5}$) it links several classes of materials. Polymers, natural materials and foams, for example share a common value of $v=10^3$ m/s. Another advantage of these charts is that many other parameters can be added to the same plot to minimise or maximise some characteristics. A typical example is when the same material is used in various structural elements such as ties, beams, panels and so forth. Although these elements can be made with the same material, their optimal performances are dictated by different criteria. Ties for instance are designed to carry tensile loads and, for structural applications, they should be a light as possible. Panels, as well as beams are designed to resist bending; the minimisation of their weight is however obtained by addressing specific variables. Thickness is the variable to minimise for panels, while cross-sectional area is the variable to minimise for beams. The minimisation (or maximisation) design requirement objectives are expressed mathematically and referred to as *Material Indexes*. Multiple indexes then are usually shown on *Ashby Charts*. The modulus against density chart with EPHPs is shown in Fig. 4-85 and it identifies the position of EPHPs with respect to all the other material classes.

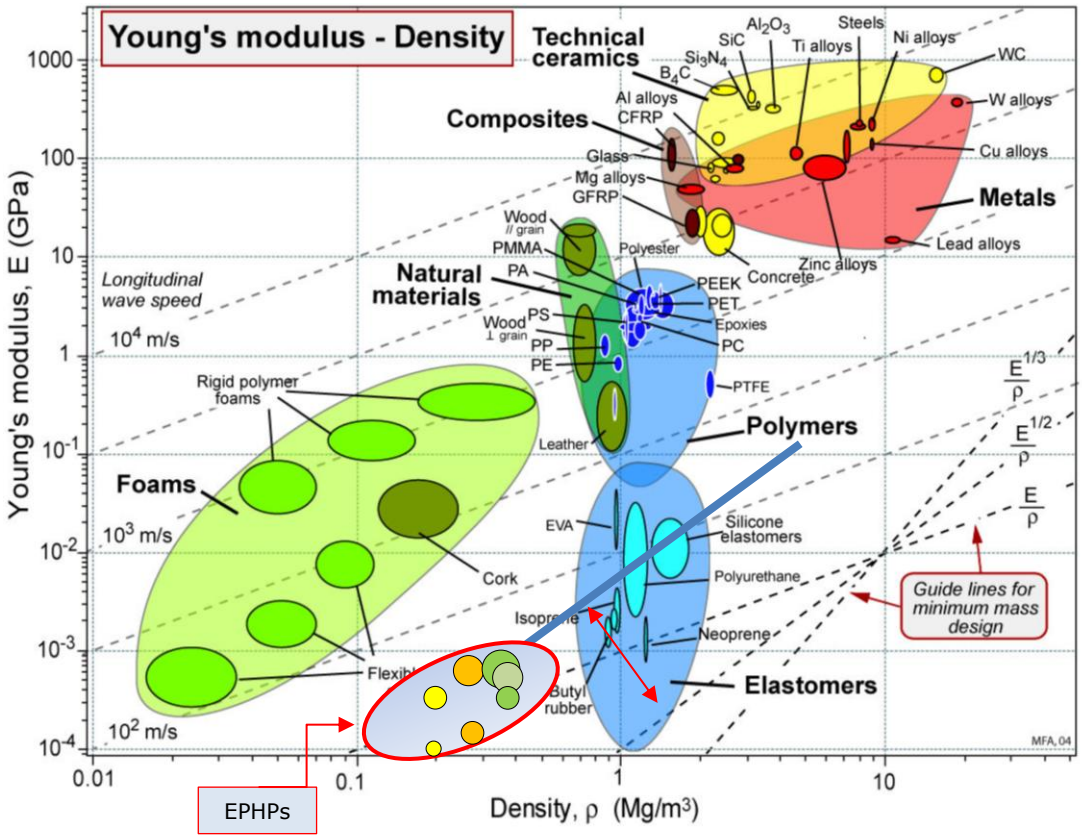

Fig. 4-85: Ashby Materials Chart showing Young's modulus against density. The envelopes enclose data for a given class of materials and the existing gap between foams and elastomers can be filled in by EPHPs. Yellow circles: S20-15 and S20-20 (larger one), Orange: S30-15 and S30-20 (larger one), Green: S40-15, S40-20 (lighter green) and S40-20 (largest circle). Solid blue-line with the same slope as $E^{1/2}/\rho$,as indicated by the double arrowed line.

The portion of modulus vs. density chart that EPHPs occupy is not occupied by any other material, or class of materials; this outcome is of fundamental relevance. EPHPs thus represent a new class of materials that fills an existing gap. Furthermore, the EPHPs are characterised by an optimal minimum mass design criteria for columns and beams (slope of $E^{1/2}/\rho$ dashed line). Hence, EPHPs offer the possibility of extending the material selection choice beyond elastomers (the envelope that includes for instance, polyurethane, rubber and neoprene). EPHPs can perform similarly but with the intrinsic advantage of being lighter. Even more importantly, for a given EPHPs density the elastic modulus can be tailored and its value can be increased about 10 times; such a feature is exploited by processing the unique hierarchical structure of the EPHPs. In light of these remarkable results, a further similar approach has been developed with the intention of providing *EPHPs Materials Process/Performance Design Chart*. By relating the square of pore radius as a function of cell wall thickness, the construction of material properties envelopes has been possible. The plot shown in Fig. 4-86 illustrates the relationship between these two EPHPs geometrical features.

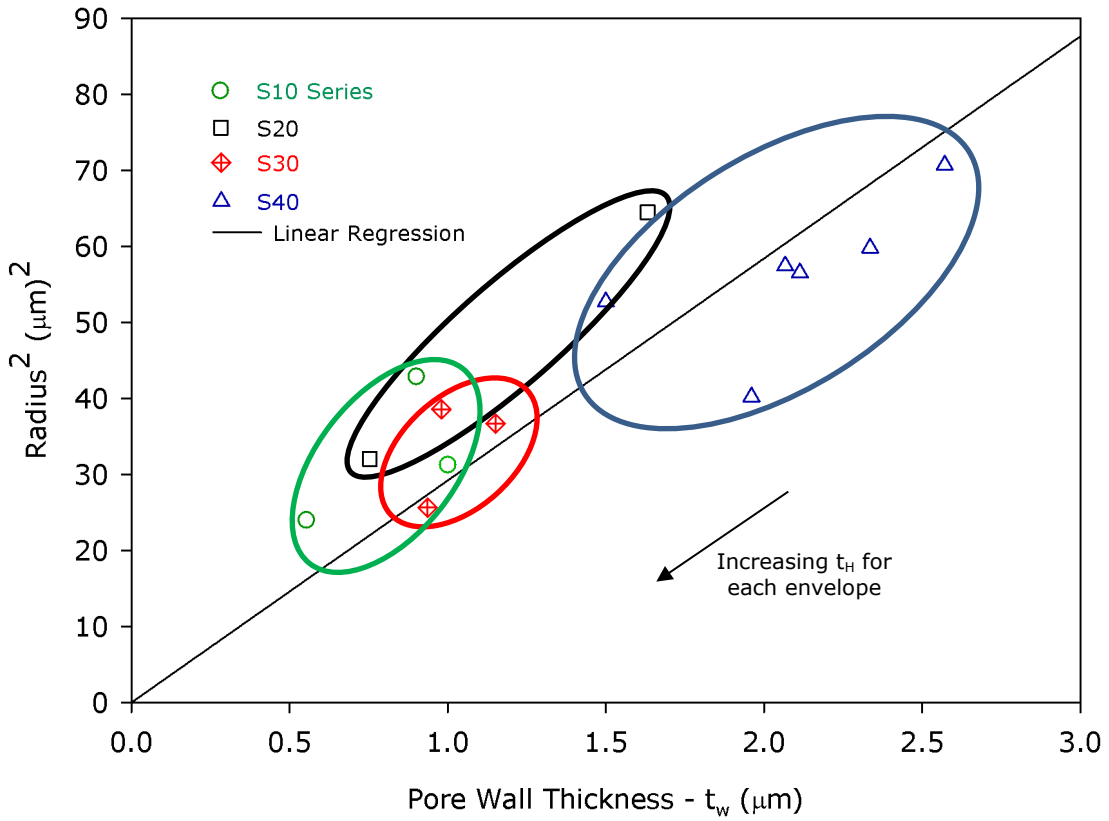

Fig. 4-86: relationship between square of pore radius and pore wall thickness for EPHPs. Homogenisation time t_H increases toward the left for each series envelope.

The radius^2 vs. wall thickness relationship is based on two assumptions: 1) the total solid volume of the system does not change with different stirring conditions and 2)

the volume fraction of the solid material around an idealised spherical pore is obtained by its surface area times its wall thickness, divided by the volume the sphere would occupy.

While the second assumption aims at simplifying the geometry of the pores, the first assumption holds as the processing volume of HIPEs remains constant.

It can then be determined that the PEHPs series envelopes position themselves onto a linear regression curve. Moreover, the increasing solid content implies that the wall thickness increases. The lowest density EPHPs (S10 series) are located at the bottom left of the graph and combine both small radius and wall thickness. As the density increases, the wall thickness and the square of pore radius increase in a rather satisfactory proportional way.

This trend thus reflects and confirms the mechanical behaviour of each EPHPs series as discussed in dedicated sections.

It is worth therefore recalling that the stirring energy input markedly modifies both the pore diameter and wall thickness of EPHPs structure. Thus these two parameters have distinct effects when subjected to compressive stress: a thicker wall reduces buckling by reducing the slenderness of the strut, hence it buckles at higher loads.

On the other hand a smaller pore size with hierarchical distribution reduces the length of the strut, making it inherently capable of bearing higher stresses without collapsing.

In summary, this chapter has presented the remarkable structure-related mechanical properties results obtained by processing high internal phase emulsions (HIPEs). The polymerisation route of HIPEs produced elastic PolyHIPE Polymers (EPHPs). The EPHPs hierarchical open-pore structure was further modified by process variables (increased homogenisation time and solid content). The average pore size and distribution of the hierarchical structure was reduced by increasing the homogenisation stirring time. The reduction in size and distribution resulted in a remarkable increase of mechanical performance.

The modelling of the mechanical properties (Young’s modulus in particular) was based on the Gibson and Ashby model. As this model is based on the bulk material elastic modulus and the relative density the results proved that both these parameters cannot fully capture the unique hierarchical structural features of the EPHPs.

The results in fact showed that the open pore structure is better described by a combination of a linear and a quadratic behaviour. This behaviour further confirms that the EPHPs are structure-dominated materials whose properties can be modified. The processing of the HIPEs is then of fundamental importance and an appropriate degree of control is even more relevant.

Chapter 5 – Conclusions and future work

"Things that are separate shall be united and acquire such virtue that they will restore to man his lost memory".

- Leonardo da Vinci

This chapter presents the conclusions that can be drawn in the light of the experimental and theoretical findings on the EPHPs process-structure property relationship and the future work that should originate from the present work.

5.1. Conclusions

The present study investigated the *Process-Structure–Properties* of Polymerised High Internal Phase Emulsions (PolyHIPEs) as impact resistant materials (IRMs). The unique hierarchical, interconnected porous structure of the elastic PolyHIPE polymers (EPHPs) was compared to that of natural materials such as orange fruit skin, whose noticeable energy absorption properties are related to the varying porosity of the skin.

Two EPHPs processing routes were chosen to mimic the Nature-design of IRMs. The oil-phase to water-phase ratio was varied and EPHPs with higher polymerizable phase content were produced. The other relevant process parameter, the homogenisation time (t_H), was increased to identify its role in modifying the EPHPs hierarchical porous structure.

Both processing routes effects on EPHPs were analysed in terms of structural changes via microscopy, and mechanical behaviour/material properties via mechanical compression testing. Structural modifications in the porous structure occurred and were expressed in terms of average pore diameter and distribution. Pores (or cells) were also characterised in terms of cell wall thickness and intersecting vertex thickness. Mechanical properties such as Young's modulus and specific absorbed energy (SAE) were obtained from stress vs. strain curves.

The two processing routes resulted in changes of EPHPs structure which, in turn, resulted in substantial modification of the mechanical behaviour. An increase of polymerizable phase (solid) content resulted in an almost proportional increase of wall and intersecting vertex thickness. However, with increasing solid content, the amount of material that accumulates at the vertexes is higher than the material that accumulates on the walls. This was found to have a profound effect on the materials behaviour: low solid content EPHPs (10%) behave like foams while

increasing solid content EPHPs (>30%) behave like composite (or spring-like) materials. Young's modulus and SAE increased up to 10 times.

The increase of solid content thus enabled the material to become stiffer and capable of absorbing more energy, while retaining its hierarchical structure. However, it was found that for solid contents exceeding 30%, the use of an oil phase initiator was necessary to obtain satisfactory polymerisation.

Longer homogenisation time t_H reduces the average pore size and narrows the pore distribution while keeping the hierarchical layout. It was also found that the impact of t_H on mechanical performance improvements is greater than that of the solid content: lower solid content EPHPs, processed with longer t_H can in fact match or exceed the mechanical properties of higher solid content EPHPs processed with shorter t_H.

Therefore, the hierarchical layout of the EPHPs plays a fundamental role and structural modification induced by longer t_H further exploit this unique feature.

In the light of the tailorability of the solid content and structure of the EPHPs, the prediction of their Young's modulus has been made by using the Gibson and Ashby model. While this model has been extensively used to predict porous materials properties it was found, as expected, that it could not adequately describe the EPHPs with constant density and varying t_H. Even more importantly, the agreement between the model and varying solid content (density) EPHPs revealed that the bulk material elastic modulus cannot be obtained by the rule of mixtures (i.e. weighted-average of the bulk material constituents). However, only the modulus of increasing solid content EPHPs (with t_H=15 min) is described by the model at an acceptable qualitative level.

It is worth recalling that t_H represents the mixing energy input parameter and it was used to assess qualitatively the EPHPs manufacturing process effectiveness. In particular, the capability of producing EPHPs with increasing solid content was assessed. As the manufacturing process and mixing devices had been originally developed to produce EPHPs with 10-20% solid content, this study has demonstrated that the EPHPs manufacturing process window is wider.

The EPHPs were tested first at room temperature. Later, two additional temperatures were used. Testing the EPHPs at low (2-6°C) and high (45-55°C) temperature revealed that they are almost unaffected by temperature variations. This is an extremely valuable behaviour because it implies that the EPHPs can perform adequately, regardless of the operating temperature.

The mechanical performances of EPHPs as IRMs were compared to those possessed by two commercially available materials. These materials GPhlex and D3O were classified respectively as a stiff-porous foam and a non-porous composite elastic material. Their properties and behaviour are markedly different due to their structure. Although their properties were often better than those of a few EPHPs at room and low temperature, both materials properties were severely affected at high temperature as a result of their lower glass transition temperature. At high temperature almost all the EPHPs performed better than *GPhlex* and *D3O*.

Studies on the combined effects of temperature and compression strain rates on the EPHPs mechanical behaviour were performed and it was confirmed that EPHPs follow the time-temperature equivalence principle. In addition, the rheology of HIPEs was investigated to identify the stability vs. time ranges of the emulsions. The stability of HIPEs was found to be in the range of 15-30 minutes with higher solid content HIPEs in the lower end of the interval. Nevertheless for practical purposes the interval proved to be sufficiently wide.

As EPHPs are structure-dominated materials, it was possible to modify the structure to such an extent that they could deliver better properties when compared to the reference materials, at any temperature. Moreover, EPHPs can not only be processed to have the same *SAE* of GPhlex or D3O materials, but also to behave as *soli-like material* (D3O). This remarkable change in behaviour and improved performances was obtained by much lower density EPHPs, thanks to their highly porous structure.

When the *Material Selection Charts* (or *Ashby Charts*) are used, the EPHPs constitute a new class of materials, as they fill in an existing gap in the Modulus against density chart.

EPHPs can extend the choice of materials available to the material engineer/scientist; in particular EPHPs offer a much lighter alternative.

5.2. Future work

In the light of the remarkably interesting process-structure-properties of EPHPs and their use as IRMs, future work should be highly considered.

First and foremost future work should consider the scale-up of the manufacturing process. In addition, continuous (or semi-continuous) manufacturing processes should be considered in conjunction with the current batch-process. HIPEs are currently produced in a batch reactor at relatively modest quantities (~1/4 of a

litre) and a process capable of producing HIPEs volumes in the range of 2-2.5 litres would represent a one-fold scale up. Such a scale up factor should be obtained with a moderate level of equipment design complexity. Furthermore, no manufacturing process modifications are expected.

Larger HIPEs volumes should be moulded under different conditions (e.g. mould shape(s), filling rate and temperature) and characterised structurally and mechanically to further assess their process-structure-properties relationship. HIPEs stability factors should also be assessed.

Additionally, processing of HIPEs should move from batch to (semi)continuous to enable a higher degree of process control. Although this change may imply substantial layout modifications, the improvements in process control should balance the increased complexity.

Mechanical and structural characterisation of EPHPs should be performed with narrower ranges of solid content EPHPs samples (5% intervals); therefore a more detailed relationship among process, structure and performances would be available. Furthermore, the compression loading should be performed with varying loading and unloading cycles to better characterise the EPHPs visco-elastic behaviour.

Modelling of the EPHPs should be based on a combination of EPHPs structure digital imaging, experimental results and Finite Element Modelling. This approach would enable to identify the combined effects of increased solid content and homogenisation time with a greater level of precision. Automated analysis of structural images should also be performed to obtain a 3D representation of the EPHPs hierarchical structure for a more accurate modelling.

References

Abbasian, Z. and M. R. Moghbeli (2010). *"Open porous emulsion-templated monoliths: Effect of the emulsion preparation conditions on the foam microstructure and properties."* Journal of Applied Polymer Science **116**(2): 986-994.

Abbasian, Z. and M. R. Moghbeli (2011). *"Preparation of highly open porous styrene/acrylonitrile and styrene/acrylonitrile/organoclay polymerized high internal phase emulsion (PolyHIPE) foams via emulsion templating."* Journal of Applied Polymer Science **119**(6): 3728-3738.

Abd El-Sayed, F. K., R. Jones and I. W. Burgess (1979). *"A theoretical approach to the deformation of honeycomb based composite materials."* Composites **10**(4): 209-214.

Ajani, J. (2011). *"The global wood market, wood resource productivity and price trends: an examination with special attention to China."* Environmental Conservation **38**: 53-63.

Akay, G. (1990). *"Flow induced polymer-filler interactions: Bound polymer properties and bound polymer-free polymer phase separation and subsequent phase inversion during mixing."* Polymer Engineering & Science **30**(21): 1361-1372.

Akay, G. (1991). *Agglomerated abrasive materials, compositions comprising same, and processes for its manufacture*.

Akay, G. (1994a). *"Flow-Induced Phase Inversion Agglomeration - Fundamentals and Batch Processing."* Polymer Engineering and Science **34**(11): 865-880.

Akay, G. (1994b). *"Flow induced phase inversion agglomeration: Fundamentals and batch processing."* Polymer Engineering and Science **34**(11): 865-880.

Akay, G. (1998). *"Flow-induced phase inversion in the intensive processing of concentrated emulsions."* Chemical Engineering Science **53**(2): 203-223.

Akay, G. (2001a). *Stable oil in water emulsions and a process for preparing same*, EP Patent 0,649,867.

Akay, G., Z. Bhumgara and R. J. Wakeman (1995a). *"Self-Supported Porous Channel Filtration Modules - Preparation, Properties and Performance."* Chemical Engineering Research & Design **73**(7): 782-797.

Akay, G., Z. Bhumgara and R. J. Wakeman (1995b). *"Self-supported porous channel filtration modules: preparation, properties and performance."* Chemical Engineering Research and Design **73**(A7): 782-797.

Akay, G., M. A. Birch and M. A. Bokhari (2004). *"Microcellular polyHIPE polymer supports osteoblast growth and bone formation in vitro."* Biomaterials **25**(18): 3991-4000.

Akay, G., M. A. Bokhari, V. J. Byron and M. Dogru (2005a). *Development of Nano-Structured Micro-Porous Materials and their Application in Bioprocess–Chemical Process Intensification and Tissue Engineering*, in *Chemical engineering: trends and developments*. M. A. Galán and E. M. d. Valle. Chichester, John Wiley & Sons Ltd**:** 171-197.

Akay, G. and D. R. Burke (2012). *"Agro-Process Intensification through Synthetic Rhizosphere Media for Nitrogen Fixation and Yield Enhancement in Plants."* American Journal of Agricultural and Biological Sciences **7**(2): 150-172.

Akay, G., M. Dogru, B. Calkan and O. F. Calkan (2005b). *Flow-Induced Phase Inversion Phenomenon in Process Intensification and Microreactor Technology*, in *Microreactor Technology and Process Intensification*, American Chemical Society. **914:** 286-308.

Akay, G., S. Downes and V. Price, J. (2000). *Microcellular polymers as cell growth media and novel polymers*. **WO/2000/034454 PCT Publication**.

Akay, G., L. Tong, M.J., Hounslow, A.S., Burbidge (2001b). *"Intensive agglomeration and microencapsulation of powders."* Colloid & Polymer Science **279**: 1118-1125.

Akay, G., Z. Z. Noor and M. Dogru (2005c). *Process Intensification in Water-in-Crude Oil Emulsion Separation by Simultaneous Application of Electric Field and Novel Demulsifier Adsorbers Based on Polyhipe Polymers*, in *Microreactor Technology and Process Intensification*, American Chemical Society. **914:** 378-392.

Akay, G. and L. Tong (2000). *"Polymer dispersion preparation by flow induced phase inversion emulsification. Part 1. The effect of silica on emulsification and dispersion characteristics."* Journal of Materials Science **35**(15): 3699-3709.

Aronson, M. P. and M. F. Petko (1986). *High internal phase emulsions*.

Ashby, F. (2010). *Materials selection in mechanical design, fourth edition*, Elsevier/Butterworth-Heinemann.

Ashby, M. and R. Medalist (1983). *"The mechanical properties of cellular solids."* Metallurgical and Materials Transactions A **14**(9): 1755-1769.

Ashby, M. F. (2011). *Materials selection in mechanical design*. Kidlington, Oxford, UK, Butterworth-Heinemann.

Ashby, M. F. and D. Cebon (1993). *"Materials selection in mechanical design."* Le Journal de Physique IV **3**(C7): C7-1-C7-9.

Ashby, M. F., L. J. Gibson, U. Wegst and R. Olive (1995). *"The Mechanical Properties of Natural Materials. I. Material Property Charts."* Proceedings: Mathematical and Physical Sciences **450**(1938): 123-140.

ASM-International (2003). *Characterization and failure analysis of plastics*. Materials Park, OH, ASM International.

Audiusa.com. (2013). *"Lightweight contruction."* Retrieved 10 April 2013, from http://www.audiusanews.com/imagegallery/view/141/111/audi-techday-lightweight-design.

Bar-Cohen, Y. (2005). *Biomimetics: mimicking and inspired-by biology*. SPIE, San Diego, CA, USA.

Bar-Cohen, Y. (2006). *"Biomimetics—using nature to inspire human innovation."* Bioinspiration & Biomimetics **1**(1): P1.

Barbetta, A. and N. R. Cameron (2004). *"Morphology and Surface Area of Emulsion-Derived (PolyHIPE) Solid Foams Prepared with Oil-Phase Soluble Porogenic Solvents: Span 80 as Surfactant."* Macromolecules **37**(9): 3188-3201.

Barbetta, A., Carnachan, R. J., Smith, K. H., Zhao, C. T., Cameron, N. R., Kataky, R., Hayman, M., Przyborski, S. A., Swan, M. (2005a). *"Porous polymers by emulsion templating."* Macromolecular Symposia **226**: 203-211.

Barbetta, A., Dentini, M., Zannoni, E. M., De Stefano, M. E. (2005b). *"Tailoring the Porosity and Morphology of Gelatin-Methacrylate PolyHIPE Scaffolds for Tissue Engineering Applications."* Langmuir **21**(26): 12333-12341.

Barbetta, A., N.R. Cameron, S.J. Cooper (2000). *"High Internal Phase Emulsions (HIPEs) containing Divinylbenzene and 4-vinylbenzyl chloride and the Morphology of the Resulting PolyHIPE Materials."* Chem. Commun.: 221-222.

Barby, D. and Z. Haq (1982). *Low density porous cross-linked polymeric materials and their preparation and use as carriers for included liquids.* **Eur. Pat. 0,060,138 (assigned to Unilever)**.

Bhumgara, Z. (1995). *"Polyhipe foam materials as filtration media."* Filtration & Separation **32**(3): 245-251.

Bokhari, M. A., G. Akay, S. Zhang and M. A. Birch (2005). *"The enhancement of osteoblast growth and differentiation in vitro on a peptide hydrogel polyHIPE polymer hybrid material."* Biomaterials **26**(25): 5198-5208.

Bowyer, J. L., R. Shmulsky and J. G. Haygreen (2007). *Forest products and wood science : an introduction*. Ames, Iowa, Blackwell Pub.

Boyd, J., C. Parkinson and P. Sherman (1972). *"Factors affecting emulsion stability, and the HLB concept."* Journal of Colloid and Interface Science **41**(2): 359-370.

Brakke, K. A. (1992). *"The surface evolver."* Experimental mathematics **1**(2): 141-165.

Bureau, M. N. (2005). *The relationship between morphology and mechanical properties in thermoplastic foams*, in *Thermoplastic foam processing: principles and development*. R. Gendron. Boca Raton, Fla., CRC Press.

Bureau, M. N. and V. Kumar (2006). *"Fracture toughness of high density polycarbonate microcellular foams."* Journal of cellular plastics **42**(3): 229-240.

Byron, V. J. (2000). *The development of microcellular polymers as support for tissue engineering*. Newcastle Upon Tyne, UK, University of Newcastle.

Callister, W. D. (2000). *Materials science and engineering: an introduction*. New York, Wiley.

Cameron, N. and D. Sherrington (1996a). *High internal phase emulsions (HIPEs) — Structure, properties and use in polymer preparation*, in *Biopolymers Liquid Crystalline Polymers Phase Emulsion*, Springer Berlin / Heidelberg. **126:** 163-214.

Cameron, N. R. (2005). *"High internal phase emulsion templating as a route to well-defined porous polymers."* Polymer **46**(5): 1439-1449.

Cameron, N. R. and A. Barbetta (2000). *"The influence of porogen type on the porosity, surface area and morphology of poly(divinylbenzene) polyHIPE foams."* Journal of Materials Chemistry **10**(11): 2466-2471.

Cameron, N. R. and D. C. Sherrington (1996b). *High Internal Phase Emulsions (HIPEs) - Structure, Properties and Use in Polymer Preparation*. **126:** 162-214.

Cameron, N. R. and D. C. Sherrington (1996c). *"Non-aqueous high internal phase emulsions. Preparation and stability."* Journal of the Chemical Society - Faraday Transactions **92**(9): 1543-1547.

Cameron, N. R. and D. C. Sherrington (1997). *"Preparation and glass transition temperatures of elastomeric PolyHIPE materials."* Journal of Materials Chemistry **7**(11): 2209-2212.

Cameron, N. R., D. C. Sherrington, L. Albiston and D. P. Gregory (1996). *"Study of the formation of the open-cellular morphology of poly(styrene/divinylbenzene) polyHIPE materials by cryo-SEM."* Colloid and Polymer Science **274**(6): 592-595.

Ceglia, G., L. Mahéo, P. Viot, D. Bernard, A. Chirazi, I. Ly, O. Mondain-Monval and V. Schmitt (2012). *"Formulation and mechanical properties of emulsion-based model polymer foams."* The European Physical Journal E **35**(4): 1-11.

Chen, H. H. and E. Ruckenstein (1990). *"Correlation between the stability of concentrated emulsions and the interfacial free energy between the two phases."* Journal of Colloid and Interface Science **138**(2): 473-479.

Chen, P., A. Lin, A. Stokes, Y. Seki, S. Bodde, J. McKittrick and M. Meyers (2008). *"Structural biological materials: Overview of current research."* JOM Journal of the Minerals, Metals and Materials Society **60**(6): 23-32.

DfT. UK Department for Transport, Vehicle Speed Statistics (2012). *"Free Flow Vehicle Speeds in Great Britain 2011."* Retrieved 10 April 2013, from https://www.gov.uk/government/uploads/system/uploads/attachment_data/file/9069/free-flow-vehicle-speeds-2011.pdf.

Dogru, M. and G. Akay (2006). *Gasification*. **U.S. Patent No. 265,954.**

Easterling, K. E., R. Harrysson, L. J. Gibson and M. F. Ashby (1982). *"On the Mechanics of Balsa and Other Woods."* Proceedings of the Royal Society of London. A. Mathematical and Physical Sciences **383**(1784): 31-41.

Eaves, D. (2004). *Handbook of polymer foams*. Shawbury, Shrewsbury, Shropshire, U.K., Rapra Technology.

Erwin, S. I. (2009). *Army Has Few Options to Lessen Weight of Body Armor National Defense*, National Defense Industrial Association.

Fischer, S. F., M. Thielen, R. Loprang, R., R. Seidel, C. Fleck, T. Speck and A. Bührig-Polaczek (2010). *"Pummelos as Concept Generators for Biomimetically Inspired Low Weight Structures with Excellent Damping Properties."* Advanced Engineering Materials **12**(12): B658-B663.

Ford, R. E. and C. G. L. Furmidge (1966). *"Studies at phase interfaces : II. The stabilization of water-in-oil emulsions using oil-soluble emulsifiers."* Journal of Colloid and Interface Science **22**(4): 331-341.

Fratzl, P. (2007). *"Biomimetic materials research: what can we really learn from nature's structural materials?"* Journal of The Royal Society Interface **4**(15): 637-642.

Gadd, C. W. (1962). *Criteria for injury potential*, in *Impact Acceleration Stress Symposium*. Washington, National Academy of Sciences-National Research Council.

Gan, Y. X., C. Chen and Y. P. Shen (2005). *"Three-dimensional modeling of the mechanical property of linearly elastic open cell foams."* International Journal of Solids and Structures **42**(26): 6628-6642.

Gendron, R. (2005). *Thermoplastic foam processing: principles and development*. Boca Raton, Fla., CRC Press.

Gibson, L. J. (1985). *"The mechanical behaviour of cancellous bone."* Journal of Biomechanics **18**(5): 317-328.

Gibson, L. J. (1989). *"Modelling the mechanical behavior of cellular materials."* Materials Science and Engineering: A **110**: 1-36.

Gibson, L. J. (2000). *"Mechanical behavior of metallic foams."* Annual Review of Materials Science **30**(1): 191-227.

Gibson, L. J. and M. F. Ashby (1982). *"The Mechanics of Three-Dimensional Cellular Materials."* Proceedings of the Royal Society of London. A. Mathematical and Physical Sciences **382**(1782): 43-59.

Gibson, L. J. and M. F. Ashby (1997). *Cellular solids: structure and properties*. Cambridge; New York, Cambridge University Press.

Gibson, L. J., M. F. Ashby, G. S. Schajer and C. I. Robertson (1982). *"The Mechanics of Two-Dimensional Cellular Materials."* Proceedings of the Royal Society of London. A. Mathematical and Physical Sciences **382**(1782): 25-42.

Gong, L. and S. Kyriakides (2005). *"Compressive response of open cell foams Part II: Initiation and evolution of crushing."* International Journal of Solids and Structures **42**(5-6): 1381-1399.

Gong, L., S. Kyriakides and N. Triantafyllidis (2005). *"On the stability of Kelvin cell foams under compressive loads."* Journal of the Mechanics and Physics of Solids **53**(4): 771-794.

Gong, L., Kyriakides, S., Jang, W. Y. (2005). *"Compressive response of open-cell foams. Part I: Morphology and elastic properties."* International Journal of Solids and Structures **42**(5-6): 1355-1379.

Goodwin, J. W. (2009). *Colloids and interfaces with surfactants and polymers*. Chichester, U.K., Wiley.

Grenestedt, J. L. (1998). *Influence of imperfections on effective properties of cellular solids*. MATERIALS RESEARCH SOCIETY SYMPOSIUM PROCEEDINGS, DTIC Document.

Griffin, W. C. (1946). *"Classification of surface-active agents by" HLB"."* J Soc Cosmetic Chemists **1**: 311-326.

Haibach, K., A. Menner, R. Powell and A. Bismarck (2006). *"Tailoring mechanical properties of highly porous polymer foams: Silica particle reinforced polymer foams via emulsion templating."* Polymer **47**(13): 4513-4519.

Hainey, P., Huxham, I. M., Rowatt, B., Sherrington, D. C., Tetley, L. (1991). *"Synthesis and ultrastructural studies of styrene-divinylbenzene Polyhipe polymers."* Macromolecules **24**(1): 117-121.

Hough, D., B., Hammond, K., Morris, C., Hammond, Rober C. (1991). *Porous polymeric support containing biological cells in interconnected voids*.

IRTAD. International Traffic Safety Data and Analysis Group, OECD International Transport Forum (2013). *"Road Safety Annual Report 2011."* Retrieved 10 April 2013, from http://internationaltransportforum.org/irtadpublic/pdf/11IrtadReport.pdf.

Jang, W.-Y., A. M. Kraynik and S. Kyriakides (2008). *"On the microstructure of open-cell foams and its effect on elastic properties."* International Journal of Solids and Structures **45**(7–8): 1845-1875.

Jang, W.-Y., S. Kyriakides and A. M. Kraynik (2010). *"On the compressive strength of open-cell metal foams with Kelvin and random cell structures."* International Journal of Solids and Structures **47**(21): 2872-2883.

Jeronimidis, G. and A. G. Atkins (1995). *"Mechanics of biological materials and structures: Nature's lessons for the engineer."* ARCHIVE: Proceedings of the Institution of Mechanical Engineers, Part C: Journal of Mechanical Engineering Science 1989-1996 (vols 203-210) **209**(43): 221-235.

Johnson, W. and S. R. Reid (1977). *"Metallic energy dissipating systems."* ASME Appl. Mech. Rev. **31**: 277-288.

Khemani, K. C. (1997). *Extruded polyester foams*. ACS Symposium Series, ACS Publications.

King, A. I. and D. C. Viano (2000). *Mechanisms of Injury*, in *The Biomedical Engineering Handbook: Second Edition*. J. D. Bronzino. Boca Raton, CRC Press LLC.

Klempner, D., V. Sendijarevi'c and R. M. Aseeva (2004). *Handbook of Polymeric Foams and Foam Technology*, Hanser Gardner Publications.

Kovačič, S., D. Štefanec and P. Krajnc (2007). *"Highly Porous Open-Cellular Monoliths from 2-Hydroxyethyl Methacrylate Based High Internal Phase Emulsions (HIPEs): Preparation and Void Size Tuning."* Macromolecules **40**(22): 8056-8060.

Krajnc, P., N. Leber, D. Štefanec, S. Kontrec and A. Podgornik (2005). *"Preparation and characterisation of poly(high internal phase emulsion) methacrylate monoliths and their application as separation media."* Journal of Chromatography A **1065**(1): 69-73.

Kraynik, A. and D. Reinelt (1999). *Foam microrheology: from honeycombs to random foams*. 15th Annual Meeting Polymer Processing Society.

Kraynik, A., D. Reinelt and H. Princen (1991). *"The nonlinear elastic behavior of polydisperse hexagonal foams and concentrated emulsions."* Journal of Rheology **35**: 1235.

Kunieda, H., N. Yano and C. Solans (1989). *"The stability of gel-emulsions in a water/nonionic surfactant/oil system."* Colloids and Surfaces **36**(3): 313-322.

Kusner, R. and J. M. Sullivan (1996). *"Comparing the Weaire-Phelan equal-volume foam to Kelvin's foam."* Forma **11**(3): 233-242.

Lakes, R. (1993). *"Materials with structural hierarchy."* Nature **361**(6412): 511-515.

Landrock, A. H. (1995). *Handbook of plastic foams: types, properties, manufacture and applications*. Park Ridge, NJ, Noyes Publ.

Laroussi, M., K. Sab and A. Alaoui (2002). *"Foam mechanics: nonlinear response of an elastic 3D-periodic microstructure."* International Journal of Solids and Structures **39**(13): 3599-3623.

Lee, S. T. (2004). *Introduction: Polymeric Foams, Mechanisms and Materials*, in *Polymeric foams: mechanisms and materials*. S. T. Lee and N. S. Ramesh. Boca Raton, CRC Press.

Lee, S. T., C. B. Park and N. S. Ramesh (2007). *Polymeric foams: science and technology*. Boca Raton, CRC/Taylor & Francis.

Lee, S. T. and N. S. Ramesh (2004). *Polymeric foams: mechanisms and materials*. Boca Raton, CRC Press.

Lissant, K. J. (1966). *"The geometry of high-internal-phase-ratio emulsions."* Journal of Colloid and Interface Science **22**(5): 462-468.

Lissant, K. J., B. W. Peace, S. H. Wu and K. G. Mayhan (1974). *"Structure of high-internal-phase-ratio emulsions."* Journal of Colloid and Interface Science **47**(2): 416-423.

Lissner, H. R., M. Lebow and F. Evans (1960). *"Experimental studies on the relation between acceleration and intracranial pressure changes in man."* Surg Gynecol Obstet: 111:329.

Lu, G. and T. Yu (2003). *Energy absorption of structures and materials*. Woodhead; CRC Press, Cambridge ; Boca Raton.

Maheo, L., P. Viot, D. Bernard, A. Chirazi, G. Ceglia, V. Schmitt and O. Mondain-Monval (2013). *"Elastic behavior of multi-scale, open-cell foams."* Composites Part B: Engineering **44**(1): 172-183.

Maiti, S., L. Gibson and M. Ashby (1984). *"Deformation and energy absorption diagrams for cellular solids."* Acta Metallurgica **32**(11): 1963-1975.

Mao, D., T. Li, H. Liu, Z. Li, H. Shao and M. Li (2013). *"Preparation of macroporous polyHIPE foams via radiation-induced polymerization at room temperature."* Colloid and Polymer Science **291**(7): 1649-1656.

Marjoux, D., D. Baumgartner, C. Deck and R. Willinger (2008). *"Head injury prediction capability of the HIC, HIP, SIMon and ULP criteria."* Accident Analysis & Prevention **40**(3): 1135-1148.

Mark, J. E. (2007). *Physical properties of polymers handbook*, Springer New York.

Martini-Vvedensky, J., F. Waldman and N. Suh (1982). *"The production and analysis of microcellular thermoplastic foam."* SPE ANTEC Technical Papers **28**: 674-676.

Martini-Vvedensky, J. E., N. P. Suh and F. A. Waldman (1984). *Microcellular closed cell foams and their method of manufacture*, Massachusets Institute of Technology, Cambridge, Mass.

Mattheck, C. and S. Burkhardt (1990). *"A new method of structural shape optimization based on biological growth."* International Journal of Fatigue **12**(3): 185-190.

Menner, A. and A. Bismarck (2006). *"New Evidence for the Mechanism of the Pore Formation in Polymerising High Internal Phase Emulsions or Why polyHIPEs Have an Interconnected Pore Network Structure."* Macromolecular Symposia **242**(1): 19-24.

Menner, A., K. Haibach, R. Powell and A. Bismarck (2006a). *"Tough reinforced open porous polymer foams via concentrated emulsion templating."* Polymer **47**(22): 7628-7635.

Menner, A., R. Powell and A. Bismarck (2006b). *"Open Porous Polymer Foams via Inverse Emulsion Polymerization: Should the Definition of High Internal Phase (Ratio) Emulsions Be Extended?"* Macromolecules **39**(6): 2034-2035.

Menner, A., M. Salgueiro, M. S. P. Shaffer and A. Bismarck (2008). *"Nanocomposite foams obtained by polymerization of high internal phase emulsions."* Journal of Polymer Science Part A: Polymer Chemistry **46**(16): 5708-5714.

Michler, G. H. (2008). *Electron Microscopy of Polymers*, Springer London, Limited.

Mills, N. J. (2007a). *Polymer foams handbook : engineering and biomechanics applications and design guide*. Oxford, Butterworth Heinemann.

Mills, N. J. (2007b). *Polymer foams handbook: engineering and biomechanics applications and design guide*. Oxford, Butterworth Heinemann.

Moghbeli, M. R. and M. Shahabi (2011). *"Morphology and Mechanical Properties of an Elastomeric Poly (HIPE) Nanocomposite Foam Prepared via an Emulsion Template."* Iranian Polymer Journal **20**(5): 343-355.

Naik, R. R. and M. O. Stone (2005). *"Integrating biomimetics."* Materials Today **8**(9): 18-26.

Onck, P. R., E. W. Andrews and L. J. Gibson (2001). *"Size effects in ductile cellular solids. Part I: modeling."* International Journal of Mechanical Sciences **43**(3): 681-699.

Osswald, T. A., L. S. Turng and P. J. Gramann (2008). *Injection molding handbook*, Hanser Gardner Publications.

Ostwald, W. (1910). *"Beiträge zur Kenntnis der Emulsionen."* Colloid and Polymer Science **6**(2): 103-109.

Painter, P. C. and M. M. Coleman (2008). *Essentials of Polymer Science and Engineering*, Destech Publications Incorporated.

Pakeyangkoon, P., R. Magaraphan, P. Malakul and M. Nithitanakul (2008). *"Effect of Soxhlet Extraction and Surfactant System on Morphology and Properties of Poly(DVB)PolyHIPE."* Macromolecular Symposia **264**(1): 149-156.

Papka, S. D. and S. Kyriakides (1994). *"In-plane compressive response and crushing of honeycomb."* Journal of the Mechanics and Physics of Solids **42**(10): 1499-1532.

Paul, E. L., V. A. Atiemo-Obeng and S. M. Kresta (2010). *Handbook of industrial mixing : science and practice*. Hoboken, Wiley-Interscience.

Pearce, P. (1990). *Structure in Nature is a Strategy for Design*, Mit Press.

Pötsch, G. and W. Michaeli (2008). *Injection molding: an introduction*, Hanser Gardner Publications.

Roberts, A. and E. Garboczi (2002a). *"Elastic properties of model random three-dimensional open-cell solids."* Journal of the Mechanics and Physics of Solids **50**(1): 33-55.

Roberts, A. and E. J. Garboczi (2002b). *"Computation of the linear elastic properties of random porous materials with a wide variety of microstructure."* Proceedings of the Royal Society of London. Series A: Mathematical, Physical and Engineering Sciences **458**(2021): 1033-1054.

Roberts, A. P. and E. J. Garboczi (2001). *"Elastic moduli of model random three-dimensional closed-cell cellular solids."* Acta materialia **49**(2): 189-197.

Roeder, R. K. (2010). *"A Paradigm for the Integration of Biology in Materials Science and Engineering."* Jom **62**(7): 49-55.

Ruckenstein, E., G. Ebert and G. Platz (1989). *"Phase behavior and stability of concentrated emulsions."* Journal of Colloid and Interface Science **133**(2): 432-441.

Sawyer, L. C., D. T. Grubb and G. F. Meyers (2008). *Polymer microscopy*. New York, Springer.

Schmitt, O. (1969). *Some interesting and useful biomimetic transforms*. *Third International Biophysics Congress***:** 297.

Schraad, M. W. (2007). *"The influence of dispersity in geometric structure on the stability of cellular solids."* Mechanics of Materials **39**(2): 183-198.

Schramm, L. L. (2005). *Emulsions, foams, and suspensions : fundamentals and applications*. Weinheim; [Great Britain], Wiley-VCH.

Seidel, R., M. Thielen, C. Schmitt, A. Bührig-Polaczek, C. Fleck and T. Speck (2010). *Fruit walls and nut shells as an inspiration for the design of bio-inspired impact resistant hierarchically structured materials*, in *Nature and Design V*. C. A. Brebbia, Carpi, A. Southampton, WIT Press**:** 421-430.

Sergienko, A. Y., H. Tai, M. Narkis and M. S. Silverstein (2002). *"Polymerized high internal-phase emulsions: Properties and interaction with water."* Journal of Applied Polymer Science **84**(11): 2018-2027.

Shinoda, K. and H. Arai (1964). *"The Correlation between Phase Inversion Temperature In Emulsion and Cloud Point in Solution of Nonionic Emulsifier."* The Journal of Physical Chemistry **68**(12): 3485-3490.

Shinoda, K. and S. Friberg (1986). *Emulsions and solubilization*, Wiley New York et al.

Silva, M. J. and L. J. Gibson (1997). *"The effects of non-periodic microstructure and defects on the compressive strength of two-dimensional cellular solids."* International Journal of Mechanical Sciences **39**(5): 549-563.

Silva, M. J., W. C. Hayes and L. J. Gibson (1995). *"The effects of non-periodic microstructure on the elastic properties of two-dimensional cellular solids."* International Journal of Mechanical Sciences **37**(11): 1161-1177.

Silverstein, M. S., H. Tai, A. Sergienko, Y. Lumelsky and S. Pavlovsky (2005). *"PolyHIPE: IPNs, hybrids, nanoscale porosity, silica monoliths and ICP-based sensors."* Polymer **46**(17): 6682-6694.

Simone, A. E. and L. J. Gibson (1998). *"Effects of solid distribution on the stiffness and strength of metallic foams."* Acta Materialia **46**(6): 2139-2150.

Singh, S. N. (2004). *Blowing agents*, in *Handbook of Polymer Foams*. D. Eaves. Shawbury, Shrewsbury, Shropshire, U.K., Rapra Technology.

Small, P. W. and D. C. Sherrington (1989). *"Design and application of a new rigid support for high efficiency continuous-flow peptide synthesis."* Journal of Chemical Society. Chemical Communications: 1589-1591.

Speck, T. and O. Speck (2008). *Process sequences in biomimetic research*, Algarve.

Tai, H., A. Sergienko and M. S. Silverstein (2001). *"Organic-inorganic networks in foams from high internal phase emulsion polymerizations."* Polymer **42**(10): 4473-4482.

Thomas, N. L. (2004). *Rigid PVC foam*, in *Handbook of polymer foams*. D. Eaves. Shawbury, Shrewsbury, Shropshire, U.K., Rapra Technology.

Throne, J. L. (2004). *Thermoplastic foam extrusion: an introduction*, Hanser Gardner Publications.

Timoshenko, S. P. and J. M. Gere (1961). *Theory of elastic stability*, Tata McGraw-Hill Education.

UN. United Nations Economic Commissions for Europe (2010). *"Improving Global Road Safety: Setting Regional and National Road Traffic Casualty Reduction Targets."* Retrieved 10 April 2013, from http://www.oecd.org/aidfortrade/48179248.pdf.

Versace, J. (1970). *A review of the severity index. . In Proceedings of the 15th Stapp Car Crash Conference***:** pp 771–796.

Vincent, J. F. V. (2009). *"Biomimetics – a review."* Proceedings of the Institution of Mechanical Engineers, Part H: Journal of Engineering in Medicine **223**(8): 919-939.

Vincent, J. F. V., O. A. Bogatyreva, N. R. Bogatyrev, A. Bowyer and A.-K. Pahl (2006). *"Biomimetics: its practice and theory."* Journal of The Royal Society Interface **3**(9): 471-482.

Wakeman, R. J., Z. G. Bhumgara and G. Akay (1998). *"Ion exchange modules formed from polyhipe foam precursors."* Chemical Engineering Journal **70**(2): 133-141.

Warren, W. E. and A. M. Kraynik (1987). *"Foam mechanics: the linear elastic response of two-dimensional spatially periodic cellular materials."* Mechanics of Materials **6**(1): 27-37.

Warren, W. E. and A. M. Kraynik (1988). *"The Linear Elastic Properties of Open-Cell Foams."* Journal of Applied Mechanics **55**(2): 341-346.

Warren, W. E. and A. M. Kraynik (1991). *"The Nonlinear Elastic Behavior of Open-Cell Foams."* Journal of Applied Mechanics **58**(2): 376-381.

Weaire, D. and R. Phelan (1994). *"A counter-example to Kelvin's conjecture on minimal surfaces."* Philosophical Magazine Letters **69**(2): 107-110.

Wegst, U. G. K. and M. F. Ashby (2004). *"The mechanical efficiency of natural materials."* Philosophical Magazine **84**(21): 2167 - 2186.

Williams, J. M. (1991). *"High internal phase water-in-oil emulsions: Influence of surfactants and cosurfactants on emulsion stability and foam quality."* Langmuir **7**(7): 1370-1377.

Williams, J. M., A. J. Gray and M. H. Wilkerson (1990). *"Emulsion stability and rigid foams from styrene or divinylbenzene water-in-oil emulsions."* Langmuir **6**(2): 437-444.

Williams, J. M. and D. A. Wrobleski (1988). *"Spatial distribution of the phases in water-in-oil emulsions. Open and closed microcellular foams from cross-linked polystyrene."* Langmuir **4**(3): 656-662.

Williams, M. L., R. F. Landel and J. D. Ferry (1955). *"The temperature dependence of relaxation mechanisms in amorphous polymers and other glass-forming liquids."* Journal of the American Chemical Society **77**(14): 3701-3707.

Wong, L. L. C., P. M. Baiz Villafranca, A. Menner and A. Bismarck (2013). *"Hierarchical Polymerized High Internal Phase Emulsions Synthesized from Surfactant-Stabilized Emulsion Templates."* Langmuir **29**(20): 5952-5961.

Wong, L. L. C., V. O. Ikem, A. Menner and A. Bismarck (2011). *"Macroporous Polymers with Hierarchical Pore Structure from Emulsion Templates Stabilised by Both Particles and Surfactants."* Macromolecular Rapid Communications **32**(19): 1563-1568.

Wu, R., A. Menner and A. Bismarck (2010). *"Tough interconnected polymerized medium and high internal phase emulsions reinforced by silica particles."* Journal of Polymer Science Part A: Polymer Chemistry **48**(9): 1979-1989.

Yildiz, E., A. Nuhoglu, B. Keskinler, G. Akay and B. Farizoglu (2003). *"Water softening in a crossflow membrane reactor."* Desalination **159**(2): 139-152.

Zhang, Q. and M. Xanthos (2004). *Material Properties Affecting Extrusion Foaming*, in *Polymeric foams: mechanisms and materials*. S. T. Lee and N. S. Ramesh. Boca Raton, CRC Press.

Zhou, Q. (2001). *Applications of cellular materials and structures in vehicle crashworthiness and occupant protection*, World Scientific, Singapore.

Zhu, H. X., J. F. Knott and N. J. Mills (1997a). *"Analysis of the elastic properties of open-cell foams with tetrakaidecahedral cells."* Journal of the Mechanics and Physics of Solids **45**(3): 319-325.

Zhu, H. X., N. J. Mills and J. F. Knott (1997b). *"Analysis of the high strain compression of open-cell foams."* Journal of the Mechanics and Physics of Solids **45**(11-12): 1875-1899.

Zhu, H. X. and A. H. Windle (2002). *"Effects of cell irregularity on the high strain compression of open-cell foams."* Acta Materialia **50**(5): 1041-1052.